UNIVERSITY OF
BIRMINGHAM

Mechanical Characterization of Therapeutic Cells and Physical Property-based Sorting in Microfluidic Systems

By

Mingming Du

A thesis submitted to
The University of Birmingham
For the degree of
DOCTOR OF PHILOSOPHY

School of Chemical Engineering
The University of Birmingham
United Kingdom

April 2017

Abstract

Bone marrow-derived mesenchymal and hematopoietic stem cells (MSCs and HSCs) have rapidly become the leading cells for consideration to aid tissue regeneration following injury. T cell therapy has also generated significant interest clinically for a different class of diseases. However, potential HSCs and MSCs migration to the injured tissue after infusion is impeded by cell trap within the upstream vessels, where physical and mechanical properties of cells play an important role. Pre-treating murine HSCs with inflammatory cytokines has previously been shown to significantly enhance their adhesion to injured tissues compared to pre-treatment of the cells with phosphate buffered saline (PBS) as control. In T cell therapy, the separation of Ag-specific T cells is challenging, which is considered to be a limiting step.

Microfluidic system has a potential to sort cells/particles based on their mechanical properties. It is hypothesized that such sorting system could be utilized to separate smaller and more deformable SCs from a cell population, infusion of which might be able to enhance the recruitment of the cells. It is also proposed that microfluidic device can be potentially utilized to separate Ag-specific T cells if activated T cells obtain different biophysical and mechanical properties from those before activation.

The mechanical properties of murine HSCs were determined and compared to murine blood neutrophils and also to murine MSCs using micromanipulation and atomic force microscopy (AFM). Moreover, the biomechanical changes of CD8+ T cells following antigen (Ag)-induced stimulation were measured. Straight and curved Microfluidic devices were fabricated to separate sub-set of HSCs, followed by the infusion of the isolated cells into ischemia-reperfusion injured animals.

It has been found that HSCs and MSCs were larger in size compared to blood neutrophils. Neutrophils and HSCs could be compressed to rupture, while MSCs did not demonstrate obvious rupture force in micromanipulation compression. Both nominal rupture stress and tension, indicative of the cellular mechanical strength, was significantly greater for neutrophils when compared to HSCs. The Young's modulus values calculated based on the force versus displacement data up to a nominal deformation of 60% determined by micromanipulation for neutrophils, HSCs and MSCs were 24.0 ± 1.8 kPa, 18.1 ± 1.3 kPa and 15.6 ± 1.2 kPa respectively. HSCs as a whole became weaker and more deformable after pre-treatment with SDF-1α and H_2O_2, but HSC surface stiffened after the same pre-treating, accompanied by the expansion and polymerization of F-actin interacting with the plasma membrane. A spiral microfluidic system with channel width 300 μm and height 40 μm was found to effectively isolate smaller and more deformable HSCs from a cell population, resulting in a significant increase of free flowing cells in vivo. Moreover, a preliminary study of CD8+ T cells showed unique biomechanical changes of activated T cells which may be utilized as a marker in future separation of the cells in microfluidic systems.

This study comprehensively characterized cell mechanics at different levels using micromanipulation and AFM, determining mechanical markers of therapeutic cells. Most importantly, a simple cell sorting system was successfully developed to isolate target cells without introducing any chemical modification, and the possible underlying mechanism was discussed, which can be valuable to cellular therapy.

Acknowledgement

My greatest thanks must go to Professor Zhibing Zhang for his invaluable guidance, advice and patience, without which this work would not have been done. I must also thank Dr Neena Kalia for her effort and time, especially her support in improving my writing and presentation skills. Dr Dean Kavanagh's contribution to this project is irreplaceable, and I appreciate his sense of humour which often made things amusing.

I also would like to thank Dr Frederick Chan and Mr Guido Frumento from the Institute of Immunology and Immunotherapy for their guidance and collaboration in the project.

I am grateful to the people in the labs, both in the School of Chemical Engineering and Institute for Biomedical Research. My thanks go to Mr Teddy Liu, Dr James Bowen and Mr Alessandro Di Maio for their training and help in using various instruments, Professor Colin Thomas for his constructive suggestions, and Dr Yan Zhang for his well-experienced insights into PhD studies. And all the other excellent colleagues in the Group of Micromanipulation for their hands-on help and support, including Javier Marques De Marino, Bingyu Zhuo, Tom Simons, Xiaotong Zhang, Cong Sui and Andrew Grey.

Ultimately, I want to express my immense love for my family for their spiritual understanding and support, which keep me going throughout everything.

Content

List of Figures

List of Tables

Nomenclature

Symbol	Definitions
a	Diameter of cells/particles, m
AFM	Atomic Force Microscopy
AR	Aspect Ratio (width/height) of rectangular channel
d	Cell diameter, m
De	Dean number
D_h	Hydraulic diameter of channel, m
E	Young’s modulus, Pa
F	Applied force, N
FACS	Fluorescent Activated Cell Sorting
F_L	Inertial lift force, N
f_L	Non-dimensional lift coefficient
F_{LS}	Shear gradient-induced lift force, N
F_{LW}	Wall-induced inertial lift force, N
F_R	Rupture force, N
H_2O_2	Hydrogen peroxide
HSC	Haematopoietic Stem Cell
KC	Keratinocyte chemoattractant
MACS	Magnetic-activated Cell Sorting
MSC	Mesenchymal Stem Cell
R	Curvature radius of curved channel, m
R_c	Original cell/AFM tip radius, m
Re	Reynolds number
SC	Stem Cell
SDF-1α	Stromal cell-derived factor 1
SCF	Stem Cell Factor

SEM	Standard Error of Mean
T_R	Nominal rupture tension, Pa
U	Average velocity, m/s
δ	Diametric compressive displacement, m
θ	Curvature ratio (channel size/diameter of curvature)
κ	Blockage ratio (cell size/channel height)
μ	Dynamic viscosity, Pa·s
ρ	Fluid density, kg/m^3
σ_R	Nominal rupture stress, Pa
υ	Poisson’s ratio

Chapter 1

General Introduction and Literature Survey

1.1 Stem Cells for Regenerative Medicine

Stem cells (SCs) are a group of ‘immature’ cells which could divide to renew themselves but also, under certain physiologic or experimental conditions, be induced to differentiate into specialised, mature cell types with different functions depending on their origin. They can be isolated from many places in the body. Embryonic SCs (ESCs) are pluripotent SCs obtained from the inner cell mass of the embryo and are able to differentiate into any tissue or organ cell (Shamblott *et al.,* 1999, Yu *et al.,* 2007, Takahashi *et al.,* 2007). Until 2006, ESCs were considered the only type of pluripotent SC. However, Takahashi and Yamanaka conducted seminal research whereby they reprogrammed adult somatic skin cells, with only four regulatory embryogenesis-related genes, to generate a new class of pluripotent SC which they called induced pluripotent SCs (iPSCs or iPS cells) (Takahashi and Yamanaka 2006). These iPS cells can also differentiate into any tissue type (Takahashi *et al.,* 2007, Park *et al.,* 2008).

Other classes of SCs, that are not pluripotent, also exist in various sites in the body. The most characterised are the haematopoietic SCs (HSCs), which are multipotent cells located in the bone marrow (BM), where they reconstitute the entire hematopoietic system. Transplantation of HSCs has been used clinically for many decades as a successful treatment for irradiation injuries, haematological and lymphoid cancers and many other disorders (Gunsilius *et al.,* 2001, Copelan, 2006). Mesenchymal stem cells (MSCs) are also multi-lineage SCs that can be isolated from many sites in the body, most commonly including the BM, adipose tissue, foetal tissue (placenta, Wharton’s jelly) and amniotic fluid. MSCs can differentiate into many tissues of mesodermal origin including hematopoietic support tissue, chondrocytes, adipocytes, osteoblasts and myoblasts (Johnstone *et al.,* 1998).

Since these various types of SCs can differentiate into many different types of adult specialised cells, there have been significant interests in using them for regeneration and repair of human tissue and organs affected by disease, trauma and ageing. Although there are ethical concerns with using ESCs, adult BM-derived SCs such as HSCs and MSCs have recently been involved in a number of clinical trials both nationally and internationally for treating various disorders. Experimental and clinical investigations provide particular optimism for their use in treating ischemic and inflammatory conditions (Ankrum and Karp, 2010), improving cardiac function (Boyle *et al.*, 2006, Segers and Lee, 2008, Garbern and Lee, 2013), regenerating liver and combatting neurological disorders (Sato *et al.*, 2005, Aurich *et al.,* 2007, Einstein and Ben-Hur, 2008).

1.2 Bone Marrow-derived Adult Stem Cells

1.2.1 Haematopoietic Stem Cells

Haematopoietic SCs (HSCs) are multipotent cells, found primarily in the SC niche of the BM, and give rise to and replenish all types of differentiated blood cells on a daily basis (**Figure 1.1**). HSCs are relatively rare cells comprising approximately 0.01 - 0.15% of the BM cells. They can be classified as long-term and short-term HSCs depending on their capacity for sustained BM reconstitution (Rennert *et al.*, 2012). The existence of HSCs was initially identified when a series of BM transplantation experiments protected humans exposed to minimum lethal doses of irradiation or chemotherapy (Barnes *et al.,* 1956). Thereafter, it was discovered that the BM contained highly proliferative progenitor cells being able to give rise to individual colonies of myeloid, erythroid and lymphocytes, as well as self-renewal and so were subsequently defined as HSCs (Morrison *et al.*, 1995). Since their discovery, advances in technology have made it possible to purify and characterize HSCs (Zsebo *et al.*, 1990, Goodell *et al.*, 1996, Gallacher *et al.*, 2000). HSC transplantation, which has replaced the term BM transplantation, is the most established form of cellular therapy and is currently used worldwide in the treatment of a variety of hematologic malignancies, immunodeficiency states, metabolic disorder and defective hematopoietic states (Buckley *et al.*, 1999, Lyden *et al*., 2001, Lazarus *et al.,* 2005). The practical progress and clinical issues in every aspect of this field were specifically discussed in the book titled "***Hematopoietic Stem Cells Transplantation in Clinical Practice"*** (Treleaven and Barrett, 2009).

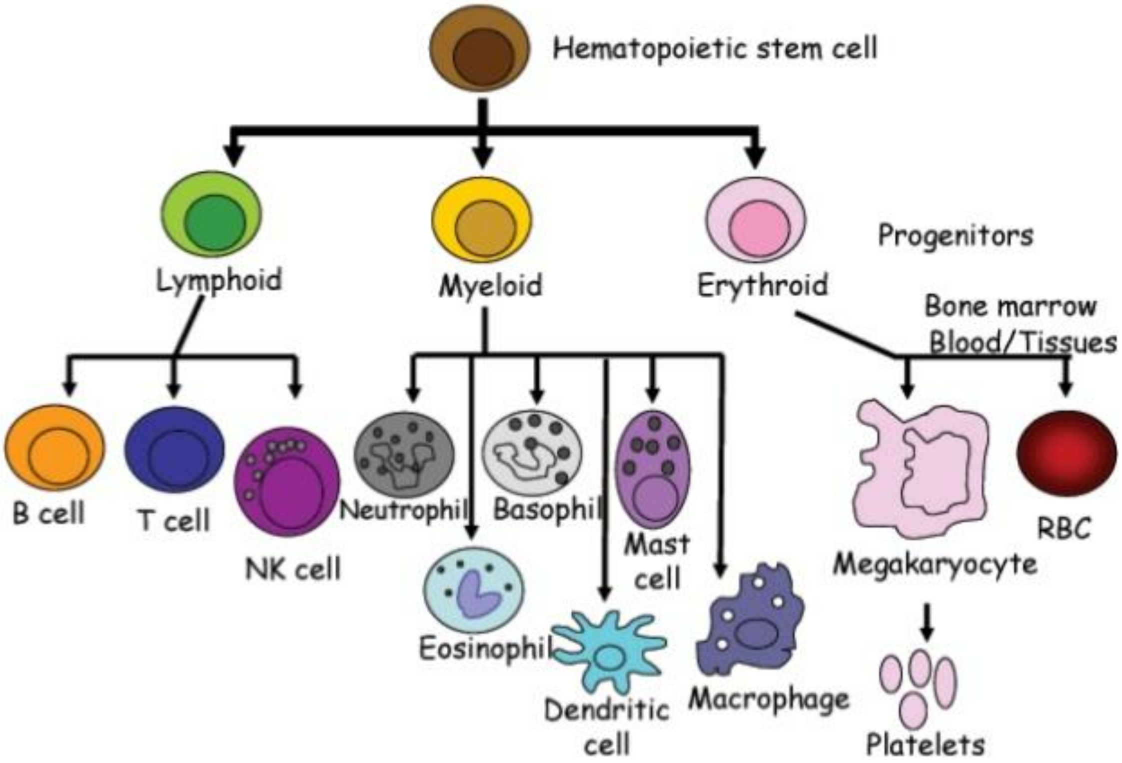

Figure 1.1. Schematic of hematopoietic development. The maintainance of the hematopoietic system is realised through differentiation of HSCs into all of the different mature blood cell types. When they proliferate, some of their daughter cells remain as HSCs, and other daughters of HSCs can be divided into three groups: (1) the lymphoid progenitor cells give rise to lymphocytes (T-cells and B-cells) and NK cells of adaptive immune system; (2) myeloid progenitor cells divide into neutrophils, eosinophil, basophils and other cell types involving in diverse roles as innate immunity, adaptive immunity and blood clotting; and (3) Erythroid progenitor cells can generate a group of short-lived cells, including blood red cells and platelets keeping the proper function of circulatory system (Zon, 1995).

1.2.2 Mesenchymal Stem Cells

The adult BM is composed of haematopoietic tissue but also associated with supporting stroma. Within the stroma, a subset of cells with multipotent differentiation capacity exists called MSCs or marrow stromal cells. These are also a rare (0.01% to 0.001%) population of SCs. Unlike HSCs which appear relatively smaller and more spherical in culture, MSCs are larger fibroblast-like cells that are thought to be essential in supporting the haematopoeisis function of HSCs. These progenitor stromal cells are also able to self-renew and tri-different into cartilage (chondrocytes), bone (osteoblasts) and adipose (adipocytes) tissue. Indeed, the ability to tri-differentiate and be plastic adherent in culture is experimentally one of the standard, key criteria that needs to be met to classify SCs as MSCs. However, depending on the culture conditions, MSCs can also differentiate into mesodermal cells, endothelial, epithelial, muscle and neural cells as well as forming haematopoiesis-supporting stroma, cartilage, bone and adipocytes (Rojas *et al.,* 2005, Zhao *et al.,* 2002). This multi-differentiation potential makes MSCs promising candidates for SC-based therapy and tissue engineering. Several studies have demonstrated that engraftment of allogeneic BM transplantation is a promising approach for treatment of children with the brittle bone disease, osteogenesis imperfecta (Horwitz *et al.,* 1999). Investigations have found in animal models that they can also enhance the engraftment of donor HSCs into the BM after co-transplantation and regenerate the BM microenvironment after myeloablative therapy (Koç *et al.,* 2000; Anklesaria *et al.*, 1987, Almeida-Porada *et al.,* 1999).

1.3 Using HSCs and MSCs for Regenerative Purposes

1.3.1 Mechanisms of HSC and MSC Mediated Tissue Repair

The therapeutic potential of adult BM-derived HSCs and MSCs has been investigated on an upward slope for tissue regeneration and repair. Endogenous HSCs have been experimentally and clinically demonstrated to mobilise from the BM into the peripheral blood and then travel via the circulation to enrich near sites of injuries resulting from inflammatory and wound-response stimuli (Whetton and Graham, 1999). Since they are rare cells, this phenomenon is not observed readily. Although mobilization of endogenous HSCs from the BM can be enhanced, it still does not appear to deliver sufficient numbers into the peripheral blood to be therapeutically effective. Therefore, isolated and subsequently culture-expanded exogenous HSCs are considered ideal for therapeutic purposes. Recent evidence suggests exogenously transplanted HSCs are able to contribute to the regeneration and repair of a number of organs. In the injured kidney, HSCs promote the proliferation of both vascular endothelial and epithelial cells (Lin *et al.*, 2003, Li *et al.*, 2010). HSCs have also been shown to facilitate regeneration of injured liver by either generating epithelial cells or altering the inflammatory response (Dalakas *et al.,* 2005, Jang *et al.*, 2004). Studies have also shown the ability of HSCs to generate cardiomyocytes through cell fusion in mice subjected to acute myocardial infarction (Nygren *et al.*, 2004). These early studies eluded to tissue repair by recruited HSCs being realized by one or more mechanisms including direct replacement of damaged cells, differentiation into the desired cells/tissue or fusion with host tissue cells. However, this concept of HSC ‘plasticity' has been disregarded and more recent evidence suggests a host of paracrine factors are released locally by HSCs and that it is these that modify the response to injury. Secretion of growth factors helps to stimulate local SC growth and differentiation and/or secretion of homing signals help recruit distant SCs (Ährlund-Richter *et al*., 2009). Furthermore, HSCs are also thought to release paracrine factors that can confer, anti-inflammatory, immunomodulatory and vasculoprotective effects (Baraniak and McDevitt, 2010).

Similar observations have been made for MSCs. Though transplantation of MSCs was initially proposed as a therapeutic approach by utilising their SC-like properties, their therapeutic function were benefited from other characteristics, such as anti-proliferative, anti-inflammatory and immunomodulatory qualities (Uccelli *et al.*, 2008; Baraniak and McDevitt, 2010). They are thought to protect injured neurons through secretion of anti-apoptotic, anti-inflammatory and trophic molecules (Li *et al.*, 2002). In spite of limitations in the existing knowledge of MSCs behaviors in disease treatment, researchers are very optimistic about their potential to treat disorders such as diabetes (Urban *et al.,* 2008), spinal cord injury (Syková *et al.,* 2006), liver disease (Kuo *et al.,* 2008), and lung cancer (Rojas *et al.,* 2005). Indeed, their capacity for immunomodulatory and anti-inflammatory effects seems somewhat greater than HSCs.

1.3.2 Mechanisms of Transplanted HSC and MSC Recruitment to Sites of Tissue Injury

Regardless of the mechanism of repair, both HSC and MSC therapy is dependent on successful engraftment of these cells within the site of injury after their systemic delivery into the bloodstream. Although local transplantation or injection directly into the injury site has been used to deliver cells, systemic infusion is considered the more preferable route for safety and broad application concerns (Karp and Teo, 2009). If HSC/MSC infusion is to assist therapy, a better knowledge of the parameters modulating engraftment to injured sites is critical for development of strategies to increase their recruitment and thus maximise their therapeutic potential. Engraftment is a multi-step process whereby HSCs/MSCs circulating in the peripheral blood firstly need to be recruited by the local injured tissue microcirculation, from where they must subsequently transmigrate into the surrounding parenchyma of the injured tissue. SC 'homing' to sites of injury refers to the phenomenon whereby circulating SCs migrate or traffick to an organ and then become retained within it through firm adhesive interactions with the microvascular endothelium. The precise mechanism that govern HSC homing to sites of injury and subsequent engraftment have been recently identified and appear to vary somewhat depending on the organ (Kavanagh *et al.,* 2011; Kavanagh *et al.,* 2013a; Kavanagh *et al.,* 2013b). Generally, adhesion molecule phenotypes are similar between HSCs and blood neutrophils, demonstrating that their recruitment follows a similar pathway used by these inflammatory cells (Kobayashi *et al.,* 1994, Turner *et al.*, 1995).

Neutrophils, continuously released from the BM, are the most abundant type of white blood cell. They are well recognised as essential players in the immune system providing the first line of defense and resistance to microbial attack. Their microvascular recruitment follows a well characterised, sequential and multistep adhesion cascade. During the inflammatory response, neutrophils when trafficking through the inflamed region, encounter a host of soluble inflammatory chemokines and cytokines. Through a series of intracellular signaling pathways, they mediate the up-regulation of adhesion molecules on the activated neutrophil surface and also induce the expression of counter-ligands on the vascular endothelium. These inflammatory stimuli include in particular tumour necrosis factor-α (TNF-α) and interleukin-1 (IL-1β). Oxygen derived free radicals, such as hydrogen peroxide (H_2O_2) can also be present, particularly in ischemic inflammatory tissues, and can also activate neutrophils. These activated free-flowing cells firstly roll on the vessel wall, then arrest as their surface adhesion molecules interact with appropriate counter-ligands expressed on the endothelial surface leading to their firm adhesion. After neutrophils arrest, intracellular signaling leads to leukocyte spreading, followed by apical migration and diapedesis to the injured or inflammatory site.

Similar to leukocytes, both HSCs and MSCs also undergo a sequence of adhesion steps involving complex signaling cascades. The initial adhesion is a rolling interaction between HSCs (less so for MSCs) and the vascular endothelium which is transient and reversible. Captured cells are then firmly arrested as they encounter local inflammatory chemokines (Butcher, 1991, Rüster *et al.*, 2006, Kavanagh and Kalia, 2011). Interestingly, the cytokines and chemokines that activate HSCs and MSCs are similar to those used by neutrophils, although stromal cell derived factor-1α (SDF-1α) is a particularly potent HSC activator. Furthermore, the repertoire of adhesion molecules utilised to permit adhesive events is also similar (Sohni and Verfaillie 2013).

1.3.3 Current Challenges in Stem Cell Recruitment for Tissue Repair

Despite that the number of experimental and clinical studies using adult HSCs/MSCs for various disorders has been increased significantly, overall clinical success has been transient and modest. There are a number of factors that can explain this poor outcome which include not fully knowing which SC type is most therapeutically effective, poor delivery and retention of SCs within sites of injury after systemic infusion, not knowing how many cells that actually deliver and not fully understanding the exact basic mechanisms by which they may be therapeutic.

1.3.3.1 Pulmonary Entrapment of Stem Cells

Although a number of challenges have been raised, one of the key factors hindering SC therapy to date is regarding the injured tissue retention of potentially therapeutic HSCs and MSCs, with few SCs actually reaching the site of injury after systemic infusion. The vast majority of cells, particularly the larger MSCs, have been identified in off-target sites such as the lungs – a phenomenon described as the 'pulmonary first-pass effect' (Fischer *et al.,* 2009). This describes the non-specific clogging or entrapment of SCs within the pulmonary capillaries of small diameter as they first pass through the lungs after injection into the bloodstream. This event is significant and leaves few, if any, cells in the peripheral blood thus reducing the number of SCs available for homing to injury sites. There is little doubt that therapeutic efficacy is limited due to the failure of sufficient homing of SCs, even if a large number of cells are infused.

To address this issue, the factors affecting cell trapping in the lungs were investigated. Studies performed by Schrepfer and colleagues suggested that smaller microspheres (4-5 µm) could pass through the lungs freely, while the majority of bigger microspheres (10-15 µm) and MSCs (15-19 µm) were trapped within the pulmonary system (Schrepfer *et al.,* 2007). This demonstrated that the mean size of suspended MSCs was much larger than the size of pulmonary capillaries. Though HSCs have a smaller size compared with

MSCs, their diameter is still larger than expected to pass through the tiny pulmonary capillaries. In an attempt to reduce the pulmonary first-pass effect, Fischer and colleagues demonstrated that pre-treatment of animals with antibodies to key endothelial adhesion molecules, namely P-selectin or vascular cell adhesion molecule-1 (VCAM-1), did not change the MSC number escaping from the lungs. However, inactivating an MSC surface adhesion molecule, namely the integrin VLA-4 that interacts with VCAM-1, resulted in a small but obvious increase in MSC passage across the pulmonary microvascular barrier and thus entering the peripheral arterial bloodstream (Fischer *et al*., 2009). This study suggested that in addition to size, factors such as active adhesion to the vascular endothelium were also involved in pulmonary cell trapping.

Entrapment within the lungs is not a phenomenon restricted to SCs. Studies have revealed that even in the absence of lung inflammation, neutrophils were found to concentrate or sequester within pulmonary capillaries compared to the systemic blood (Mizgerd, 2002). Furthermore, injury stimuli increased their sequestering possibly by leading to neutrophil stiffening and also due to activation enhancing their adhesion to pulmonary endothelium thus prolonging their retention (Xiao *et al*., 1997). Whether neutrophils and HSCs/MSCs share similar biomechanical properties which encourage this pulmonary retention is currently not known.

1.3.3.2 Cell Deformability – an Important Determinant of Efficient Stem Cell Homing

It is also possible that the specific deformability of circulating cells can be an important determinant of pulmonary passage. Since the diameter of the capillary pathway is smaller than the typical sizes of neutrophils and BM-derived SCs, they have to undergo deformation within a short time in order to successfully pass through and therefore to reduce blockage. Wiggs and colleagues demonstrated that the delay of neutrophil transit was primarily due to the discrepancy between neutrophil and pulmonary capillary size. However, they further showed that neutrophils had less deformability than the highly deformable RBCs, which also explained the delay in neutrophil transit compared to RBCs (Wiggs *et al.*, 1994). Their study also suggested that when compared with non-deformable microspheres, neutrophils underwent a rapid deformation in one transit through the pulmonary circulation, with larger deformations requiring longer times (Wiggs *et al.*, 1994).

The importance of deformability in permitting SC passage through the lungs has been investigated and reported by the Kalia group (Microcirculation Research Group, University of Birmingham). Intravital microscopy, a method of directly imaging circulating cells at the cellular level *in vivo*, was used to monitor the trafficking of systemically injected HSCs to the injured kidney in mice. Using this technique, White and colleagues compared the renal recruitment of control and SDF-1α pre-treated HSCs (White *et al.,* 2013). Free-flowing control HSCs were observed to pass through the kidney with some becoming adherent. Importantly, no cells were noted after the first renal pass with the majority of cells observed being retained within the lungs. However, significantly more SDF-1α pre-treated cells homed to the injured kidney and importantly were continuously observed passing through the kidney at various time points post-infusion (White *et al.,* 2013). This resulted in an increased adhesion within the injured kidney. The whole cell micropipette aspiration assay was performed to test whether SDF-1α impacted on HSC deformability. This basic method, which determined how quickly whole cells were aspirated into a micropipette, demonstrated that the increase of HSC recruitment was potentially attributed to the pre-treatment increasing their deformability, thus reducing circulating HSC non-specific entrapment (White *et al.,* 2013). It seems that, this is the only study that has demonstrated how changing SC deformability can positively impact on their recruitment to injury sites.

1.3.4 Strategies for Enhancing Stem Cell Recruitment Following Injury

The limited efficiency of SC recruitment has led to the development of a number of pre-clinical techniques to enhance this process. Previous attempts to enhance SC recruitment within injured tissue included techniques, such as genetic manipulation and modification of SCs to either express more surface adhesion molecules or using plasmid DNA encoding for SDF-1α to increase tissue levels of this potent HSC chemokine (Hiasa *et al.,* 2004). However, this approach could pose a potential risk due to the misguided insertion of genetic material and a lack of clarity on what potential problems this could create *in vivo* in the long term. Various non-genetic, biochemical pre-treatment strategies have also been considered to increase the interaction between SCs and the microcirculation of the injured tissue. This idea was primarily proposed based on the fact that the adhesion of SCs to microvasculature was shown to depend on local, soluble inflammatory factors that can activate those circulating cells to adhere. From this knowledge it was hypothesised that pre-exposure of SCs to an environment containing critical soluble inflammatory factors prior to infusion would prime or pre-activate them. Indeed, this was shown to be the case using H_2O_2 which resulted in a significant increase in HSC recruitment to injured mouse colon and small intestine, but importantly was associated with reduced pulmonary adhesion (Yemm *et al.,* 2014; Kavanagh *et al* 2013a). Mechanisms of action included increasing the HSC surface adhesion molecule lateral clustering and enhancing their affinity for endothelial counterligands. Whether an additional mechanism involved increasing the deformability of HSCs was not investigated. Interestingly, H_2O_2 is also able to regulate the adhesive process of leukocytes by increasing their rolling and adhesion on vascular endothelium (Fraticelli *et al.,* 1996). H_2O_2 is not the only effective pre-treatment strategy as using the chemokine SDF-1α also enhanced HSC recruitment to murine injured intestine (Kavanagh *et al.,* 2013b) and kidney (White *et al.*, 2013). As reviewed earlier, the mechanical properties (size and deformability) of therapeutic cells are important parameters affecting pulmonary entrapment. However, there is a paucity of literature examining whether such pre-treatment strategies with chemokines or free radicals also impacts on the deformability of SCs to modify their recruitment.

1.4 Mechanical Property of Living Cells

1.4.1 Cell Mechanics and the Cytoskeleton

The ability of cells to resist deformation and maintain their shape when the various stresses exerted on them in the body, or to modify shape during mobilisation, depends mainly on their cytoskeleton. This is an interaction and complex network of filamentous polymers and regulatory proteins. There are three types of proteins contributing to the cytoskeleton: actin, tubulin and intermediate filament (IF) composing filaments of F-actin, microtubules and intermediate filaments (IFs) respectively. *In vitro* experiments have extensively identified and characterised the basic building blocks of cytoskeleton, including their roles in controlling the mechanical properties of the cell. F-actin, as the critical component of the cytoskeleton, is particularly abundant beneath the plasma membrane in the form of a network which is able to determine the cell shape, mechanical properties and regulate cell migration (Cooper, 2000). IFs, as the least stiff of the three polymers, are the most diverse and mainly located throughout the cytoplasm and the nucleus (Fletcher and Mullins, 2010). Microtubules are involved in nucleic and cell division, organization of intracellular structure and transport. Experiments involving selectively disrupting any one of the three cytoskeleton elements have demonstrated that microtubules do not provide mechanical support to spherical cells in terms of cell rigidity on the whole-cell scale (Brown *et al., 2*001). F-actin networks have attracted considerable interest in the mechanical response of the cell for the reason of their diversity in structures that they form and their function acting as semi-flexible polymers. When the F-actin, extracellular and intermediate networks are all together resistant to the applied forces, the additional deformation is resisted by filament entanglement. When the stress is applied merely on a single cell with highly organized architecture, the bending of actin filaments contributes to the elastic properties. In response to compressive forces, the F-actins existing near the cell membrane demonstrate nonlinear stiffening at small deformations, followed by structure softening at large deformations (Chaudhuri *et al.*, 2007). These results provide useful knowledge in the understanding of cell mechanics when different characterisation techniques are used.

1.4.2 Techniques for Measuring Cell Mechanics

There is significant literature on the mechanical properties of blood cells, their responses to stresses in the circulation and the change in their mechanical properties to enable their flow through small vessels (Rand *et al*., 1964; Nash *et al*., 1984). However, little is currently known about these mechanical properties with regards BM-derived SCs. Increasing our knowledge of the SCs' mechanical behaviour under stress may allow us to identify a biophysical marker(s) which can be exploited for cell sorting of a specific sub-population. For example, this sub-population may have mechanical properties that allow for improved delivery to sites of injury. Measuring the mechanical properties of live cells requires applying some kind of controlled force to them and recording their corresponding deformations. Clearly deformation responses will vary depending on the cell stiffness, strength, etc.

Several methods or techniques which can probe cell mechanics have been developed in the last few decades including micropipette aspiration (Hochmuth, 2000), micromanipulation (Mashmoushy *et al.,* 1998), atomic force microscopy (AFM) (Kuznetsova *et al.,* 2007), magnetic tweezers (Alenghat *et al.,* 2000), optical tweezers (Dao *et al.,* 2003), shear flow (Eggleton and Popel, 1998) and cell stretching (Trepat *et al.,* 2007). These techniques can apply different types of forces on cells which are conveniently classified into three types: local probes to compress or stretch a portion of a single cell, big probes to compress an entire cell, or simultaneously load a population of cells. These approaches have been used to study either the mechanics of the integrated whole cell or the micro- and nano-mechanics of individual cell structure components separately, such as the isolated membrane plasma, cell nuclei and even the actin filaments. These various methods utilise different ways by which the force probe can contact and sample the cell or its surface (**Figure 1.2**). Each method has its own strengths and weaknesses. Among these techniques, micropipette aspiration, AFM and micromanipulation are described in the following section due to their importance and wide uses. Other techniques, which are not repeated here, have been discussed extensively by Janmey and McCulloch (2007).

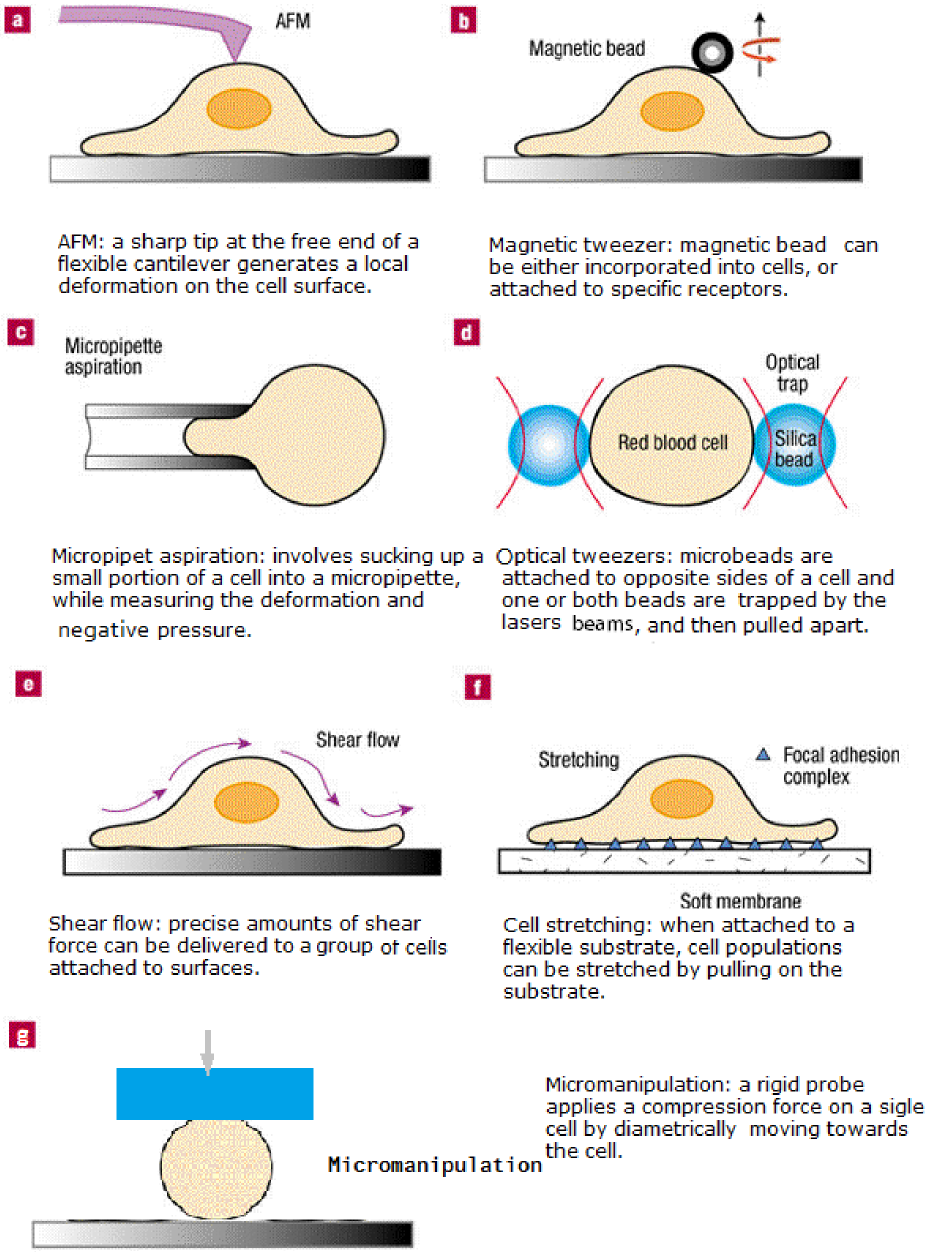

AFM: a sharp tip at the free end of a flexible cantilever generates a local deformation on the cell surface.

Magnetic tweezer: magnetic bead can be either incorporated into cells, or attached to specific receptors.

Micropipet aspiration: involves sucking up a small portion of a cell into a micropipette, while measuring the deformation and negative pressure.

Optical tweezers: microbeads are attached to opposite sides of a cell and one or both beads are trapped by the lasers beams, and then pulled apart.

Shear flow: precise amounts of shear force can be delivered to a group of cells attached to surfaces.

Cell stretching: when attached to a flexible substrate, cell populations can be stretched by pulling on the substrate.

Micromanipulation: a rigid probe applies a compression force on a sigle cell by diametrically moving towards the cell.

Figure 1.2. Modes of probing the cell to determine its mechanical properties. The various methods utilise different ways by which the force probe can contact and sample the cell. Each method has its own strengths and weaknesses.

1.4.2.1 Micropipette Aspiration

Micropipette aspiration has been utilised to investigate the whole-cell mechanics. It involves sucking up a small portion of a cell into a small glass tube in response to negative pressure and tracking the leading edge of its surface. The changes of the edges are tracked with a light microscope. The applied vacuum pressure, the time it takes to aspirate the whole cell, the cell length that is sucked into the pipette, the inner diameter of the pipette and the diameter of the spherical portion outside the pipette can be used to calculate the elastic and viscoelastic moduli of the cell based on basic continuum models (Janmey and McCulloch, 2007). Though this technique is simpler and the cost to build the device is relatively lower compared to other methods, the approach is somewhat hindered in the spatial resolution to the micron scale, the cells have to be deformed to a large deformation, and its accuracy is dependent on the optical imaging resolutions.

1.4.2.2 Atomic Force Microscopy (AFM)

AFM-based compression is the most recent and powerful technique to understand the spatial distribution of mechanics within a single cell. The basic operation of AFM relies on the laser tracking of the deflection of a micro-sized cantilever, which with a fine tip can probe the cell surface. Its deflection determines the applied compression or adhesion force, as well as the displacement (**Figure 1.3a**) (Kirmizis and Logothetidis, 2010). AFM can be operated in several different modes depending on the nature of the interaction between the tip and the sample surface. These include contact, tapping, and force mode. In force mode, an advanced, so-called force-mapping mode is most useful for the study of cell mechanics. Force mode is used to measure forces acting between the AFM tip and the sample surface at a specific point. The cantilever simply goes up and down, and its tip is therefore elevated and approached to the surface at a certain velocity. As a result, a force profile is recorded and typical extend and retract curves can be generated (**Figure 1.3b**). The vertical deflection of the cantilever is plotted against the height (vertical position of the probe). When the cantilever tip is distant from the sample surface, there is no deflection, which means the force is zero (baseline).

The relative force at which value the cantilever stops moving and retracts away from the surface can be controlled. Correspondingly, in the retraction region, the force decreases as the tip leaves the sample, and the sample may display viscous and elastic properties resulting in hysteresis between the extension and retraction curves. With this force mode, the force applied on the specific point of the sample surface can be calculated. However, the mechanics of a single point on the cell surface is not sufficient to represent the mechanics of the cell, and the relative position of the sample has to be localized precisely which appears to be difficult to control. In this case, the force-mapping mode is introduced in order to make up for the weakness of just compressing a single position. While working in the force-mapping mode, AFM cantilever moves vertically as it does in force mode. After one circle of extension and retraction, the tip advances in the lateral direction to a certain distance, force curves are again recorded, and then the action is repeated. The number of measurements in one scan is controlled by the AFM operator. For instance, in a scan area of 100 x 100 µm, 64 x 64 pixels are set before scanning. Thus in one measurement, all immobilized cells in this area, as well as the substrate surface can be scanned and over four thousands force curves, which represent the compression of the cells or the substrate surface, are acquired.

AFM can also generate cellular geometry information during this scanning that can be recorded from the height of the compressed points. This allows a rough 3D image to be produced from the software processing. Knowledge of the cell geometry can be used to select force curves from a certain area on the cell surface to determine the elastic modulus of biological samples. For example, the Hertz model used for calculation of the Young's Modulus is based on an assumption that the spherical probe compresses the flat surface of the sample/cell (Dimitriadis *et al.,* 2002). Thus, force curves in relatively flat area can be selected with the help of geometry information. Additionally, AFM is able to generate compression force curves of cells at very small deformations of individual cells corresponding to pico-Newton force, and it is far more sensitive than other techniques.

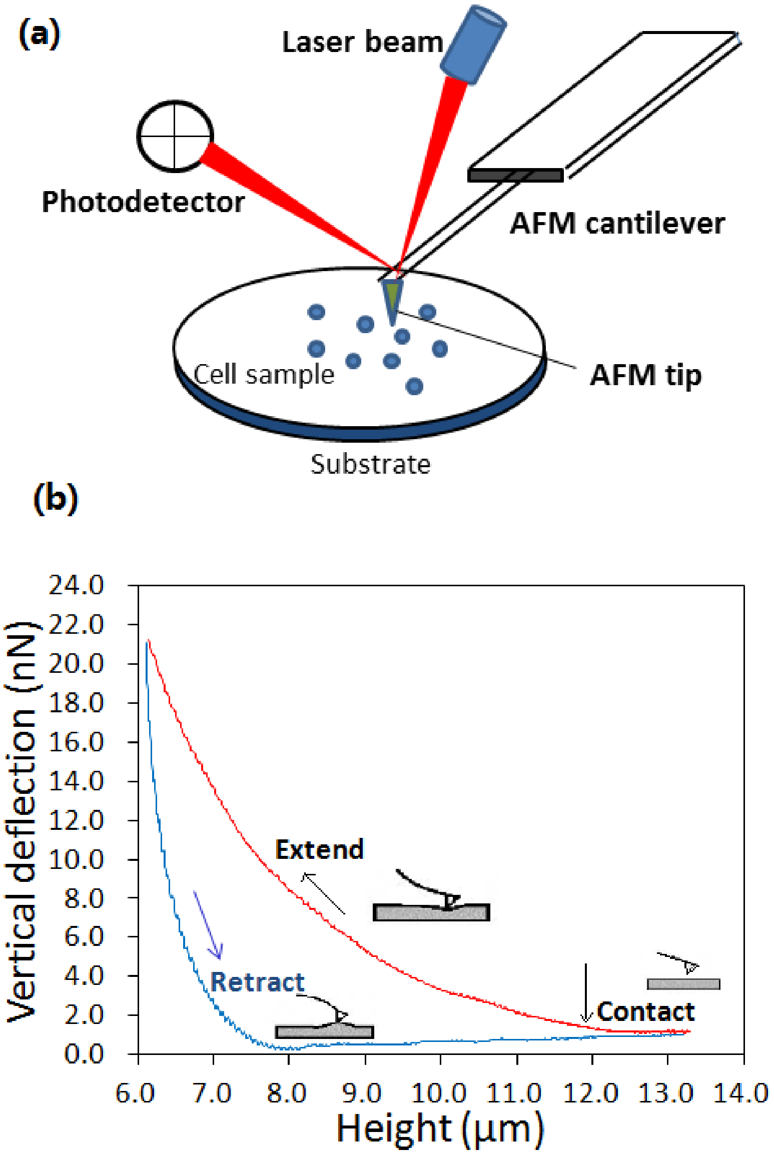

Figure 1.3. A schematic view of the AFM method and typical force-height curves generated using AFM. (a) The basic operation of AFM relies on the laser tracking of the deflection of a micro-sized cantilever, the flexible cantilever with a fine tip can probe the cell surface, and its deflection determines the applied compression or adhesion force, as well as the displacement. **(b)** When the cantilever tip is distant from the sample surface, there is no deflection. At some point, the sample is compressed with the increase of the force (**red line**). When the force reaches to a set point, the tip retracts from the sample and the force decreases (**blue line**).

1.4.2.3 Micromanipulation Technique

The micromanipulation technique was developed 20 years ago for the purpose of testing the mechanics of mammalian cells and micro-particles (Zhang *et al.,* 1991). Biological cells tested with this method have included cartilage, namely chondrocytes and chondrons in suspension (Nguyen *et al.,* 2010). This technique was ideal for these cells because it allowed their mechanical properties to be determined after large deformations, which is what these cells experience under joint pressure. Circulating cells also experience large deformations in flow conditions and so micromanipulation is an ideal methodology for testing their mechanical properties.

The principle of micromanipulation involves compressing single cells suspended in medium/buffer solution or dry particles on a stage, between two parallel surfaces which are the bottom of the substrate (generally a chamber or glass slide) and the force transducer probe of borosilicate glass (**Figure 1.4**). The probe, which is connected to a force transducer, can be driven by a stepping motor either upwards or downwards at varying speeds. The force applied to the cell is obtained simultaneously by the force transducer. From this measurement, force versus displacement and force versus time data can be collected for further calculation (Nguyen *et al.,* 2010). Transducers with varying sensitivity can be chosen to do the probing, depending on the stiffness and mechanical strength of the material of interest. Micromanipulation is a simple and effective technique to probe the mechanics of the whole cell.

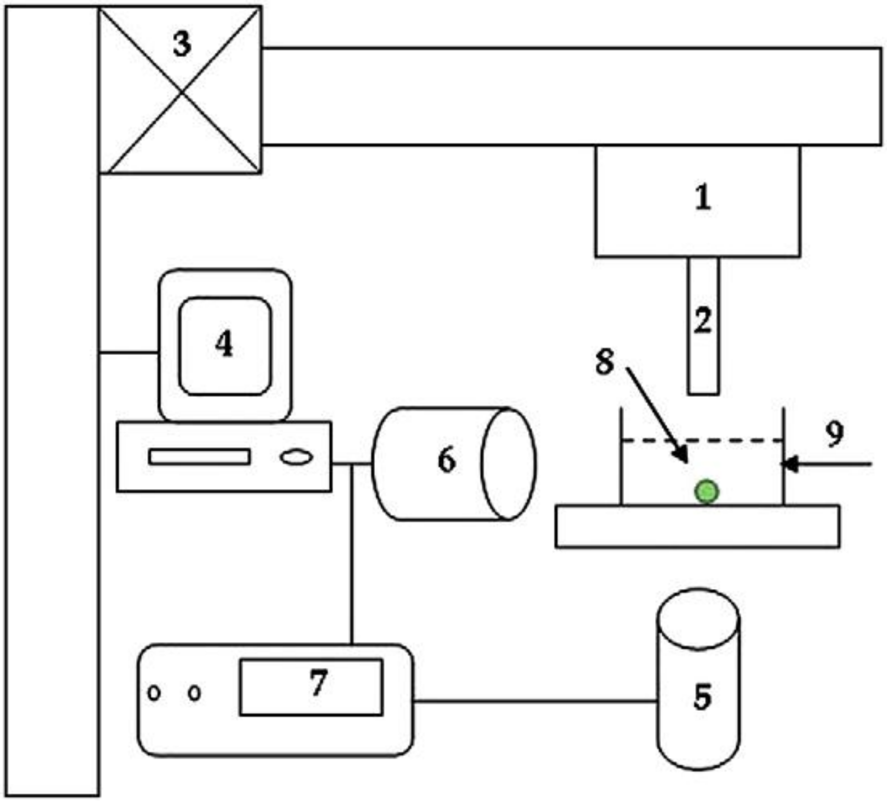

Figure 1.4. Schematic diagram of the micromanipulation rig. (1) Force transducer; (2) probe; (3) stepping motor; (4) computer with motor control and data acquisition boards; (5) bottom-view microscope; (6) side-view microscope; (7) high-speed camera; (8) single cells in suspension; (9) glass chamber (Yan *et al*., 2009).

1.5 Label-free Cell Separation in Microfluidic Systems

1.5.1 Introduction

Although the mechanical properties of cells can be investigated with micromanipulation and AFM, these techniques cannot separate the tested cells physically into sub-populations with different characteristics. This can be achieved using active cell separation methods, routinely found in most laboratories, that involve biochemical modification or labeling of cells, such as fluorescent activated cell sorting (FACS) and magnetic-activated cell sorting (MACS) (Parks *et al.*, 1989, Miltenyi *et al.,* 1990, Gossett *et al.,* 2010). However, these techniques are often labour intensive and not very effective. Recently, label-free passive microfluidic systems for cell sorting have been developed and are based on using the intrinsic biophysical markers of the cell to separate them. These markers can include cell mechanical properties (size, shape and deformability), electrical properties (polarizability and impedance), and hydrodynamic properties.

When a cell suspension sample flows through the microfluidic channel, cell separation and sorting can be accomplished physically by using microscale filters, or techniques which can manipulate fluid dynamics in microscale, such as hydrodynamic filtration, field-flow fractionation and inertial microfluidics. **Table 1.1** summarizes different cell sorting methods and the characteristics of each method regarding their mechanisms, separation markers and throughput. Compared with the conventional active cell separation systems, these passive microfluidic separation devices offer a number of advantages including: 1) reduced sample and reagent cost; 2) high throughput; 3) high sensitivity and spatial resolution; 4) increased portability and 6) relatively low cost (Sia and Whitesides, 2003, Bhagat *et al.,* 2010).

1.5.2 Passive Cell Separation Techniques

Traditionally, passive cell separation techniques make use of the heterogeneity of the intrinsic properties of the cells in one population to achieve their separation. Because of their high sensitivity and efficicacy, several different methods have been developed in recent years. Cell size is a common physical property used for differentiation. Generation of cell flow in micro-scale filters can selectively direct cells into different paths and is mainly based on arrays of microscale constrictions or pores which can trap the larger and more rigid cells. Four types of microfilters have been experimentally applied for whole blood cell separation: weir, pillar, cross-flow and membrane (Ji *et al.,* 2008) (**Figure 1.5a**). Though using the microscale filters is a conceptually straightforward strategy for cell separation, there are a number of challenges with regards the throughout and efficiency of the application. Heterogenous cell sizes can induce mesh clogging or membrane fouling by small cells, resulting in irregular flow locally. Also, very fragile cells can become damaged or lost when they are pushed through the pores, especially when throughput is increased.

Table 1.1. List of the different active and passive separation techniques used to separate cells into specific sub-populations. This table summarizes a variety of passive and active techniques in cell separation and the characteristics of each technique regarding their mechanisms, separation markers and throughput.

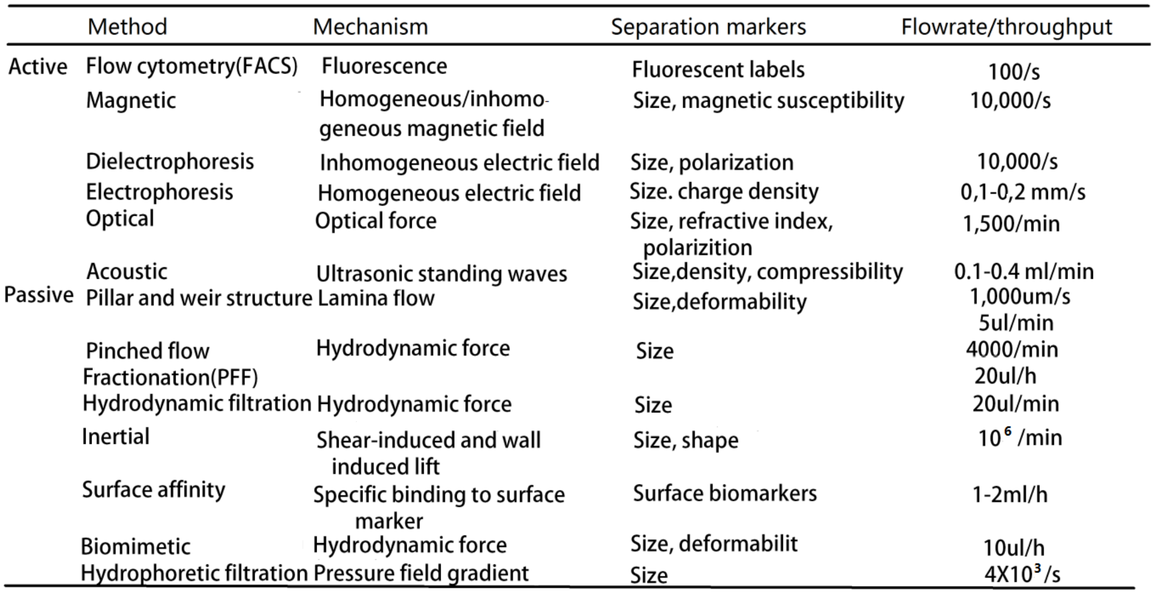

	Method	Mechanism	Separation markers	Flowrate/throughput
Active	Flow cytometry(FACS)	Fluorescence	Fluorescent labels	100/s
	Magnetic	Homogeneous/inhomogeneous magnetic field	Size, magnetic susceptibility	10,000/s
	Dielectrophoresis	Inhomogeneous electric field	Size, polarization	10,000/s
	Electrophoresis	Homogeneous electric field	Size. charge density	0,1-0,2 mm/s
	Optical	Optical force	Size, refractive index, polarizition	1,500/min
	Acoustic	Ultrasonic standing waves	Size,density, compressibility	0.1-0.4 ml/min
Passive	Pillar and weir structure	Lamina flow	Size,deformability	1,000um/s 5ul/min
	Pinched flow Fractionation(PFF)	Hydrodynamic force	Size	4000/min 20ul/h
	Hydrodynamic filtration	Hydrodynamic force	Size	20ul/min
	Inertial	Shear-induced and wall induced lift	Size, shape	10^{6} /min
	Surface affinity	Specific binding to surface marker	Surface biomarkers	1-2ml/h
	Biomimetic	Hydrodynamic force	Size, deformabilit	10ul/h
	Hydrophoretic filtration	Pressure field gradient	Size	$4X10^{3}$/s

Hydrodynamic filtration in microfluidic devices is a method developed for separating cells according to size with the use of laminar flow. The microchannel device has multiple branch points and side channels. The cell suspension in laminar flow is continuously injected to a branch channel in the direction shown by the arrow in **Figure 1.5b**. When a cell “a” flows along the sidewalls (the right side wall for instance), if the centre position of the cell is located in the right region of the borderline A, the cell migrates to the side channel. While the centre position is on the left of the borderline A, like cell “b” and cell “c”, the cells do not enter the side channel, flowing in the main direction. This technique has been applied for separating liver cells from two different populations, based on the difference in sizes between hepatocytes and non-parenchymal cells (Yamada *et al.,* 2007). A particle suspension was also accurately and continuously focused by utilizing the hydrodynamic filtration (Aoki *et al.*, 2009).

Deterministic lateral displacement (DLD) is also a hydrodynamic microfluidic technology capable of separating cells based on their size in continuous flow. The mechanism relies on the interaction between suspended cells with an ordered, specific arrangement of micro-sized circular or triangular posts within the channel where the cell suspension is pushed in a laminar flow. These posts can divide the fluid into many narrow streams, the width of which corresponds to the critical diameter (D_c). Cells smaller than the critical size are allowed to pass following the direction of the main laminar flow (vertical direction as shown in **Figure 1.5c**). However, bigger cells are forced to interact with the posts, the streamlines are changed many times, thus the migration direction is laterally changed, and cells follow the tilted lanes of the pillar array. The DLD based separation has been modelled and applied in a variety of biological cells, such as classification of whole blood (Inglis *et al.*, 2011), separation of cancerous cells (Liu *et al.*, 2013) or parasite from human blood (Holm *et al.*, 2011).

In the field-flow fractionation (FFF) separation technique, a field (flow, electric, gravitational, centrifugal, etc.) applies on the fluid suspension or solution in an orientation perpendicular to the channel flow (**Figure 1.5d**). Thus particles in the fluid are separated based on the balance of the force produced by the velocity profile and the forces provided by the field. The FFF technique has been successfully applied to mammalian cell separation from a mixture consisting of human breast cancerous cells and normal blood cells using dielectrophoretic/gravitational FFF (Yang *et al.,* 1999). Fixed human and avian red cells and viable Hela cells were separated by steric FFF in a time frame of less than 15 minutes and their viability was maintained after flowing through the separation channel (Caldwell *et al.,* 1984).

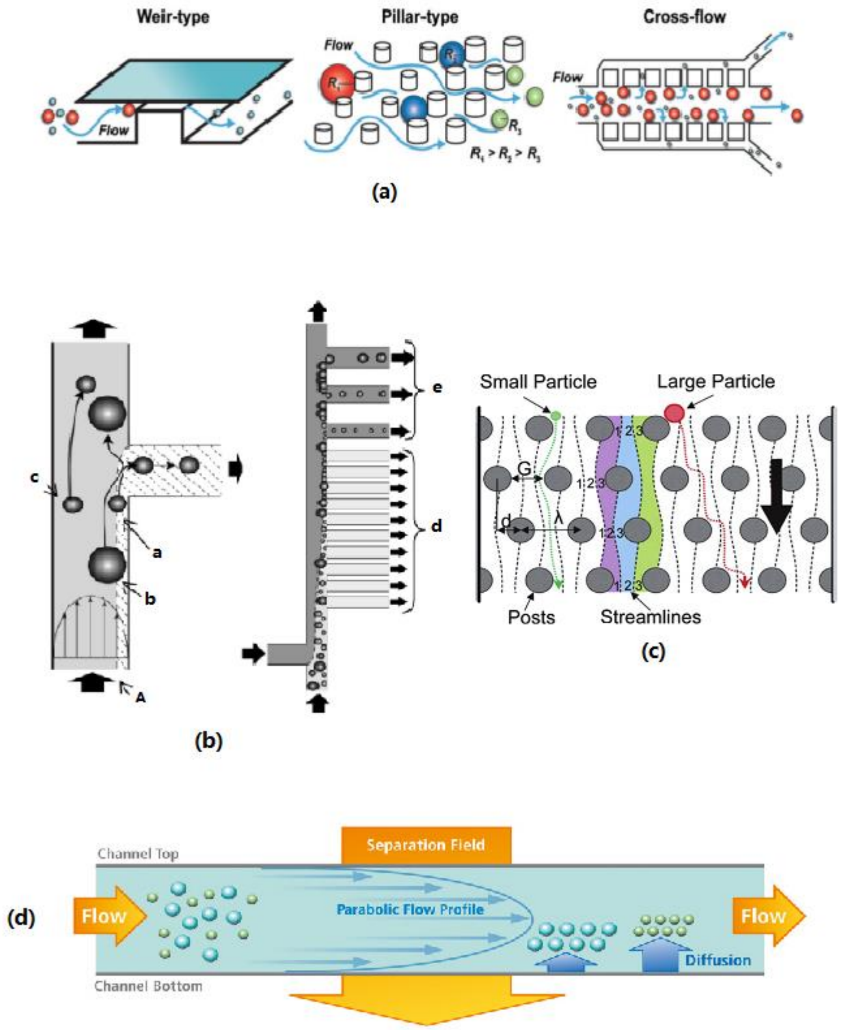

Figure 1.5. Different passive separation techniques. (a) Schematics of the microfilter designs. In the weir design, barriers obstruct the flow path to trap cells based on size allowing smaller cells through. In the pillar design, rows of small pillars spaced apart at certain dimensions allow certain size cells to pass between them. The cross-flow filter is derived from the pillar type except that the pillars are perpendicular to the flow path to avoid problems associated with obstructed flow. **(b)** The principle of the hydrodynamic filtration method to separate and sort cells. **(c)** Schematic of a deterministic lateral displacement (DLD) pillar array for cell separation **(d)** Illustration of field-flow fractionation (FFF) principle for cell separation (Bhagat *et al.,* 2010; Autebert *et al.,* 2012).

1.5.3 Microfluidic Separation Based on the Inertial Effect

One of the most promising microfluidic techniques to separate and concentrate cells of interest is called inertial focusing, originally discovered in the 1960s (Segré and Silberberg, 1961). One of its major recent uses has been to detect cancerous cells within a blood sample (Hou *et al.,* 2013). Among passive microfluidic techniques, inertial microfluidics has attracted the most interest in the past two decades due to its precise manipulation, simple structure, and high throughput (10^6 cells/min). The flowing behaviour of a fluid in the microfluidic channels are characterized by a dimensionless parameter called the Reynolds number (Re), defined as $\mathrm{Re} = \rho\mathrm{UH}/\mu$, where ρ*,* U and μ are the fluid density, average velocity and dynamic viscosity respectively, and *H* is the characteristic channel dimension (usually < 1mm). Hence Re can describe the competing action between inertial and viscous forces in the flow. Since the dimensions of microchannels are very small (normally in micron scale), the Re is usually much less than 100, often less than 1.0. Hence in conventional microfluidics, fluid inertia is regarded negligible because Re is close to 0 (Re → 0) in Stokes flow regime due to small channel length and low flow velocity. In this regime, the flow is absolutely laminar without turbulence. The turbulent flow generally occurs when the Reynolds number increases to 2000. In a laminar flow, generally the transportation of fluids through microchannels can be predicted. However, when the microfluidic system is working in an intermediate range between stokes regime and turbulent regime (1 < Re < 100), the Stokes assumption is no longer valid. In this system both the inertia and the viscosity of the fluid become finite, in which case nonlinear and unpredictable movements of fluid and particles are observed. Two resulting effects are thus found in these microchannels: (1) inertial particle migration and (2) geometry induced secondary flows. Such fluid physics have been utilized to control and manipulate the movement of the particles/cells in the channel.

1.5.3.1 Physics of Inertial Migration

Inertial focusing occurs when particles/cells in a flow spontaneously migrate across streamlines to equilibrium positions across the microchannels. Particles/cells flowing in a confined channel experience both shear and normal forces applying on their surfaces. These forces can be parallel or perpendicular to the main flow direction respectively and work to drag particles to an equilibrium position where they are force free. In seminal studies in the 1960's, it was observed that in a 1 cm-diameter tube, the randomly distributed particles moves in the cross-section surface to form an annulus with a diameter of ~0.6 times the tube diameter (Segré and Silberberg, 1961) (**Figure 1.6a**). In such systems, since Re is finite and inertia is significant, it is difficult to explain this phenomenon with dynamic theory at that time. After that, the technique of matched asymptotic expansions was used to determine the lift forces (F_L) acting on particles with diameter a, in microchannels with hydrodynamic diameter D_h, which is given by:

$$F_L \propto \rho U^2 a^4 / D_h{}^2 \tag{1.1}$$

Later studies theoretically predicted additional dependence of F_L on channel Reynolds number and the lateral position of particles, such that:

$$F_L \propto f_L(\mathrm{Re}, x/h) \bullet \rho U^2 a^4 / D_h{}^2 \tag{1.2}$$

where f_L is a function of Re and the particle cross-sectional position (x/h), which is a non-dimensional lift coefficient. Recently, a novel scaling for F_L was found to be further dependent on a particle's position in the channel. Di Carlo's that (Di Carlo, 2009) work showed:

$$F_L \propto \rho U^2 a^3 / D_h \text{ , near the channel centreline} \tag{1.3}$$

$$F_L \propto \rho U^2 a^6 / D_h{}^4 \text{ , near the side walls} \tag{1.4}$$

The channel wall and centreline were scaled separately suggesting that two disparate fluid dynamics effects worked to yield the equilibrium positions between centre and wall of the channel. A balance of two opposing forces was proposed: 1) the wall-induced lift force (F_{LW}) which drags the particles away from the wall by interaction between the particle and the adjacent wall and 2) the shear-gradient-induced lift force (F_{LS}), directing the particles to the channel wall due to the curvature of the axial velocity profile (Amini *et al*., 2014). The two forces act together to direct the particles to an equilibrium position where the particles are laterally force free (**Figure 1.6b**).

In a tube flow, the particles migrate in the radical direction due to the sole force balance. However, the current fabrication methods normally generate microchannels with square or rectangular cross-sections, in which the particles behave in a different manner. The follow-up experiments and numerical simulations have been done to determine the complicated dependence of equilibrium positions on the blockage ratio κ (κ = a/H), where a is the diameter of the particle and H is the channel height), channel Re and the channel aspect ratio AR (AR = W/H, where W and H are the channel width and height respectively). Experiments and simulations performed by Kilimnik *et al.* (2011) produced results with Re = 0 - 100 and AR = 1 - 10. Rigid spherical particles equilibrated near the channel centre of the long walls at small AR (≤ 4), whereas for large AR (4 - 10), the equilibrium position was close to the side walls, which demonstrated that there is a monotonic dependence of equilibrium position on the channel AR. It also revealed that larger particles (lower κ) equilibrated more closely to the channel centreline. Data for different Re almost overlap demonstrating a weak dependence of equilibrium position on Re (Kilimnik *et al.,* 2011).

1.5.3.2 Inertial Migration in Straight Rectangular Microfluidic Channels

Within straight, rectangular microchannels, inertial lift forces (F_L) dominate and consist of two opposing forces: the wall-induced lift force (F_{LW}) directing particles/cells to the channel centre and the velocity or shear gradient-induced force (F_{LS}) directing particles/cells to the channel walls. The balance of these two forces determines the equilibrium position(s) within the microchannels. Focusing of particles/cells occurs as a result of these forces when the Re is finite and low (1 - 100). In a straight channel with a rectangular cross-section, these forces lead to a pair of equilibria centred on the long faces of the channel.

The inertial lift forces vary depending on the fluid density, velocity, particle/cell diameter, channel diameter and the particle position within the channel. Importantly, it has been demonstrated that simply changing the geometry of the microchannel can control the equilibrium positions of particles/cells of different sizes. For biological cells that behave more like deformable droplets, individual cells can also be moved to equilibrium positions in more complex manners that are related to cell deformability as well as the ratio of density and viscosity between the cell and the surrounding flow. In the application of inertial lift for cell sorting, there are several parameters which can be controlled to optimize the separation efficiency including the geometry of the channel and flow rate.

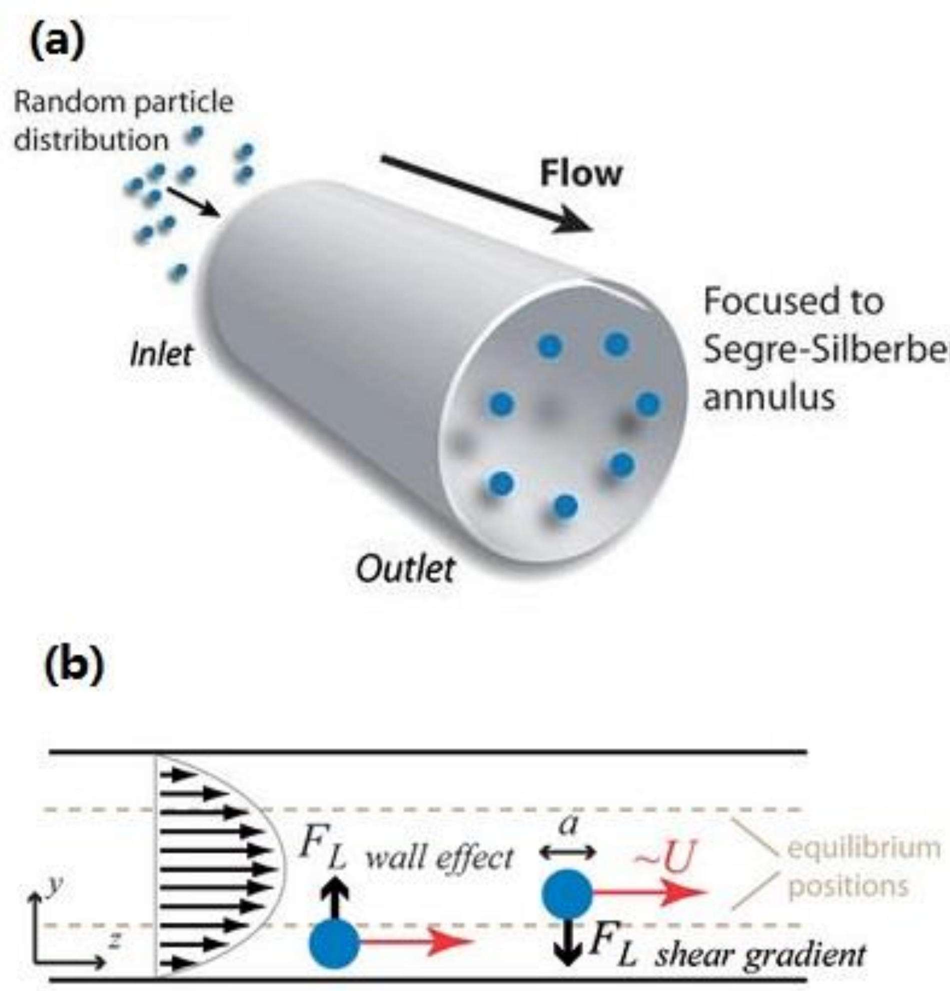

Figure 1.6. Schematic diagram to describe inertial lift generated in a flow. (a) In a tube, at moderate Reynold number (Re), randomly distributed particles are observed to migrates to an annulus located between the channel centre and wall. **(b)** Two lift forces in perpendicular direction of the flow direction acting to form equilibrium positions in the channel (Di Carlo *et al.,* 2009).

1.5.3.3 Inertial Migration in Curved Microfluidic Channels - Dean Secondary Flow

In addition to lift forces arising from different forms of nonlinearities or particle asymmetry in the straight channels discussed above, the effect of having a curved channel induces secondary flows and can be utilized to manipulate the motions of particles/cells and fluid. In a curved channel, this secondary transverse flow arises due to the mismatch of velocity between fluid near the centreline and fluid in the side walls in the downstream direction as it passes around a curve. Fluids in the centreline have larger velocity, thus, they obtain larger inertia than fluids near the channel wall, and tend to migrate outward around a curve. As a results, the pressure gradient in the radical direction of the channel is generated (**Figure 1.7**). Because this is an enclosed channel, relatively stagnant fluids in the top and bottom walls move inwards, creating two symmetric vortices (Di Carlo, 2009). The strength of this secondary flow varies depending on the curvature of the microchannel and is characterized by the non-dimensional Dean number, De. Therefore, although in straight channels channel dimensions, particle size, Re impact the equilibrium positions, in curved channels an additional De dictates particle/cell focusing. De, describing the magnitude and qualitative feature of this flow, was proposed by W. R. Dean (Dean, 1927) as:

$$De = \frac{\sqrt{(centripeta\ lforces)(inertialfo\ rces)}}{viscousforces} = \frac{\sqrt{(\rho \frac{R}{D_h} \frac{U^2}{(R/D_h)^2})(\rho U^2)}}{\mu \frac{\upsilon}{D_h}} = \sqrt{\frac{D_h}{2R}} \frac{\rho U D_h}{\mu} = \mathrm{Re}\sqrt{\frac{D_h}{2R}} \qquad \textbf{(1.5)}$$

where ρ is the density of the fluid, μ is the dynamic viscosity, U is the axial velocity scale, R is the radius of the channel curvature, and D_h is the channel hydraulic diameter. It demonstrates that the strength of the secondary flow depends on the Re and the curvature ratio, which means that a higher flow rate and faster turn in the channel can lead to a stronger Dean flow.

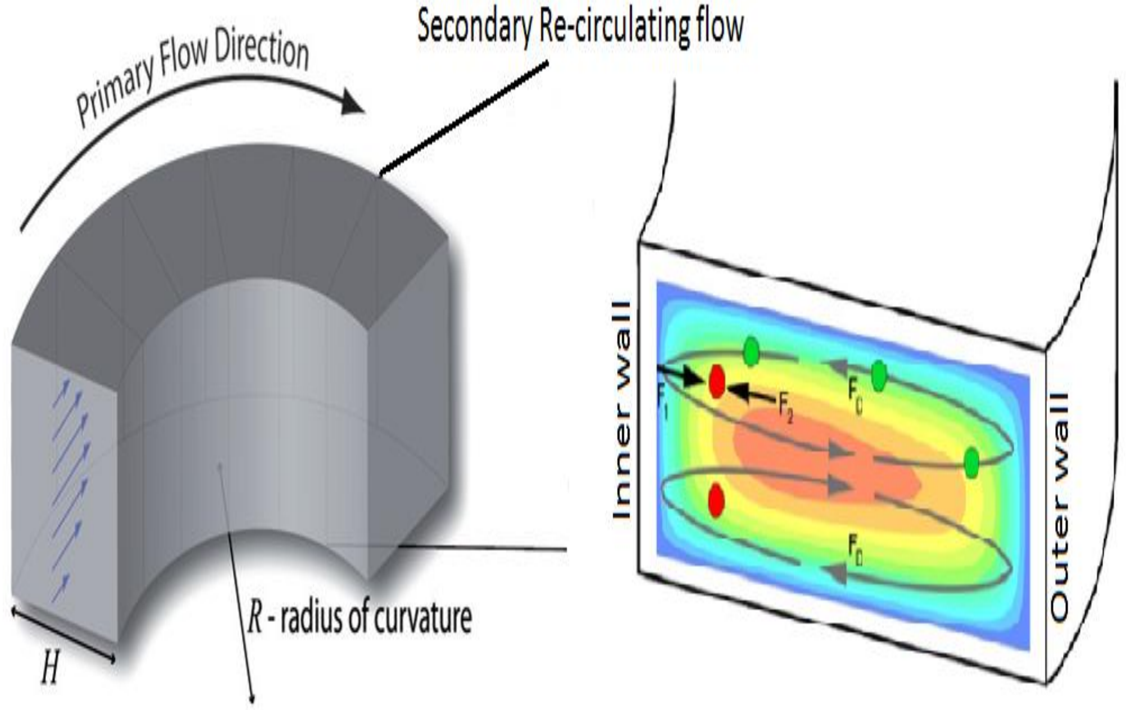

Figure 1.7. Inertial migration due to secondary flows arising in curved channels. Dean flow with two counter-rotating vortices is created in curved channels due to the mismatch of velocity direction between fluid in the central and near-wall regions. D_e is used to characterize the magnitude of secondary flow, De= Re $(D_h/2R)^{1/2}$ where D_h is the microchannel hydraulic diameter and R is the curvature radius. De has important effects on the degree of the secondary flow, the centres of the symmetric vortices move towards the outer wall and boundary layers are developed with the increase of De. Flowing cells in a curved channel experience an interaction of inertial lift force (F_L) and Dean drag force (F_D), and the magnitude and direction of these forces are dependent on their size and deformability (Di Carlo *et al.,* 2009).

For particles flowing in this system, it is assumed that particles are manipulated in superposition of the inertial focusing and secondary flow. Therefore, particles that have moved to inertial lift equilibrium positions would experience the Dean drag force that at its maximum can be directly proportional to the local secondary flow velocity, which is perpendicular to the primary flow direction. Consequently, particles would experience a drag force which is in competition with lift forces, directing particles to new equilibrium positions. To describe the particle behaviour in this system, a ratio of the two types of forces (inertial lift/Dean drag) was proposed (Hasabnis, 2015):

$$R_f = F_L / F_D = a^2 R / H^3 \tag{1.6}$$

This equation describes the order of magnitude scaling between the inertial and secondary forces. It is useful to predict the particle behaviour: $R_f \rightarrow 0$, secondary flow plays the dominating role, and particles remain entrained in it, and $R_f \rightarrow \infty$, for sufficiently high flow rate, particles would focus to inertial lift equilibrium positions without the effect of the Dean flow. While for intermediate R_f, particles will migrate to inertial equilibrium positions which can be modified by the Dean flow, creating new migration modes and applications. The equation also demonstrates that R_f is related to particle size so that particles with different sizes can experience different focusing behaviour. Despite that R_f is a simple parameter to characterise the curved channel system, the precise mechanism of secondary flow focusing is complicated and not fully understood experimentally and theoretically, but this does not prevent us from applying these systems for particle/cell focusing.

1.5.3.4 Inertial Focusing of Deformable Particles

In describing inertial focusing behaviour, rigid particles have been used as simple components for theoretical and experimental studies. Such research has provided a solid foundation for microfluidic applications in particle separation and enrichment based on size. However, in applications of interest, particles are often not rigid, but deformable, such as biological cells and two-phase emulsion droplets. In these cases, the flow behaviour of these particles may not be the same as that of rigid particles and their noticeable deformations caused by hydrodynamic forces should be considered. To study the motion of these particles in flow, three models have been used to approximate a deformable particle: 1) an elastic solid particle, which is considered as a continuous single solid body, 2) a deformable droplet - a boundary filled with fluid which can also slip under the driving flow, and 3) a deformable capsule – a deformable but solid shell filled with fluid (Amini *et al.,* 2014). HSCs of interest in this study are considered to be deformable and they may behave more like droplets than rigid particles in microchannels (Hur *et al.,* 2011). It was first demonstrated that deformable droplets could migrate in lateral direction in Strokes flow, indicating that droplets can migrate even at Re = 0, only if they deform (Karnis *et al.*, 1966). Several theoretical, numerical and a few experimental studies on lateral motion of deformable particles have been conducted to explain this phenomenon. The essential factor responsible for the deformation and consequent lateral migration of droplets is found to be stress matching type of boundary conditions at the corresponding interface instead of non-slip condition at the boundary of rigid wall. Later studies report that the direction of migration depends on the type of deformable particles and its relative viscosity with respect to the surrounding fluid. The latter parameter can be quantified by the viscosity ratio of the droplet to the surrounding flow, $\lambda = \mu_{in}/\mu_{ex}$. Karnis and colleagues reported that in Stokes flow (Re << 1), the highly deformable droplets migrated to the centreline if λ is low (0.0002 - 4.8), while droplets with high λ behaved like rigid particles and suspended at a position between the centreline and channel wall (Karnis *et al.*, 1966). Therefore, the droplet migration in non-zero R_e depends on the competition or balance between the deformability-induced lift and the inertia lift, and the deformability-induced lift increases with increasing deformability. A number of investigations have demonstrated that with AR of 2, 3 and 5, deformable droplets and cells tended to migrate to near the channel centre when the relatively rigid ones obtained equilibrium positions near the channel walls (Stan *et al.*, 2013, Kilimnik *et al.,* 2011). It can be simply attributed to that the deformability-induced lift can move deformable particles away from the migration direction of rigid particles that do not have deformation.

1.6 Adoptive T Cell Therapy

1.6.1 Procedure and Challenges of T Cell-Based Therapy

The use of SC-based therapies has increased for a variety of different inflammatory, ischemic and degenerative disorders. However, cells other than SCs, particularly immune cell therapy have also witnessed tremendous expansion in the past two decades. Most explored has been the use of adoptive antigen (Ag)-specific T cell immunotherapies for viral infections and cancers (Mount *et al.,* 2015). T cells for adoptive immunotherapies can be generated through *in vitro* expansion or immunomagnetic isolation of pre-existing Ag-specific lymphocytes from blood or tumor-infiltrating lymphocytes. The former method has the drawback of driving T cells to exhaustion through repeated cycles of in vitro antigen stimulation and expansion, which ultimately impacts on their efficacy to eliminate tumour or infected cells (Klebanoff *et al.,* 2012). This is in contrast to direct *in vitro* selection which requires minimal manipulation and thus retains the proliferative capacity and therapeutic functionality of the lymphocytes. For this reason, immunomagnetic selection of fresh *ex vivo* cells has been adopted in recent clinical trials where a small number of pre-existing circulating virus-specific T cells can be directly selected from donor blood to target viral infections and tumours in stem cell transplant patients (Peggs *et al.,* 2003, Moosmann *et al.,* 2010, Feuchtinger *et al.,* 2006). This method has been used in the treatment of cytomegalovirus, adenovirus infections and Epstein–Barr virus, and also lymphomas such as post-transplant lymphoproliferative disorder. Immunomagnetic selection systems utilize antibody or ligand-recognition of unique phenotypic markers on the cell surface to separate cells. With the recent breakthrough in utilizing T cells expressing the CD19-specific chimeric antigen receptor (CAR) to treat B cell acute lymphoblastic leukaemia, selection of Ag-specific cells could also become a key purification step in the *in vitro* expansion of immunoreceptor engineered cells. However, there are limitations in immunomagnetic methods with regards to the loss of low frequency cells through multiple processing steps such as washes and sub-optimal purity and recovery from the selection itself, and not least, the costs of the specialized GMP reagents. An alternate approach to immunomagnetic isolation, is to select cells using clinical grade FACS (Cepok *et al.*, 2005, Kodituwakku *et al.,* 2003, Sung *et al.,* 2008). Though highly sensitive and specific, FACS sorting of rare cells (< 1%) to therapeutic quantities, is time consuming and associated with the risk of reduced cell viability (Wulff *et al.*, 2006).

1.6.2 Potential Use of Microfluidic Systems in Isolation of Antigen-Specific T cells

As stated earlier, the biophysical properties of cells also allow different cell types to be discriminated. For example, in flow cytometry the cell size determines light scattering properties, and in apheresis, centrifugal forces separate blood into its constituent cellular components based on their sizes. An emerging technique based on microfluidic separation utilizes the biophysical properties of live cells by applying different hydrodynamic forces on the target particles or by utilizing the natural biomechanical variation of the cells to guide them into different flow paths (Tsutsui and Ho, 2009). Studies reporting cell sorting based on size or stiffness demonstrate the potential applications of the microfluidic cell sorting technique for separating tumour cells, erythrocytes as well as activated Ag-specific T cells (Chwee Teck Lim, 2014, Hou *et al.,* 2010, Hur *et al.,* 2011, Preira *et al.,* 2013). It should therefore be possible to use natural or induced variations in biomechanical properties to separate activated lymphocytes from non-activated lymphocytes and other cell types.

1.7 Summary

Despite the emerging evidence that SCs, such as HSCs, can help to treat a variety of ischaemic and inflammatory disorders, their benefits are either minor or less efficient. This has been partly attributed to poor homing or trafficking of systemically delivered

HSCs to actual sites of injury. If SCs are to be potentially used in the treatment of regenerative diseases or the repair of ischemic or inflamed organs, it is obvious that strategies to increase HSC retention within injured tissues need to be urgently developed. The route of administration for cell delivery is critical in the introduction of SCs into the injured organ. Cardiac tissue repair has been approached using intracoronary and direct intramuscluar delivery of SCs locally (Dimmeler *et al*., 2008, Ott *et al.*, 2005, Sherman *et al.,* 2006). However, this local delivery method may not always be practically possible for other organs. Indeed for inflammatory diseases of the gut such as Crohn's disease, colitis or inflammatory bowel disease, often a significant, if not whole, length of the gut is damaged. For such organs, local injection of SCs would not be possible as multiple sites of injection would be required, making this a very 'cell hungry' means of delivery. For such disorders, systemic administration of SCs into the bloodstream would be preferable (Willing *et al.,* 2008). Systemic delivery relies on the local microcirculation of the injured organ to capture SCs as they home or traffick through that organ. This homing efficiency and subsequent capture or adhesion of SCs within injured organs is certainly poor and may be explained by a number of factors including a loss of SCs to the peripheral circulation as they pass through the pulmonary microcirculation where they become entrapped. This occurs either due to their size or poor deformability making it difficult for them to pass through the limited space of the capillaries.

It is possible therefore that the infusion of a more deformable sub-population of SCs may improve their homing efficacy by preventing non-specific tissue entrapment and thus increasing the number of circulating cells available for capture from the peripheral blood. However, no studies to date have investigated whether isolated SCs actually even exist as a heterogeneous population with regards their biomechanical properties. If they do, this could be exploited to isolate and inject in patients only SCs with physical properties that can potentially enhance their therapeutic efficacy clinically. It is anticipated that microfluidic devices, particularly those based on the combined inertial effect and secondary flow, may have the potential to perform this isolation procedure. Indeed, it has been experimentally demonstrated that particles and different cell populations can be separated in either straight or curved microchannels depending on the variation of their sizes and deformability.

The use of microfluidics may not be restricted to improving the efficacy of just SC-based cellular therapy. T cell therapy has also garnered significant recent interest clinically for a different class of diseases. However, their efficacy would be improved if the separation of Ag-specific T cells could be performed as currently this is the limiting step. It is proposed that activated T cells obtain different biophysical and mechanical properties compared with T cells before activation. This phenomenon may aid in their separation using microfluidics. However, before we can utilise microfluidic assays to separate lymphocytes for clinical therapeutic purposes, a more precise study of their biomechanical properties is needed. Parameters such as cell rigidity and deformability can be measured using several techniques including AFM, micromanipulation, magnetic tweezers, micropipette aspiration, optical tweezers, shear flow, cell stretching and microelectromechanical systems (Neubauer *et al.,* 2014). Powerful techniques such as AFM have previously been used to describe the elastic properties of lymphocytes, but only deform a portion of the cell surface (nano-indentation) rather than cell mechanical properties on the whole cell scale (Cai *et al.,* 2010). However, circulating lymphocytes experience significant repeated hydrodynamic and mechanical stresses in blood vessels, which are applied along their entirety leading to large deformations in the microcirculation. These are particularly seen following lymphocyte activation when they transmigrate out of blood vessels into the surrounding interstitial tissue. Therefore, it is important to characterise the mechanical property parameters of lymphocytes under large, as well as small, deformations. Of the techniques mentioned, micromanipulation, on the basis of compressing single cells by two flat parallel surfaces, can be used to generate large deformations of cells, including deformations until they rupture, but can also reversibly compress cells to small deformations (Nguyen *et al.,* 2010).

To summarise, the need to identify strategies that can separate (i) smaller and more deformable SCs and (ii) activated T cells is required to improve the benefits of these various types of cellular therapies. If microfluidic systems can isolate one type of cell from a heterogenous mixture of cells with high efficiency, then it is quite likely that they are able to separate sub-populations of the same cell type based on mechanical differences. However, a detailed characterisation of the mechanical properties of these cell types is needed and micromanipulation and/or AFM methods may be able to provide this information.

1.8 Aims and Hypotheses

The aim of this thesis was firstly to utilise micromanipulation and AFM methodologies to characterise in detail the mechanical properties of HSCs after exposure to large and small deformations. It is hypothesised that HSCs isolated from the same site, such as the BM, potentially exist as a heterogenous population with regards their deformability. Specifically, this study aimed to compare the stiffness of HSCs with another BM-derived SC, namely the MSC, and also with blood neutrophils. For lymphocytes, this project aimed to also use micromanipulation to test whether antigen activation can change their biochemical properties. It has been demonstrated that pre-treating HSCs with soluble inflammatory mediators such as SDF-1α or H_2O_2 enhanced their adhesion within injury sites. Basic micropipette aspiration methodology suggested this may be due to improvements in SC deformability, which would have limited non-specific entrapment. This project aimed to characterise, in a more sensitive assay, whether biochemical pre-treatment strategies using pro-inflammatory soluble mediators could modify the physical parameters of SCs.

The ultimate aim was to assess whether sub-populations of SCs (if they exist) based on physical properties could be isolated and whether infusion of the more deformable sub-group maintained a circulating pool of SCs *in vivo*. A range of fabricated microfluidic devices will be tested to identify the most efficient and effective at separating cells. Two straight and three curved microfluidic devices, in which their geometry is altered, will be designed and used to allow identification of a device that can effectively separate SCs based on size and deformability. Spiral devices will permit to assess whether the coupling of inertial focusing and secondary Dean flows impacts on the efficiency of SC separation. It is hypothesized that sub-populations of SCs with different sizes and deformability can be separated when passing through at least one of these devices by modulating the channel aspect ratio and flow parameters. This hypothesis will be validated by microfluidic flow experiments.

The impact of deformability on SC trafficking *in vivo* to the injured mouse gut will be assessed using fluorescent intravital microscopy (IVM). This technique allows direct imaging of the microcirculation of various organs *in vivo* in anaesthetised mice. Indeed, recent advances in intravital imaging methods have made it possible for live monitoring of infused cells in living animals (Rodriguez-Porcel, 2010). Following this, the ability of HSCs to home to the ischaemia-reperfusion (IR) injured small intestine will be investigated. IR injury induces a significant cellular and microvascular damage to tissues and organs resulting from the return/reperfusion of blood flow to previously ischemic tissues or organs. This injury often occurs during a wide array of routine surgical procedures, such as organ transplantation which can inevitably hamper the blood supply (King *et al.*, 2000), as well as many other clinical pathologies including stroke, myocardial infarction and limb ischaemia (Collard and Gelman, 2001). The return of the blood supply or reperfusion produces a number of inflammatory responses that both heighten local tissue and microvascular damage and lead to a systemic insult as well (Dorweiler *et al.,* 2007). The clinical outcomes of IR injury can be severe and diverse including direct organ dysfunction, breakdown of the gastrointestinal barrier, systemic inflammatory response syndrome and multi-organ dysfunction syndrome (Collard and Gelman, 2001).

1.9 Outline of the Thesis

Chapter 1 contains a literature review on the background and emerging challenges of cellular therapy, techniques used to test the mechanical properties of animal cells, and the current marker free approaches using microfluidic devices to separate cells of interest.

Chapter 2, the materials and methods section explains clearly how this study was conducted and describes the used experimental techniques and data analysis in detail.

Chapter 3 presents the key results of mechanical characterization of HSCs with micromanipulation and AFM techniques. The values of Young's modulus and nominal rupture tension/stress of single HSCs from micromanipulation measurements were calculated to determine the mechanical parameters of the whole-cell network. The Young's modulus of cell membrane was extracted from AFM measurements by fitting the experimental data to the Hertz model. Reorganization of actin filaments in response to SDF-1α or H_2O_2 pretreatment was displayed. The mechanical parameters of neutrophils and MSCs based on micromanipulation were obtained and compared with HSCs.

Chapter 4 presents the results of HSCs sorting using different microfluidic systems. The separation effectiveness of each system was assessed in terms of precision and throughput. The optimum operating conditions of the microfluidic systems for cell sorting were determined with the help of micromanipulation tests on isolated HSCs. The possible underlying mechanism of the lateral migration of cells was revealed. The isolated HSCs using a spiral microfluidic system were infused into intestine IR injured mice. The free flowing and adherent cells were continuously observed and quantified to verify the benefit of the cell sorting system.

Chapter 5 presents preliminary mechanical property data of CD8+ T lymphocytes before and after being activated for a period of time (4 days). The size and mechanical property change accompanying the activation process were displayed, and the mechanical property parameters include Young's modulus, nominal rupture stress/tension and deformation at rupture.

Chapter 6 summarises and discusses the major findings, and proposes recommendations for future research.

Chapter 2

Materials and Methods

2.1 Introduction

In this study, the mechanical properties of murine HSCs were determined and compared to murine blood neutrophils and also to murine MSCs. Two methods were utilised – micromanipulation to assess cell mechanical properties corresponding to large deformations and atomic force microscopy (AFM) causing small deformations of the cell surface. All types of circulating cells experience significant repeated hydrodynamic and mechanical stresses in blood vessels, which are applied along their entirely leading to large deformations in the microcirculation. Therefore, it is important to characterise the physical properties of stem cell populations at large deformations, as well as small deformations. Micromanipulation, on the basis of compressing single cells between two flat parallel surfaces, can be used to generate small to large deformations of cells, including deformations where the cells are actually ruptured (Nguyen *et al.,* 2010). Important mechanical parameters such as percentage deformation at rupture, rupture force, nominal rupture stress (σ_R), nominal rupture tension (T_R) and the Young's modulus (elastic modulus of the cell) were determined. The effects of pre-treating with key inflammatory markers, including stromal cell derived factor-1 (SDF-1α), keratinocyte chemoattractant (KC), and hydrogen peroxide (H_2O_2) on cell deformability were also comprehensively measured using the micromanipulation and AFM techniques. To provide some indication of how potential changes in deformability were induced, the polymerization of F-actin filaments after pre-treatment was analysed quantitatively using flow cytometry and confocal microscopy. These results are presented in **Chapter 3**.

After cell mechanical properties were characterised, it was further investigated whether any heterogeneity in the mechanical properties of HSCs could be exploited to separate cells into more soft/deformable and more rigid sub-populations. To do this, microfluidic devices were utilised to separate cells based on various principles, including micro-scale filters, hydrodynamic filtration (laminar flow), deterministic lateral displacement, field-flow fractionation and inertial effect. In this project, the inertial effect in five different microchannels was used to sort cells. Inertial force is the force due to the momentum of the fluid. These microfluidic systems provide a label-free method to sort cells based on their size and deformability variations with the ultimate aim of injecting only the more deformable sub-population to enhance HSC circulation and recruitment *in vivo*. Microfluidic systems with different channel geometries were designed and fabricated for separating smaller and more deformable HSCs from one heterogeneous population. The separation efficiency and throughput of the five different devices were assessed at varying flow rates. These results and the *in vivo* implications are presented in **Chapter 4**.

In addition to separating stem cells on the basis of their deformability, it should also be possible to use natural or induced variations in biomechanical properties to separate activated lymphocytes from non-activated lymphocytes and other cell types. Before we can utilize microfluidic assays to separate lymphocytes for clinical therapeutic purposes, a precise study of their biomechanical properties is needed. The micromanipulation technique was thus applied to measure the temporal biomechanical changes of CD8+ T cells following antigen (Ag)-induced stimulation. Again, the various mechanical strength parameters such as rupture force, rupture deformation, nominal rupture stress/tension for resting (unactivated) and activated T cells were determined. The compression data of T cells corresponding to smaller deformations obtained by micromanipulation was modelled to obtain a measure of the elasticity, defined as the Young’s modulus. This work provides important new data on the biomechanics of activated CD8+ T cells which can be used for future development of microfluidic separation of cells that can selectively respond to specific antigen stimulation. These results are presented in **Chapter 5**.

The current chapter details the sample preparation, reagents, techniques and experimental procedures used to generate thesis data.

2.2 Preparation of the Different Cell Types

2.2.1 Haematopoietic Stem Cells –Immortalised HPC-7 Cell Line

Since HSCs are rare cells, it is difficult to isolate enough cells from the mice for experimental research. Indeed, intravital microscopy studies looking at HSC circulation *in vivo* have been hampered by the difficulty in separating enough numbers for observation following systemic infusion (Chen *et al.,* 1997). Therefore, all studies utilized a murine hematopoietic progenitor cell line called HPC-7 (kind gift of Professor Leif Carlsson, Umea University, Sweden). This functionally relevant cell line was generated and immortalised by transfection of LIM-homeobox gene, Lhx2 into murine embryonic SCs. This cell line displays the critical characteristics of pure primary HSCs, such as being highly enriched for surface markers characteristic of the most immature HSCs (c-kit$^+$, Sca-1$^+$, CD34$^-$, Lin$^-$) (Pinto *et al.,* 1998, Pinto *et al.,* 2002). The Kalia group (University of Birmingham) have further characterised the HPC-7 surface adhesion molecule profile and found it to be similar to primary HSCs (Kavanagh *et al.*, 2013, Kavanagh *et al.,* 2010). They have also utilized HPC-7s to model hepatic HSC recruitment for intravital studies. Such studies include investigating the mechanisms of adhesion and subsequent steps of HPC-7s in the injured kidney or intestinal microcirculation and their retention to injured murine liver sinusoids (Kavanagh *et al.*, 2013, Kavanagh *et al.,* 2010). Therefore, the immortalized HPC-7 cell line was also used in this study. HPC-7s were cultured in Stem Pro-34 SFM media with the manufacturer’s medium supplement (Life Technologies, Paisley, UK), 100 ng/ml Stem Cell Factor (SCF, Life Technologies), 2 mM L-Glutamine (PAA, Somerset, UK), 50 U/mL penicillin and 50 U/mL streptomycin (PAA).

2.2.2 Culture of the Murine HSC Cell Line, HPC-7s

Since HPC-7 growth was sensitive to their density, cells were counted on a daily basis and maintained at the density of between 0.8 - 1.3×10^6 cells/mL by controlling the medium volume. To determine cell density, trypan blue (1:1 v/v) was added to the cell suspension. Cells that had taken up the trypan blue dye were considered non-viable and those that excluded the dye were counted as viable. Approximate 20 µL of the mixed suspension was viewed under a microscope with a ×10 objective. The number of cells not taking up the blue stain (viable cells) in four 1 × 1 mm^2 grids of a standard haemocytometer was counted. The average number from the four grids was calculated and multiplied by 2 × 10^4 to yield the density of cells (cells/mL). Cells were harvested from the cell suspension by centrifugation (300 × g, 5 min) for further experiments.

2.2.3 Isolation and Expansion of Murine Bone Marrow-derived MSCs

Bone marrow-derived MSCs were obtained as described in detail elsewhere (Houlihan *et al.,* 2012). Briefly, muscles and surrounding tissues were taken off from the fibulae and tibiae of male C57Bl/6 mice aged between 8 and 12 week adult. Bones were broken, followed by the digestion of marrow contents in 0.2% collagenase solution(Wako Chemicals, Osaka, Japan) in DMEM (Sigma-Aldrich, Poole, UK). Then cells were isolated as a result of mechanical dissociation from the bone. Subsequently, MSCs were selectively collected from suspensions by the use of flow cytometry (MoFlo XDP, Beckman Coulter, HighWycombe, UK). FITC conjugated anti-mouse Sca-1 (Ly6A/E; Clone D7, eBioscience, Hatfield, UK), PE conjugated anti-mouse CD45 (30-F11, eBioscience, Hatfield, UK), PE conjugated anti-mouse TER-119 (Clone TER-119, eBioscience, Hatfield, UK) and APC conjugated anti-mouse CD140a (PDGFRα; Clone APA5, eBioscience, Hatfield, UK) were labelled to the suspensions. Suspensions after being labelled were washed and re-suspended in Hanks' balanced saline solution (Sigma-Aldrich) with propidium iodide (eBioscience, Hatfield, UK). MSCs were sorted and enriched resulting from positive staining for Sca-1 and CD140a, and negative staining for TER-119, CD45 and PI (Kavanagh *et al.*, 2015). This criterion harvests an enriched population of proliferative murine MSCs. Isolated MSCs were cultured in a 6-well plate and maintained in Minimum Essential Medium Eagle - Alpha (MEMα) supplemented with 10% fetal bovine serum (FBS; Sigma-Aldrich), L-glutamine (PAA Laboratories, Yeovil, UK), penicillin/streptomycin (PAA) and 10 ng/mL transforming growth factor-β (TGFβ; New England Biolabs, Herts, UK). This culture medium was changed every 3 days to obtain a cellular confluence of 90%. Cells between passage 4 and 9 used for experiments were recovered by incubating them for 5 min at 37°C with 0.25% trypsin/EDTA solution. Immediately after trypsinization, cells were collected with a pipette, transferred to a 15mL conical tube and centrifuged at 300 × g for 5 min. Cells were re-suspended in phosphate buffered saline (PBS) for mechanical testing.

2.2.4 Isolation of Murine Neutrophils

The density gradient separation method was used to isolate murine neutrophils from bone marrow as previously described in detail (Nauseef, 2007). Briefly, rear legs were removed from 8-12 week adult male C57Bl/6 mice, and the bone marrow was carefully aspirated into a syringe. This cell suspension was filtered, washed and centrifuged and cells re-suspended in 2mL EDTA (Sigma-Aldrich). A percoll gradient (2.5 mL 72%, 2.5 mL 64%, 2.5 mL 52%) was set up in a 15mL falcon tube, onto which the cell suspension was added. The percoll gradient dilutions were prepared from 100 % percoll (Sigma-Aldrich) and PBS. The gradient was spun at 1500 × g for 3 min to separate the neutrophils, from which a fuzzy band of cells were seen at the interface of the 72% and 64% Percoll. By removing the percoll and cells above it, which was then discarded, the neutrophils were collected, washed and re-suspended in 1 mL PBS for mechanical testing.

2.2.5 Pre-treatment of HPC-7's Using SDF-1α, KC and H_2O_2

SDF-1α and KC (Peprotech, UK) solution was made at a primary concentration of 10 µg/mL which contained 0.1% bovine serum albumin (Sigma-Aldrich, Poole, UK). Both were then diluted to working concentrations of 10 ng/mL in 1 mL PBS for pre-treatment studies. H_2O_2 (Sigma-Aldrich, Poole, UK) was made at a high concentration of 8.8 M prior to use and diluted to 100 µM with PBS (Life Technologies) for subsequent pre-treatment experiments. 1×10^6 HPC-7 cells were obtained from a cell suspension by centrifugation (300×g, 5min) and pre-treated for 30 min with either the vehicle control (PBS), SDF-1α, KC or H_2O_2 at 37°C. After pre-treatment, cells were washed and re-suspended in PBS and mechanically tested within 2 h.

2.2.6 Isolation, Culture and *in vitro* Activation of Human T Lymphocytes

Peripheral blood was collected from three healthy drug-free donors after informed consent (Ethics ref: 11/WM/0315). Peripheral blood mononuclear cells (PBMC) were isolated by Ficoll separation (Reinherz *et al.,* 1979). Briefly, the contaminating erythrocytes were removed by osmotic lysis and 1 ml of distilled water was added to the cell pellet. After 30s, 14 ml of RPMI 1640 (Sigma-Aldrich) was added, and the cells were washed once. CD8+ T lymphocytes were isolated by negative immunomagnetic separation using a commercial CD8+ T Cell Isolation Kit and LS columns (Miltenyi Biotec, Bergisch Gladbach, Germany). PBMC were labelled with anti-CD3/PE antibody (Dako, Denmark) and $CD3^+$ cells were separated using anti-PE MicroBeads and LS columns following the manufacturer’s instructions. Cell purity was checked using a FacsCanto II flow cytometer (BD, San Jose, CA, USA) and in all the cases the T lymphocyte purity was above 90%. Enriched T lymphocytes were re-suspended in RPMI 1640 plus 10% foetal calf serum (Sigma-Aldrich). Some cells were activated by culturing in the presence of 30ng/mL of the anti-CD3 antibody OKT3 (BioLegend, San Diego, CA, USA) plus 600 U/mL IL-2 (Chiron, Emeryville, USA). The mechanical properties of resting and activated CD8+ T lymphocytes were measured either immediately after harvesting (day 0) or tested 2 days or 4 days post-activation. Cells were diluted with PBS to reduce cell density in suspension and mechanical testing was completed within 3 h.

2.3 Calibration of Micromanipulation System

2.3.1 Introduction of the Micromanipulation Rig

The mechanical properties of cells were measured with a micromanipulation as shown in **Figure 1.4** in Chapter 1. The principle and details of this technique have been given elsewhere (Nguyen *et al.*, 2009a, Nguyen *et al.,* 2010). Briefly, the technique involves compression of a single cell between the flat end of a probe and the bottom of a glass chamber containing the culture medium. Suspended single cells were allowed to settle to the bottom of the transparent chamber, and images were captured with a side-view high-speed digital camera. A probe with a 25 µm diameter flat end was driven downwards by a stepping motor towards the single cells. The probe had been made by pulling a borosilicate glass rod (~500 μm diameter) in heat and polishing one end using a microgrinder (NARISHGE Ltd, United Kingdom). The probe was connected to a force transducer (406A-ER, Aurora Scientific Inc. Canada) which collected the data of instantaneous force imposed on single cells at a frequency of 50 Hz. From the measurement, force versus time and force versus displacement data could be obtained.

2.3.2 Calibration of Force Transducer Sensitivity

The sensitive 406A-ER force transducer was used to collect the data of forces imposed on single cells. On this force transducer, the manufacturer perpendicularly glued a glass tube onto a cantilever beam which could deflect when a force was applied on it and induce the output of a voltage alteration. The bigger the force applied onto the tube, the more cantilever beam deflected, resulting in a bigger change of output voltage. The force transducer sensitivity was defined as a change in the applied force per unit change of voltage which needed to be calibrated prior to the experimental test.

The calibration procedure has been specifically presented elsewhere (Liu, 2010). Briefly, the 406A-ER force transducer was inversely placed on a flat stage and fixed by Blue-Tac.

A piece of paper was cut into tiny papers in square shape which had various weights (0.75 mg, 1.5 mg, and 3 mg). When there was no paper on the tube, the output voltage was recorded as the baseline. The calibration procedures were undertaken in triplicate by considering the possible signal fluctuation and weight variation. Subsequently, one or several pieces of paper were put onto the top of the tube in sequence in order to get different loading force. The corresponding voltage was recorded after each piece of paper was carefully added and remained stable. The force applied onto the transducer was calculated by multiplying paper weight with the gravitational constant G (9.8 m/s^2). The relationship between the applied force and change of voltage is shown is by **Equation 2.1**.

$$\mathbf{F = \Delta V * Ks} \qquad \mathbf{(2.1)}$$

where F is the applied force, ΔV is the change of voltage compared with the baseline and Ks is the transducer sensitivity.

The calculated sensitivity of the 406A-ER transducer was 0.0558 mN/V. Additionally, transducers could be selectively connected with a ×10 signal amplifier to further increase the sensitivity considering the fragile property of cells.

2.3.3 Calibration of Image Size on the TV Screen

The side view camera was connected to a ×35 objective used to capture the image of the cells. The diameter of these cells could then be measured through the TV screen. The dimention of images on the screen was accurately calibrated before performing such measurements. A standard measurement graticule of 100 µm in length was vertically fixed in front of the lens and the scale image on the screen was accurately and clearly marked.

2.3.4 Calibration of Compression Speed

After the calibration of image size on the TV screen, the force probe was driven by the stepping motor downwards or upwards for a distance δ with different speeds set by the software. The time, **t**, used for the probe to travel was simultaneously recorded using a stop watch, and triplicate experiments were undertaken for each speed calibration. The speed (v) was calculated as $v = \delta/t$ and the speed used in the present study was set at 2 μm/s.

2.4 Measurement with the Micromanipulation Technique

2.4.1 Experimental Procedure to Compress Cells to Rupture

For each sample, 20 single cells were randomly compressed- in order to geerate statically representative results. Before compression, the diameter of the selected cell was directly measured from its image on the screen of the TV monitor. The probe was located on the top of a single cell and then moved downwards to compress the cell at a speed of 2 μm/s until the cell was ruptured and the probe contacted the bottom of the substrate (**Figure 2.1a**). From the measurement, force versus time or force versus displacement data were obtained.

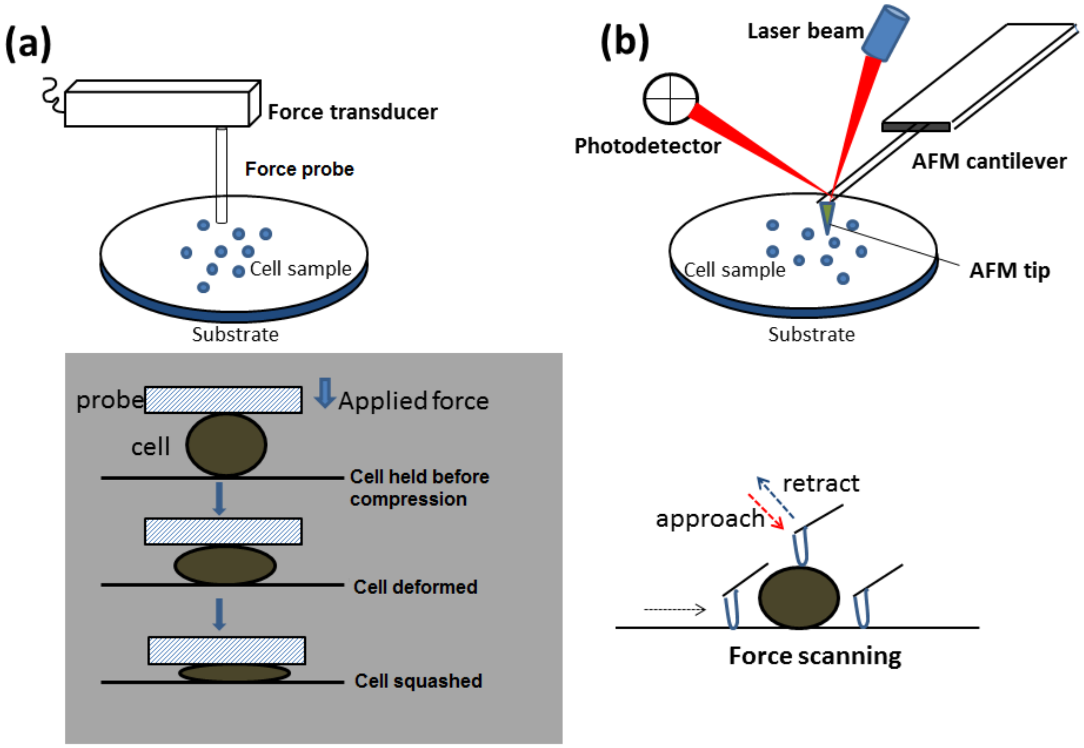

Figure 2.1. Schematic diagrams illustrating the micromanipulation and AFM compression methods. (a) The compression process of an individual cell between two flat surfaces with the micromanipulation technique. The big probe was located on the top of a single cell and then moved downwards to compress the cell with a speed of 2 μm/s until the cell was ruptured. From the measurement, the data of force versus time or force versus displacement data were obtained. **(b)** Local probing of cell surface mechanics with AFM. A cantilever was elevated and approached to the sample. Forces acting between the tip and the sample/surface at a specific point were recorded in a single force-height curve. In the meantime, the cantilever was moved in the lateral direction, thus force curves from all the compressed points formed a scanning map.

2.4.2 Determination of Mechanical Property Parameters from Micromanipulation Data

2.4.2.1 Young's Modulus

Stiffness is the ability of cells to resist deformation under a given applied stress, which can be characterised by the Young's modulus. Theoretically speaking, the Hertz contact model is valid and commonly used to describe the relationship between the imposed force and displacement for small deformations of an elastic object. It has been successfully applied to yield the Young's modulus of different particles including cells when compressed to a small deformation (Kuznetsova *et al.,* 2007, Martens and Radmacher, 2008, Yan *et al.,* 2009). In this study, the Hertz contact model was also applied to calculate the Young's modulus, having presumed that the individual cells were homogeneous, incompressible, elastic spheres and there was no friction between the cell-substrate interfaces, given by **Equation 2.2**.

$$F = \frac{E * \sqrt{2R_c}}{3(1-\upsilon^2)} \delta^{3/2} \tag{2.2}$$

Where F is the applied force, E is the Young's modulus of the cell, E is the original cell radius, υ is the Poisson's ratio of the cell (υ assumed to be 0.5 since cells are assumed to be incompressible material) and δ is the diametric compressive displacement.

From the model, there should be a linear relationship between F and $\delta^{3/2}$. Theoretically, by fitting the model to the force versus displacement data, the value of Young's modulus, E, could be determined since the values of other parameters were known. Hence from the slope of the linear fitting, known values for the cell's radius and Poisson's ratio, the value of Young's modulus was determined. Higher values indicated cells that are less deformable for a given applied force and *vice versa.*

2.4.2.2 Nominal Rupture Stress and Nominal Rupture Tension

When compressed to a large deformation the cell can be ruptured and the corresponding force used to determine the cells' mechanical strength. Since the force required to rupture a cell depends on the initial size of the cell, it is difficult to compare the rupture force between different samples of cells if they have different sizes. Therefore, two additional parameters were quantitated which take into account the actual size of the tested cells. This allowed meaningful comparisons between different cell groups. These parameters were nominal rupture stress (σ_R) and nominal rupture tension (T_R). These values provide a comparable indication of the mechanical strength of cell.

The combination of nominal rupture stress/tension and the percentage deformation at rupture may be used to decide whether cells are strong/brittle, strong/flexible, weak/brittle or weak/flexible. The real rupture stress and tension can be determined by applying the appropriate mathematical models (Ferguson *et al.*, 2015), but this is beyond the scope of this study.

The nominal rupture stress (σ_R) was defined by the ratio of the rupture force (F_R) to the initial cross-sectional area, given by **Equation 2.3**.

$$\sigma_R = \frac{4F_R}{\pi d^2} \qquad \textbf{(2.3)}$$

where F_R is the rupture force and d is the original cell diameter before compression.

The nominal rupture tension (T_R) was defined by the ratio of the rupture force and the original cell diameter, as shown in **Equation 2.4**.

$$T_R = \frac{F_R}{d} \qquad \textbf{(2.4)}$$

2.4.3 Compression/Holding Experiments

Cells may also show visco-elastic behaviour In order to ascertain this, compression/holding experiments were carried out to determine if there was obvious force relaxation. Approximate 20 cells were selected and single cells were compressed to different deformations before rupture, and then held for several seconds. The data of force versus time were obtained for further analysation.

2.4.4 Statistical Analysis of Data from Micromanipulation Compression

The various values of the cell mechanical property parameters are presented as mean ± standard error. A paired Student's t-test was performed to determine whether significant differences exist in the mechanical properties between different samples, with statistical significance reported at 95% ($p < 0.05$) and 99% ($p < 0.01$) confidence levels.

2.5 AFM Measurement Procedures

2.5.1 AFM Instrument

When a cell was compressed using micromanipulation to small fractional deformations, e.g. < 10% (ratio of the cell displacement), it was found that the force imposed on the cell was small, and comparable to the noise level of the force measurement. Therefore, a JPK NanoWizard^{R} AFM system was used to carry out the mechanical experiments, particularly on small deformations (nano-indentation) which deformed only a portion of the cell surface (**Figure 2.2**). The instrument was placed on an anti-vibration platform in order to reduce the noise level due to possible vibration of surrounding environment. The AFM system interrogates the surface of the cell by means of a sharp probe or tip situated at the end of a flexible cantilever. This AFM head with a cantilever is the most important part of the system and was installed on an inverted optical microscope. The cell sample could be observed in reflected light through the CCD camera and the long-distance top-viewed optics. The cantilever could be driven by the motor both horizontally and vertically to scan across the sample surface. To form an image, the tip was brought close to the cell and raster-scanned over its surface, causing the cantilever to be deflected as a result of probe-cell force interactions. A line-by-line image of the cell surface was formed as a result of this deflection. JPK software was used to give instantaneous commands and collect force and image data. In this study, the force-mapping mode was adopted to measure the forces imposed on cell surface at a number of points (or pixels), taking into account of the cell geometry to get a sufficient number of force curves for statistical analysis.

2.5.2 Procedure of Force Scanning on Cell Sample with AFM

The groups of PBS control, SDF-1α and H_2O_2 pre-treated HPC-7s were mechanically measured with the AFM system (**Figure 2.1 b**). Single cells were required to be immobilized to reduce the lateral movement during the force scan. However, HPC-7s were not able to adhere to the surface and their gravity was not sufficient to keep them still. To address this issue, the adhesive substrate was prepared by coating a polystyrene surface with Cell-Tak solution (Corning, USA) prior experiments, and spherical cells were allowed to immobilize for 20 min. The immobilized cells were placed on the XY stage and visualized by the optical microscopy. An oxide sharpened silicon nitride (Si_3N_4) cantilever with a specialized spherical tip of 4 μm in diameter and a spring constant of 0.2 N/m was elevated and approached to the sample, forces acting between the tip and the sample/surface at a specific point were recorded in a single force-height curve. In the meantime, the cantilever was moved in lateral direction, and thus force curves from all the compressed points formed a scanning map. The scan area was 100 X 100 μm with pixels of 64 x 64 and vertical speed was 15 μm/s, thus in one measurement, approximately 20 cells could be scanned and over four thousand force curves which represented the compression of substrate surface and cells were acquired.

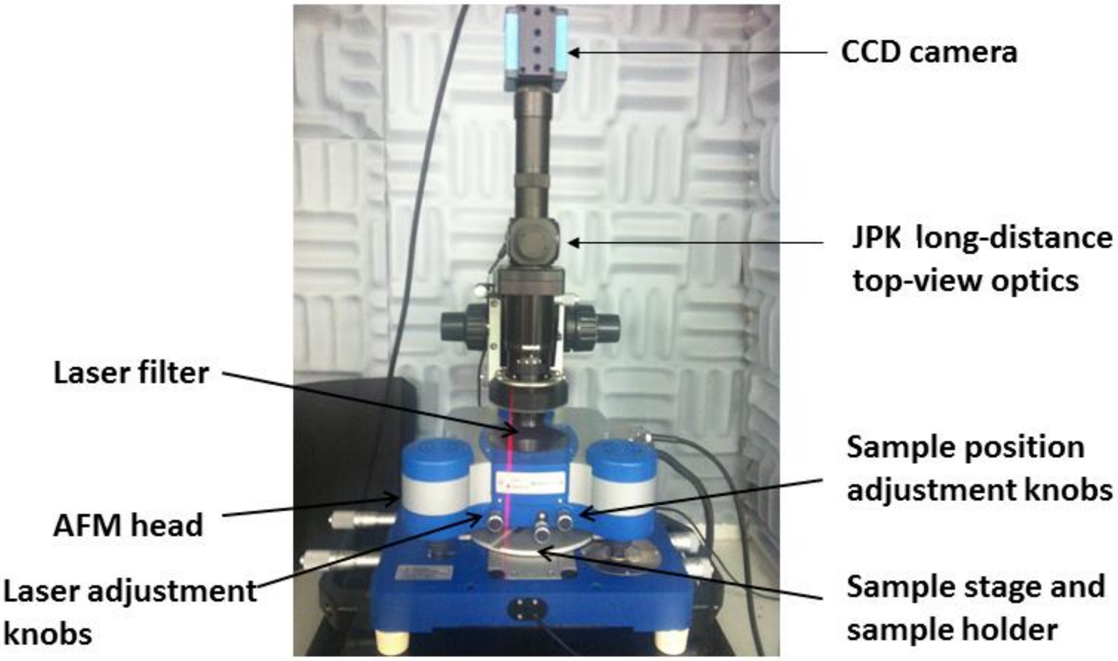

Figure 2.2. Image of a JPK NanoWizard^{R} AFM system. The instrument was placed on an anti-vibration platform in order to reduce the noise level potentially due to vibration of the surrounding environment. The most important part of the instrument is the AFM head with a cantilever, which was installed on an inverted optical microscope. The cell sample can be observed in reflected light through the CCD camera and the long-distance top-viewed optics. The cantilever could be driven by the motor both horizontally and vertically to scan across the sample surface.

2.5.3 Calculation of Young's Modulus of the Cell Membrane as Determined by AFM

As discussed above, the force mapping mode can collect single force curves either of the substrate surface or the cell and the relative height data at specific positions as well, obtaining the 3-D geometry of cells. It is important to select force curves on a relatively flat area of single cells in order to satisfy the presumption of contact model for calculation of Young's Modulus — the Hertz Model typically assumes the probe of known geometry (spherical) over a flat surface. Subsequently, selected force curves were analyzed with **Equation (2.5)** to fit the force data for calculation of Young's modulus of cell membrane (Kuznetsova *et al.*, 2007).

$$F = \frac{4\sqrt{R_c}E}{3(1-\upsilon^2)}\delta^{3/2} \tag{2.5}$$

where R_c is the radius of the probe, and other parameters are the same as those in **Equation (2.2)**. For each sample, more than 20 cells were investigated for statistical analysis.

2.6 Analysis of F-actin with Flow Cytometry and Confocal Microscopy

To assess the effects of pre-treatment on F-actin, HPC-7 cells were pre-treated with PBS (vehicle control), SDF-1α or H_2O_2 as described earlier and then fixed by incubating in 1 mL 2.5% formaldehyde for 10 min. After washing twice in PBS, cells were transferred to a polypropylene tube with 1mL PBS containing 0.1% Triton-100 to be permeabilized for 5-7 min. Cells were blocked for 1 h in PBS containing 5% normal fetal bovine serum followed by being labeled for 1 h in PBS with FITC-Phalloidin (Life Technologies, USA). All staining steps were performed on ice. After washing in PBS, the cell suspension was aliquoted into two tubes, one containing cells for flow cytometry experiments and the other containing cells for imaging using confocal microscopy. A minimum of 10000 fluorescent cells from each sample were analyzed on a BD FACS Calibur cytometer (Becton Dickinson, USA), and background green fluorescence (FL) was evaluated on cells pre-treated with PBS. Data were analyzed with CellQuest (Becton Dickinson, USA). FL intensity was automatically calculated and presented in a probability distribution. Cell samples in another tube were examined on a Leica SP2 laser-scanning confocal microscope using a 100× objective and pinhole settings providing optical sections of around 0.5 µm. HPC-7 cells without apparent damage or aggregation were randomly selected. An automated macro then acquired two perpendicular Z-scans (XZ and YZ profiles) crossing the geometric centre of the XY region of interest.

2.7 Microfluidic System Preparations and Cell Sorting Procedures

2.7.1 Design Principles of Microfluidic Devices

Different types of microchannels with various geometries have been designed to separate particles/cells into specific equilibrium positions within the microchannel cross-section. Within straight, rectangular microchannels, inertial lift forces (F_L) dominate in focussing particles/cells into these positions and consist of two opposing forces: the wall-induced lift force (F_{LW}) directing particles/cells to the channel centre and the velocity or shear gradient-induced force (F_{LS}) directing particles/cells to the channel walls. The balance of these two forces determines the equilibrium position(s) within the microchannels. Changing the aspect ratio (channel width /height) and/or the Reynold's number (Re) are two different ways to control the equilibrium positions of particles/cells of different sizes and deformabilities. Re can be simply altered by changing the flow velocity of the fluid within the microchannel. Therefore, in the current study, two straight microfluidic devices with different geometries, **Device A** and **Device B**, were utilised under different flow velocities to allow identification of a device that can effectively separate cells based on size and deformability.

In addition to the two straight microchannel devices, three curved/spiral devices, **Device C, Device D** and **Device E** were also tested. Although in straight channels, the particle size, channel dimensions, F_L and Re impact the equilibrium positions, in curved channels an additional Dean number, D_e, also dictates particle/cell focussing. In this study, it is hypothesized that sub-populations of cells with different sizes and deformability can be separated when passing through curved channel with a spiral shape by modulating the channel aspect ratio and flow parameters. To assess whether the coupling of inertial focusing and secondary Dean flows impacts on the efficiency of stem cell separation, three different curved microchannels with different curvature ratios (θ) were also designed and investigated.

2.7.2 Fabrication of Microfluidic Devices

Two types of microfluidic systems either with straight channels or curved (spiral) channels were utilized in the present study. Both straight microchannels had one inlet and three outlets but had two different geometries (**Figures 2.3a**). **Device A** had an AR = 5 (height = 30 µm; width = 150 µm; length = 20 mm) and **Device B** had an AR = 10 (height = 20 µm; width = 200 µm; length 20 mm). All three spiral microchannels also had one inlet but two outlets. The spiral designs had an initial radius of curvature of 8mm, the width of microchannels was fixed at 300 µm, while the channel height was varied be 40 µm (**Device C**), 60µm (**Device D**) and 80µm (**Device E**). **Device C** and **Device D** both consisted of 4 loops (**Figure 2.3b and c**), whereas **Device E** consisted of 6 loops (**Figure 2.3d**). The devices were all made of polydimethylsioxane (PDMS), customized from a professional company (Wenhao Chip Tech., Suzhou, China).

The microfluidic channel inlet was connected to a pump syringe (Cole-Parmer, UK) using flexible tubing. Similar tubing was connected to the outlets for harvesting cells (**Figures 2.3e** and **f)**. In this work, the effects of channel Re, cell blockage ratio (κ = a/H) and De on the cell separation in straight and spiral channels of rectangular cross-section were studied. The distributions of cells in different outlets in terms of number and mechanical strength after separation were assayed to compare the cell separation efficiency using varying operational conditions and microchannels.

2.7.3 Preparations of Microfluidic Systems

The PDMS chip was added to the stage of an EVOS cell imaging system equipped with a microscope and a camera (Thermo Fisher Scientific, USA; **Figure 2.3g**). The channel was washed with 70% ethanol using the syringe pump for around 10 min at a flow rate of 10 ml/h, and then the channel was washed once with PBS buffer for 10 min at the same flow rate. Only after washing was the chip considered ready to use. HPC-7 suspensions were centrifuged and re-suspended in PBS at a certain concentration. A 5 mL vertically oriented syringe was used to pump the cells through the device using the syringe pump. Instantaneous images near the downstream region of the microchannel were captured from the screen and videos recorded for real time control of the sorting system. Sub-populations of HPC-7s were harvested from the outlets for further mechanical assessment or for use in intravital *in vivo* trafficking studies.

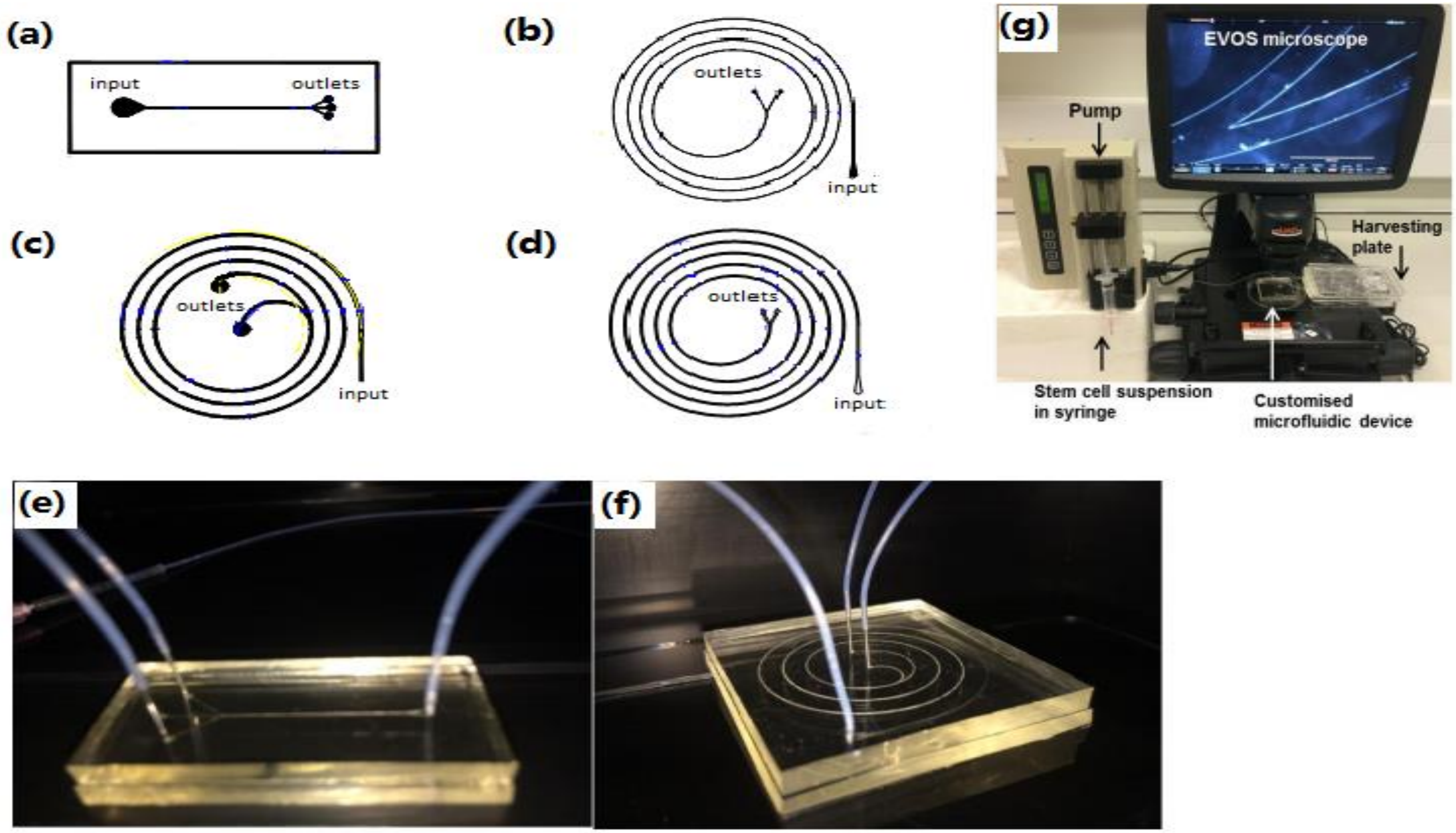

Figure 2.3. Microfluidic systems used for separating small/deformable HSCs from a heterogenous population. (a) Schematic diagram of **Device A** and **Device B** that varied only in their aspect ratio with Device B having less height and being wider. Schematic diagrams of **(b)** Device C **(c)** Device D and **(d)** Device E that varied in their height (40µm, 60µm or 80µm) and the number of loops (4 or 6). Typical photographs of PDMS fabricated chips with **(e)** straight and **(f)** spiral microchannels with connected tubing. The inlet tubing was connected to a syringe pump which infused the cells at varying velocities. **(g)** The PDMS chip was mounted onto an EVOS cell imaging system equipped with a microscope and camera. A vertically oriented 5ml syringe attached to the pump was connected to the inlet of the chip through flexible tubing.

2.7.4 Cell Sorting Procedures

In order to obtain reproducible data, it was essential to make sure that the mechanical strength of cell populations used in each experiment was consistent. However, preliminary experiments showed that the cell mechanical properties varied with complex factors like medium, culture time, and other external environmental factors. Moreover, building blocks of cytoskeleton played important roles in cell proliferation, thus, cells in different proliferative stages could also lead to different cell mechanical properties. Therefore, before pumping cells through the microchannel, the mechanical properties had to be tested in advance to make sure the consistency of experiments performed at different times. For all experiments, 4 mL HPC-7 suspension with density of 2×10^6/mL was initially injected into the microchannel at various flow rates (2.5 mL/h, 5 mL/h, 7.5 mL/h and 10 mL/h), and subpopulations harvested from the two outlets were counted and processed for further studies. During the cell sorting experiments, any bubbles and clogging in the channel were avoided.

2.7.5 Mechanical Analysis of Harvested Cells

HPC-7's harvested from the side and central outlets of the straight microchannels and from the inner and outer outlets of the curved/spiral microchannels were mechanically tested with the micromanipulation technique. The mean values of nominal rupture stress were used to demonstrate the mechanical strength of isolated cells and compare the separation efficiency, as described above.

2.7.6 Cell Viability Assay

The viability of HPC-7s before and after undergoing separation was assessed via trypan blue exclusion assay, and the number of cells that excluded the dye was counted for comparison. Additionally, since the mechanical properties of cells can change in accordance with their physiological state or in response to stimuli within the environment (Rodriguez *et al.,* 2013), the obtained cell mechanical properties after separation experiments can also be regarded as an indicator of cell viability.

2.8 Animal Experimental Procedures

2.8.1 HPC-7 Culture, Separation and Labelling

HPC-7 cells were maintained in a Stem-pro medium as described previously. The experiments conducted using the 5 microfluidic devices demonstrated that **Device C** was most effective and efficient at separating deformable HPC-7 cells at a flow rate of 10mL/h. Therefore for intravital studies, **Device C** was used to conduct cell isolation. A 4mL HPC-7 cell suspension with a concentration of 2 × 10^6/mL was pumped into the microchannel at a flow rate of 10 mL/h. A more deformable sub-population of cells harvested from the inner outlet were processed for a second flow through the microchannel. Cells that were further separated from the inner outlet were used for the intravital study. HPC-7s harvested from the outer outlet in the first flow were used for comparison purposed intravitally. Isolated cells were washed with PBS, and then re-suspended in 4 mL PBS containing 5 µM carboxyfluorescein diacetate succinimidyl ester (CFDA-SE), followed by incubation at 37 °C for 10 min. CFDA-SE is a cell permeable dye that enters cells by diffusion. It is cleaved by intracellular esterases to produce CFSE which fluoresces a green colour after excitation at 488 nm. Fluorescently labelled cells were centrifuged and re-suspended in 200 µL warm StemPro media (37 °C) prior to systemic injection in mice for intravital imaging.

2.8.2 Animals

Male C57BL/6 mice (8 - 12 week old; Harlan, UK) were utilised for experiments in accordance with the Animals Act of 1986 (Scientific Procedures; PPL:7008204 held by Dr Kalia). Local Birmingham Ethical Reviews Sub-Committee (BERSC) approval was also sought before Home Office approval. All studies were performed under terminal anesthesia with animals being sacrificed by cervical dislocation, as approved by Home Office. Anaesthetised animals (100 mg/kg ketamine hydrochloride; 10 mg/kg xylazine hydrochloride; I.P.) can keep breathing by tracheostomy and carotid artery cannulation to allow administration of labelled cells and any additional maintenance anesthetic.

2.8.3 Intestinal IR Injury Model

Intravital microscopy was involved to observe HPC-7 trafficking with the injured intestinal microvasculature as previously described (Kavanagh *et al.,* 2015). The injury induced was ischaemia-reperfusion (IR) injury, which was prepared through occlusion of the small mesenteric artery using a non-traumatic artery clamp for 45 minutes. Reperfusion was generated after the clamp was removed. The small intestine was gently pulled away from the animal using a surgical swab onto a sterile petri dish, avoiding puncture of the organ and vasculature. The mucosal surface was visualised after cautery incision alongside the anti-mesenteric border.

2.8.4 Intravital Microscopy and Tracking of HPC-7s *in vivo*

Exposed mucosal villi were visualised under the inverted intravital microscope (motorised Olympus IX-81, Olympus, UK). For observation, a single x10 field of view was randomly selected prior to cell infusion. A single dose of 2 x 10^6 HPC-7s pre-labelled with CFDA-SE, was intra-arterially infused at 30 minutes post-reperfusion and cell attachment/movement in the mucosal villi were accounted. Cells were introduced at this time point to allow IR injury to be prepared in the gut. Digital videos were recorded from the selected field of view for one minute, at a frequency of every 5 minutes, for an hour post-reperfusion. The number of free flowing and adherent cells at each time point was counted. Free flowing HPC-7s were counted as cells that freely moved through the field of view without stay for more than 30 seconds. Adherent HPC-7s were defined as those that remained stationary for more than 30 seconds. At the end of the experiment, the small intestine was excised and 5 additional fields of view were monitored to make sure the events in the pre-selected area were representative. The lungs were also removed from the mouse and five fields were randomly selected and entrapped cells were counted. Data was stored digitally and analysed off-line (Slidebook, Intelligent Imaging Innovations, USA).

Chapter 3

Mechanical Characterisation of Neutrophils, HSCs and MSCs Using Micromanipulation and AFM

3.1 Introduction

HSCs and MSCs have increasingly acted as the leading cells for consideration to treat a whole host of inflammatory and degenerative diseases. Clinically, the preferred route of infusion of stem cells for cellular therapy is directly infusion into the bloodstream. This provides both a non-invasive administration method and permits repeated injections of cells (Houlihan and Newsome, 2008). Therefore, the capture of exogenously infused circulating stem cells by injured tissue microvessels is a prerequisite event for successful therapy, regardless of the reparative mechanisms used by these cells. However, this event seems to be limited partially due to poor delivery of circulating stem cells to sites of injury, which may contribute to explaining the poor current success of cellular therapy clinically.

This is a particular problem for MSCs, which are known to be a larger cell type compared to HSCs. Indeed, the Kalia group have provided results that very few administered MSCs actually homed to and became retained within the injured site, unlike HSC recruitment which was four- to five fold higher within a similarly injured tissue (Kavanagh *et al.,* 2015). This lack of delivery to the intended site might be due to large MSCs becoming trapped in upstream microvessels. It is hypothesized that possibly more deformable stem cells may be able to migrate to the injured organ by avoiding entrapment elsewhere. Indeed, mechanical deformation is a key player in permitting neutrophils, with diameters of 6-8 μm, to traverse smaller pulmonary capillaries, with diameters of 2 – 15 μm (Doerschuk *et al.,* 1993, Tse *et al.,* 2005). In their transit through the pulmonary and systemic microcirculations, neutrophils tend to undergo a mechanical deformation when being subjected to mechanical stimulation in narrow capillaries (Yap and Kamm, 2005). Neutrophils in capillaries tend to present with an elongated shape whereas those in arterioles are generally more spherical. Indeed, some neutrophils are even found to concentrate in the pulmonary capillaries compared to the arterioles (Mizgerd, 2002). This ability to mostly avoid entrapment explains why neutrophils are typically the first leukocytes to be recruited to an inflammatory site where they can eliminate pathogens by multiple mechanisms, and they are obviously recruited more rapidly than HSCs and MSCs (Summers *et al.,* 2010, Kolaczkowska and Kubes, 2013).

Some evidence already exists to suggest better deformability may hold a key to improving stem cell delivery to sites of tissue injury. Pre-treating murine HSCs with inflammatory cytokines has previously been shown by the Kalia group to significantly enhance their adhesion to a number of different injured tissues both *in vitro* and *in vivo* when compared to pre-treatment with PBS controls (White *et al.,* 2013, Kavanagh *et al.*, 2013). Basic micropipette aspiration methodology suggested this may be partially due to improvements in cell deformability. This was postulated to have resulted in reduced non-specific entrapment in small capillaries and maintenance of a pool of stem cells circulating within the peripheral blood, available for capture by microvessels within injured sites. However, the micropipette aspiration methodology is somewhat limited in spatial resolution to the micron scale. Its accuracy to measure deformability changes is dependent on the optical imaging resolutions.

Currently, very little is known about the basic mechanical properties of HSCs and MSCs, particularly with regards their deformability characteristics. Comparisons with other circulating blood cells such as the neutrophil have also not been made. Therefore, to investigate the mechanical properties of these stem cells more precisely, including their mechanical behaviour at both large and small deformations, micromanipulation and AFM techniques were used to measure the forces applied to the cytoskeleton structure, as well as the plasma membrane respectively. This study aimed to directly derive or calculate various mechanical property parameters of both HSCs and MSCs, from large and small deformations and compare these values to those obtained for the blood neutrophil. For HSCs, the effects of pre-treatment with soluble inflammatory factors on their mechanical behaviour were also determined. The mechanical property parameters calculated included cell diameter, the rupture deformation, the force required to rupture the cell, nominal rupture stress, nominal rupture tension and also the Young's or elastic modulus. The polymerization of F-actin after pre-treatment of HSCs with inflammatory factors was also assessed using flow cytometry and imaged using fluorescent confocal microscopy. The mechanics of the whole-cell cytoskeleton, the localized membrane mechanical stiffness of cells and the potential underlying mechanisms are discussed.

3.1.1 Hypothesis

It was hypothesized that the poor recruitment of both HSCs and MSCs, when compared to the rapid response of inflammatory neutrophils, was due to their larger size. Furthermore, since MSCs demonstrate significantly more non-specific entrapment, it was hypothesized that in addition to size being a major factor, these cells also were the more 'stiff' cell type which hindered their easy transit through small capillaries. Since studies on pre-treatment with inflammatory factors had previously alluded to improvements in stem cell deformability, it was also hypothesized that both micromanipulation and AFM methodologies would better detect and confirm improvements in this mechanical property following exposure to a host of different soluble inflammatory factors.

3.2 Methods

3.2.1 Cell Samples

Mechanical testing was conducted on HPC-7s (murine HSC immortalised line), murine bone marrow-derived MSCs and murine neutrophils. Details on how these cells were isolated, cultured and maintained can be found in **Section 2.2.** For some studies, HPC-7s were pre-treated with SDF-1α (10 ng/mL for 1 hour), Keratinocyte chemoattractant (KC, 10 ng/mL for 1 hour) and H_2O_2 (100 µM for 1 hour), which were prepared in suspension and in spherical phenotype. Control cells were pre-treated with PBS.

3.2.2 Compression of Single Cells with Micromanipulation

In brief, cells were allowed to settle down to the bottom of a transparent chamber, and a bigger flat probe was driven downwards to compress a single cell at a speed of 2 μm/s. Forces applied on the cell were acquired instantaneously, and the force versus time curve was obtained for further data analysis. In each experiment, 20 cells were randomly selected for compression.

3.2.3 Probing of Cells with AFM

HPC-7 cells were immobilized with Cell-Tak adhesive prior to AFM experiments. A force-mapping mode was used to probe the cells at specific positions, as well as the substrate surface. Forces in nano-Newton level were recorded for data processing, thus localized mechanics of cell surface was derived from this sensitive characterization.

3.2.4 Calculation of Mechanical Property Parameters

In the micromanipulation method, cells were compressed until they were ruptured. Therefore, the rupture force, nominal rupture stress, nominal rupture tension and Young’s modulus were calculated to illustrate the mechanical strength and stiffness of cells. The Young’s modulus was determined using the Hertz model to fit the force versus displacement data up to a deformation of 60%. In AFM probing, force data derived from a relatively flat area of the cell surface (usually the topmost region) were selected to fit the Hertz model, and again values of Young’s modulus were calculated, which this time represented the stiffness of cell membrane.

3.2.5 Flow Cytometry and Fluorescent Confocal Assay

Flow cytometry and confocal microscopy were performed to determine the alteration of F-actin after pre-treating HPC-7 cells with SDF-1α and H_2O_2. Briefly, HPC-7s were fixed with 2.5% formaldehyde and permeabilized with 0.1% Triton-100, followed labelling for 1 h with FITC-Phalloidin. After staining, cells were analyzed in a flow cytometer, phalloidin-labelled HPC-7s without apparent cell damage or aggregation were randomly examined qualitatively on a laser-scanning confocal microscope.

3.3 Results - Mechanical Properties of Cells Corresponding to Large Deformations as Determined Using Micromanipulation

3.3.1 Size of Neutrophil, HPC-7 and MSC after Pre-treatment with Inflammatory Factors as Determined by Micromanipulation

The mean diameter (μm) and size range (μm) of randomly selected single HPC-7s and MSCs, as well as HPC-7s after pre-treating with SDF-1α, H_2O_2 and KC, were measured directly from a video camera attached to the micromanipulation rig (**Table 3.1**). The data shows that all types of stem cells were larger in diameter when compared to neutrophils and that MSCs were the largest type of cell. Stem cells, particularly the larger MSCs, also demonstrated the relatively wider size span range, suggesting the smaller neutrophils were more homogenous in their size distribution.

There was no significant difference in the size of HPC-7s pre-treated with SDF-1α, H_2O_2 or KC when compared to those pre-treated with the PBS control group. The diameter of the smallest capillaries in the microvasculature of the heart and skeletal muscles in rodents has previously been demonstrated, using corrosion casts, to be approximately 5 μm (Potter and Groom, 1983). This suggests large deformations are required in order for HSCs, and especially MSCs, to circulate or squeeze through these limited spaces without becoming entrapped.

3.3.2 Neutrophils and HPC-7s Share Similarities in the Force-displacement Curves Generated during Micromanipulation Compression

Single neutrophils, HPC-7s or MSCs were compressed between two parallel surfaces at a speed of 2 μm/s. The force (μN) imposed on the cell was plotted against the distance (μm) the probe moved towards the glass chamber on which the cells were placed (force vs displacement). A typical relationship between the force and displacement each for neutrophils and HPC-7s is shown in **Figure 3.1a** and **Figure 3.1b** respectively. Despite their biological variation, common characteristics can be observed between neutrophils and HPC-7s in their compression curves. At a lower applied load, the force-displacement curve shows a relatively small slope (region A-B of the curve) i.e. force increases slowly with displacement. At point A the probe started to touch the cell and so Point A-B therefore informs the resistance of the cell cytoskeleton to the pressure being applied. At point B it is likely that the cell nucleus was also being compressed. Hence at deformations of $\epsilon \sim 0.6$, the cytoskeleton played a critical role in the mechanical resistance offered (ϵ = cell height change / initial cell diameter). At deformations in the region of $\epsilon \sim 0.6$ - 0.8, the force increased rapidly (region B - C of the curve) indicated by the gradient of the force versus displacement curve becoming bigger. This is followed by a stress peak (point C of the curve) in the force versus deformation curve at which point the cell burst. Thereafter, the force decreases rapidly (to point D of the curve). The forces responding to this region are highly nonlinear. Although the cell nuclei may have been involved in resisting the applied load, the cell membrane burst at the peak and the subsequent leakage of cell fluid caused a force drop. Beyond 80% deformation, the slope of the force curve increases more rapidly (region DE of the curve). This region corresponds to the compression of the cell nuclei, cell debris and the glass bottom/substrate on which cells were placed.

Unlike neutrophils and HPC-7s, there is an absence of a peak force, indicative of cells bursting, in the force curves of MSCs (**Figure 3.1c**). In these cells, the force increased smoothly and slowly at low applied loads inducing deformations of $\epsilon \sim 0$ - 0.8 of the cell membrane and cytoskeleton. The slope increased at deformations larger than 80% because of the addition of cell nuclei in force resistance until the probe touched the bottom substrate where the slope of force curve increased more rapidly. The absence of stress peak demonstrated that there was no obvious rupture point or force for MSCs.

Table 3.1. Pre-treatment with inflammatory factors does not change neutrophil, HSC or MSC size as determined by micromanipulation. The diameter of single cells was measured directly from the images captured using a camera attached to the micromanipulation rig. Neutrophils were the smallest in size compared to both stem cell types and MSCs were bigger than HSCs. Pre-treatment of HPC-7s did not significantly affect their size. Stem cells showed greater variation or heterogeneity in their size distribution than neutrophils. For each cell type, n = 200 cells were measured. Data are presented as the means ± SEM.

Cell type	Mean (µm)	Size range (µm)
Neutrophils	6.6±0.2	5-7
HPC-7s	10±0.2	6-13
HPC-7s(SDF-1α)	10±0.1	6-13
HPC-7s(H_2O_2)	10±0.3	6-13
HPC-7s(KC)	10±0.2	6-13
MSCs	16±0.5	12-20

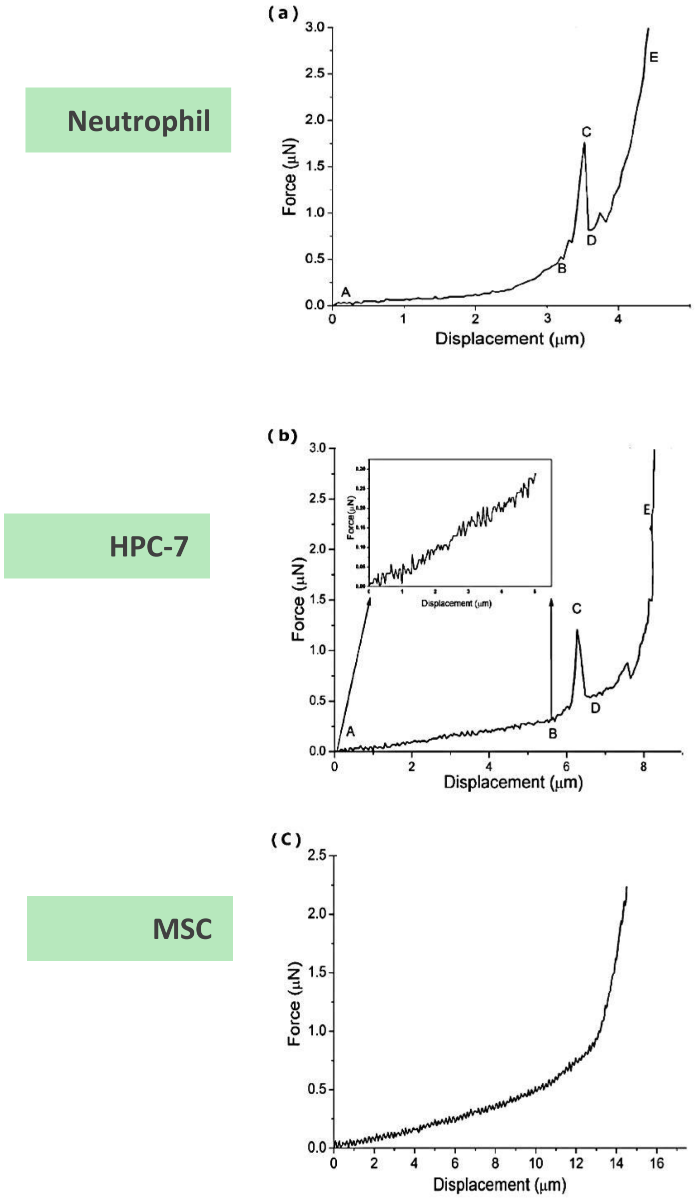

Figure 3.1. Similarities between Neutrophils and HPC-7s in the force-displacement curves generated from micromanipulation compression. Typical force-displacement curves for **(a)** neutrophils **(b)** and HPC-7s show that force increases slowly with displacement as shown in region AB of the curve. At deformations in the region of about 0.6 ~ 0.8, the gradient of force versus displacement becomes bigger as shown in region BC of the curve. This is followed by the cell bursting at point C, with the force decreasing rapidly to point D, after which the force increases rapidly corresponding to the compression of cell debris and glass substrate as shown in region DE. For **(c)** MSCs, the force increases smoothly with displacement and no cells demonstrated a clear rupture point. All cells were compressed at a speed of 2 μm/s. N = 20 single cells for each cell type.

3.3.3 Mechanical Properties of Different Cell Types

3.3.3.1 Nominal Rupture Stress and Tension of HPC-7s is Less Than Neutrophils

Following micromanipulation compression, neutrophils and HPC-7s demonstrated rupture behaviour. The rupture deformation was not significantly different ($p > 0.05$), with mean values of 75.3 ± 1.0% and 79.3 ± 1.5% obtained respectively. Both neutrophils and HPC-7s ruptured when they were deformed to almost 80% of their original size (**Figure 3.2a**). The mean cell rupture force (µN) was determined from the force vs displacement curves (y-axis value at **point C** on **Figure 3.1a** and **3.1b**). The mean values of rupture force for neutrophils and HPC-7s were 2.3 ± 0.2 µN and 2.2 ± 0.3 µN respectively and these values were not significantly different ($p > 0.05$; **Figure 3.2b**).

Since the rupture force is related to the size of the cell, the force at rupture is not an intrinsic material property parameter and cannot be used to compare the material properties between cell populations of different sizes. Therefore, intrinsic material properties such as the elastic modulus and additional stress and strain at rupture are required. However, determination of cell stress and strain at rupture requires finite analysis combined with the force versus displacement data (Mercadé - Prieto *et al*, 2012). Here the nominal rupture stress (σ_R) and the nominal rupture tension (T_R) data were therefore calculated from the data of rupture force and the cell size. Both σ_R and T_R were quantified using **Equation (2.3)** and **(2.4)**. Both σ_R ($p < 0.01$) and T_R ($p < 0.01$) of neutrophils, indicative of the cellular mechanical strength, was significantly greater than HPC-7s (**Figure 3.2c** and **Figure 3.2d** respectively).

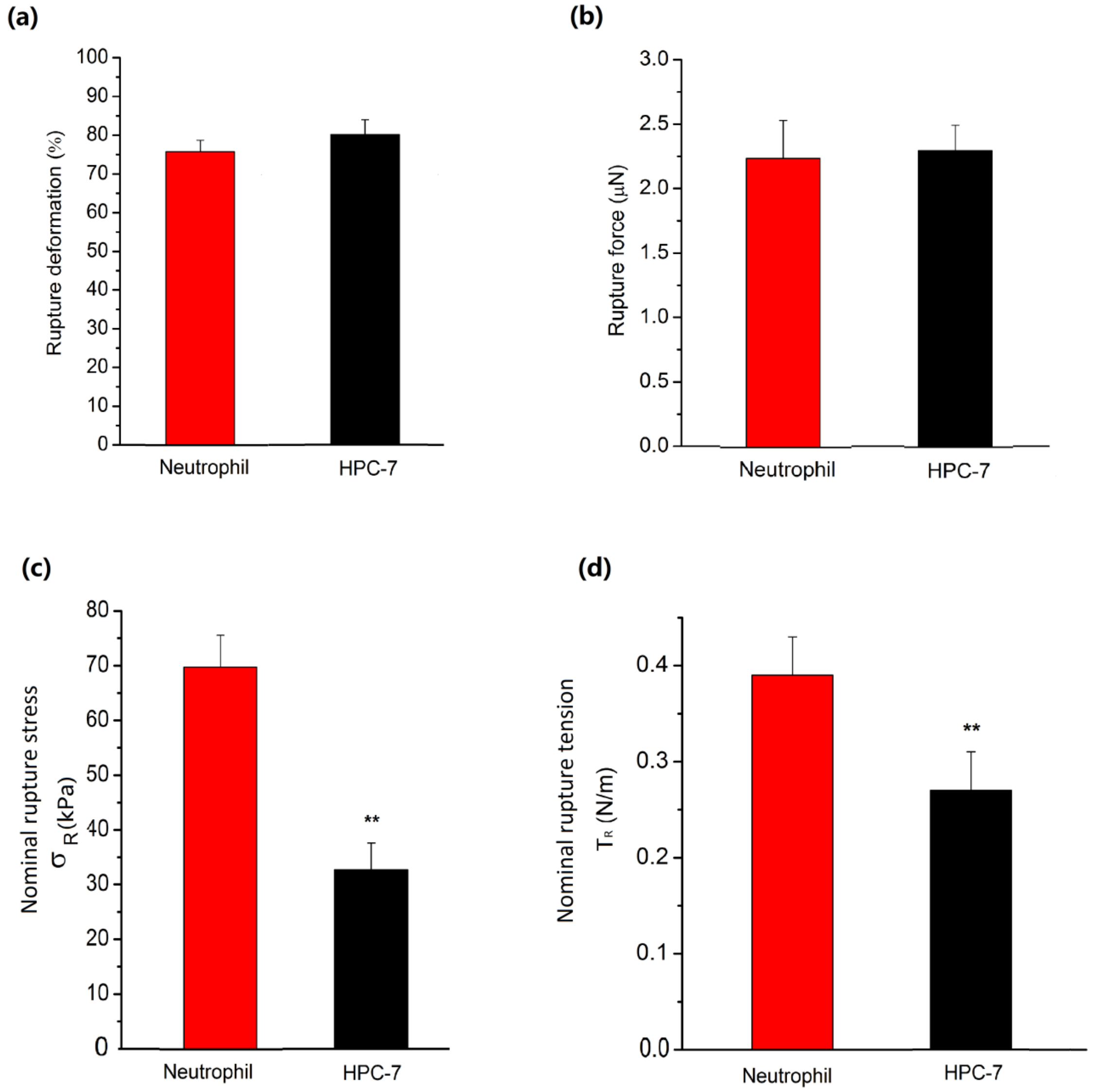

Figure 3.2. Nominal rupture stress and tension of HPC-7's and neutrophils (a) Neutrophils and HPC-7's were ruptured when their rupture deformation was close to 80%. **(b)** The forces required to rupture neutrophils and HPC-7 were not significantly different. **(c)** The nominal rupture stress (σ_R) of neutrophils was significantly greater than that calculated for HPC-7s. **(d)** The nominal rupture tension (T_R) of neutrophils was also significantly greater than HPC-7s. For each cell sample, n =20 cells were tested. **$p < 0.01$ as determined using a paired Student t-test.

3.3.3.2 Young’s Modulus of HPC-7s & MSCs Determined Using the Data up to Large Deformations

The Young’s modulus is a parameter calculated to represent the stiffness of the elastic material or cell being studied. The force data obtained using micromanipulation of cells to large deformations was fitted to **Equation (2.2)** for calculation of the Young’s modulus value. The results demonstrate that the Hertz model was valid up to a nominal deformation of 60%. **Figure 3.3a** illustrates the typical linear fitting based on the Hertz model to the experimental data and the value of correlation coefficient obtained was 0.9. The calculated Young’s modulus value for neutrophils, HPC-7s and MSCs were 24.0 ± 1.8 kPa, 18.1 ± 1.3 kPa and 15.6 ± 1.2 kPa respectively (**Figure 3.3b**). It was possible to calculate the Young’s modulus value for MSCs as only deformation to 60% data was used and no rupture data was required (MSCs did not demonstrate rupture). Since a higher Young’s modulus indicates less deformable cells, the data obtained demonstrated neutrophils were significantly stiffer than both HPC-7s ($p < 0.01$) and MSCs ($p < 0.01$). Interestingly, MSCs obtained similar stiffness to HPC-7s despite the fact that their overall cell size (**Table 3.1**) was much bigger than HPC-7s (**Figure 3.3b**).

3.3.3.3 Compression/holding Curves of Neutrophils, HPC-7s and MSCs at Different Deformations

The Hertz model does not account for viscoelasticity. In principle, the Hertz equation applies to relatively small deformations (< 10%) of a material with linear elasticity (Mercadé-Prieto and Zhang, 2012). While in this study, the model still fits the data of large deformations up to 60%, in order to understand whether the cells were viscoelastic, single cells were compressed to different deformations (∼ 30% and ∼ 60%) at 2 μm/s and then held for a few seconds. After the compression / holding to 30% deformation, the force was released from the cells and the same cell was again compressed to 60% deformation and held for several seconds.

Figure 3.4 shows typical force-time curves of neutrophils, HPC-7s and MSCs from compression/holding experiments. Clearly, the larger the deformation at the end of compression, the bigger the force loaded on the cell. For all the tested cell types, there was no significant force relaxation at deformations of 60% and less. This data demonstrates that up to a deformation of 60%, the elastic behaviour was still dominant and the data of force versus displacement could therefore be used to fit the Hertz equation for calculating the Young's elastic modulus.

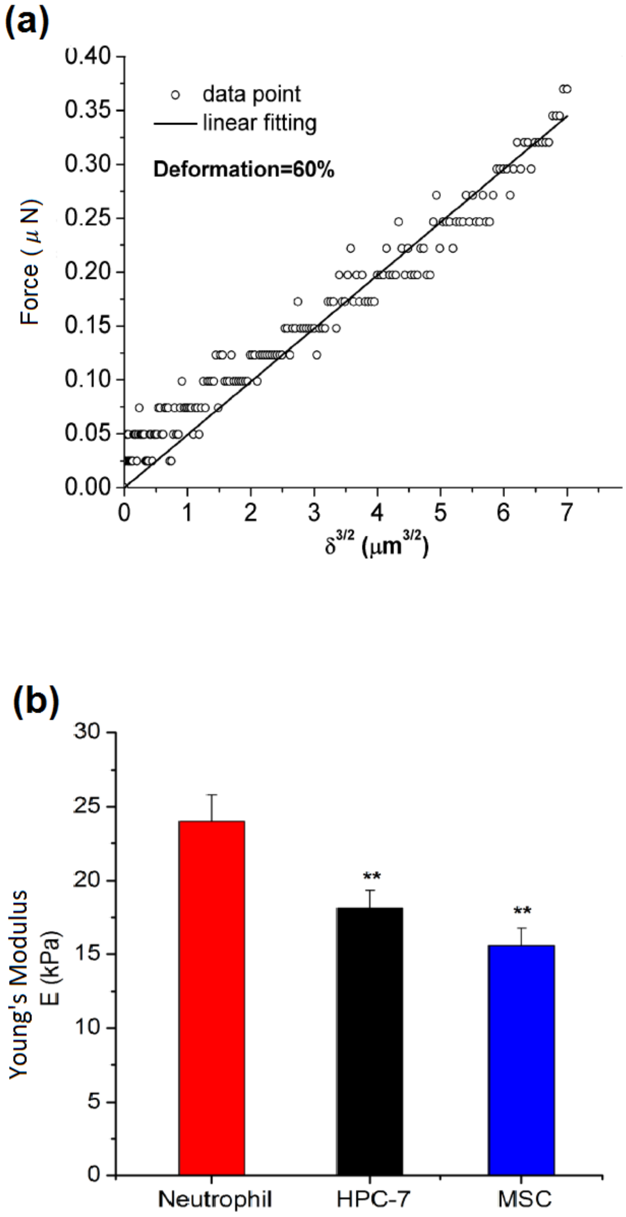

Figure 3.3. Whole cell deformation with micromanipulation for the determination of the Young's modulus of HPC-7s, MSCs and neutrophils up to large deformations. (a) Overall, the force versus displacement curves obtained from the compression of all single cells up to a maximum deformation of 60% can be fitted to the Hertz model well. A typical linear line of the Hertz model was fitted to the force-displacement data (dot) obtained using micromanipulation. **(b)** Values of the Young's modulus for HPC-7s and MSCs were determined and shown to be less than neutrophils. Hence, although HPC-7s, and particularly MSCs, had larger cell sizes, they were less stiff when compared to neutrophils. For each cell sample, n = 20 cells were tested with micromanipulation. Data is presented as Mean ± SEM. **$P < 0.01$ as determined using a paired Student t-test.

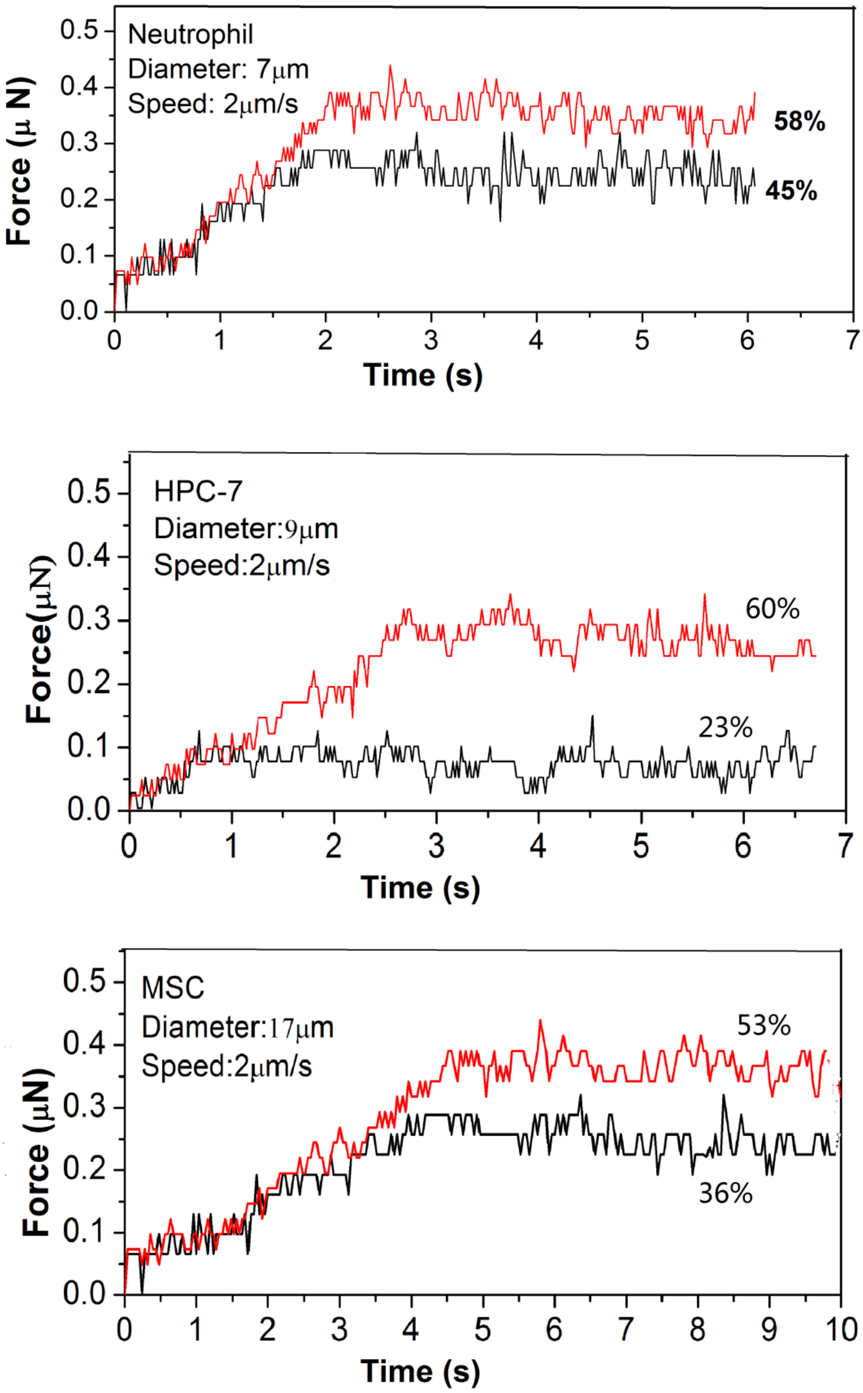

Figure 3.4. Compression/holding curves of neutrophils, HPC-7s and MSCs at different deformations provided supportive evidence that the Hertz modelling can be used to calculate the Young's Modulus for up to 60% deformations. Typical force-time curves of a single neutrophil, HPC-7 cell and an MSC compressed to different deformations at a speed of 2 μm/s and then held for several seconds. For each sample, n=20 cells were tested.

3.3.4 Mechanical Properties of HPC-7 Cells after SDF-1α, H_2O_2 or KC Pre-treatment

3.3.4.1 Rupture Force and Nominal Rupture Stress/tension Decreases with SDF-1α and H_2O_2 pre-treatment

To determine whether pre-treatment of HPC-7s with inflammatory factors affects their mechanical properties, they were pre-treated with PBS (control), SDF-1α, H_2O_2 or KC prior to mechanical testing with the micromanipulation technique. Values for the deformation at rupture and the force required for rupture were derived from their respective force-displacement curves. Pre-treatment did not affect the % deformation at rupture and demonstrated similar deformations for all cells of ~ 80% (**Figure 5.5a**). However, the force required to induce rupture significantly decreased from 2.2 ± 0.3 μN after pre-treatment with the PBS control to 1.3 ± 0.1 μN and 1.6 ± 0.2 μN after pretreating with SDF-1α ($p < 0.01$) and H_2O_2 ($p < 0.01$) respectively. In contrast, the force required to rupture KC pre-treated cells did not change significantly compared to the PBS control group (**Figure 3.5b**). Both SDF-1α ($p < 0.01$) and H_2O_2 ($p < 0.01$) also significantly reduced the nominal rupture stress (σ_R). Again, KC did not affect this value (**Figure 3.5c**). A similar pattern was observed for nominal rupture tension (T_R) (**Figure 3.5d**). This data suggested HPC-7 cells became weaker after pre-treating with SDF-1α or H_2O_2 making it easier to deform and rupture them, while the KC group showed similar mechanical strength to PBS control cells.

3.3.4.2 Young's Modulus of HSCs Determined from Data up to Large Deformations Decreases with SDF-1α and H_2O_2 Pre-treatment

The micromanipulation data up to large deformations was again used for calculation of the Young's modulus of HPC-7s before and after pre-treating with SDF-1α, H_2O_2 and KC. The results demonstrated that the Hertz model was valid up to a nominal deformation of 60%. The values of Young's modulus for PBS, SDF-1α, H_2O_2 and KC pre-treated HPC-7s were 18.1 ±

1.2 kPa, 13.8 ± 0.8 kPa, 14.5 ± 0.8 kPa and 17.8 ± 1.4 kPa respectively (**Figure 3.5d**). Since a lower Young's modulus indicates more deformable cells, the data obtained demonstrated that pre-treatment with SDF-1 α ($p < 0.01$) and H_2O_2 ($p < 0.01$) generated HPC-7 cells which were significantly more deformable than PBS pre-treated cells. KC pre-treatment did not generate any significant effect on the Young's modulus of HPC-7 cells.

3.3.4.3 Compression/holding Curves of Pre-treated HPC-7's at Different Deformations

Typical force-time curves of HPC-7s for PBS control, SDF-1α, H_2O_2 and KC groups were generated from compression / holding experiments (**Figure 3.6**). There was no significant force relaxation at a final nominal deformation of 60% and less for all the three cell samples ($n = 10$ per sample). Likewise, it can be concluded that at a compression speed of 2 μm/s, there was not significant visco effect for HPC-7s up to a deformation of 60%, and the Hertz model is valid to quantify the stiffness of the whole cell.

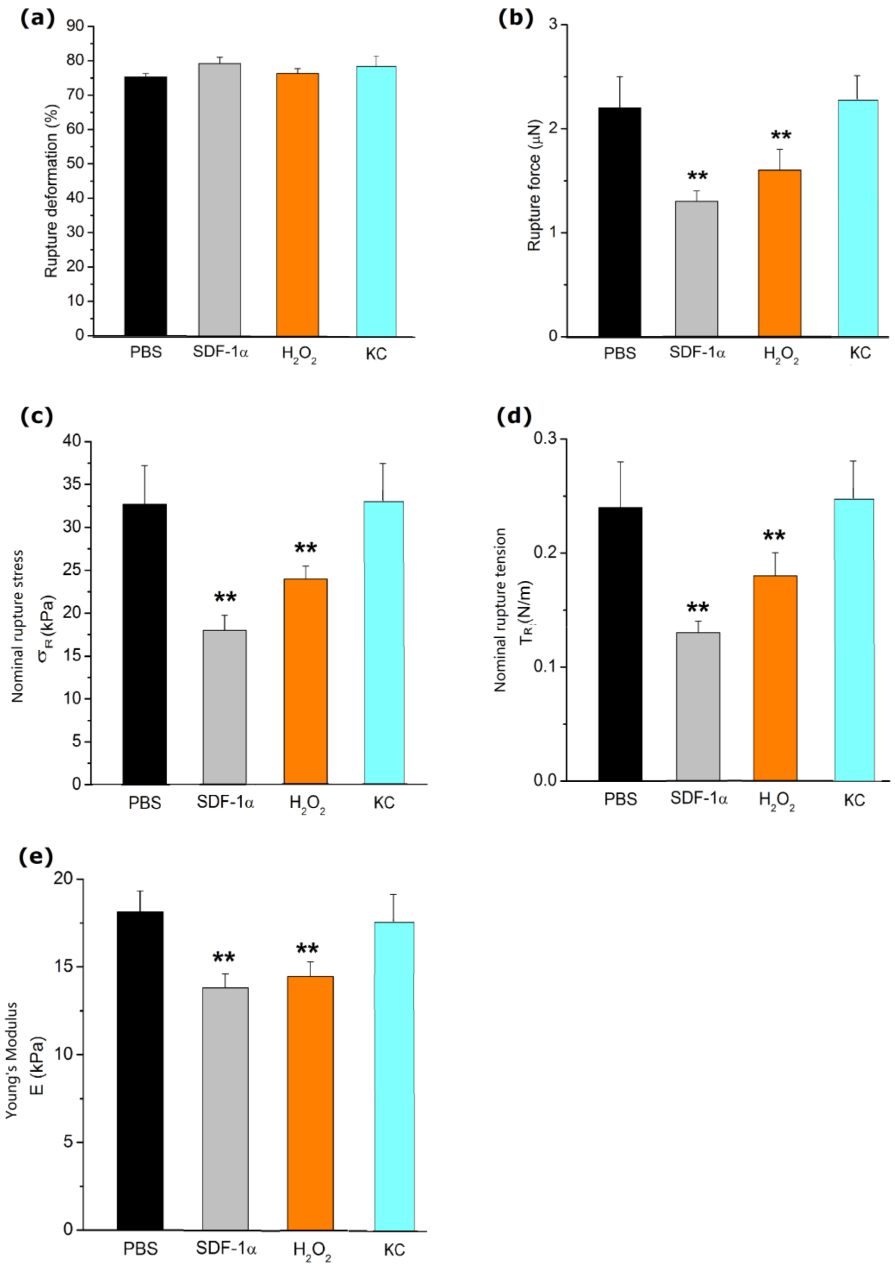

Figure 3.5. Rupture force, nominal rupture stress/tension and Young's modulus values significantly decrease with SDF-1α and H_2O_2 pre-treatment as determined using micromanipulation. (a) The mean rupture deformation for all of the pre-treatments was ~80%. **(b)** Forces required to rupture SDF-1α and H_2O_2 pre-treated HPC-7s were significantly smaller than that required to rupture PBS control cells. KC pre-treatment did not significantly affect the rupture force when compared to PBS control cells. **(c)** Nominal rupture stress (σ_R) of HPC-7s after pre-treating with SDF-1α and H_2O_2 significantly decreased, with no changes observed with KC pre-treatment. A similar pattern of events was observed for **(d)** nominal rupture tension (T_R) and **(e)** values of the Young's modulus. For each cell sample, n=20 cells were tested. Data is presented as mean ± SEM. ** $P < 0.01$ as determined using a paired Student t-test.

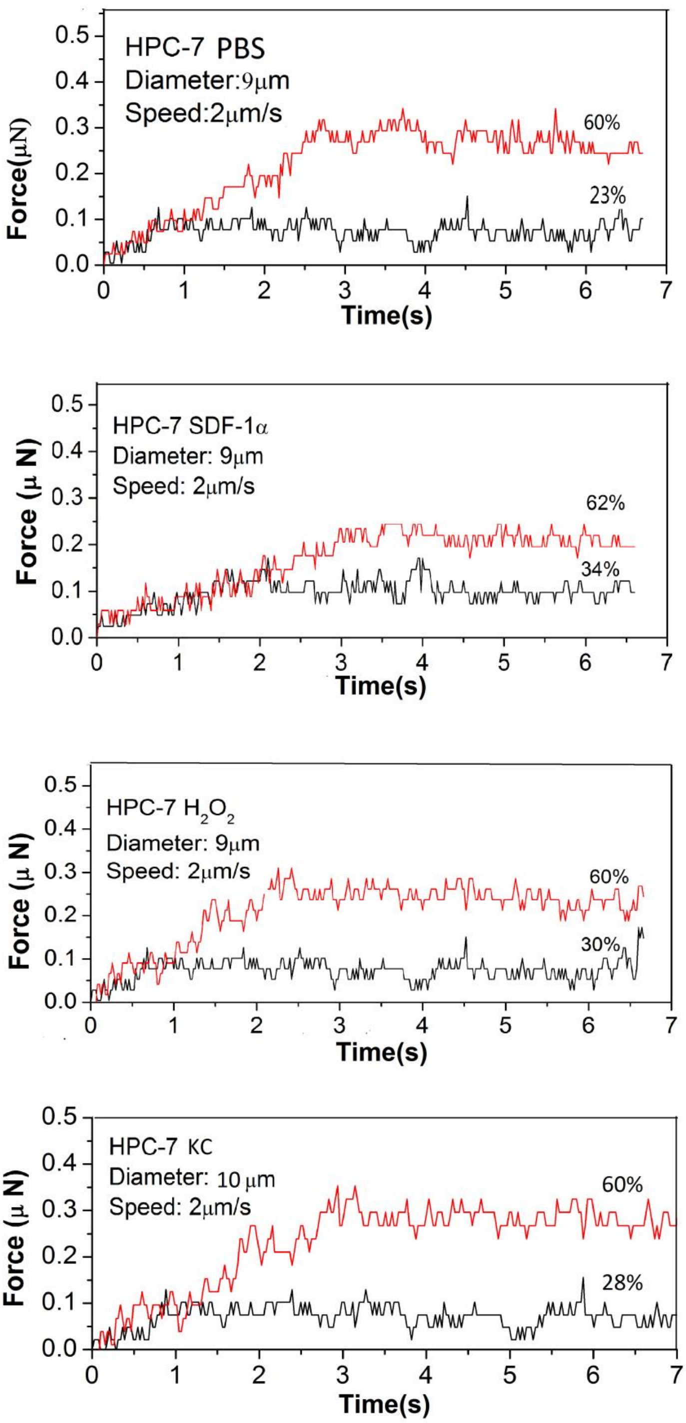

Figure 3.6. Compression/holding curves of pre-treated HPC-7s provides supportive evidence that the Hertz modelling can be used to calculate the Young's modulus for up to 60% deformation. Typical force-time curves of single pre-treated HPC-7s compressed to different deformations at a speed of 2μm/s and then held for several seconds. For each sample in each experiment, n=20 cells were tested.

3.4 Results - Mechanical Properties of HSCs Corresponding to Small Deformations as Determined Using AFM

3.4.1 Force Mapping Mode of AFM Identifies Relatively Flat Regions on the Spherical HPC-7 Cell Surface

Immobilised HPC-7 cells were visualised through an optical microscope which allowed identification of those cells which were to be scanned in detail using AFM (**Figure 3.7a**). AFM allows an insight into the surface, structure and topography of cells to be gained in 3D, as well as an investigation of tip induced deformation of the cells. An area of 64x64 pixels was identified in which the cantilever was to be applied (containing approximately 20 HPC-7 cells). At each point or pixel in this image a measurement of surface height was made using the *force mapping mode* of the software. By 'touching' the cells with a small tip attached to a cantilever, and measuring the vertical displacement needed to do so, the height could be measured as the tip scanned the 64 x 64 pixel region. These measured heights were displayed as colors (dark-is-low, bright-is-high) with a gradient of color (red-orange-yellow). This generated a multicolor image of surface topography (**Figure 3.7b**). Height information mapped to color value was also used to distinguish single cells from the underlying substrate (darkest colour). This height information could also be represented as a histogram showing the height distribution across the cross-section of a single cell (**Figure 3.7c**). These histograms demonstrated that cells had some relatively flat areas, usually at the centre of the cell, which made contact with the AFM cantilever tip. This region meets the condition of contact mode for calculation of Young's modulus with the Hertz model (Note). Hence the collection of force curves at relatively flat areas (center area of the cell) could be obtained (**Section 3.4.2**). At least 20 cells were randomly selected and 4 curves at the highest position of each cell were generated for further data analysis. The data containing all the force curves and corresponding spatial information were recorded in one single scan.

With real height numbers in hand, images in a 3D perspective could also be generated which showed the geometry of whole single cells (**Figure 3.7d**). This clearly demonstrated that the cells of interest were all intact and had a spherical phenotype during the process of force mapping. Importantly, these images showed that the immobilization of cells effectively reduced the effect of cell movement when the tip was moving laterally on their surface (**Figure 3.7d**).

3.4.2 Young's Modulus of HPC-7s at Small Deformations Increases with SDF-1α and H_2O_2 Pre-treatment

To determine the elasticity of each cell in a scan area, force versus displacement curves were obtained. The position of single cells was determined from the force maps (**Section 3.4.1**) and force curves were derived for processing from the flat surface region in the centre of the cell. Force curves, showing the relationship between the piezo (z-height) movement and the cantilever deflection, were generated (**Figure 3.8a)**, and the height was converted to displacement (**Figure 3.8b**). The force-displacement data generated from single curves was converted into 'force vs displacement$^{3/2}$, which showed a linear relationship and could be fitted with the Hertz Model at deformations less than 10% (**Figure 3.8c**), the correlation coefficient obtained was 0.99. Compared with the force data generated from micromanipulation experiments, AFM was a lot more sensitive.

The values of Young's modulus for small deformations were subsequently obtained for HPC-7s pretreated with PBS, SDF-1α and H_2O_2 (**Figure 3.8d**). Since KC did not affect the mechanical properties of HPC-7s, they were not tested in AFM studies. Since a higher Young's modulus indicates less deformable cells, the data obtained demonstrated SDF-1α ($p < 0.01$) and H_2O_2 ($P < 0.01$) pre-treated cells were significantly stiffer than PBS pre-treated controls on their cell surface. Moreover, H_2O_2 pre-treatment induced a more significant change in stiffness compared with the effects of SDF-1α. This is in contrast to the data obtained for HPC-7s at larger deformations up to 60% in which both pre-treatments decreased the Young's modulus.

3.5 Pre-treatment of HPC-7s with SDF-1α and H_2O_2 Induced Polymerization and Reorganisation of F-actin

F-actin content in HPC-7 cells was analysed by flow cytometry using phalloidin staining. Cells incubated with PBS acted as control group. Results demonstrated significantly increased F-actin accumulation in SDF-1α ($p < 0.05$) and H_2O_2 ($p < 0.05$) pre-treatment groups compared to PBS control cells (**Figure 3.9a**). H_2O_2 induced a more significant change in content than SDF-1α, which concurs with the change of local mechanics measured by AFM.

Confocal microscopy revealed that cells pre-treated with SDF-1α or H_2O_2 appeared to lose the characteristic rounded shape that was observed for the PBS control treated cells. Within control cells, the F-actin network was diffuse and distributed evenly within the whole cell. However, with both SDF-1α and H_2O_2 pre-treatment, this staining pattern was disrupted and replaced with more punctate staining which was primarily localized to the plasma membrane (**Figure 3.10**). Hence, although the overall F-actin content was increased, the content of F-actin appeared reduced in the cell interior and increased in the outer cortical region close to the membrane. Furthermore, the cell membrane appeared more ruffled in appearance compared to the control cells. Moreover, the level of cellular fluorescence from confocal microscopy images was semi-quantified using ImageJ, the histogram results of the corrected total cell fluorescence (CTCF) below the images suggested that pre-treated samples had higher F-actin content, and H_2O_2 induced more significant changes on the content change, which is in consistent with the flow cytometry results (shown in **Figure 3.9**) .

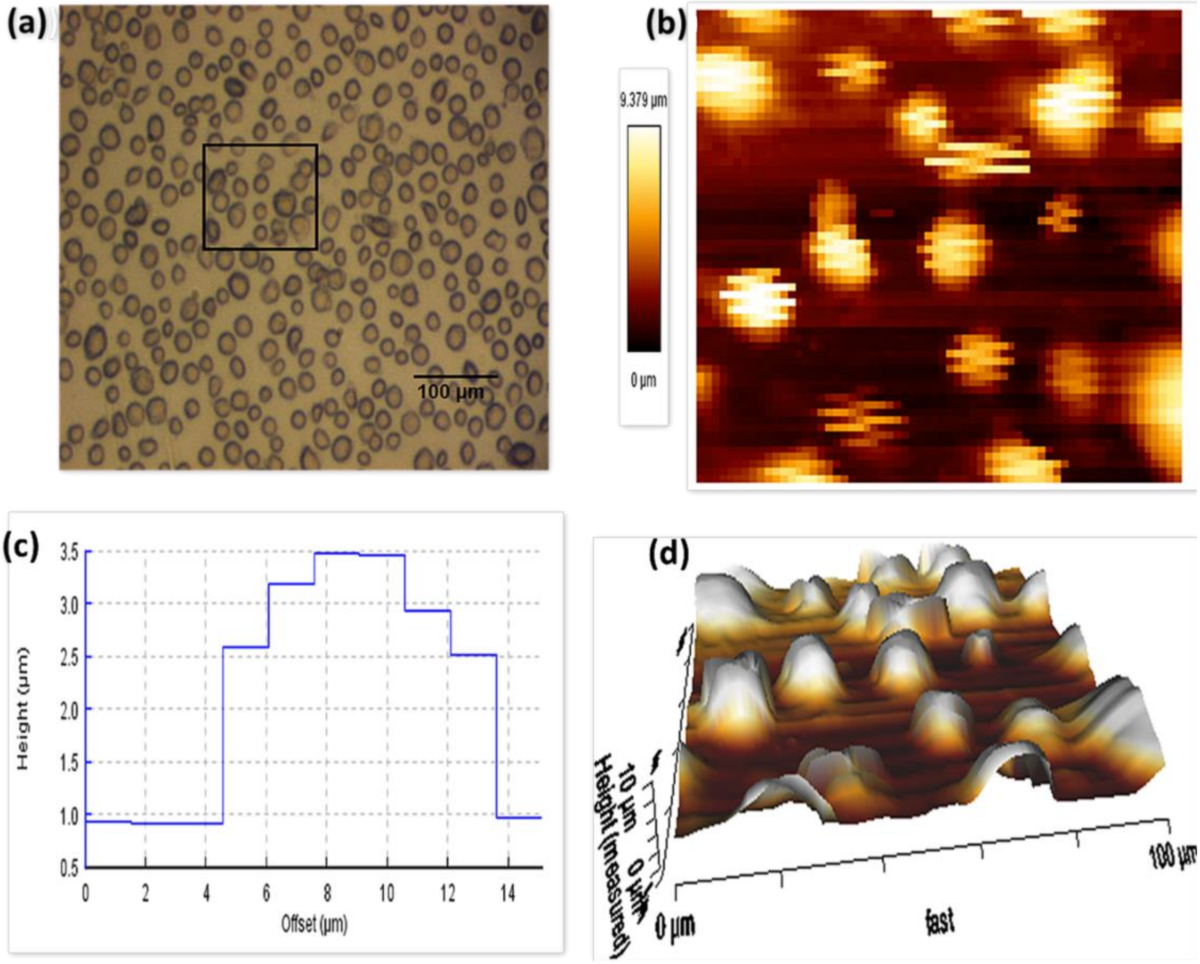

Figure 3.7. Optical image and topography information of HPC-7s using the force mapping mode of AFM identifies relatively flat regions on the HPC-7 cell surface. (a) An image of the cell sample was observed through an optical microscope. The square box indicates an area of 100x100 µm that was further analysed using AFM. Force scanning was conducted in this 100x100 µm area, a region equivalent to 64x64 pixels. **(b)** A typical 100x100 µm area is shown in which the height data was mapped to a colour value from which force curves were derived from the central area of the cell. **(c)** Cross section of a single cell's height is shown based on plotting data with steps representing that the top points of the cell are relatively flat. **(d)** 3D height projection showing the rough geometry of the cells in a 100 x 100 µm area.

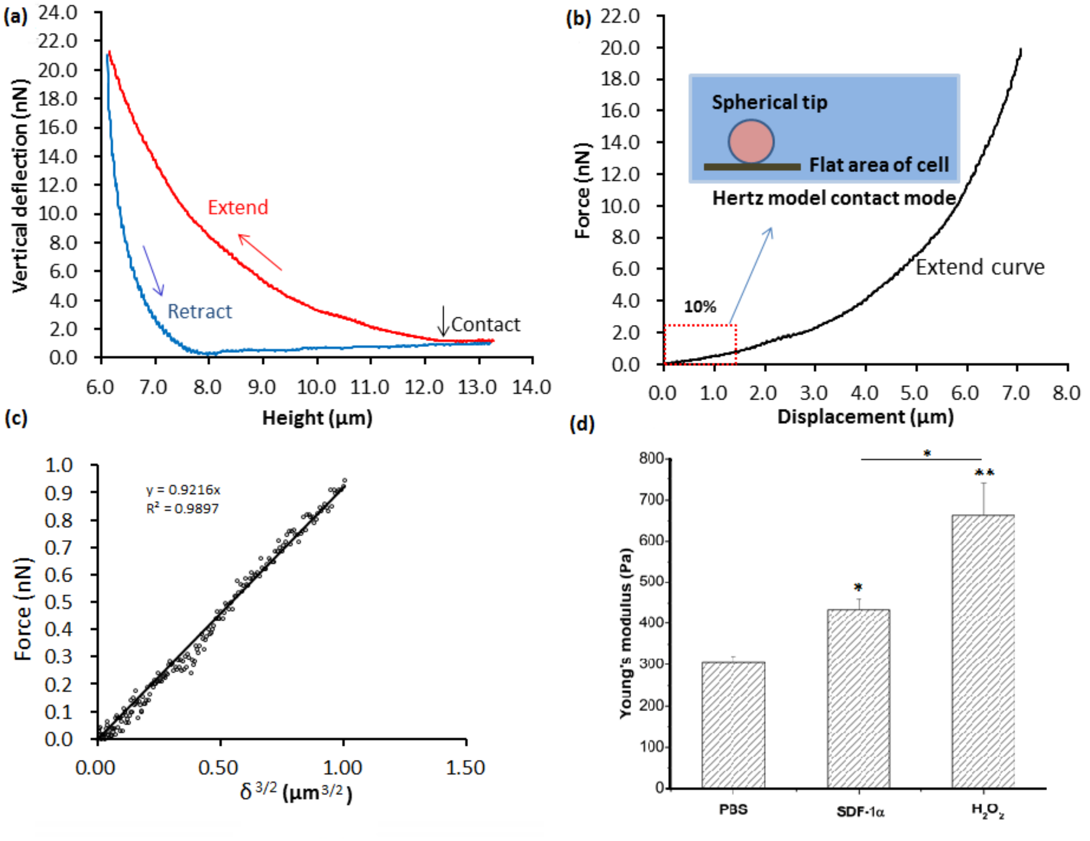

Figure 3.8. Localised cell surface indentation with AFM for the determination of the Young's modulus of HPC-7s at small deformation. The Young's modulus of HSCs at small deformations increases with SDF-1α and H_2O_2 pre-treatment. (a) The force curves obtained by measurements of cantilever deflection versus height during extension and retraction of the probe. **(b)** The force-height curves were converted to force-displacement curves. The schematic illustrates compression of a spherical tip on the top area of the cell which was thought to be relatively flat. **(c)** The force-displacement curve, obtained at a deformation of less than 10% can be fitted to the Hertz model to calculate the Young's modulus. **(d)** The values of Young's modulus of the cell surface increased after pre-treating with SDF-1α or H_2O_2. N = 3 sets for each sample with 20 randomly selected single cells. * $p < 0.05$ and ** $p < 0.01$ as determined using a paired Student t-test.

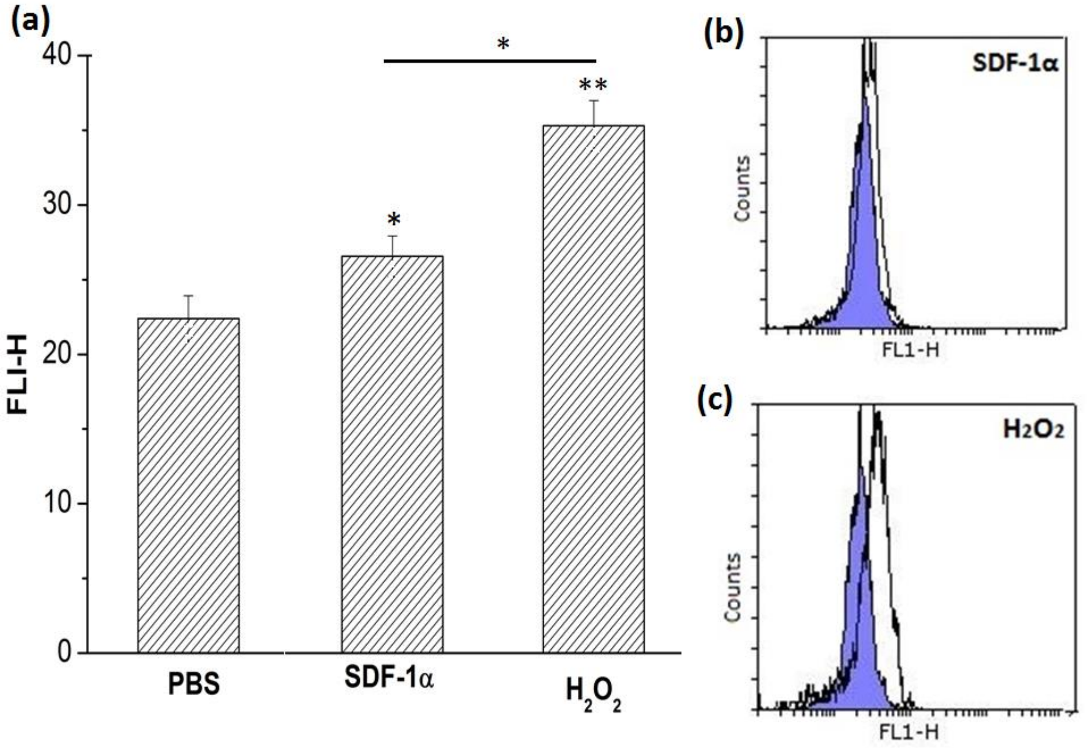

Figure 3.9. Pre-treatment of HPC-7s with SDF-1α and H_2O_2 induced polymerization of F-actin as determined by flow cytometry. (a) represents the mean fluorescence intensity (FLI) for each group. Cells pre-treated with SDF-1α or H_2O_2 increased F-actin accumulation compared to PBS control group ($p < 0.05$). H_2O_2 induced a more significant change in content than SDF-1α. Typical histograms obtained for **(b)** SDF-1α and **(c)** H_2O_2 group. The blue shaded area represents the control and the black line the F-actin test antibody. A shift to the right hand side indicates increased F-actin detection. Results are presented as mean ± SEM of 3 experiments.

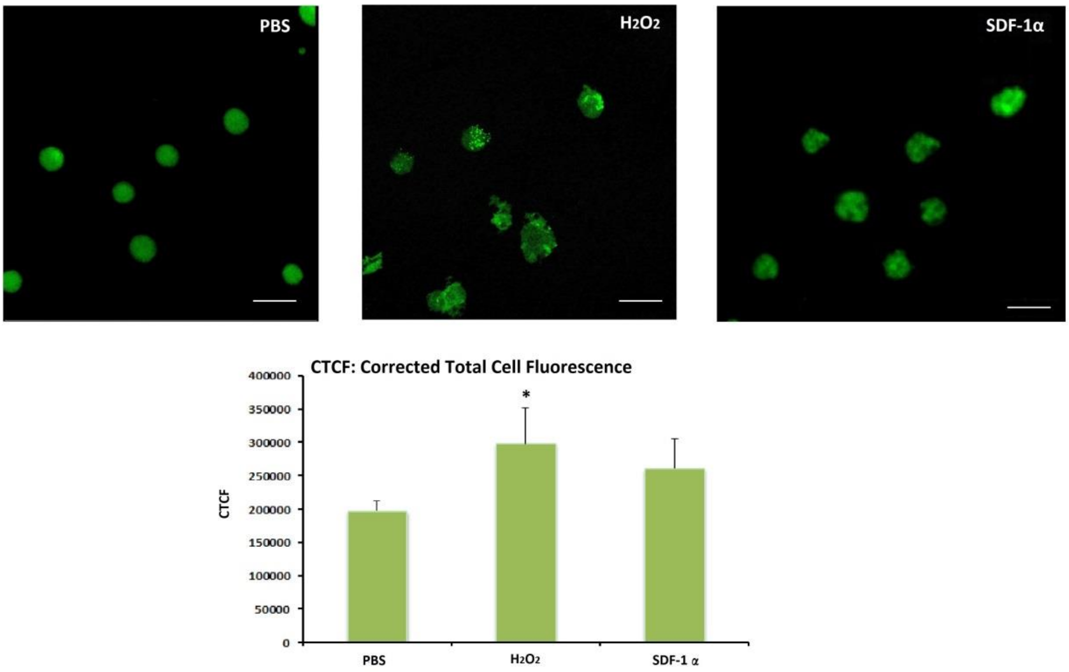

Figure 3.10. The characteristic distribution of actin filaments in response to PBS, SDF-1α and H_2O_2. PBS control cells showed more spherical morphologies and smooth surfaces with more diffuse and uniform F-actin staining within the cell cytoplasm. However, within pre-treated HPC-7s, the uniform F-actin staining was replaced with more punctate staining which was localized to the plasma sub-membrane region. Hence, although the overall F-actin content was increased, it appeared that the content of F-actin was reduced in the cell interior and increased in the outer cortical region close to the membrane. Furthermore, the cell membrane appeared more irregular and ruffled in appearance compared to the control cells. Some cells showed lamellipodia formation which contained F-actin within them. Scale Bar = 20 μm.

3.6 Mechanical Properties of Microcapsules Measured by AFM and Micromanipulation Confirms the Reliability of These Techniques for Cells

To confirm the reliability of micromanipulation and AFM in mechanical characterization of a heterogeneous population of cells, a relatively more homogeneous material was tested using these two methods at small deformations (< 10%). This was crucial to validate as both compression techniques had different features. Therefore, microcapsules with a core of perfume and polymer shell (made of polyacrylamide) (P&G, UK) were also mechanically tested using both techniques. Microcapsules were of a similar size to the cells tested but were more homogeneous in size and chemical composition. The operational procedures used were similar to those used to compress cells, except that the AFM cantilever had a much bigger spring constant of 60 N/m compared with the 0.2 N/m for cells. Also, the sensitivity of the force transducer for micromanipulation experiments was changed from 0.05 to 0.5 mN/volt. Typical force versus displacement curves were obtained using both AFM and micromanipulation (**Figure 3.11**). Fitting of the Hertz model to the micromanipulation and AFM data generated values for Young’s modulus that were 11.3 ± 2.1 MPa and 15. 9 ± 3.9 MPa, respectively. These values are not significantly different from each other, which therefore validated both techniques. Thus, the mechanical property data of the cells obtained using micromanipulation and AFM can be considered to be reliable, and the mechanical property variations of the same cell sample identified using the two methods were due to the substantial spatial heterogeneity in the stiffness of cells.

AFM

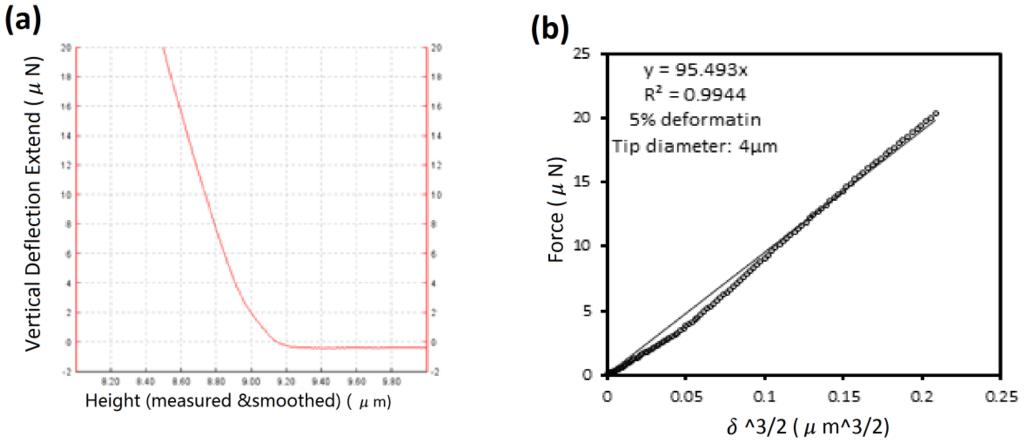

Micromanipulation

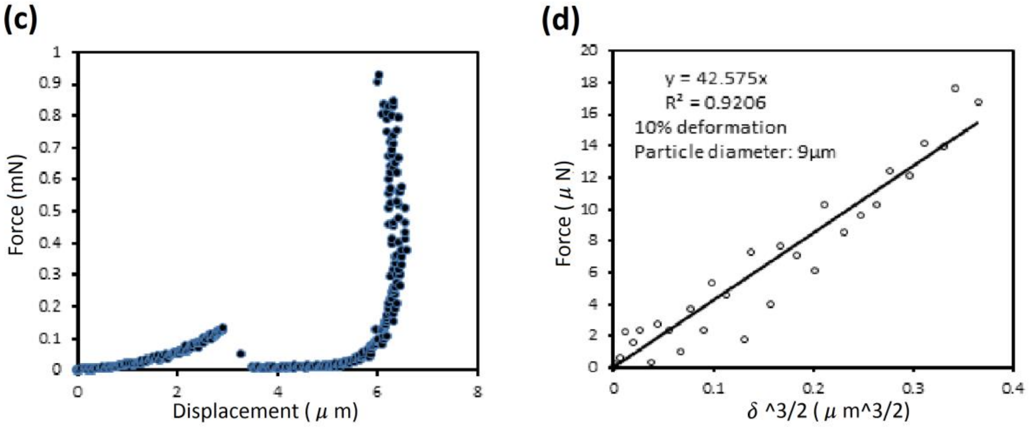

Figure 3.11. Mechanical properties of perfume microcapsules measured by AFM and micromanipulation. To confirm the reliability of micromanipulation and AFM in mechanical characterization of of a heterogeneous population of cells, a relatively more homogeneous material was tested using these two methods at small deformations (< 10%). **(a)** A typical vertical deflection versus height curve derived from AFM data. **(b)** AFM force and displacement data fitted with the Hertz model. **(c)** A typical force-displacement curve obtained from micromanipulation. **(d)** Micromanipulation force and displacement data fitted with the Hertz model. For each test 10 capsules were randomly selected.

Table 3.2. Summary table showing the changes in the mechanical properties of HSCs after pre-treating with PBS (control), SDF-1α , H_2O_2 and KC as characterised by AFM and micromanipulation. The Young's modulus, nominal rupture stress and nominal rupture tension significantly decreased with SDF-1α and H_2O_2 pre-treatment when determined from the data corresponding to deformations up to 60% using micromanipulation. KC pre-treatment did not induce any changes in these values. However, the Young's modulus significantly increased with SDF-1α and H_2O_2 pre-treatment when cells were tested under smaller deformations using AFM. ↑ and ↓ indicate whether these values increased or decreased compared to PBS pre-treated control cells.

	Cells **Mechanics**	**PBS-HSCs**	**SDF-1α-HSCs**	**H_2O_2 -HSCs**	**KC-HSCs**
AFM	Young's Modulus 10% (Pa)	306.2 ± 15.2	434.9 ± 24.5 ↑	662.8 ± 76.6 ↑	-
Micromanipulation	Young's Modulus 60% (kPa)	18.1 ± 1.2	13.8 ± 0.8 ↓	14.5 ± 0.8 ↓	17.8 ± 1.4
	Nominal rupture stress (kPa)	32.70 ± 4.48	17.96 ± 1.77 ↓	23.90 ± 1.51 ↓	33.3 ± 3.6
	Nominal rupture tension (N/m)	0.23 ± 0.04	0.13 ± 0.02 ↓	0.17 ± 0.02 ↓	0.24 ± 0.03

3.7 Discussion

Reducing the entrapment of injected stem cells within the microvessels of non-specific sites, and thus increasing and maintaining their circulation in peripheral blood, is a potential mechanism for enhancing their homing to sites of injury. This can be achieved either by improving stem cell deformability using pre-treatment strategies or by separating stem cells based on their deformability and only injecting the more deformable sub-set. However, no studies have investigated in detail whether chemical pre-treatment strategies can modify stem cell deformability or even characterised the deformability of *per se*. This chapter therefore aimed to characterise and compare the mechanical properties of naïve and pre-treated bone marrow-derived murine HSCs (HPC-7s) and MSCs with micromanipulation and AFM techniques. A summary of major HSC findings can be found in **Table 3.2**. Briefly, initial experiments firstly showed that HSCs and MSCs were larger in size compared to blood neutrophils. Also, both cell types were a more heterogenous population with regards their size as demonstrated by the diameter range. Micromanipulation experiments showed both neutrophils and HSCs could be compressed to rupture, unlike MSCs which did not demonstrate obvious rupture force. Furthermore, it was demonstrated that neutrophils were stronger/stiffer cells with HSCs being mechanically ‘weaker’ cells. The Young’s modulus (elastic modulus) was also determined which represents the stiffness of the cells being studied. Greater Young’s modulus values for neutrophils determined from data up to large deformations again indicated they were significantly stiffer mechanically than the more deformable HSCs. Interestingly, HSCs and MSCs were shown to possess similar deformability despite their size difference. More importantly, micromanipulation studies also demonstrated that SDF-1α and H_2O_2, but not KC, significantly increased HSC deformability. This was evidenced by less force required to rupture pre-treated cells, decreased nominal rupture stress/tension and significantly reduced Young’s modulus values at large deformations. Interestingly, the Young’s modulus values significantly increased with SDF-1α and H_2O_2 pre-treatment when cells were tested under smaller deformations (10%)

using AFM.

3.7.1 Mechanical Properties as Determined by Micromanipulation Studies

HSC/MSC-based therapies are limited by inefficient homing of systemically injected cells to the tissue/organ that is actually injured (Kavanagh *et al.,* 2014). This is primarily due to non-specific entrapment within capillaries, with the lungs being a particularly common site in which stem cells become physically lodged. Entrapment of MSCs is evidenced by their striking elongated and distorted appearance, when observed *in vivo* using intravital microscopy, within numerous microvessels upstream of the injured tissue (**Figure 3.12**). This is sometimes associated with partial or complete obstruction of the blood flow within the microvessel (Kavanagh *et al.,* 2015). In contrast, cells that successfully home to injured tissue appear more rounded in morphology, suggesting that possibly smaller stem cells are delivered to actual sites of injury. The wide diameter range of both HSCs and MSCs does suggest size may indeed be a likely important factor in maintaining stem cells within the peripheral blood and allowing their active recruitment.

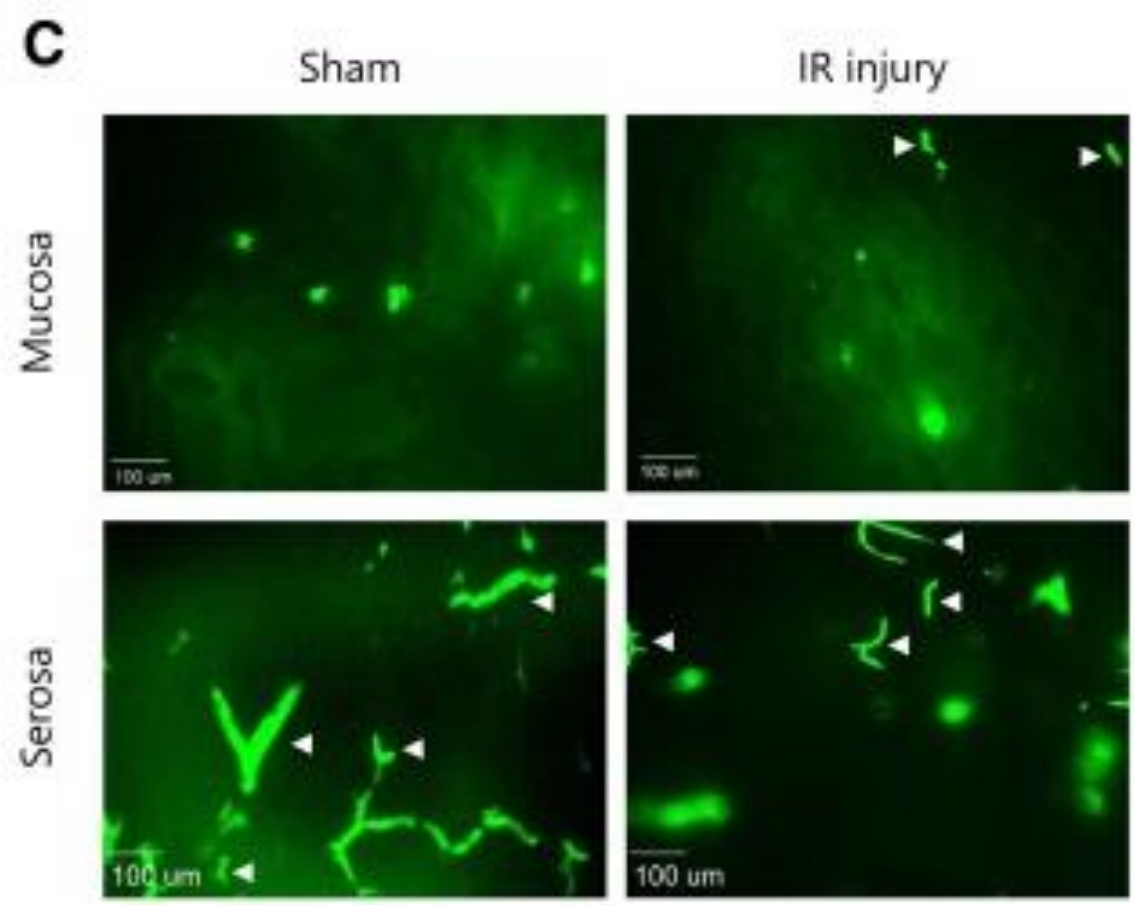

Figure 3.12. Only MSCs that are either small and/or deformable are able to home to sites of tissue injury. Representative fluorescent intravital microscopy images are shown of CFSE-labelled MSCs adherent within the microcirculation of the healthy (sham) and ischemia-reperfusion (IR) injured mucosa of the mouse small intestine *in vivo*. These MSCs are more rounded in appearance. It is possible that these MSCs are either smaller and/or a more deformable sub-set. Entrapment of MSCs that are either too large and/or poorly deformable can be seen in other regions of the body (e. g. the intestinal serosa as shown). Here the MSCs appeared elongated and contorted (white arrows).**Image taken from Kavanagh *et al.,* 2015.**

However, size does not necessarily limit the ability of circulating cells to traverse small diameter capillaries. For example, red blood cells have an approximate diameter of 8 μm diameter but can easily circulate through capillaries that are as small as 2–2.5 μm in diameter (Kwan *et al.,* 2013). This suggests large cells, if they possess appropriate deformability capabilities, could avoid entrapment within capillaries of non-specific sites, and thus increase the opportunity for their active recruitment from flow. As such, it is possible that the MSCs that actually home to, and become adherent within, injured tissues may have been those that possessed sufficient deformability to avoid entrapment in smaller microvessels elsewhere.

To determine and compare HSC and MSC deformability, two methods were employed, namely micromanipulation and AFM. The former can be used to determine the mechanical properties of single cells of various sizes over a wide range of deformations including high deformations that lead to cell rupture. In contrast, AFM is powerful in measuring local elastic properties corresponding to small deformations, primarily impacting only the cell surface rather than the whole cell. Although AFM can detect the mechanics of the cell surface with perfect accuracy, micromanipulation is much more straightforward to use and cells do not need to be immobilized using adhesive proteins which simplifies the sample preparation procedure. Therefore, micromanipulation was the main choice of experimental tool for most of the studies described within this chapter. HSC/MSC mechanical properties were compared to neutrophils. It is firstly demonstrated that only neutrophils and HSCs could undergo rupture. In terms of cell size, MSCs > HSCs > neutrophils. The large size of MSCs is well established (Ge *et al.,* 2014). In the current study, the murine BM-derived MSCs used had a diameter span of 12-20 μm. However, MSCs can be much larger, especially when grown in 2D culture rather than as 3D suspensions, where MSCs extending > 50 μm have been identified (Ge *et al.,* 2014). However, despite their large size, the rupture parameters that were derived from the force versus displacement curves showed neutrophils were stronger than both HSCs and MSCs. The force required to rupture neutrophils and HSCs was similar (2.2 - 2.3 μN) with both cell types rupturing at just under 80% cellular deformation. At first glance, this suggested both neutrophils and HSCs were equally 'strong' or 'stiff'. However, this data did not take into account that the size of these cells was different. Therefore to make meaningful comparisons between the mechanical properties of neutrophils and HSCs, nominal rupture stress and nominal rupture tension was calculated, which took into account the different cross-sectional area and diameter of the cells respectively. Once corrected for size, it became apparent that neutrophils were stronger/stiffer cells with HSCs being 'weaker' cells. The Young's modulus determined from data corresponding to large deformations up to 60%, was also confirmed that neutrophils were indeed significantly stiffer than HSCs. A Young's modulus value, at 60% deformation, was also determined for MSCs which, interestingly, demonstrated that they were only slightly more deformable than HSCs despite the fact that their overall cell size was much bigger.

This novel data primarily demonstrated that the naïve/un-treated, smaller blood neutrophils were stiffer than naïve stem cells. This is interesting when considering that fact that recruitment of the more deformable stem cells is not as rapid or as efficient as 'stiffer' neutrophil recruitment during inflammatory processes (Summers *et al.,* 2010, Kolaczkowska and Kubes, 2013). Indeed, the Kalia group have frequently observed large numbers of neutrophils infiltrating injured tissues within minutes of an inflammatory insult, numbers that far exceed those of recruited HSCs or MSCs. Of the two stem cell types, the recruitment of HSCs is much higher than MSCs within a similarly injured tissue (Kavanagh *et al.*, 2015). Collectively, this suggests that size is likely to play an important and dominant factor in the recruitment of different free flowing circulating cell types *in vivo*. Smaller cells clearly circulate and adhere better than larger cells even though they are a lot stiffer, and therefore deformability may be considered as being of secondary importance.

3.7.2 Why MSCs Did not Demonstrate Rupture

One of the interesting observations made within this chapter was the fact that MSCs did not demonstrate rupture. During compression with the micromanipulation probe, neutrophils and HSCs demonstrated obvious rupture behavior, whilst MSCs showed an absence of clear rupture force. These two different mechanical responses are in likely agreement with the two main mechanical behaviour models that have previously been described for cells (Stamenović & Ingber, 2002; Lim *et al.,* 2006; Fei *et al.,* 2014; Bansod and Bursa, 2015). These models suggest specific structures in a cell dominate its deformability and play a major role in transmitting and distributing mechanical stresses within the cell after exposure to an external force. Cells can behave either more similarly to a *'cortical shell - liquid core'* structure (membrane-like; also called the liquid drop model) or as a *'homogeneous solid state'* structure (cytoskeleton-like) when being compressed by the applied forces. Their response to this stress is suited to the biological processes they need to undergo. The *'cortical shell - liquid core'* model assumes that the main cellular structures resisting any external forces are confined within the thin (∼100 nm) actin-rich deformable cortex beneath the plasma membrane of the cell (Ge *et al.,* 2014, Saito *et al.,* 2002, Liu *et al.,* 2014). In these models, it is assumed that the liquid cell interior or cytoplasm plays little role in resisting mechanical forces. In contrast, some believe the cortical layer does not play a significant role in resisting force and that cells follow a more *'homogenous solid state'* model which assumes the whole cell is a homogeneous, viscoelastic solid material and that the internal cytoplasmic cytoskeleton is the dominant structure resisting mechanical load. In this model, the contribution of the cortical layer is considered negligible. The *'cortical shell - liquid core'* model is widely applied to model suspended cells that are found as spheres in suspension in the body i.e. blood cells. The *'homogenous solid state'* model is generally applied to more adherent cells (Stamenović and Ingber, 2002, Lim *et al.,* 2006, Bansod and Bursa, 2015). Previous studies conducted by Zhang's group also demonstrated that adhered cells, e.g. chondrocytes, ruptured when compressed by micromanipulation (Nguyen *et al.,* 2009). Therefore, the different mechanical models may not necessarily be responsible for the rupture behaviours of cells, and it is still debated whether cells behave more similarly to a ‘*cortical shell - liquid core’* structure or to a ‘*homogeneous solid state’* structure. However, we demonstrated two different force responses in this chapter, which indicated that it is possible that the tested cells follow one or the other of the two models described above regarding their *in vivo* functions. Although HSCs are adherent cells within the BM, they can exit the BM following trauma and travel via the circulation, similarly to blood neutrophils, to sites of injury. Hence both these cell types probably follow the ‘*cortical shell - liquid core’* model applied to spherical cells found in suspension. The clear rupture force of neutrophils and HSCs, most likely resulted from the breakage of their cortical shell. The subsequent compression of the liquid interior after shell rupture induced the rapid measured decrease in the force in the force-displacement curves. In contrast to suspended cells, MSCs are primarily classed as adherent that do not generally exit their niche (e.g. BM) and circulate in peripheral blood under physiological conditions. Hence for MSCs the *‘homogenous solid state’* model may be more relevant as this is applied to adherent cells (Stamenović and Ingber, 2002). The homogenous, viscous nature of the whole cell most likely explained their ability to withstand force and therefore not undergo rupture. Indeed, in culture MSCs can readily assume a flattened appearance.

These mechanical properties therefore mirror the *in vivo* functional distinctions of these cell types. For neutrophils, which naturally exisit in the circulation as spherical entities, and HSCs which can be made to do so, the *‘cortical shell - liquid core’* model is an advantageous strategy as their free circulation may be attributed to the self-rotation of individual cells in response to shear stress, similar to liquid drops under a driving flow (Abkarian and Viallat, 2005, Hur *et al.,* 2011, Chau *et al.*, 2013). MSCs, not naturally designed to circulate in the peripheral blood, generally adhere to each other or to their substrate throughout their lifetime, and so the ‘*homogenous solid state*’ cellular structure plays an important role in transmitting and distributing mechanical stress within the cell (Stamenović and Ingber, 2002).

3.7.3 Mechanical Properties as Determined by AFM Studies

Micromanipulation (micro-Newton forces) data were used to generate parameters of stiffness and mechanical strength at large deformations on the whole cell scale. However, AFM, which provides forces at a nano-Newton level, was used to probe cell mechanics at small deformations. For the same HSC cell type, the Young's modulus calculated from micromanipulation data at deformations up to 60% was about 40 times bigger than that calculated at smaller deformations up to 10% using AFM. Similar force-dependence of the Young's elastic modulus has been seen previously - the mechanical stiffness can vary by several decades from surfaces and crosslinked cytoskeletal networks, which can be explained in part by the actin concentration in the network at large deformation (Xu *et al.*, 2000, Gardel *et al.*, 2004, Storm *et al.*, 2005). Previous studies using AFM being mounted with a spherical tip to measure different types of mammalian cell modulus gave values of 0.3 ~ 6.5 kPa at small deformations (~15%) (Darling *et al.,* 2008, Vargas-Pinto *et al.,* 2013), elastic values of HSCs obtained in this study also fall into this range. The modulus of single chondrocytes and chondrons tested with micromanipulation at large deformations (30-60%) have been presented as 15 to 29 kPa, which are similar to the values (14 – 18 kPa) in the present study (Nguyen *et al.,* 2010).

3.7.4 Mechanical Properties of Pre-treated Cells

Mechanical properties of pre-treated HSCs were comprehensively characterised at different deformations. Micromanipulation and AFM studies were conducted on HSCs pre-treated with well known inflammatory factors, namely SDF-1α, H_2O_2 and KC. These non-genetically modified approaches to increase SC retention provide the potential of them being used clinically as an adjuvant therapy to enhance the stem cell efficiency. The Kalia lab have previously shown that such pre-treatment strategies improve the recruitment of HSCs within sites of injury, which was postulated to be due, partly, to their ability to improve cell deformability and thus prevent non-specific microvascular mechanical entrapment.

The Young's modulus calculated from micromanipulation data at deformations up to 60% decreased when HSCs were pre-treated with SDF-1α and H_2O_2. Similarly, the nominal rupture stress/tension of these pre-treated HSCs also decreased. This collectively suggested the cells as a whole became weaker and more deformable after pre-treatment with SDF-1α and H_2O_2. This 'softening' after pre-treatment is in accordance with a previously published work using a more basic micropipette aspiration method. White and colleagues showed that when 10 μm HPC-7 cells were sucked into 5 μm (inner diameter) micropipettes, and were thus squeezed to large deformations, the time it took to fully aspirate them was reduced following SDF-1α pre-treatment (White *et al.*, 2013). This may be due to the re-organization/disruption of actin filaments from highly-ordered 3-D structure to a more diffuse pattern. Although this improved deformability may well enhance SC homing to sites of injury, it is important to state at this stage that additional effects included modifying the clustering of HSC surface integrins and increasing their affinity for endothelial counterligands can also explain the improved recruitment of pre-treated cells (Kavanagh *et al.*, 2013a; Kavanagh *et al.*, 2013b).

In contrast to the micromanipulation data, the values of the Young's modulus calculated from the AFM experiments increased with similar pre-treatments which suggested that the HSC surface stiffened after pre-treating with SDF-1α and H_2O_2. This stiffening of the cell surface after pre-treatment can potentially be explained by the expansion and polymerization of F-actin to the plasma membrane. Indeed, the increased immunostaining of F-actin filaments noted (higher component concentration) in the cortical membrane after pre-treatment may allow for the observed increase in the elasticity modulus at small deformations. It is well established that one of the earliest effects (within 1 minute) of inflammatory mediators on neutrophils is to cause them to become stiffer and less deformable. Most often these effects are short-lived and disappear after ~30 minutes (Hajime *et al*., 2002; Wai *et al*., 2005). These changes have been extensively studied *in vitro* by measuring the pressure required to aspirate them into a narrow micropipette. This enhanced stiffness is thought to be due to the polymerisation of G-actin to F-actin that forms a subcortical shell beneath the membrane. Actin is a key component of the neutrophil cytoskeleton and contributes to the cell stiffness. Polymerization from a globular monomeric G-actin form to a filamentous form F-actin form leads to neutrophil stiffening. This increased stiffness enhances the margination of neutrophils in inflamed regions and delays their transit which encourages binding through integrin activation. On the downside, this increased stiffening can lead to neutrophil sequestration within the pulmonary microvessels. Similar F-actin observations were made in the current study in which HSCs also showed sub-membrane localisation of F-actin after pre-treatment with SDF-1α and H_2O_2. This would suggest the pre-treated HSCs were stiffer in their cortical region than PBS treated cells because of the increased F-actin beneath the plasma membrane. This may explain why AFM studies generated Young's modulus values under small deformations that were higher for the pre-treated cells.

Interestingly, it has previously been shown that the mechanical properties of cells are anisotropic in the axial direction with respect to actin concentration – ie. the architecture of the actin network in the cell surface/lamellipodia determines the elasticity of that region (Fleischer *et al.,* 2007). However, the mechanical property parameters derived in this study may not be able to perfectly reflect the inherent architectural structure of the cells' actin networks. Nevertheless, the calculations of Young's modulus derived from the data can still be used to evaluate the stiffness of individual cells. Due to the complex contributions of various cellular components (actin, nucleus, cytoskeleton etc.) in response to different applied load, more complex mathematical modelling methods such as finite element analysis (FEA) would be an ideal approach to completely quantify the data. FEA is a computerized method for predicting how different components within cells would specifically react to physical forces applied to them. However, this is beyond the scope of this study. Briefly, it is assumed that at small deformations (< 10%), the membrane contributes to force resistance which is largely elastic. At large deformations (~ 60%), the membrane stretching and cytoskeleton contribute to the mechanical strength. When the deformation increases further, the nucleus participates in mechanical resistance, and the membrane is burst at a certain deformation. In this chapter, only simpler equations were used to extract some important mechanical property parameters from the measurements collected using micromanipulation and AFM.

3.8 Conclusions

Improving the retention efficiency of circulating stem cells within sites of injury may depend on manipulating the mechanical properties of these cells or isolating smaller and more deformable sub-populations for infusion. Microfluidic systems have been shown to separate cells based on their mechanical properties, such as shape, size and stiffness (Gossett *et al.*, 2010, McFaul *et al.*, 2012). Prior to conducting such separation studies, some information on the mechanical properties of different therapeutic cells was required. This was obtained using micromanipulation and AFM methods for HSCs and MSCs. To summarize, it has been demonstrated that mechanical distinctions exist amongst different therapeutic cells with regards their size, deformability and also their rupture response to applied stress. Although distinct differences were observed between these two SC populations, this study also suggests intra-population variation exists within naïve and pre-treated HSCs. These different mechanical parameters can potentially be utilized as label-free markers in cell sorting systems to separate different sub-populations of stem cells. Mechanical properties of individual HSCs are force/deformation-dependent and highly non-linear from the cell surface to the internal cytoskeleton regarding the structure and concentration of actin filaments. This mechanical heterogeneity of HSCs confirms the possibility of isolating sub-populations from a mixed population of cells using the physical markers found in this chapter, followed by fabrication and optimization of microfluidic sorting systems.

Chapter 4

HSC Sorting with Microfluidic Systems

4.1 Introduction

To improve the recruitment of circulating HSCs, a number of different strategies have been employed including genetically modifying the adhesion molecule expression on the stem cell surface, pre-treating them with inflammatory stimuli or increasing the presence of soluble stem and endothelial activators within the injured mileu (Kumar and Ponnazhagan, 2007, White *et al.,* 2013). To be effective, all of these strategies require the HSCs to actually traffick through the tissue or organ of interest so that stem cell-endothelial interactions can take place. Although adhesive events are indeed increased when stem cells are passing through, none of these strategies necessarily increases the actual trafficking process. Indeed, most injected cells are lost after ‘first pass’ to non-specific sites by entrapment. Therefore, in addition to manipulating the adhesive molecules through genetic, biological or chemical manipulations, additional strategies are required to maintain a pool of circulating cells in the peripheral blood.

A promising approach to achieve this would be to separate sub-populations of cells with smaller size and/or less stiffness from a blend of HSC cells and using them for infusion. The previous chapter demonstrates HSCs are actually more deformable than blood neutrophils, but importantly, not all HSCs share the same mechanical properties and that there is a broad range of deformabilities within a single heterogenous population. Therefore it may be possible to utilise this to separate out the more deformable cells. This should theoretically avoid the ‘first pass only’ problem and ensure HSCs are retained in the circulation. Current strategies for cell separation depend on biochemical modification or labeling of the cells, such as fluorescent activated cell sorting (FACS) and magnetic-activated cell sorting (MACS) (Herzenberg *et al.,* 1976, Schmitz *et al*., 1994, Fong *et al*., 2009). Recently, a number of intrinsic biomarkers have been discovered to separate cells, including mechanical properties (size, deformability and shape). There has been an increased interest in using techniques that make use of separation chips/microfluidic channels and the intrinsic physical or mechanical properties of cells for sorting purposes. Different microfluidic channels are available including straight and curved which use different forces to separate cells into ‘equilibrium positions’ within the fluid. In straight channels, inertial lift forces depending on *particle / cell size* are able to focus them as they migrate across different streamlines to different equilibrium positions, for example the periphery (Martel and Toner, 2013). However, the accuracy can be low as the length of the channel may not give sufficient time for particles to migrate to these equilibrium positions (Gossett *et al*., 2010).

Inertial lift forces used to separate cells, which depend on their sizes, can be combined with *deformability*-dependent forces for separation purposes. The rotational Dean drag force generated the secondary flow type exits in spiral or curved channel geometries that can be balanced with inertial forces to focus cells in streams into a particular channel of a separating device. In spiral rectangular channel devices, the counter-rotating Dean vortices, induced due to the curvature, disrupt the balance of the inertial forces and the particles are refocused in different positions. In the present study, the inertial lift in straight microchannels and the secondary flow in curved channels were made use of to sort HSCs. The principles by which these channels work have been described in detail in Chapter 1, **Section 1.5.3.** Briefly, it is hypothesized that it should be possible to separate sub-populations of HSCs with different sizes and deformability when passing them through microchannels by controlling the channel geometries and flow conditions.

To further assess whether injection of a sub-population of more deformable HSCs isolated by microfluidics can indeed actually improve the homing and subsequent adhesion within injury sites, potentially by avoiding pulmonary entrapment, fluorescent intravital microscopy was utilised. This technique allows direct imaging of the microcirculation of various organs *in vivo* in anaesthetised mice. Indeed, recent advances in intravital imaging methods have allowed the successful monitoring of infused cells in living animals (Rodriguez-Porcel, 2010). This study investigated the ability of HSCs to home to the ischaemia-reperfusion (IR) injured small intestine. IR injury induces a significant cellular and microvascular damage to tissues and organs resulting from the return / reperfusion of blood flow to previously ischemic tissues or organs. This injury often occurs during a wide array of routine surgical procedures, such as organ transplantation which inevitably hampered the blood supply (King *et al*., 2000), as well as many clinical pathologies including stroke, myocardial infarction and limb ischaemia (Collard and Gelman, 2001). The return of the blood supply or reperfusion produces a number of inflammatory responses that both heighten local tissue and microvascular damage and lead to a systemic insult as well (Dorweiler *et al.,* 2007). The clinical outcomes of IR injury can be severe and diverse including direct organ dysfunction, breakdown of the gastrointestinal barrier, systemic inflammatory response syndrome and multi-organ dysfunction syndrome (Collard and Gelman, 2001).

Modulating the physical properties of transplanted cells through isolating smaller and more deformable cells is an option to overcome the mechanical obstacles in circulation and thus enhance HSC retention at the site of injuried organs. The ability of a number of microfluidic devices with different geometries to separate cells of interest based on their intrinsic mechanical heterogeneity was developed and tested. Microfluidic and micromanipulation results presented in this Chapter suggested **Device C** had a relatively higher separation efficiency for HPC-7 cells with these specific mechanical property parameters than the others deivces. To evaluate the potential clinical benefit of this cell sorting system, intravital experiments were conducted. Following cell separation under the optimum conditions with **Device C**, the changes of free flowing and adherent HPC-7 cells in the IR injured mouse small intestine over time were assessed.

In this Chapter, five different microfluidic devices were tested to identify the one which could most effectively and efficiently separate HSCs based on their size and deformability. In order to evaluate and determine the performance of each device, several separation performance metrics were utilized:

1) **degree of separation –** which was defined by the size and deformability differences between different sub-populations. The mean values and coefficients of variation (CV) of these parameters, as well as the mechanical property distribution of individual cells, were used to illustrate the separation efficiency at varying flow conditions.
2) **viability –** defined as the percent of the number of viable cells in the total number of cells before and after sorting. Cell viability was asssessed using trypan blue in which those cells taking up this dyes were considered non-viable.
3) **throughput –** typically, the volumetric flow rate and cell density were used to calculate the number of cells sorted per unit time.

Young's Modulus (E) is a measure of cell stiffness and calculated as $\mathrm{E} = \frac{\sigma}{\varepsilon}$, where σ represents the stress applied on the material, and ε is the strain the material underwent. It can be seen from this equation that the Young's modulus is proportional to the stress, suggesting that the deformability of different materials can be compared by the values of stress when their deformations are similar. Therefore, in the present study **nominal rupture stress** (σ_R) was used to assess the separation efficiency of microfluidic sorting systems due to the simpler data processing procedure compared to the calculation of Young's modulus. Moreover, the possible underlying physics of the lateral migration of cells was revealed to quantify the relative importance of the relevant physical phenomena in cell sorting.

The dimensionless numbers used in this study, namely hydraulic diameter of the microfluidic device, its aspect ratio, Reynolds number, blockage ratio, Dean and inertial force number and the curvature ratio, and how they were derived are shown in **Table 4.1**.

Table 4.1 Dimensionless numbers used in this chapter and equations used to derive these values. w: width of the channel ; h: height of the channel ; a: diameter of the cell ; R: curvature of the spiral microchannel ; U: average velocity ; ρ: fluid density ; μ: dynamic viscosity. In the calculation of Reynolds number, the fluid density and viscosity of PBS was presumed to be the same as water which is 1g/mL and 8.90×10^{-4} Pa at 25℃. The diameter "a" was the mean value of cell size (10μm).

D_h	Hydraulic diameter	$D_h=2hw/(h+w)$	$4\frac{\text{Cross-section area of channel}}{\text{wetted perimeter of duct}}$
AR	Aspect ratio	$AR=w/h$	Channel width/height
Re	Reynolds number	$Re= \rho U D_h/\mu$	Inertial force/viscous force
κ	Blockage ratio	$\kappa=a/h$	Cell size/channel height
De	Dean number	$De=Re(D_h/2R)^{1/2}$	(Dean×inertial forces)$^{1/2}$/viscous force
R_f	Inertial force ratio	$R_f =2Ra^2/D_h^3$	Lift force/Dean drag force
θ	Curvature ratio	$\theta=D_h/2R$	Channel size/diameter of curvature

4.2 Materials and Methods

4.2.1 Fabrication of Microfluidic Chips

The geometries of the five microfluidic chips or systems used in this chapter are shown in **Table 4.2.** They were fabricated using soft lithography techniques based on standard methods that have been described previously (Sun *et al.,* 2010, Yuan *et al.,* 2012). Soft lithography uses soft, elastic and opaque materials, notably polydimethylsiloxane (PDMS), to construct sealed structures on a nanometer scale. Briefly, a photolithography mask or template of the microchannel device was drawn in AutoCAD, a commercial design software package, and produced on a silicon substrate mold. A PDMS slab was peeled off from the mold and bonded with a flat PDMS substrate. Plastic tubing was inserted through the inlet port and connected to a syringe pump used to pump the cells through the channels. Further plastic tubing was inserted in all the outlet ports to collect the cells. The curvature radius of the spiral channel was from 8 mm to 24 mm and the mean value of the radius, 16 mm, was used to calculate the curvature ratio θ.

4.2.2 Cell Sorting Procedures

4 mL of the HPC-7 cells in medium suspension with a cell density of 2×10^6/mL was initially injected into a microchannel with various flow rates. Subpopulations harvested from the two outlets were counted and processed for further mechanical studies.

4.2.3 Cell Viability Assay

The viability of HPC-7s before and after undergoing separation was assessed via the trypan blue exclusion assay and the number of cells that excluded the dye counted.

4.2.4 Mechanical Testing of Cells after Sorting Using Micromanipulation

The diameter of sorted HPC-7 cells was directly measured from the monitor screen of the micromanipulation rig, and nominal rupture stress of sorted cells was calculated from the force curves of micromanipulation compression, as described in detail in **Section 2.4.2**. The mean values of size and nominal rupture stress, as well as their coefficient of variation were calculated to represent the separation efficiency.

4.2.5 Surgical Preparation to Induce Intestinal IR Injury in Mice

Briefly, intravital procedures were performed on healthy male C57BL/6 wild type mice that had been intestinal IR injured by atraumatic clamping of the superior mesenteric artery for 45 minutes followed by removal of the clamp to induce reperfusion.

4.2.6 Intravital Imaging of the Mucosal Surface of the IR Injured Small Intestine

To image the trafficking of HPC-7s *in vivo* within the small intestinal mucosal villous mirocirculation, a fluorescent intravital microscopy study was performed. The animal was anaesthetised and intestinal IR injury was induced. Microfluidic **Device C** was used to conduct cell isolation with a flow rate of 10 mL/h and a cell density of 2×10^6/mL. HPC-7s isolated from the inner (lower nominal rupture stress likely to correspond to deformable cells) and outer outlets (higher nominal rupture stress therefore more rigid cells) were harvested for intravital experiments. The isolated cells were washed with PBS, and then labelled using the fluorescent dye CFDA-SE to enable them to be tracked *in vivo*, followed by incubation at 37 °C for 10 minutes. 2×10^6 labelled cells were centrifuged and resuspended in 200μL warm StemPro media (37°C water bath) before infusion into mice as a bolus dose. Isolated HPC-7 cells were injected after 30 min reperfusion. A single pre-selected field of view was identified microscopically using a x10 objective and videos were taken every 5 min for 1 hour. At each time point the numbers of freely flowing and adherent HPC-7s were quantitated. At the end of the experiment, the number of adherent HPC-7s present within the lungs was also quantified. A total of 5 mice were used for each group i.e. 5 mice imaged for the trafficking of the more deformable HPC-7s harvested from the inner outlet of **Device C** and 5 mice receiving the more rigid HPC-7s isolated from the outer outlet.

Table 4.2. Geometries of the 5 microfluidic devices used to separate murine HSCs. Two straight devices that varied in the width and height were tested. The 3 spiral devices varied in their height, curvature ratio and the number of loops they contained.

		Width (μm)	Height (μm)	Curvature ratio (θ)	Length (cm)
Straight channel	**Device A**	150	30	0	2 cm
	Device B	200	20	0	2 cm
Spiral channel (curvature radius: 8-24mm)	**Device C**	300	40	0.0044	4 loops
	Device D	300	60	0.0063	4 loops
	Device E	300	80	0.0079	6 loops

4.3 Results

4.3.1 Geometry Characterization of Microfluidic Devices

A cell suspension was injected into a single inlet in the microfluidic device being tested for sorting purposes and potentially different subsets were harvested from either three (straight device) or two (spiral device) outlets into a collecting tubing attached to the outlets. Channel blockage is a serious problem that can affect the separation performance and must be avoided throughout the experiments. This could be bought about by the formation of cell aggregations becoming stuck within the various micro-channels. Therefore, the channels were constantly monitored with the help of an EVOS optical microscope. If any blockage was observed, the sorting system was stopped and the experiment repeated. Fortunately, this was not a frequent occurrence. The optical images in **Figure 4.1**, taken using the EVOS microscope, illustrate the downstream microchannel sections of each type of microfluidic device. The three outlets of the straight microfluidic device were equally spaced (**Figure 4.1a**). The spiral microfluidic design had an initial radius of curvature of 8mm and consisted of 4 or 6 loops, with the length of the two outlets being the same (**Figure 4.1b**).

4.3.2 Effect of Culture Condition on the Mechanical Strength of HPC-7s

The heterogeneity in the mechanical strength of cells due to the culture environment, cell metabolism and proliferation stage, thus affecting the consistency and reproducibility of subsequent separation experiments, was first investigated. Though there are many known and unknown factors that can influence cells mechanics, the culture procedure is at least a relatively controllable parameter that can be considered precisely. HPC-7s were cultured with the standard procedure for 5 days (described in **Section 2.2.2**), which involved adding fresh media daily but completely removing old media and replacing every other day (i.e. day 2 and 4). On days 6, 7 and 8, the old culture medium was not removed and cell density was adjusted only through adding fresh medium daily.

Cells were imaged microscopically and on each day were observed to be intact, spherical and bright **(Figure 4.2a)**. However, changes in nominal rupture stress, determined using micromanipulation, varied with regular and irregular medium feeding. HPC-7s cultured by removing old and adding new media every other day demonstrated relatively stable nominal rupture stress values, which did not change significantly each day (**Figure 4.2b**). However, when old media was not removed, a loss in HPC-7 mechanical strength was observed as a decrease in nominal rupture stress. This was possibly due to accumulation of metabolic waste on days 6 to 8. Therefore, to ensure the consistency in their mechanical strength, only cells cultured in the first 5 days were used for subsequent cell separation experiments.

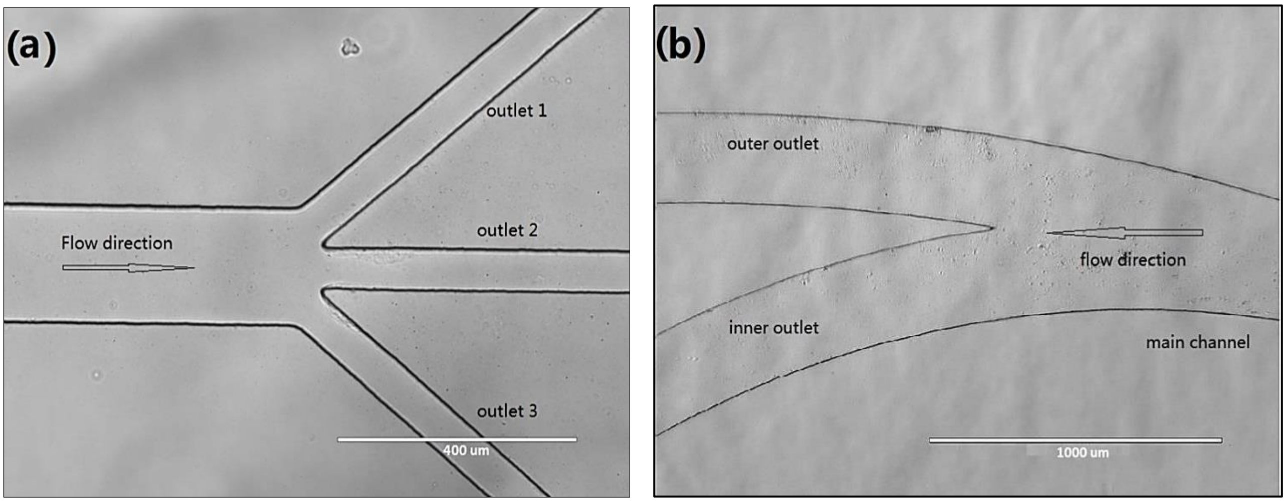

Figure 4.1. Optical brightfield images illustrating the outlet section of the (a) straight and (b) spiral microchannel. The three outlets of the straight trifurcated microchannel were equally spaced and the spiral bifurcated design had an initial radius of curvature of 8 mm and consisted of 4 or 6 loops, with the length of two outlets being the same. Images were aquired using an EVOS microscope with a x 4 objective.

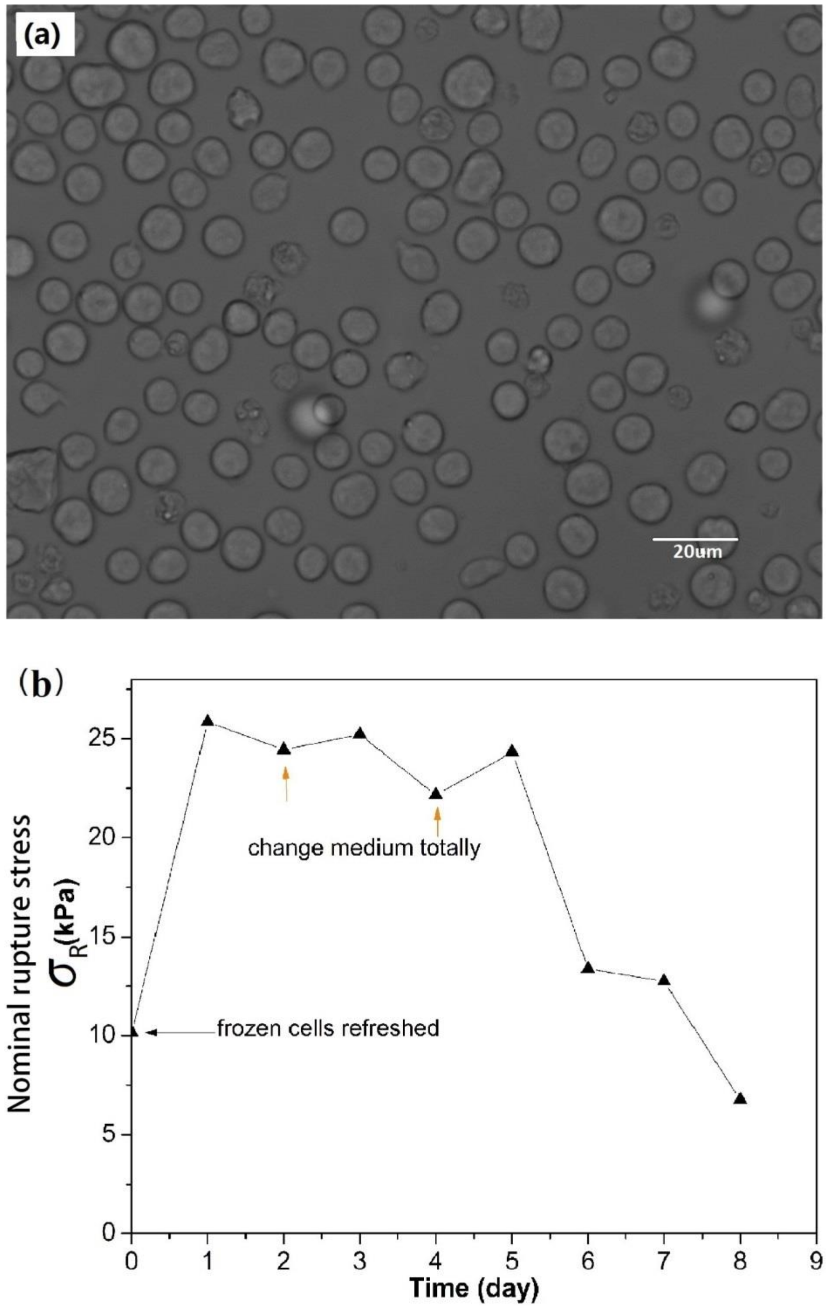

Figure 4.2. The effect of culture condition on the phenotype and nominal rupture stress of HPC-7. (a) Brightfield image of healthy HPC-7 cells, which are intact, spherical and bright when observed under the EVOS microscope. **(b)** Changes in the nominal rupture stress of HPC-7s with culture time and different protocols for medium addition. Cells were maintained at a density of 1 × 10^6 /mL through changing the medium volume daily, the medium was totally changed every other day (on day 2 and day 4), and on other days more medium was just added to adjust the density. At the later stage of culture, the cells tended to lose their mechanical strength possibly due to the accumulation of metabolic waste.

4.3.3 HPC-7s Demonstrate a Wide Variation in Nominal Rupture Stress but not Size Suggesting a Heterogeneity in Their Mechanical Properties

The diameter and mechanical properties of 200 single HPC-7 cells were measured using the micromanipulation technique, and the nominal rupture stress (σ_R) was used to represent their mechanical strength. The spread of the size ranged from from 6 μm to 12 μm with ~60% of cells being within 8-10 μm. Relatively fewer cells were smaller than 8 μm or larger than 10 μm (**Figure 4.3a**). The standard deviation was 0.94 μm indicating a narrow size distribution. Therefore, although cells could be classified based on their size difference, the sensitivity for isolation purposes may not be expected to be very high due to the narrow size span.

The nominal rupture stress (σ_R) distribution of cells was fitted by a normal distribution with a confidence of 95% (**Figure 4.3b**). The majority of cells had a mechanical strength around a mean value of 28 kPa, while fewer cells had values near the lowest (2 kPa) or highest strength values (62 kPa). The standard deviation was 14 kPa, confirming that the cells in this population had a wide distribution in their nominal rupture strength, which may be exploited for sorting cells in a microfluidic device.

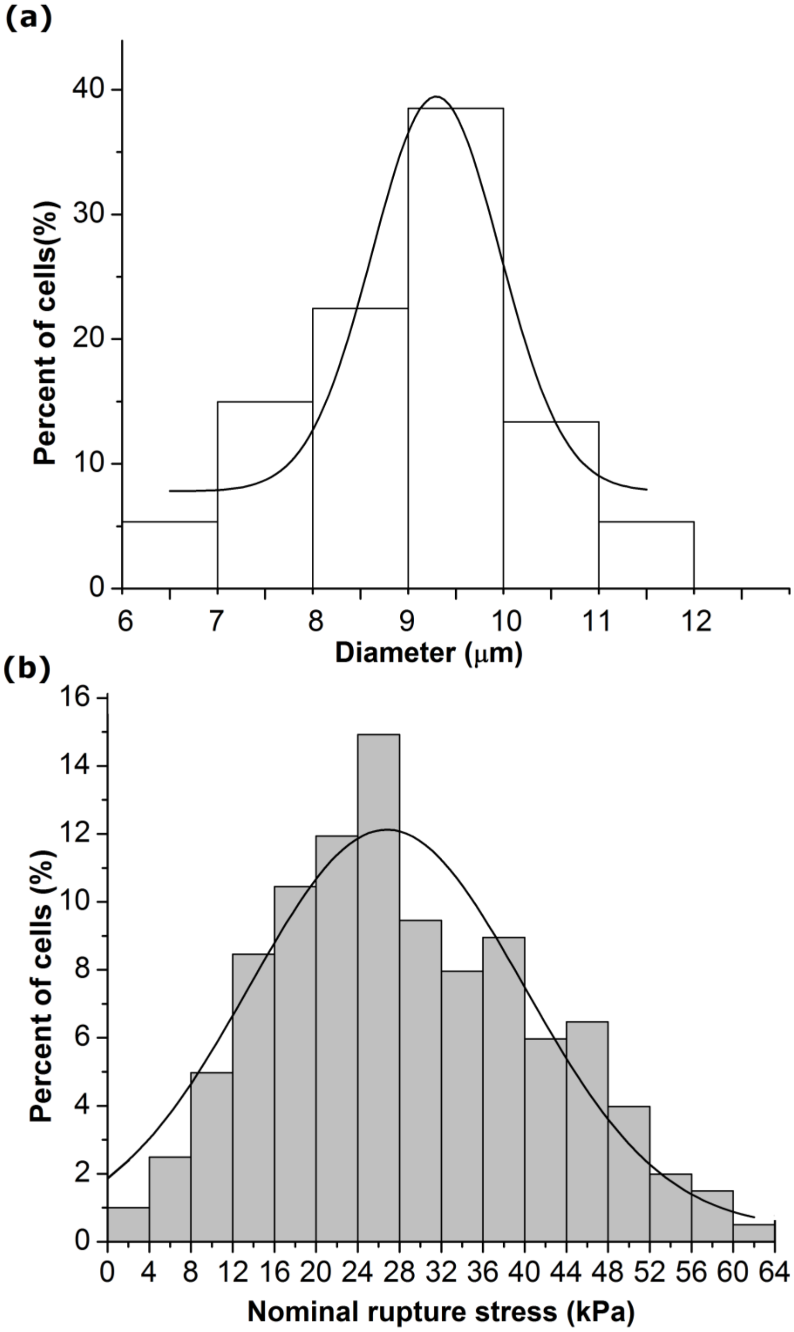

Figure 4.3. HPC-7s demonstrate a wide variation in nominal rupture stress but not size suggesting a heterogeneity in their mechanical properties. In order to isolate cells based on their size and deformability, the heterogeneity of cells in one HPC-7 population (200 cells) were tested with the micromanipulation technique. **(a)** Histogram of cell diameter fitted with normal Gaussian distribution. The spread of the size ranged from from 6 μm to 12 μm with ~ 60% of cells being within 8 - 10 μm. **(b)** Histogram of nominal rupture stress (σ_R) fitted with normal Gaussian distribution. The majority of cells had a mechanical strength around the mean value of 28 kPa.

4.3.4 Performance of the Two Straight Microchannel Devices

4.3.4.1 Separation Efficiency Using the Straight Microchannel Device A with AR = 5

The dimensional parameters of the straight trifurcated **Device A** have been described previously in **Table 4.2**. A cell suspension was injected into the channel at different flow rates, namely 0.5 mL/h, 2 mL/h, 5 mL/h and 10 mL/h. This was associated with an increase in Reynolds number (Re) from 3.4, 13.4, 33.6 to 67.1 respectively. Sub-populations harvested from the three outlets were counted and mechanically tested by micromanipulation. Since the channel is symmetrical about the centre in the axial direction, cells collected from the two side outlets should obtain similar properties. Therefore cells were categorized into two populations, i.e. those from the two side outlets and those from centre outlet.

Generally, as flow rate was increased, the cells migrated from the centre channel to being collected from the outer side outlets (**Figure 4.4a**). Hence the percentage cell number harvested from the centre outlet decreased with the increasing Re. Accordingly, the number of cells from the side channels followed an opposite tendency. When the flow rate was low (0.5 mL/h; Re = 3.4), the majority of cells focused near the channel centre and only ~5% of the cells migrated near the outer side walls. This indicates that cells were barely separated at this flow rate. At intermediate flow rates, 2 mL/h and 5 mL/h, better separation was observed. When the flow rate was hightest, ~ 80% of the cells reached the side outlets, again indicating poor separtaion. Since effective cell separation with a high throughput was required, the lowest flow rate was no longer used in the following experiments.

The separated cells were then evaluated by micromanipulation, which demonstrated there was no significant difference in the nominal rupture stress between the two populations collected from the centre and side outlets ($p > 0.05$; **Figure 4.4b**). Similarly, the diameter of the cells collected from centre and outer side outlets did not show significant difference either ($p > 0.05$; **Figure 4.4c**). Collectively, these results suggest that this device was not effective for sorting cells by considering the big mechanical difference between sub-populations required for application use.

4.3.4.2 Separation Efficiency Using the Straight Microchannel Device B with AR =10

To achieve better separations, another straight trifurcated microchannel with a modified geometry was fabricated. The dimensional parameters of the modified straight trifurcated **Device B** have been described previously in **Table 4.2**. **Device B** was wider and less tall than **Device A** (AR = 5) and thus had an aspect ratio (AR: width/height) of 10. A cell suspension was injected into the channel at different flow rates, namely 0.5 mL/h, 2 mL/h, 5 mL/h and 10 mL/h. This was associated with an increase in Re from 5.1, 20.2, 50.6 to 101.2 respectively. Generally, in this device, as flow rate was increased, the cell number distributions shifted in the opposite direction compared with the performance of **Device A** i.e. the cells migrated to the centre channel with the increase of flow rate up to 10mL/h (Re = 101.2) (**Figure 4.5a**). Unlike **Device A**, the separated cell populations significantly differed in their nominal rupture stress, particularly at 10 mL/h (**Figure 4.5b**). At this flow rate, the cells from the outer side outlets were significantly ($p < 0.05$) less stiff or more deformable (lower nominal rupture stress) than those collected from the centre outlet (higher nominal rupture stress). Although good separation based on the cell stiffness was observed at 5 mL/h, it was not dramatic. The diameter of cells from centre and side outlets did not show significant difference even at the high flow rate (**Figure 4.5c**).

The percentage of cells collected from the side and centre outlets at a flow rate of 10 mL/h was further plotted against a distribution range for nominal rupture stress. HPC-7s collected from the side outlets had a narrower distribution (coefficient of variation = 0.31) than cells collected from the centre outlet (coefficient of variation = 0.46), suggesting side outlets collected mostly deformable cells. However, HPC-7s collected in the centre outlet covered a wider spread of nominal rupture stresses with both deformable and more stiff cells being collected. Overall, it can be concluded that the straight microchannel **Device B** is relatively more effective than the straight microchannel **Device A** in terms of the observed difference in nominal rupture stress between the cells from the centre and side outlets.

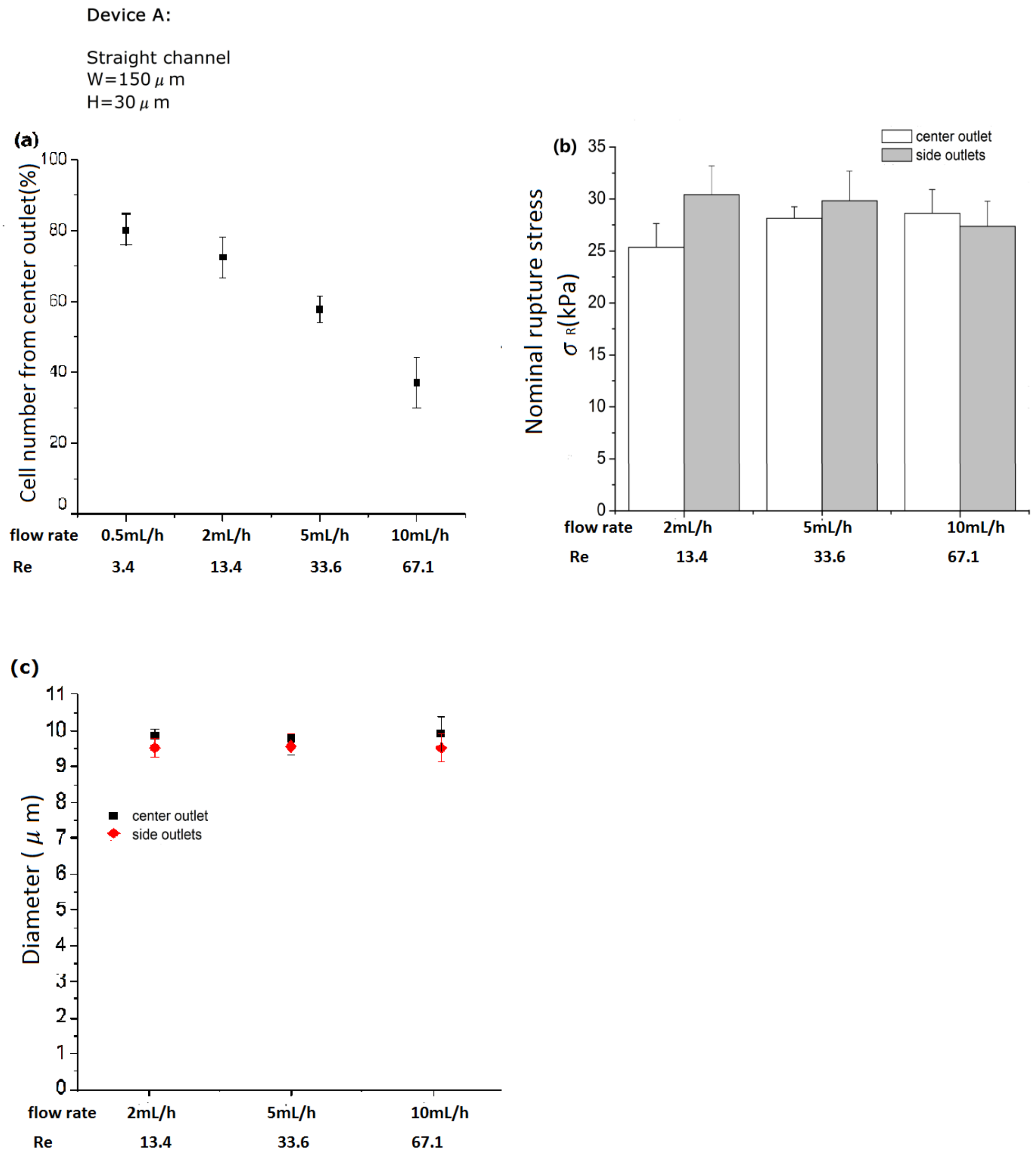

Figure 4.4. Separation efficiency of HPC-7s using the straight, trifurcated Device A with AR = 5 and κ=0.3. (a) With the increase of flow rate (and thus Reynold's number, Re) more cells moved to the side walls of the channel and were collected mostly from the side outlets. **(b)** There is no significant difference in the nominal rupture stress of cells in populations collected from the centre outlet and side outlets based on micromanipulation. **(c)** Sizes of cells in sub-populations collected from centre and side outlets were also similar. Data were analysed using a paired Student t-test.

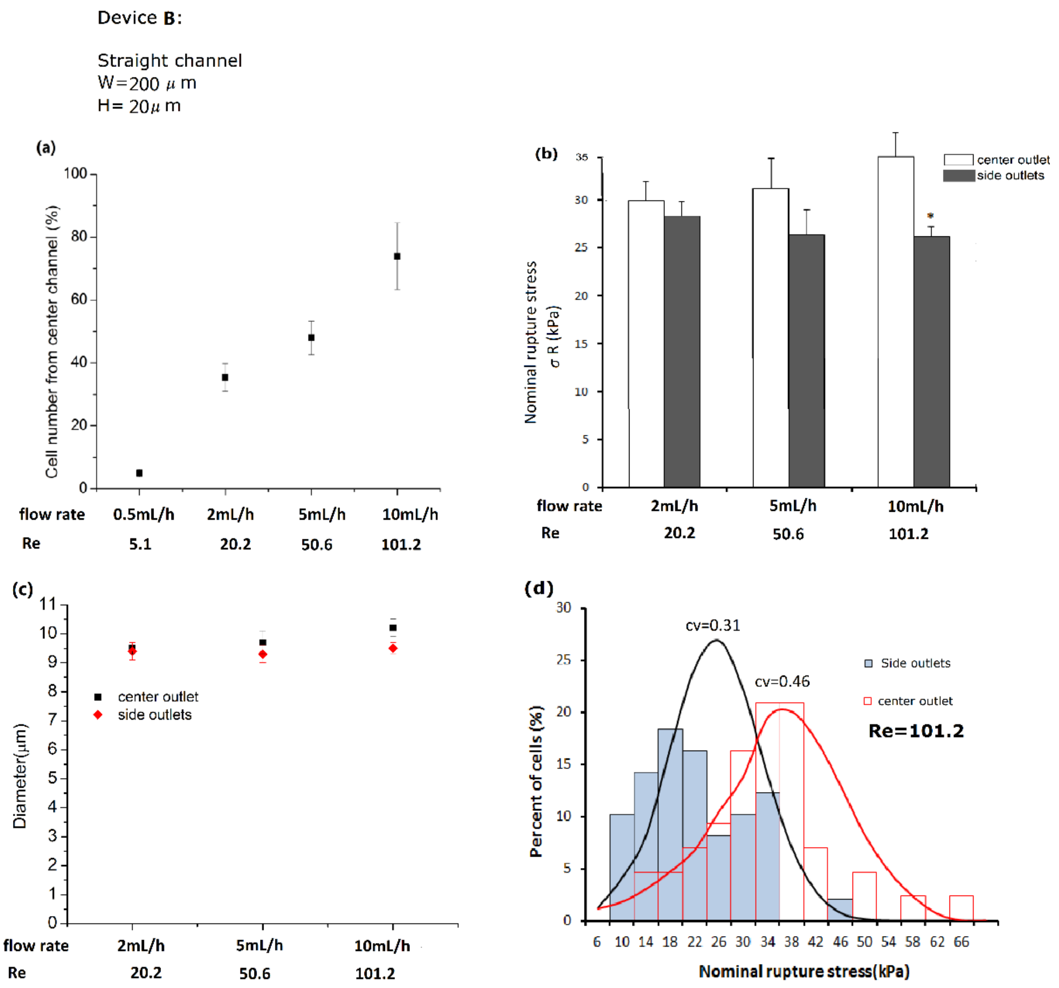

Figure 4.5. Separation efficiency of HPC-7s using the straight, trifurcated DEVICE B with AR = 10 and κ=0.5. (a) With the increase of flow rate (and thus Reynold's number, Re), more cells moved to being collected from the central outlet. **(b)** A relatively rigid sub-population of cells, with higher nominal ruptures stress, were harvested from the centre outlet. This separation efficiency increased with the increase of flow rate. **(c)** Sizes of cells in sub-populations collected from centre and side outlets were similar. **(d)** The percentage of cells collected from the side and central outlets at a flow rate of 10mL/h was plotted against a distribution range for nominal rupture stress. HPC-7s collected from the side outlets had a narrower distribution (CV = 0.31) than cells collected from the centre outlet (CV=0.46), suggesting cells in the inner outlet were mostly deformable cells. However, those collected in the central outlet covered a more wide spread of nominal rupture stress with both deformable and more stiff cells being collected. * $p < 0.05$, as determined using a paired Student t-test.

4.3.5 Performance of The Three Spiral Microchannel Devices

4.3.5.1 Determination of Velocity Limit and Cell Number Distribution for Spiral Devices

The effects of the channel Re, the curvature ratio, θ (corresponding Dean number, De = R $\theta^{1/2}$), and the cell blockage ratio, κ on the cell separation efficiency were investigated. Re was controlled by changing the flow rate. The flow rate limits in the three bifurcated spiral microchannels were determined by visualizing cell motions near the downstream region of the channel. Qualitatively, it was observed from the EVOS microscope that changing the flow rates focused the cells to different lateral positions in the channel. At lower flow rates (0.5 mL/h; Re = 1.8), most cells moved closer to the outer wall of the channel and were collected from the outer outlet. However, at the higest flow rate (15 mL/h; Re = 55), the majority of cells shifted to the opposite direction and were harvested from the inner outlet (**Figure 4.6a**). This suggests that when the Re was smaller than 1.8 or bigger than 55, there was a loss of separation. Thus intermediate flow rates (2.5 mL/h, 5 mL/h, 7.5 mL/h and 10 mL/h), corresponding to Re between 8 - 35, were chosen for further experiments.

For all three bifurcated spiral devices tested, namely **Devices C, D** and **E**, as the flow rate and thus Re increased, the percentage of HPC-7s collected from the inner outlet also increased. Correspondingly, the percentage cell number collected from the outer outlet decreased (**Figure 4.6b**). Considering that a high throughput device is required and that cell sedimentation within the syringe needs to be reduced, 2.5 mL/h was no longer used. It can also be seen that for **Device D** and **E,** when the flow rate was 10 mL/h, more than 80% of cells migrated near the inner side wall, resulting in a lower separation. Therefore, in these two devices, flow rates of 5 mL/h and 7.5 mL/h were used for cell separation, and the isolated cells were mechanically tested.

4.3.5.2 Separation Efficiency Using the Spiral Microchannel Device C with AR=7.5 and Curvature Ratio θ=0.0044

For successful isolation of stem cells in curved channels, the ideal performance is for cells of different mechanical properties to focus in the channel as far as possible from each other. This will increase the separation efficiency, as well as allow us to infuse a sufficient number of the cells of a specific nominal rupture stress into mice when conducting intravital studies to image their trafficking *in vivo*. Hence, the mean values of nominal rupture stress, as well as their coefficient of variation (CV), were used to compare the separation efficiency of three different microfluidic systems at varying Re.

The dimensional parameters of the spiral bifurcated **Device C** have been described previously in **Table 4.2**. A cell suspension was injected into the channel at different flow rates, namely 5 mL/h, 7.5 mL/h and 10 mL/h. This was associated with an increase in R_e from 17.8, 26.7 to 35.6 respectively. In this device, the separated cell populations significantly differed in their mechanical strength or nominal rupture stress, particularly at the higher flow rates (**Figure 4.7a**). At 7.5 mL/h and 10 mL/h, the cells from the inner outlet were significantly ($p < 0.05$) less stiff or more deformable (lower nominal rupture stress) than those collected from the outer outlet (higher nominal rupture stress). Interestingly, at these flow rates, cells collected in the inner outlet were not only weaker/more deformable but also significantly ($p < 0.05$) smaller (**Figure 4.7b**). Nominal rupture stress distribution of cells for these two flow rates indicated that the mechanical strength of single cells from the inner outlet was more dispersed at 7.5mL/h (R_e = 26.7; CV = 0.35; **Figure 4.7c**) than with 10mL/h (Re = 35.6; CV = 0.26; **Figure 4.7d**). This indicates that this device achieved more effective separation at 10mL/h (Re = 35.6). Cell throughput at this flow rate was 2.3×10^5 cells/min. Thus, this flow rate can be desirable for cell separation in the system of **Device C**.

4.3.5.3 Separation Efficiency Using the Spiral Microchannel Device D with AR=5 and Curvature Ratio θ=0.0063

The dimensional parameters of the spiral bifurcated **Device D** have been described previously in **Table 4.2**. A cell suspension was injected into the channel at either 5mL/h or 7.5mL/h. This was associated with an increase in Re from 16.8 to 25.2 respectively. In this device, the separated cell populations significantly differed in their nominal rupture stress at both flow rates (**Figure 4.8a**). At both 5 mL/h and 7.5 mL/h, the cells from the inner outlet were significantly ($p < 0.05$) less stiff or more deformable (lower nominal rupture stress) than those collected from the outer outlet (higher nominal rupture stress). Interestingly, only at 7.5 mL/h, were cells collected in the inner outlet significantly ($p < 0.05$) smaller (**Figure 4.8b**). Nominal rupture stress distribution of cells for these two flow rates indicated that the mechanical strength of single cells from the inner outlet was more dispersed at 5mL/h (Re = 16.8; CV = 0.49; **Figure 4.8c**) than with 7.5mL/h (Re = 25.2; CV = 0.41; **Figure 4.8d**). This indicates that this device achieved more effective separation at 7.5 mL/h (Re = 25.2). Cell throughput at this flow rate was 1.5×10^5 cells/min. Thus, the flow rate of 7.5 mL/h can be desirable for cell separation in the system of **Device D**.

4.3.5.4 Separation Efficiency Using the Spiral Microchannel Device E with AR=3.75 and Curvature Ratio θ=0.0079

The dimensional parameters of the spiral bifurcated **Device E** have been described previously in **Table 4.2**. A cell suspension was injected into the channel at either 5mL/h or 7.5mL/h. This was associated with an increase in Re from 15.9 to 23.8 respectively. In this device, the separated cell populations significantly differed in their mechanical strength or nominal rupture stress at both flow rates (**Figure 4.9a**). At both 5 mL/h and 7.5 mL/h, the cells from the inner outlet were significantly ($p < 0.05$) less stiff or more deformable (lower nominal rupture stress) than those collected from the outer outlet (higher nominal rupture stress). Interestingly, at both flow rates, cells collected from the inner outlet were not only weaker / more deformable but also significantly ($p < 0.05$) smaller (**Figure 4.7b**). Nominal rupture stress distribution of cells for these two flow rates indicated that this device achieved more effective separation at 7.5 mL/h (Re = 23.8), as shown in **Figure 4.9c** and **Figure 4.9d**. This indicates. Cell throughput at this flow rate was 1.6×10^5 cells/min. Thus, the flow rate of 7.5 mL/h can be desirable for cell separation in the system of **Device D**.

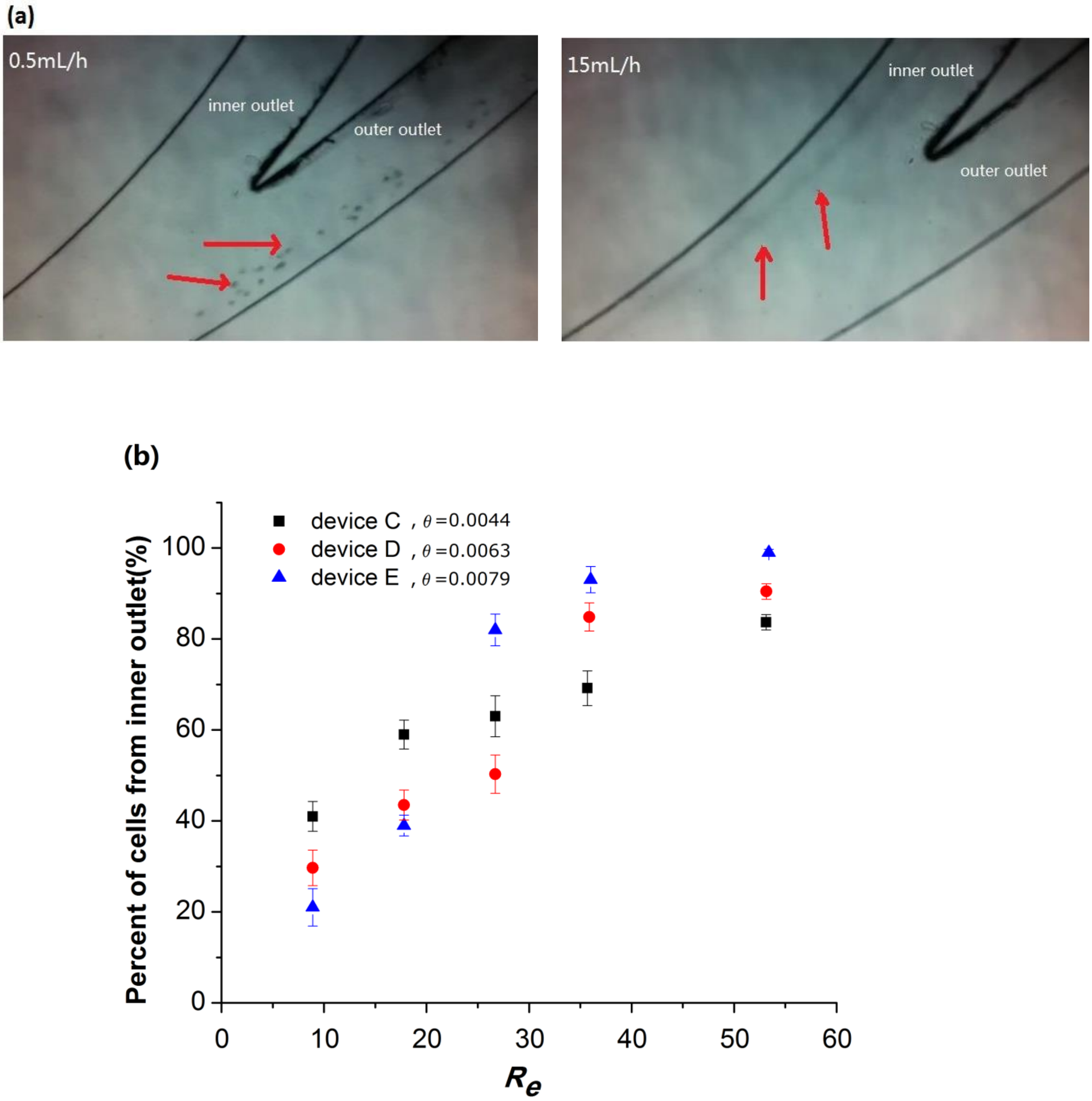

Figure 4.6. Determination of the velocity limit and cell number distribution at varying flow rate for the 3 SPIRAL devices. Differential cell number distribution of cells in spiral channels with cross sections 300 µm × 40 µm (**Device C**), 300 µm × 60 µm (**Device D**) and 300 µm × 80 µm (**Device E**). **(a)** 0.5 mL/h and 15 mL/h were determined as the lowest and highest flow rate for cell separation experiments. When imaged microscopically, it was noted that at the lower limit of flow rate, all the cells moved to the outer outlet, while the majority of cells focused to the inner outlet at the highest limit of flow rate. **(b)** Intermediate flow rates were used for separation, and cells gradually shifted to the inner outlet with the increase of flow rate.

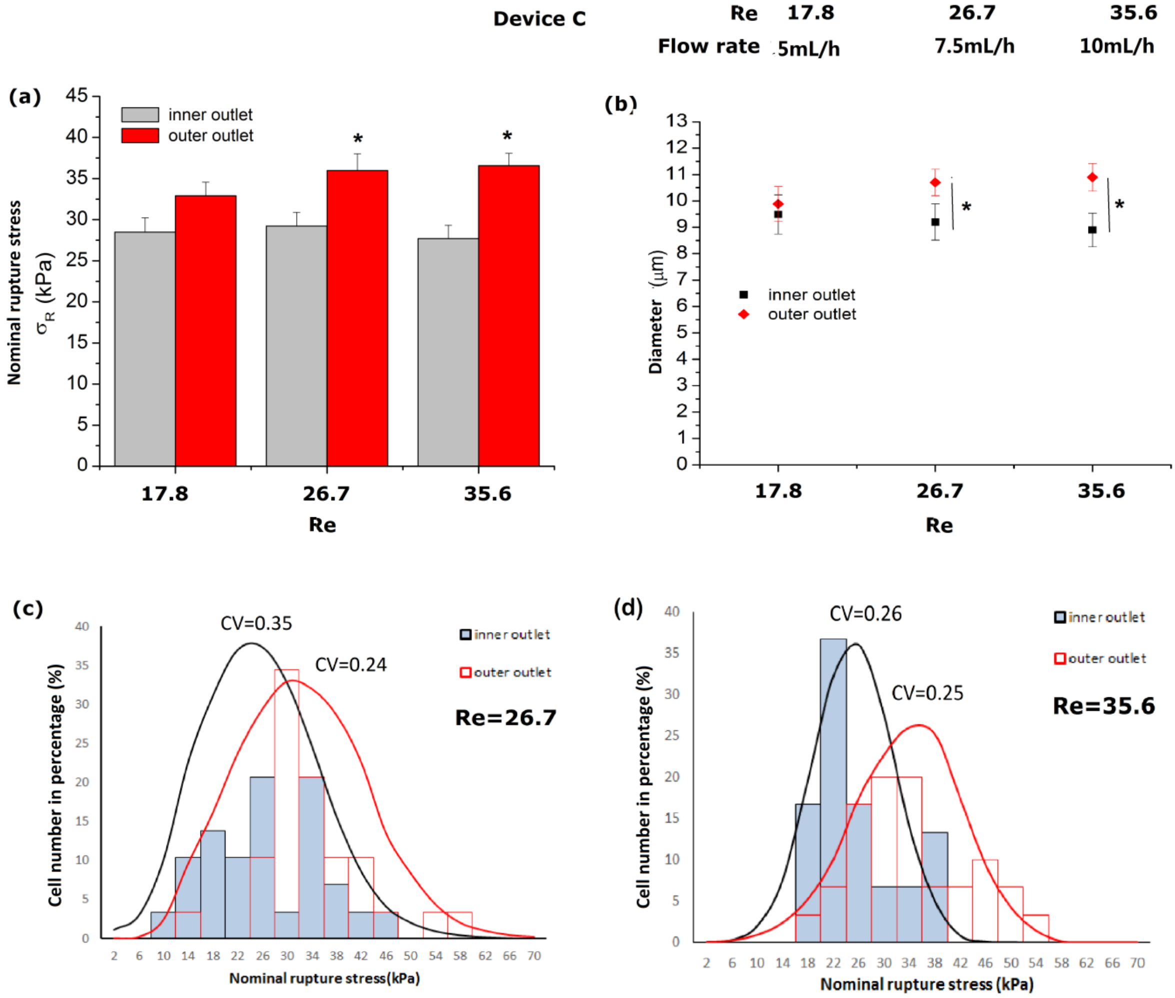

Figure 4.7. Separation efficiency of HPC-7s using spiral and, bifurcated DEVICE C with AR=7.5 and θ=0.0044. (a) With the increase of flow rate (and thus Reynolds number, Re), a relatively rigid sub-population of cells, with higher nominal rupture stress, were harvested from the outer outlet, with cells collected from the inner outlet demonstrating a clear loss of strength. This was only significantly different with the two higher flow rates (7.5 mL/h and 10 mL/h); **(b)** The mean diameter of cells from the inner outlet was significantly smaller than those from the outer outlet for the two higher flow rates. **(c)** and **(d)** At the highest flow rate (10 mL/h; Re = 35.6; CV = 0.26; **(d)**), the nominal rupture stress (σ_R) distribution of the inner outlet HPC-7s was narrower than at the lower flow rates (7.5 mL/h; Re = 26.7; CV = 0.35; **(c)**). This suggests more sensitive separation was achieved at higher flow rates and higher Re. * $p < 0.05$, as determined using a paired Student t-test.

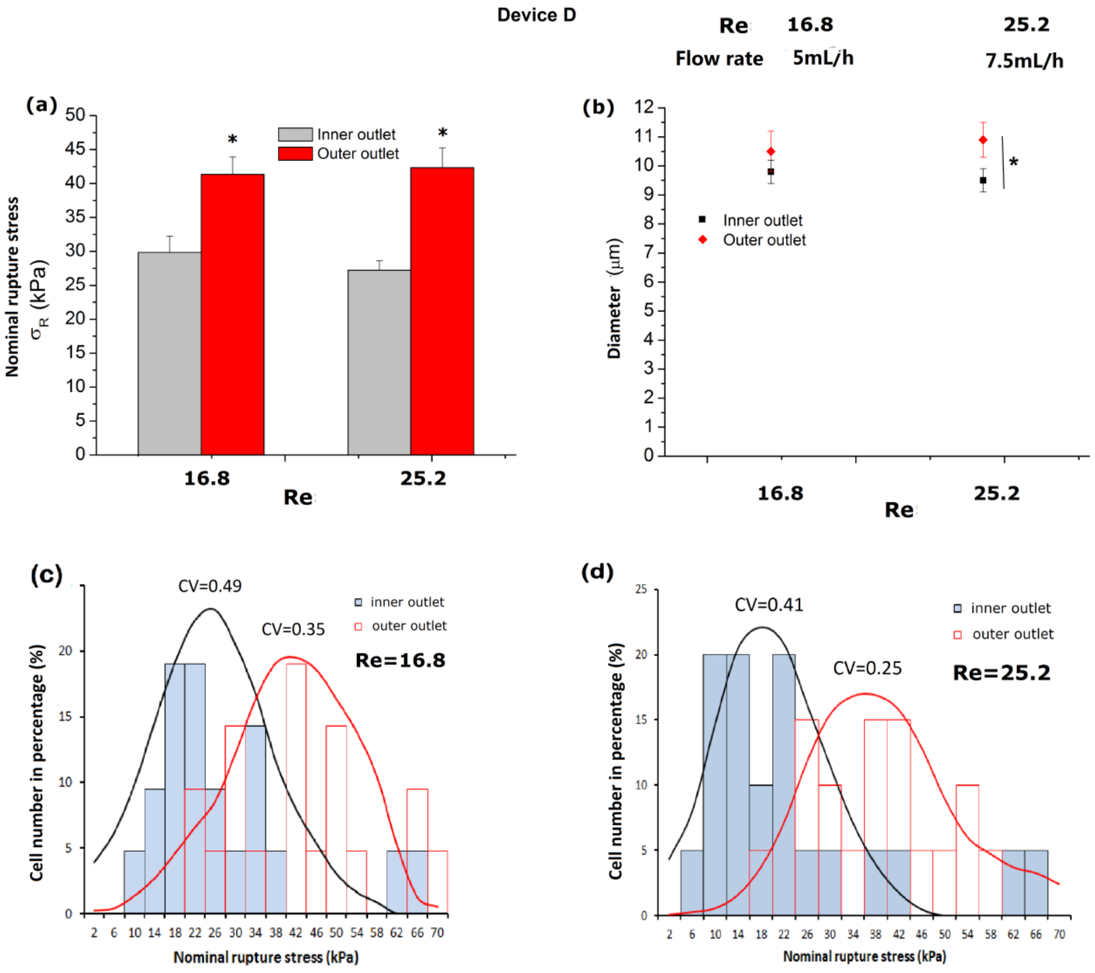

Figure 4.8. Separation efficiency of HPC-7s using spiral and, bifurcated Device D with AR=5 and θ=0.0063. (a) With both flow rates (and thus Reynolds number, Re), relatively rigid sub-populations of cells, with higher nominal rupture stress, were harvested from the outer outlet, with cells collected from the inner outlet demonstrating a clear loss of strength. **(b)** The mean diameter of cells from the inner outlet was significantly smaller than those from the outer outlet for both flow rates. **(c)** and **(d)** At the higher flow rate (7.5 mL/h; Re = 25.2; CV = 0.41; **(d)**), the nominal rupture stress (σ_R) distribution of the inner outlet HPC-7's was narrower than at lower flow rates (5 mL/h; Re = 16.8; CV = 0.49; **(c)**). This suggests more sensitive separation was achieved at higher flow rates and higher Re. *$p < 0.05$, as determined using a paired Student t-test.

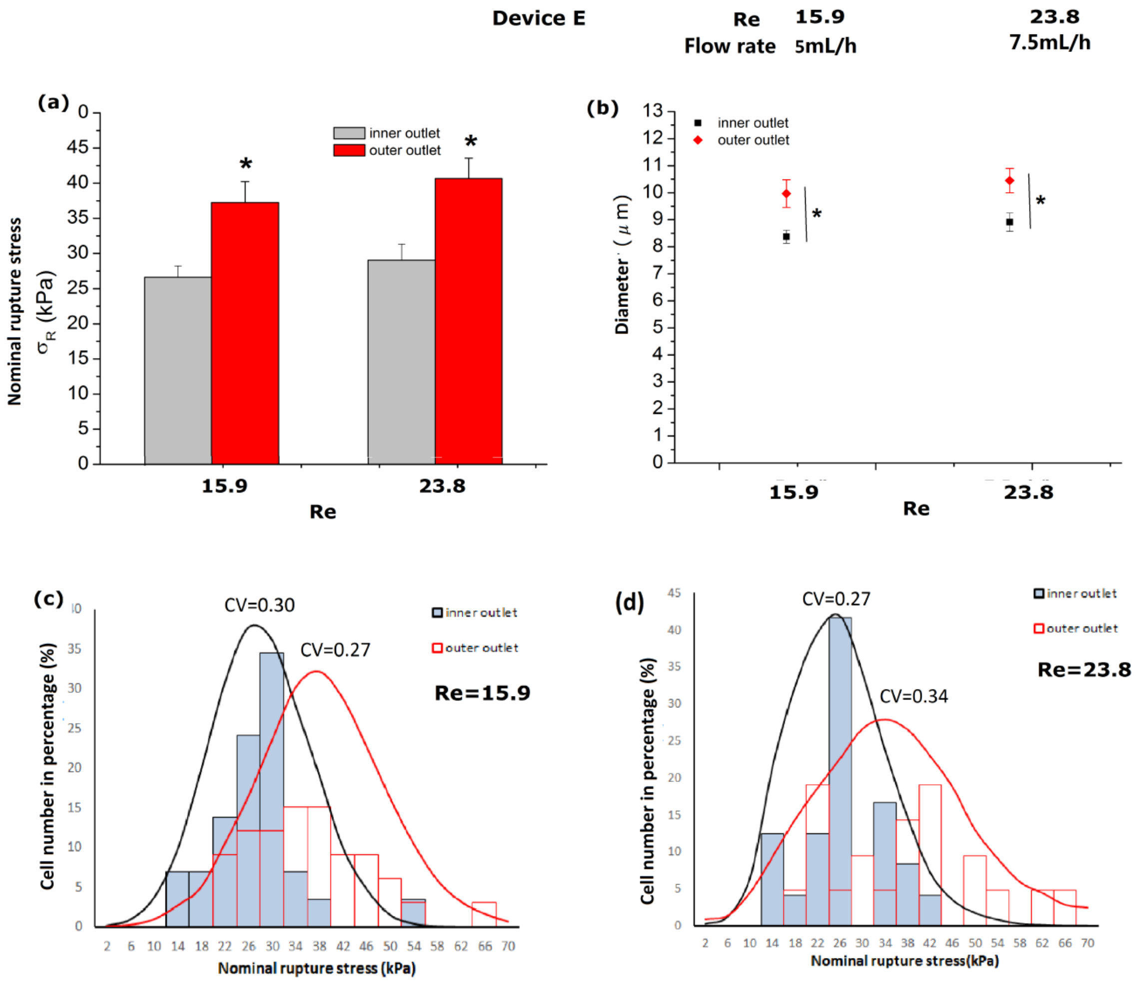

Figure 4.9 Separation efficiency of HPC-7s using spiral and, bifurcated DEVICE E with AR=3.75 and θ=0.0079. (a) With both flow rates (and thus Reynolds numbers, Re), a relatively rigid sub-population of cells, with higher nominal rupture stress, were harvested from the outer outlet, with cells collected from the inner outlet demonstrating a clear loss of strength. **(b)** The mean diameter of cells from the inner outlet was significantly smaller than those from the outer outlet for both the flow rates. **(c)** and **(d)** At higher flow rate (7.5 mL/h; Re = 23.8; CV = 0.27; **(d)**), the nominal rupture stress (σ_R) distribution of the inner outlet HPC-7s was narrower than at lower flow rates (5 mL/h; Re = 15.9; CV = 0.30; **(c)**). This suggests more sensitive separation was achieved at higher flow rates and higher Re. * $p < 0.05$, as determined using a paired Student t-test.

4.3.6 Summary of Separation Efficiency of all Devices

The performance of the 5 different microfluidic systems under optimum conditions is summarized in **Table 4.3** below. It highlights that the straight channel **Device B** with a higher AR (10) achieved relatively more significant cell separation based on cell stiffness than the straight channel **Device A** with a lower AR (5). A significant difference in nominal rupture stress (σ_R) between the sub- populations of cells was observed at a high flow rate (10 mL/h; Re = 101.2), although no significant difference in cell size was observed between the subsets in this straight channel device. For spiral channels at intermediate flow rates (**Device C** at 7.5 mL/h & 10 mL/h; **Device D** at 5 mL/h & 7.5 mL/h; **Device E** at 5 mL/h & 7.5 mL/h) , all three devices showed similar results of the mean values of σ_R and size with significantly weaker/more deformable and smaller cells being separated from the inner outlet of the channels.

Although it has been demonstrated that HPC-7s are indeed heterogeneous, the mean values of σ_R only are not sufficient to compare their separation efficiency. Thus, the data of σ_R distribution of cells were used to present the separation efficiency of different designs, shown as values of coefficient of variation (CV). Of all the five microfluidic devices, the spiral microchannel **Device C** (AR = 7.5 and θ = 0.0044) was able to focus weaker / more deformable and smaller cells near the inner channel wall at a flow rate of 10mL/h, with a relatively higher separation efficiency (lowest CV value of 0.26) and throughput than the other devices. Hence this device was utilized for further intravital experiments at a flow rate of 10 mL/h (Re = 35.6).

Table 4.3. Summary of the performance of the 5 different microfluidic systems in separating cells based on the mechanical strength and size. Only data from flow rates that demonstrated significant differences in the nominal rupture stress (σ_R) of the sub-populations of HPC-7 cells collected from the different outlets are summarised above. Of all the five microfluidic devices, the spiral microchannel **Device C** (AR = 7.5 and θ = 0.0044) was able to focus weaker / more deformable and smaller cells near the inner channel wall at a flow rate of 10mL/h , with relatively higher separation efficiency (lowest CV value of 0.26) and throughput than the other devices. Hence this device was utilized for further intravital experiments at a flow rate of 10mL/h (R_e = 35.6). **Abbreviations :** θ = curvature ratio; Re = Reynold's number; σ_R = nominal rupture stress, CV = coefficient of variation, SE = standard error of the mean.

	θ	**Flow rate mL/h**	**Re**	**Nominal rupture stress - σ_R (kPa)**				**Size (μm)**		**Throughput of weaker cells**
				Weaker cells		**Stronger cells**		**Small cells**	**Large cells**	
				Mean ± SE	**CV**	**Mean ± SE**	**CV**	**Mean ± SE**	**Mean ± SE**	
Device A	0		-	-	-	-	-	-	-	No significant difference between subsets
Device B	0	10.0	101.2	26.4 ± 1.9	0.31	34.9 ± 3.7	0.46	9.7±0.4	10.5±0.3	1.9×10^5 cells/min
Device C	0.0044	7.5	26.7	26.9 ±2.1	0.35	35.6 ±2.0	0.24	9.4±0.3	10.6 ±0.5	1.2×10^5/min
		10.0	**35.6**	**23.7 ±1.5**	**0.26**	**37.1 ±2.2**	**0.25**	**9.1 ±0.5**	**10.5 ±0.4**	**2.3×10^5/min**
Device D	0.0063	5.0	16.8	29.1 ±3.2	0.49	40.4 ±3.2	0.35	9.9 ±0.3	10.4 ±0.5	0.7×10^5/min
		7.5	25.2	26.0 ±2.5	0.41	39.8 ±2.2	0.25	9.2 ±0.3	10.8 ±0.5	1.5×10^5/min
Device E	0.0079	5.0	15.9	26.3 ±1.8	0.30	37.0 ±2.3	0.27	8.4 ±0.2	10.1 ±0.4	1.0×10^5/min
		7.5	23.8	27.7 ±1.8	0.27	39.6 ±3.1	0.34	9.0 ±0.3	10.5 ±0.4	1.6×10^5/min

4.3.7 Relationship Between Size and Nominal Rupture Stress (σ_R) for Cell Populations before and after Separation Using Device C

The mechanical properties of HPC-7 cells, isolated using the various devices, suggest that weaker sub-populations also possess the smaller size with stronger sub-populations being larger. In order to reveal the underlying mechanisms by which cells were isolated based on their variation in size and deformability, the relationship between cell size and their mechanical strength (σ_R) before and after separation was correlated and analyzed. A typical trend for σ_R versus diameter, generated from mechanical testing of 100 single cells before separation, was generated (**Figure 4.10a**). As can be seen from the correlation coefficient ($R^2 = 0.19$), σ_R is weakly and negatively correlated with the cell diameter.

To discriminate between cells harvested from the inner (I) and outer (O) outlets of sprial **Device C**, size and σ_R of ~50 single cells from each sub-population were plotted (**Figure 4.10b**). Generally, 4 separate areas could be identified (named I1, I2, O1, O2). Cells harvested from the outer outlet were located mostly at the top and right of this panel with cells harvetsed from the inner panel located mostly at the bottom and left. Cells with significant size difference (i.e. those in the left-most and right-most of the size distribution), migrated in opposite directions with smaller cells focusing to the inner channel walls (I1) and larger cells in the outer channel walls (O1) regardless of their deformability. In this case, the size may play a dominant role in cell migration. However, the majority of the cells were of similar sizes i.e. between 8-10 μm, and were separated primarily based on their mechanical strength variation. This was responsible for the smaller σ_R value for cells collected in the inner channel (I2) compared to the higher σ_R value for cells collected in the outer channel (O2).

4.3.8 Viability of Cells

The most deformable cell sub-population will be used for subsequent *in vivo* studies. However, it should be confirmed that cells isolated using Device C were still viable post-collection. To verify the viability of HPC-7s after they passed through the microfluidic system, cells that were collected from the channel outlets were dyed with Trypan blue. The number of cells that excluded the dye was counted. No significant difference was seen in the number of viable cells passing through Device C when compared to those which did not undergo separation (**Figure 4.11a**). Separated cells can therefore be used for further studies and expansion studies. Additionally, the isolated cells still maintained their mechanical strength as those before isolation (**Figure 4.11b**).

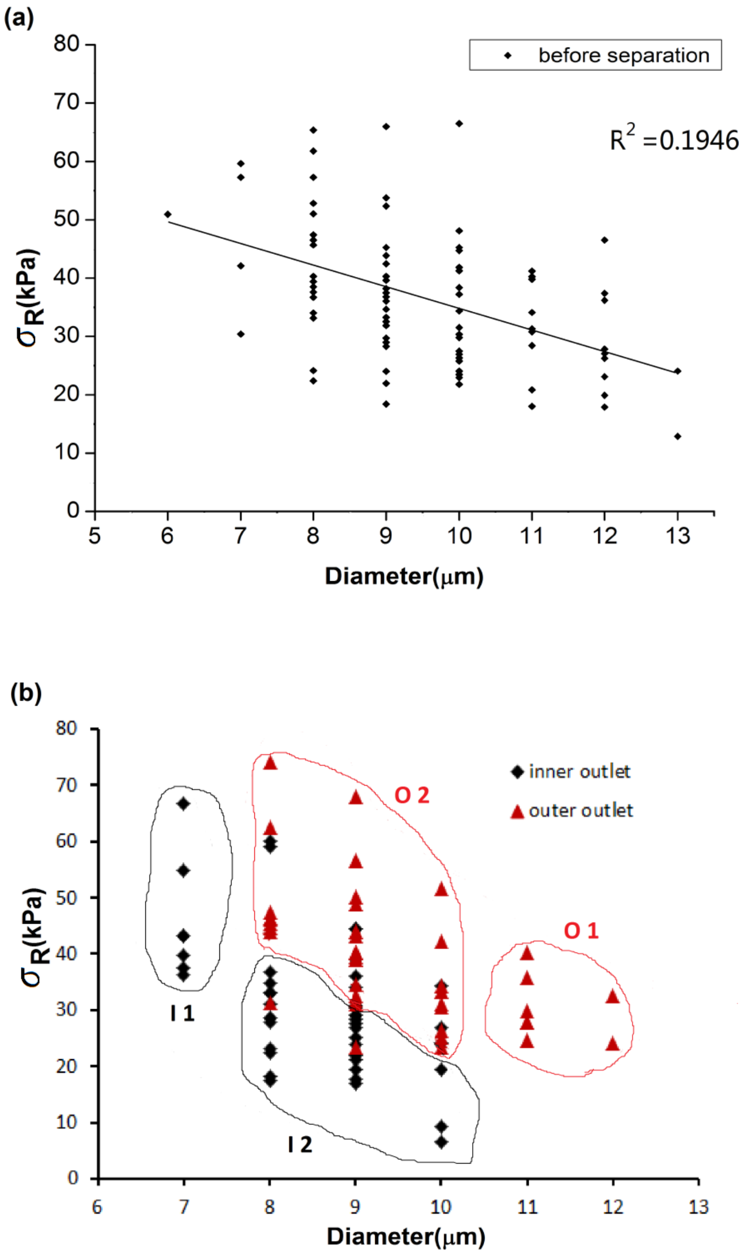

Figure 4.10. Relationship between size and nominal rupture stress (σ_R) for cell populations before and after separation using <u>Device C</u>. (a) Correlative relationship between nominal rupture stress (σ_R) and diameter of HPC-7 cells before separation. Data was generated by micromanipulation by testing of 100 individual HPC-7 cells. σ_R is weakly and negatively correlated with the cell diameter. **(b)** Correlative relationship between the nominal rupture stress (σ_R) of cells collected from the inner outlet (dark, bottom and left panel) and outer outlet (red, top and right panel). 50 indivudal cells were randomly selected from each subset.

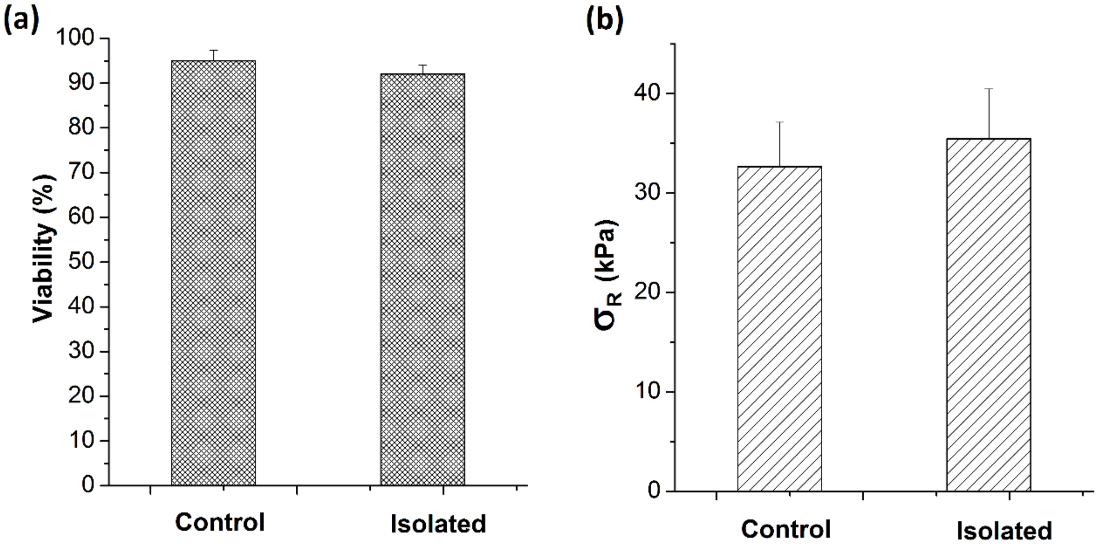

Figure 4.11. Viability and nominal rupture stress of HPC-7s before and after separation using Device C. (a) Cell viability using the trypan blue dye indicates high viability of cells after they passed through the microchannel device. **(b)** Furthermore, the nominal rupture stress of HPC-7s is similar between un-sorted and sorted HPC-7s.

4.3.9 Intravital Micorscopy to Assess the Trafficking of HPC-7 Isolated Using Device C

4.3.9.1 More Free Flowing HPC-7s Harvested from the Inner Outlet Observed than from the Outer Outlet

HPC-7s were infused as a single dose at 30 minutes post-reperfusion. The numbers of freely flowing **Device C** separated inner outlet / deformable cells and outer outlet / rigid cells were highest at this point but for both cell types the numbers rapidly decreased at later observation times after administration (**Figure 4.12a**). However, immediately upon infusion, significantly ($p < 0.001$) more free flowing cells from the inner outlet cell population were observed passing through the mucosal microcirculation than from the outer outlet cell population. Indeed, the number of freely circulating cells from the inner outlet cell population counted at 30 minutes was almost double the number of freely circulating cells from the outer outlet cell population (**Figure 4.13 a - b**). This number is most likely an underestimation of actual trafficking cells as many had a velocity too high to allow them to be counted. This difference decreased with time until there was no significant difference between the cells from the two outlets at the end of the observation period. However, at all time points, HPC-7s could still be observed trafficking through the mucosal microcirculation, thus demonstrating that there were always cells able to continually re-circulate through the injured gut.

4.3.9.2 Adhesion of HPC-7s Harvested from the Inner and Outer Outlets was not Different

The numbers of firmly adhesion HPC-7 cells were also counted in the same field of view every 5 minutes. There was a general trend to observe more HPC-7s (that had been harvested from inner outlet of **Device C** and were more deformable) adherent within the mucosal microcirculation, particularly within 24 - 65 minutes post-reperfusion (**Figures 4.12b** and **4.13c-d**). However, this did not attain statistical significance when compared to outer outlet/more rigid cells.

4.3.9.3 Presence of HPC-7s Harvested from the Inner and Outer Outlets was not Different in the Lungs

After the endof the intravital experiment, the lungs were removed and four fields of view were randomly selected and imaged for HPC-7 presence. The mean numbers of HPC-7s present in the lungs were 44.5 ± 2.9 and 47.8 ± 3.1 for the cells from inner and outer outlet groups respectively separated by **Device C**, which were not significantly different (**Figure 4.14**). It should be noted that since this quantification was conducted on static tissue from culled mice, it was not possible to state whether the counted cells were actively adherent, trapped or trafficking through at the time of tissue imaging.

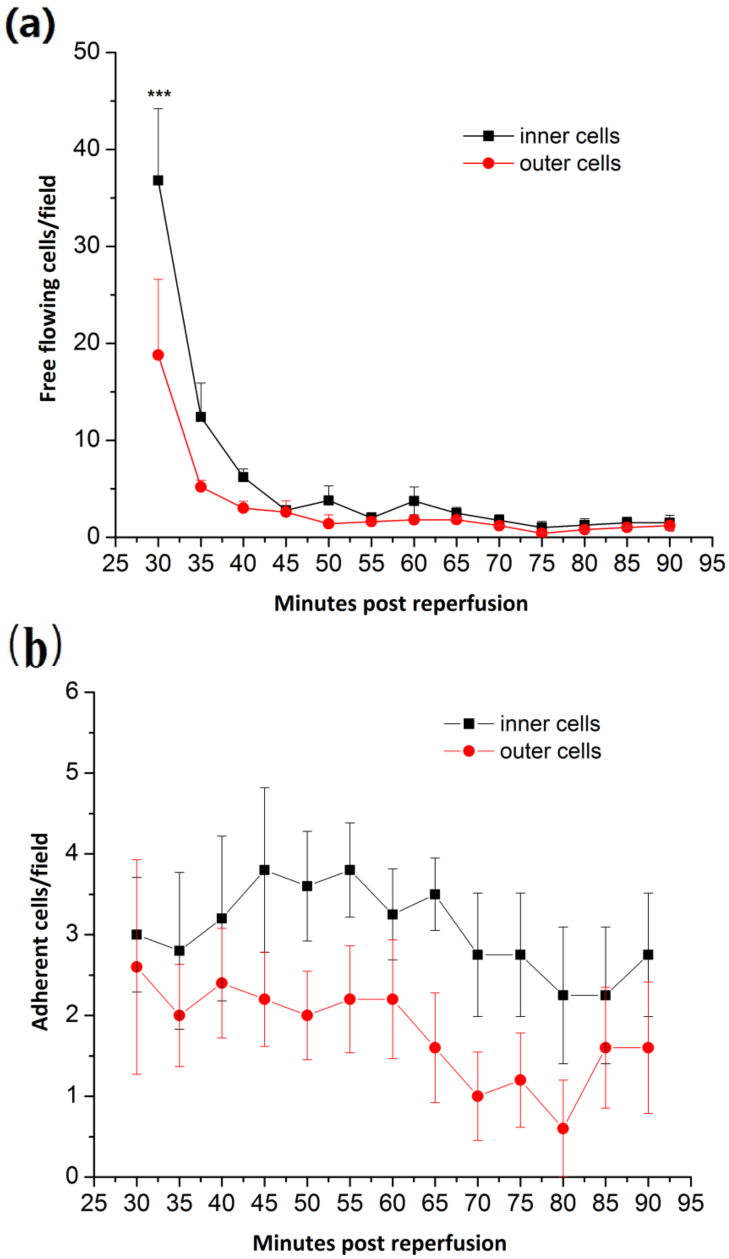

Figure 4.12. Changes of free flowing and adherent HPC-7 cells in IR injured colon over time. (a) At the point of infusion, more HPC-7s from the inner outlet of the spiral channel were observed to pass through the IR injured colon than those from the outer outlet, but their difference was not significant at the end of observation. (b) There was no significant difference in adhesion of HPC-7s between the two isolated groups. Results are presented as mean ± SEM (n = 5) and *** $p < 0.001$.

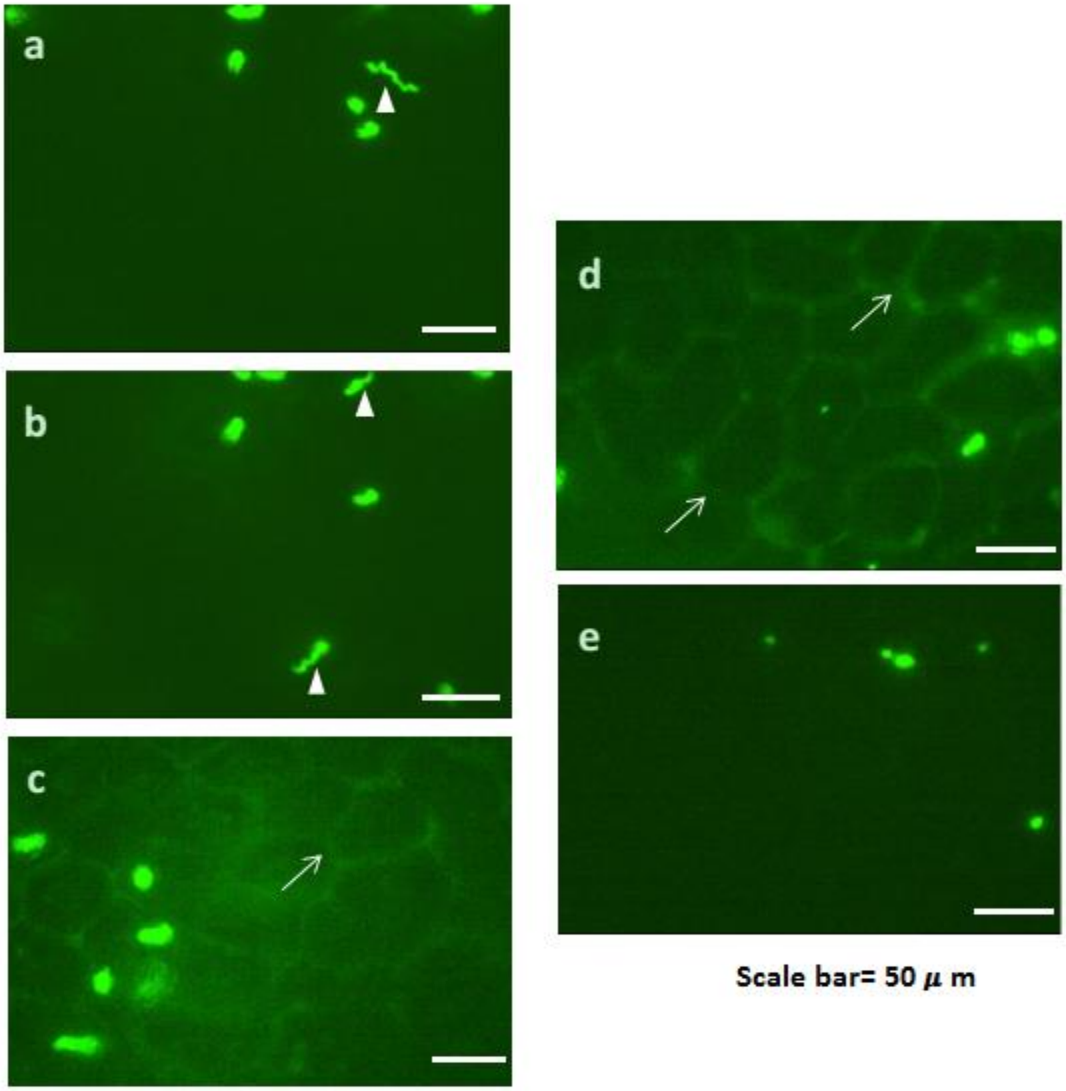

Figure 4.13. Intravital microscopy images of fluorescent CFSE-labelled HPC-7 cells either freely circulating or adherent within IR injured murine small intestinal mucosal villi. Numbers of **(a-b)** freely flowing HPC-7s harvested from the inner outlet of **Device C** trafficking through the mucosal microcirculation was significantly ($p < 0.001$) higher than the numbers of **(c)** freely flowing cells from outer outlet. The velocity of some circulating HPC-7s was very high and thus resulted in them appearing as streaks in the gut mucosal microcirculation (arrowheads). It appears in theses static images as if there are similar numbers of free flowing cells from the inner and outer outlet sources. However, over a continuous recording period of 1 minute more circulating cells would have been quantitated in dynamic videos. The numbers actually quantitated is most likely an underestimation due to the velcocity of many trafficking cells being too high to enable individual cells to be counted. Numbers of **(d)** adherent HPC-7s from the inner outlet within the mucosal microcirculation was not significantly different from those of **(e)** adherent cells from the outer outlet. In some images the outline of mucosal vilous capillaries can be seen (arrows).

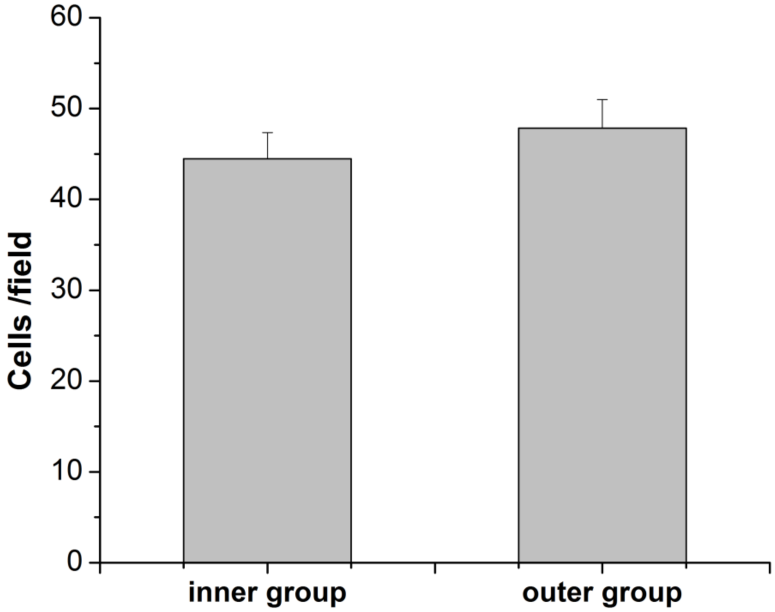

Figure 4.14. The number of cells present with lungs removed from mice undergoing intestinal IR injury was similar between the sub-poulations tested. Since this quantification was conducted on static tissue from culled mice, it was not possible to state whether the counted cells were actively adherent, trapped or trafficking through at the time of tissue imaging. Results are presented as mean ± SEM (n = 5) and after performing a Student-test, no significant difference was observed.

4.4 Discussion

In this chapter, straight and curved microchannels with different geometries were utilized to separate sub-populations of smaller and/or more deformable HPC-7s for future use in *in vivo* studies. To attain the most efficient separation, five microfluidic devices with different designs were fabricated and the effects of Reynold's number (Re), aspect ratio (AR) and curvature ratio (θ) were investigated. The underlying mechanisms by which size and deformability-based cell separation was achieved will be discussed. In order to isolate cells based on their varying deformability, it was firstly demonstrated that a heterogenous population of cells existed even in an immortalised cell line of HSCs. Therefore a sample of ~ 200 individual HPC-7 cells were tested with regards to their size and nominal rupture stress. Although the size variation was not large (6 – 12 μm), the stiffness of cells varied greatly. Nominal rupture stress values between 2 – 64 kPa were obtained which fitted a normal Gaussian distribution. This broad range clearly underscores the need to identify microfluidic isolation methods that can enrich for a more homogenous sub-population of more deformable cells.

4.4.1 Separation of HSCs Using Straight Channels

Two **straight** rectangular microchannels which had a curvature ratio of 0 and varying height, width, AR and Re, were mechanically tested. Generally, rectangular microchannels are more widely employed in cell focusing and separation methods than square or circular channels as they appear to more effectively separate particles (Liu *et al.,* 2015). Results demonstrated that the focusing of cells in straight microchannels behaved in a very complex manner. In **Device A**, cells harvested from the two side outlets and the centre outlet did not show any significant difference in their nominal rupture stress or size, regardless of changing the flow rate. This therefore resulted in no effective separation of HSCs based on the mechanical properties. However, in **Device B**, increasing the flow rate resulted in the migration of the more rigid cells, with higher nominal rupture stress, away from the channel walls, towards the channel centre hence increasing their collection from the centre outlet. Conversely, the side outlets primarily collected softer or more deformable cells with lower noiminal rupture stresses. In this respect, **Device B** is generally a good microchannel device for separating HSCs for subsequent use *in vivo*.

These differential cell focusing behaviours in straight channels could be explained by taking into account the two competing 'lift forces' (F_L) acting on the cells perpendicular to the direction of Poiseuille flow: the shear-gradient lift force (F_{LS}) directing cells to the channel walls and the wall-induced lift force (F_{LW}) moving cells in the direction of the channel centreline (**see Figure 4.15**). It is accepted that both of the two forces increase with increasing flow rate or Re (Asmolov, 1999, Gossett *et al.,* 2012). In **Device A** with a smaller aspect ratio (AR=5), as the flow rate is increased, the F_{LS} may increase more greatly than the F_{LW}. As the F_{LS} becomes more dominant, it consequently leads to more cells moving towards the channel wall (**Figure 4.4**). This was indeed observed as the number of cells being collected from the centre outlet decreased with increased flow rate. The net F_L is also proportional to the cell size. For bigger cells, the magnitude of the net F_L grows faster with the flow rate. Therefore, smaller cells move more slowly than the bigger ones and become entrained near the centreline of the channel. Interestingly, no difference in the size of cells was observed from the side or centre outlets with either **Device A** or **B,** but this may be due to the small variation in HPC-7 size.

Cells are not solid or rigid structures but are deformable. This deformability will also induce additional lift forces. Similar to F_{LS} and F_{LW}, deformability-induced lift force ($F_{LDeformation}$) also acts perpendicular to flow (Zhang *et al.,* 2016). Therefore, theoretically for cells with *similar* diameter, the more deformable HSCs could be displaced by $F_{LDeformation}$ away from the migration direction of relatively rigid cells, resulting in them being directed to the channel centreline – similar to smaller cells (Zhang *et al.,* 2016). However, since no effective mechanical separation was observed with **Device A**, it is possible that the channel length was not sufficiently long enough to enable cell separation. Certainly in the case of devices with higher Re, the time for cells going through the channel was less than microchannel devices with lower *Re*.

Device B was wider but the height was also reduced leading to a larger aspect ratio compared to Device A (AR = 10). Therefore the velocity profile became flattened and the F_{LS} across the width of the channel would drop compared to **Device A** with its lower AR (5) at a given Re. With the increase of Re, the increase of F_{LW} might be stronger than the increase of F_{LS}. Consequently, it was observed in this device that more cells migrated to the channel centreline, with larger cells moving more abruptly than smaller cells (**Figure 4.15**). More importantly, more deformable cells were displaced towards the channel walls, and higher R_e induced more significant separation particularly at a flow rate of 10mL/h. Moreover, due to the greater difference between the changes of the two lift forces in **Device B**, the channel length was long enough for cells to be significantly separated (**Figure 4.15**). Overall, the ratio of the nominal rupture stress and the standard deviation suggested that higher flow rate yielded high sensitivity and specificity classification of more deformable population near the side walls of the channel.

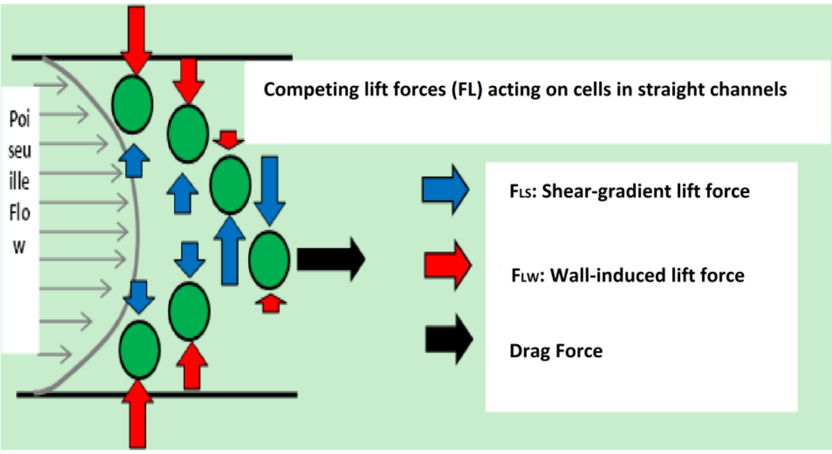

Figure 4.15. The inertial lift forces acting on particles flowing in a straight microchannel.

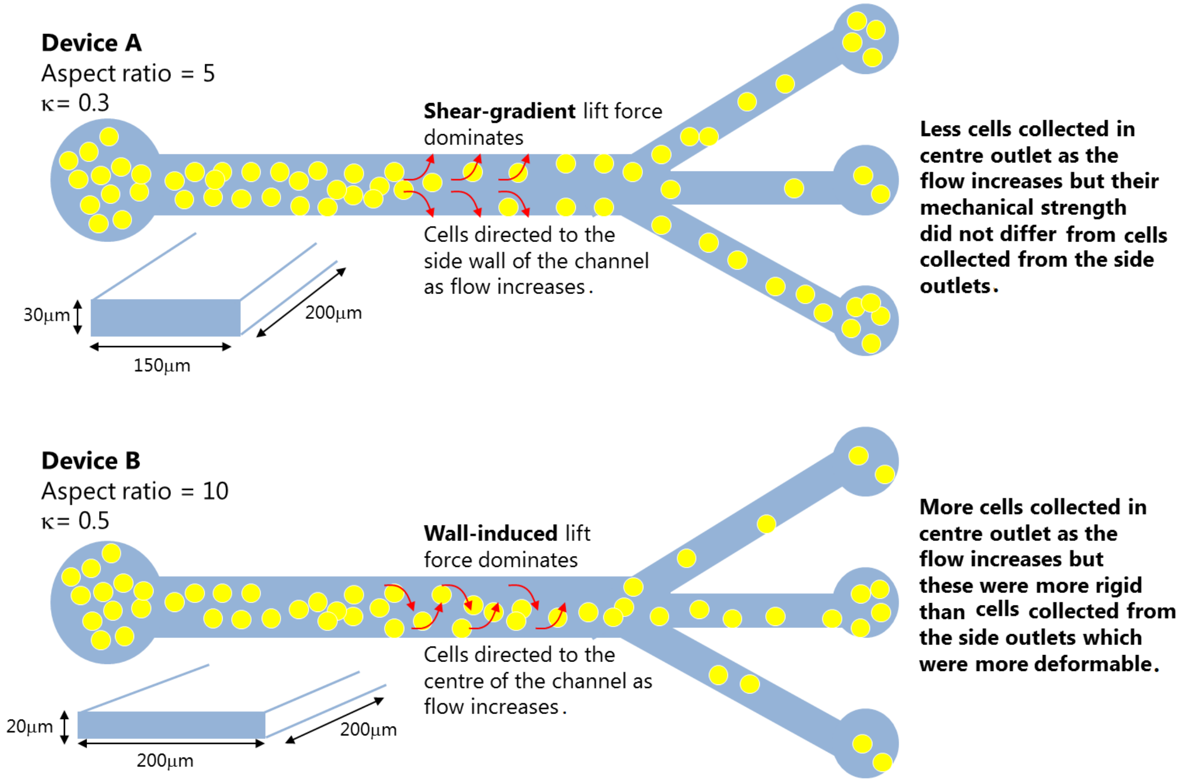

Figure 4.16. The effects of increasing flow rate on the movement of HSCs within the two STRAIGHT trifurcated microfluidic devices with varying aspect ratios. Since more cells were collected from the side outlets in **Device A**, it is likely that the increase in flow rate led to shear-gradient lift forces dominating which directed cells towards the sides of the channel. This resulted in more cells being harvested from the side outlets. However, with this device, no differences in the nominal rupture stress or cell size was observed when cells collecting in side and centre outlets were tested mechanically. Since more cells were collected from the centre outlet in **Device B**, it is likely that the increase in flow rate led to wall-induced lift forces dominating which directed cells towards the centreline of the channel. With this device, at high flow rates, the nominal rupture stress of cells in the side outlets was significantly reduced indicating these cells were softer/more deformable than those in the centre outlet when tested mechanically. No significant differences in the cell size was observed.

For the smaller κ (0.3; blockage ratio) in **Device A**, the number of stable equilibrium positions might have increased at the short walls (height direction), cells would have migrated in a more complex manner and the difference between subsets became narrower than that in **Device B** (κ = 0.5). This is in accordance with the very recent study of the effect of AR, Re and κ on particle migration in rectangular channels (Liu *et al.*, 2015).

4.4.2 Separation of HSCs Using Spiral Channels

For curved channels, similar trends in cell number and nominal rupture stress distribution were observed in the three channels with different curvature ratios (**Device C,** θ = 0.0044; **Device D,** θ = 0.0063; **Device E,** θ = 0.0079). Firstly, it was observed that most cells were dragged towards the outer wall of the channel when the flow rate was 0.5mL/h (Re =1.78) or less. Alternatively, it could be said that at the highest flow rates of 15mL/h or when R_e was the highest, all cells were dragged to the inner wall and hence collected from the inner outlet of the spiral devices. This suggests that when the R_e was very small or very large, there was a loss of separation efficiency. Thus intermediate flow rates were chosen for further experiments. This shifting of cells to the inner half of the channel was most likely the result of competition between F_L and a secondary force called Dean's drag force (F_D). In the intermediate flow rates, more effective separation was achieved at relatively faster flow rates. The separation efficiency under the optimized parameters of each channel was slightly different in terms of the mean values and CV of cell diameter and σ_R, and their throughput, as summarized in **Table 4.3**. Of all the devices tested, **Device C** was able to separate cells of interest i.e. those with low nominal ruptures stress and hence high deformability, with higher efficiency at a flow rate of 10 mL/h, and can be desirable for subsequent *in vivo* studies.

Though the exact mechanism responsible for cell sorting in curved channels is still unclear and requires further investigations, some hypothesis based on experiments and simulation have been proposed and could help improve our understanding of the cell migration (Gossett and Carlo, 2009, Martel and Toner, 2012, Guan *et al.,* 2013). When fluid flows through a curved channel, a secondary flow called Dean drag, centrifugal or vortex flow (F_D) arises due to the velocity mismatch in the downstream direction between fluid in the central and near-wall regions. In curved channels, Dean drag follows the underlying secondary velocity field. It is characterised by two counter-rotating vortices in the height direction and perpendicular to the primary flow direction. As such, flow is directed outwards near the channel centre and inwards near the up and bottom walls (Hille *et al.,* 1985). In addition to adding Dean drag force, the curvature can also change the F_{LS} through redistributing the velocity profile which can change the vertical position of particles. This redistribution becomes significant with the increase of θ values (De Vriend, 1981).

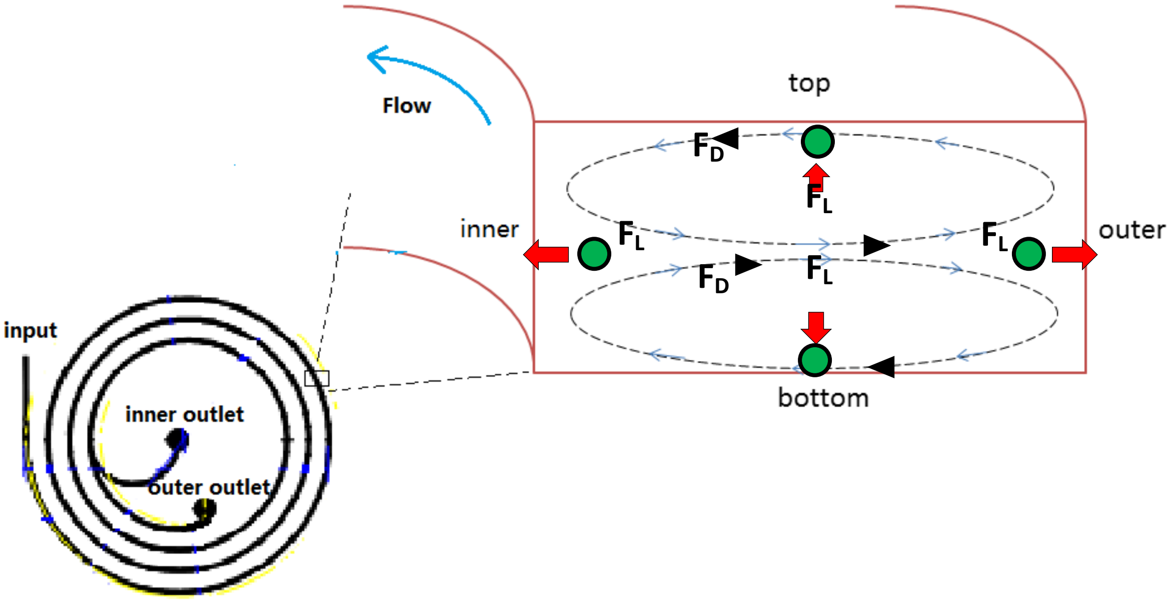

Figure 4.17. Schematic illustrating how spiral microfluidic devices exhibit Dean flow (F_D) in addition to the net lift forces (F_L). These secondary Dean flows (dotted arrowed lines) arise in curved channels in the height direction and are characterised as two counter-rotating vortices. A combination of lift (F_L) and Deans forces (F_D) creates different equilibrium positions within the devices from those observed in straight channels.

Based on this hypothesis, the cell migration in one spiral channel at varying flow rate is discussed here. The F_{LS} in the height direction in the inner half of the channel decreases compared to the parabolic profile in the $\theta = 0$ case, and F_{LW} or wall-induced inertial becomes more dominant which allows cells to take vertical equilibrium positions near the channel centre (Martel and Toner, 2013). By crossing the vertical position, the bigger and/or rigid cells move faster towards the centre and experience a switch in the direction of Dean flow, moving outwards of the channel. Smaller and/or more deformable cells near top or bottom walls move inwards, thus separation can be achieved. Indeed, this was observed for all the three spiral devices whereby smaller cells with lower nominal rupture stresses (deformable) were harvested from the inner outlets and larger cells with larger nominal rupture stresses (rigid) were collected from the outer outlets. This separation was observed to be significant at higher flow rates.

The F_L and F_D act as counter balancing forces, and a ratio of $R_f = F_L/F_D = a^2\mathrm{R}/H^3 f(R_{e,}\ x/w\,, y/h, h/w)$ can be used to predict the particle behavior: $R_f \rightarrow 0$, secondary flow plays the dominate role, and particles remain entrained in it, and $R_f \rightarrow \infty$, for sufficiently high flow rate, particles would focus to inertial focusing equilibrium positions independent of the secondary flow (Hasabnis, 2015). With the increasing Re, the shear gradient becomes high enough to counter F_D and so more cells tend to move away from the channel centre and are directed towards the inner half. Eventually, all the cells were dragged inwards. This proposed hypothesis can explain the behaviors of cell migration with the increase of flow rate in each spiral device.

The mechanism that can lead to 100% cell migration to the outer half of the channel at lower flow rate could be due to the density mismatch between the cells and fluid as proposed by Amini and colleagues (Amini *et al.,* 2014). In this regime, the fluid inertia becomes less significant because the R_e is close to 0 ($Re \leq 1.78$) due to low flow velocity. If the fluid suddenly changes direction due to addition of curvature, the cells which have larger density than the fluid may continue for a time on a straight trajectory due to its inertia, resulting in focusing outwards. This relatively simple physical mechanism of particle migration in spiral channels can often be understood as an effect of centrifugal force due to density mismatch rather than Dean flow (Di Carlo *et al.,* 2007, Hou *et al*., 2013).

In this study, the nominal rupture stress of cells was calculated from the micromanipulation data, which took into account the initial cross-sectional area and diameter of the cells. It should be pointed out that the initial cross-sectional area may be different from the real contact area between the force probe or bottom substrate and cell at rupture, and the latter depends on the deformation at rupture. Micromanipulation results demonatrated that all the tested HPC-7 cells were ruptured at similar deformations (~ 80% - **See Section 3.3**). Moreover, at similar deformation, E is proportional to σ, thus the choice of using nominal rupture stress (σ_R) was valid to make comparisons between the mechanical properties of isolated sub-populations. The viability and mechanical strength of isolated HPC-7s indicate that the majority of cells (≥ 90%) survived the complex hydrodynamic force generated in the fluidic device, and the physical structures of cells were not affected during sorting in microchannels which is crucial to maintain cell viability. The microfluidic system is therefore able to isolate cells based on mechanical property variations without introducing any additional changes of the cells.

4.4.3 Intravital Studies

Previous *in vivo* studies have reported that the systemic infusion of stem cells did not yield a large number of cells reaching the organ of interest primarily due to the majority of cells being trapped in remote capillaries (Schrepfer *et al*., 2007, Gao *et al.,* 2001). Therefore, it was hypothesized that after systemic injection, the smaller and more deformable HPC-7 cells harvested from the spiral channel **Device C** would avoid non-specific entrapment and thus lead to increased numbers in the peripheral circulation. This would subsequently enhance cell numbers available for adhesion within injured tissues as they trafficked through it. To test this, the homing and adhesion of HPC-7s from the inner outlet of **Device C**, which were more deformable, was investigated in a mouse model of intestinal inflammatory injury. Results were compared to **Device C** harvested outer outlet/more rigid HPC-7s. This particular model of intestinal injury was used as inflammatory gut injuries such as Crohn's and colitis which are difficult to treat, with current treatment regimens rapidly losing effectiveness (Singh *et al.,* 2010, Lichtenstein *et al.,* 2009). Theoretically, it should be pointed that the comparison would have been performed between mixture HSCs and inner outlet HSCs, however, no significant difference in mechanical properties was observed between isolated HSCs and un-isolated HSCs (data not shown). Therefore, in this study, the clinical benefit of smaller and more deformable HSCs was investigated by comparing to the performance of larger and less deformable isolated cells. It was hypothesised that mechanical based isolation would not affect the biological properties of HSCs, especially their adhesion molecules which regulate cell recruitment, to make the comparison reasonable. Sub-populations from either inner or outer outlet that obtained significant mechanical difference were intravitally compared, Likewise, there are also difficulties in the treatment of acute intestinal inflammatory injuries such as IR injury. Ultimately, inefficient therapies occurred in both acute and chronic bowel injuries, and result in high morbidity rates. Thus, new, effective therapeutic options are needed. It has been suggested experimentally and clinically that HSCs are capable of directly repairing gastrointestinal tissue as well as combating the excessive immune responses triggered by these inflammatory injuries. Therefore, cellular therapy, especially HSC-based therapy, could offer this required alternative but only if their delivery to inflamed sites can be improved.

Intravital studies clearly demonstrated that the cells harvested from the inner outlet of **Device C** resulted in significantly more free flowing cells (almost double the number) passing through the intestine in a one minute period of continuous recording immediately upon infusion when compared to those from the outer outlet. The blood circulation time for a mouse is approximately 4-6 seconds (White *et al.,* 2013) which means the blood circulates about 10 times during the 1-minute visualisation period. Hence the injected HPC-7s would have passed around the body/lungs/gut etc. approximately 10 times during this period of recording. The higher number of free flowing HPC-7s from the inner outlet suggests they were able to reduce entrapment or adhesion in non-specific sites. These findings demonstrate that HPC-7s isolated from the inner outlet of the spiral microchannel do have advantages over those from the outer outlet due to their smaller size and less stiffness, which permits their better retention within the peripheral blood. However, this advantage only happens at the first few cycles of circulation after their infusion. Thereafter, cells from both groups were rapidly lost from the peripheral circulation.

Previous studies have shown that smaller microspheres (4 - 5 µm) can pass straight through the lungs while the majority of large stem cells such as MSCs (15 - 19 µm) are trapped in the pulmonary system (Schrepfer *et al.*, 2007). Similar observations were made by Fisccher and colleagues who demonstrated that the passage of bone marrow-derived mononuclear cells (7 µm) was 30-fold higher compared to MSCs (18 µm) (Fischer *et al.,* 2009). These significant differences in lung entrapment between MSCs and other blood cells is likely due to the considerable difference in their sizes. However, for HPC-7s, the mean cell diameter of isolated samples in this study were 9.1 ± 0.5 µm and 10.5 ± 0.4 µm. It is not anticipated that this degree of difference in size would be sufficient to result in a significant difference in the number of cells in circulation. Therefore, it is highly likely that the deformability differences between inner and outer outlet cells contributes to the increase in the number of free flowing cells in first minute observation. These novel results clearly highlight the critical impact HSC rigidity/softness has on their trafficking capabilities to injured tissues.

Although increased homing to and trafficking through the injured gut was observed, disappointingly, this did not result in significantly enhanced adhesion and thus intestinal retention. The absence of a significant difference in adhesion between the two isolated sub-populations of HSCs may be due to the fact that although more cells homed to the gut, they did not become activated on transit to actually adhere. HSC adhesion to endothelial cells lining microvessels is regulated by the interplay of a whole host of soluble inflammatory factors including cytokines and chemokines that activate both cell types to express adhesion molecules (Kumar and Ponnazhagan, 2007, White *et al.,* 2013). This adhesion cascade is very similar to that observed for inflammatory leukocytes. Recent evidence has shown that modulating the expression of adhesion molecules and/or activatory chemokines is able to enhance the adhesion of many types of stem cells including HSC and MSC recruitment (Kavanagh *et al.,* 2013). It was postulated that increasing the numbers of free flowing HPC-7s circulating through the gut using microfluidic systems combined with other cell pre-treatment strategies to activate surface adhesion molecules would be an effective dual strategy to enhance the efficiency of stem cell therapy.

Interestingly, this increased trafficking at 30 minutes post-reperfusion was despite the fact that the numbers of cells observed within the pulmonary microvasculature was not significantly different between the two groups. It could be that less cells became entrapped in sites other than the lungs and this would need to be investigated further. Certainly entrapment with the small diameter capillaries of the spleen is also routinely observed. It may be that the deformable cells have avoided physical entrapment in these sites rather than the pulmonary capillaries. Many studies, including those from the Kalia lab, have aimed to improve HSC homing and retention via over-expression of chemotactic factors or pre-conditioning of cells with inflammatory compounds, but interfering with their entrapment in these non-specific sites may provide the most significant therapeutic benefit.

It has also been tested whether a second flow of HPC-7s isolated from the inner outlet of the microchannel of **Device C** could purify a sub-population with even reduced size and stiffness. However, preliminary experiments (data not presented) suggested that after repeated use of the channel without cleaning, some cells accumulated near the downstream section, a place between the main channel and its branching into the two outlet channels, which disturbed the orientation of moving cells. Hence this strategy was not pursued further. Moreover, the re-circulation procedure would have prolonged the separation. Also the mechanical strength of cells may have been affected by the room temperature (25°C)at which the experiments were conducted as this is not the optimum temperature (37 °C) for keeping HSCs viable. Future study can try to perform the cell sorting using several devices in series connection or modify the geometries of the spiral channel.

4.5 Conclusions

Previous studies using microfluidic systems for cell sorting are mainly focused on separating target cell populations from heterogeneous samples of *different* cell types, such as isolating tumor cells from whole blood in curved channels (Sun *et al.*, 2013, Hou *et al.,* 2013, Warkiani *et al.*, 2014), enriching platelets in blood using asymmetrical serpentine microchannels (Di Carlo *et al.*, 2008), or classifying various cell types using size and deformability as markers in inertial microfluidics (Hur *et al.*, 2011). In these investigations, the mechanical differences between different cell types are generously very significant. This study applied the microfluidic systems to separate sub-populations from one cell type based on the intrinsic mechanical heterogeneity of individual cells in one cell population. This is a novel and challenging application which can provide prospects of developing new clinical and research instruments thus benefiting cellular therapy.

In this chapter, the separation efficiency of a number of different straight and spiral microfluidic devices to separate target HPC-7 cells in a label-free manner have been presented. The most effective, high throughout device was the spiral **Device C** which utilized both inertial and secondary Dean forces inside a curved geometry at a micro-level to separate rigid and more deformable cell sub-populations. The cell number, size and nominal rupture strength distribution within isolated sub-populations and throughput were used to determine the optimum channel geometry and flow conditions required to demonstrate highly efficient separation. For straight channels, the rectangular cross-section which is wider and lower (**Device B**; AR=10) is effective to isolate the HSC sub-population of interest. When curvature was added, there was a loss of separation efficiency at flow rates slower than 0.5 mL/h or faster than 15 mL/h. However, within intermediate flow rates, higher separation efficiency could be obtained in the spiral channel with a bigger AR at a relatively higher flow rate (**Device C**; 10 mL/h). It is anticipated that similar microfluidic systems could clinically benefit cell therapy and provide fundamental studies of label free cell separation from one single cell population. Importantly, these novel results indicate that regulating the mechanical properties of HSCs is one possible approach to enhance their recruitment efficiency, but future studies would need to focus on combining different strategies together, such as chemical, molecular and mechanical manipulations, to benefit cellular therapy.

Chapter 5

Biomechanical Properties of Human T Cells

5.1 Introduction

In the previous chapters, the work presented has focused on characterising the mechanical properties of stem cells, and determining whether they can be sorted into specific sub-populations using microfluidic devices for therapeutic purposes. The use of stem cell-based therapies has clearly increased for a variety of different inflammatory, ischemic and degenerative disorders. However, the use of cells other than stem cells, particularly the host’s immune cells, have also witnessed tremendous growth and enthusiasm in the past two decades. In particular, the use of adoptive antigen (Ag)-specific T cell immunotherapies for the treatment of chronic viral infections and cancers has received significant interest (Klebanoff *et al.,* 2012). This approach involves the isolating disease-fighting T cells from a cancer or infected patient, expanding and possible engineering them *in vitro* and then infusing them back into the patient's body for attacking the cancer / virus. Hence adoptive cellular therapy uses the body’s own T cells to boost its immune system to target disease. With the recent breakthrough in utilising T cells expressing the CD19-specific chimeric antigen receptor (CAR) for the treatment of B cell acute lymphoblastic leukaemia (Davila *et al.,* 2014), selection of Ag-specific cells could also become a key purification step in the *in vitro* expansion of immunoreceptor engineered cells.

Current immunomagnetic selection systems utilize antibody or ligand-recognition of unique phenotypic markers on the T cell surface to separate them. However, there are limitations to these methods with regards to the loss of low frequency cells through multiple processing steps such as washes and sub-optimal purity and recovery from the selection itself, and not least, the costs of the specialized GMP reagents. An alternate approach to immunomagnetic isolation, is to select cells using clinical grade fluorescence-activated cell sorting (FACS) (Cepok *et al.*, 2005, Kodituwakku *et al.*, 2003, Sung *et al.,* 2008). Though highly sensitive and specific, FACS sorting of rare cells (< 1%) to therapeutic quantities, is time consuming and associated with the risk of reduced cell viability (Wulff *et al.,* 2006).

In the previous chapters, it has been demonstrated that microfluidic cell sorting systems can be used to isolate cells based on their size and stiffness. Studies reporting cell sorting based on size or stiffness also demonstrate the potential applications of the microfluidic cell sorting technique for separating tumour cells, erythrocytes as well as activated Ag-specific T cells (Chwee Teck Lim, 2014, Hou *et al.,* 2010, Hur *et al.,* 2011, Preira *et al.,* 2013). It should therefore be possible to use natural or induced variations in biomechanical properties to separate activated lymphocytes from non-activated lymphocytes and other cell types. However, before we can utilise microfluidic assays to separate lymphocytes for clinical therapeutic purposes, a precise study of their biomechanical properties is needed. Circulating lymphocytes experience significant repeated hydrodynamic and mechanical stresses in blood vessels, which are applied along their entirety leading to large deformations in the microcirculation. These are particularly seen following lymphocyte activation when they transmigrate out of blood vessels into the surrounding interstitial tissue. Therefore, it is important to understand the mechanical properties of lymphocytes under large, as well as small, deformations.

The micromanipulation technique was therefore used to measure the temporal biomechanical changes of T cells following Ag-induced stimulation. Moreover, the studies were conducted on live cells rather than fixed cells. The mechanical strength parameters such as rupture force, rupture deformation and nominal rupture stress / tension for resting (unactivated) and activated T cells compressed to rupture were determined. The data of T cells reversibly compressed to smaller deformations were modelled to obtain a measure of the elasticity, defined as the Young’s modulus, of the whole cell. This work provides important new data on the biomechanics of activated T cells which can be used for future development of microfluidic separation of cells that have selectively responded to specific antigen stimulation. The results from this chapter have been published as an original manuscript (Du *et al.,* 2016).

5.2 Methods

5.2.1 Isolation, Culture and *in vitro* Activation of T Lymphocytes

Peripheral blood was collected from three healthy drug-free human donors after informed consent, and untouched CD8+ T cells were isolated by negative immunomagnetic selection as described in detail in **Section 2.2.6**. Some cells were activated by culturing in the presence of 30 ng/mL anti-CD3 antibody OKT3. For control samples, the non-activated CD8+ T cells were cultured in the medium for up to 4 days. All the cell samples were mechanically tested on Day 0, Day 2 and Day 4.

5.2.2 Diametric Compression with Micromanipulation Technique

The mechanical properties of resting or unactivated T cells were measured either immediately after harvesting (day 0) or tested 2 days or 4 days post-activation. Cells were diluted with PBS to reduce cell density in suspension and mechanical testing was completed within 3 hours using micromanipulation. Suspended single cells were allowed to settle to the bottom of the chamber, and images were captured with a side-view high-speed digital camera. A probe with a 25 μm diameter, connected to a force transducer, was driven down by a stepping motor towards the single cells at a probe speed of 2 μm/s in order to collect the data of instantaneous force imposed on single cells at a frequency of 50 Hz.

5.2.3 Determination of Activation-related Changes in Cell Size

The diameter of CD8+ T cells was directly measured from the screen of a TV monitor which was connected with the side view camera on the micromanipulation rig. The cell size was also evaluated by flow cytometry. Enriched T cells from different samples were stained with anti CD3/PE and 7AAD (BD). The forward scatter (FSC-A) value of the 7AAD-/CD3+ cells was recorded using the FacsCanto II flow cytometer (BD, San Jose, CA, USA).

5.2.4 Determination of Mechanical Property Parameters

Briefly, 20 single cells from each of the 3 donor samples were selected randomly and compressed to large deformations until they were ruptured. The force (μN) imposed on the cell was plotted against the distance (μm) the probe moved towards the glass chamber until the cell was ruptured (force versus displacement). These graphs were then used to determine the mean rupture force and the percentage (%) deformation at rupture for resting and activated cells. Two additional parameters, which took into account the actual size of the tested cells and allowed meaningful comparisons between groups to be made, were also determined using relevant calculation equations, namely nominal rupture stress (σ_R) and nominal rupture tension (T_R). The Hertz model was involved to calculate the Young's Modulus of T cells at small deformations as described in Chapter 3.

5.2.5 Statistical Analysis

Values for the mechanical property parameters of the lymphocytes were presented as mean ± standard error. Paired Student t-tests were conducted to determine significant differences among the mechanical properties of different samples, with statistical significance reported at the 95% confidence level ($p<0.05$).

5.3 Results

5.3.1 Activation of CD8+ T Lymphocytes Increases their Cell Size

The diameter of resting CD8+ T cells (day 0) was 6.1 ± 0.6 μm as determined using micromanipulation. This increased significantly ($p < 0.05$) upon activation to 9.7 ± 1.1 μm on day 2 post-activation and remained significantly ($p < 0.05$) greater on day 4 post-activation when compared to resting cell values (**Figure 5.1a**). There was no significant difference between the activated samples at day 2 and day 4 post-activation. Changes in cell diameter are also shown by the data generated using flow cytometry (**Figure 5.1b**). The FSC-A values of resting T cells are again significantly greater on day 2 ($p<0.05$) and day 4 post-activation ($p<0.05$). Interestingly, it was noted that CD8+ T cells that had been activated and tested on day 2 post-activation tended to 'stick' to the force transducer probe, possibly indicating some change in their adhesive nature in the early stages of activation.

5.3.2 Compression Curves of T lymphocytes to Rupture

Micromanipulation studies demonstrated that the individual CD8+ T cells tested in the same sample were heterogeneous in their diameter and their force versus displacement curves even for single cells of same diameter. However, all tested single cells showed common characteristics in their compression curves. Typical curves showing the relationship between the force and displacement during continuous diametrical compression of a single lymphocyte to rupture at day 0, 2 and 4 days post-activation are shown (**Figures 5.2 a-c**). At point A, the probe started to touch the cell, and the resistant force increased until point B where the cell ruptured. As a result of rupture, the force decreased rapidly to point C, followed by curve CD where the force increased continuously which represents the compression of cell debris until the probe touched bottom of the glass chamber.

5.3.3 Rupture Force Increases at 4 days Post-activation

The mean cell rupture force (μN) was determined from the force vs displacement curves (y-axis value at point B). The rupture force was similar between the resting (day 0) and activated cells at 2 days post-activation with mean values of 2.3 ± 0.8 μN and 2.6 ± 0.9 μN respectively. However, when activated cells were analyzed at 4 days, the rupture force significantly ($p < 0.05$) increased to 4.6 ± 1.6 μN ($p < 0.05$) when compared to resting cells (**Figure 5.3a**). The % rupture deformations of resting T lymphocytes and activated lymphocytes at 2 and 4 days post-activation were not significantly different with mean values of 78.3 ± 1.3%, 79.7 ± 1.6% and 77.5 ± 1.5% obtained respectively (**Figure 5.3b**).

5.3.4 Nominal rupture stress / tension Decreases at 2 days Post-activation

The nominal rupture tension significantly ($p < 0.05$) decreased from 0.58 ± 0.07 N/m for resting cells to 0.45 ± 0.07 N/m for cells at 2 days post-activation. This increased to 0.62 ± 0.10 N/m on day 4 post-activation, a value not significantly different from resting cells (**Figure 5.4**). A similar pattern was observed for nominal rupture stress (**Figure 5.4**).

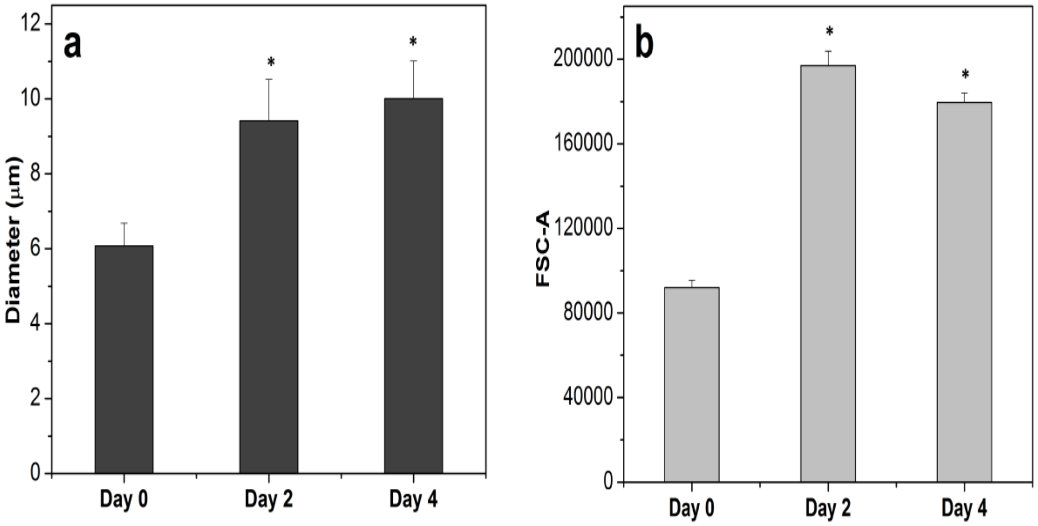

Figure 5.1. Diameter changes of T lymphocytes in the process of activation. Changes in the diameter of T cells was quantitated using **(a)** direct measurement of a microscopy image generated using the side-view camera on the micromanipulator and **(b)** flow cytometry. Both methods showed a similar significant increase in cell diameter as a result of T cell activation. 20 single cells were randomly selected in each sample, experiments were repeated from 3 donors. * $p < 0.05$ as determined using a paired Student t-test.

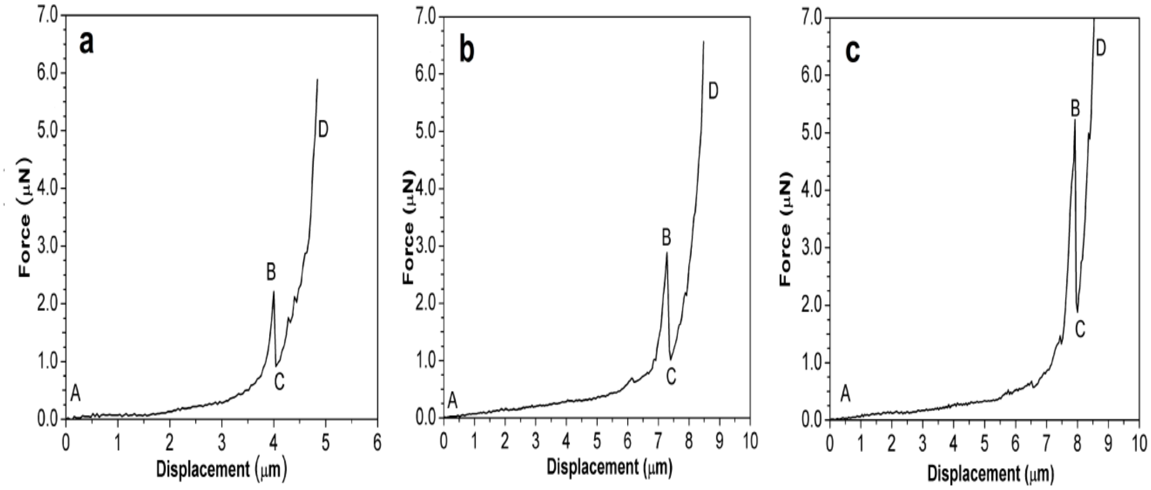

Figure 5.2. Typical force-displacement curves for T lymphocytes. Typical force-displacement curves obtained at a compression speed of 2μm/s for T cells to rupture on **(a)** day 0 prior to activation (resting cells) **(b)** day 2 post-activation and **(c)** day 4 post-activation. At point A, the probe touched the cell and the resistant force increased until point B where the cell ruptured. Rupture resulted in the force decreasing rapidly to point C, followed by curve CD where force increased until the probe touched bottom of the glass chamber. 20 single cells were randomly selected in each sample, experiments were repeated from 3 donors. *$p < 0.05$ as determined using a paired Student t-test.

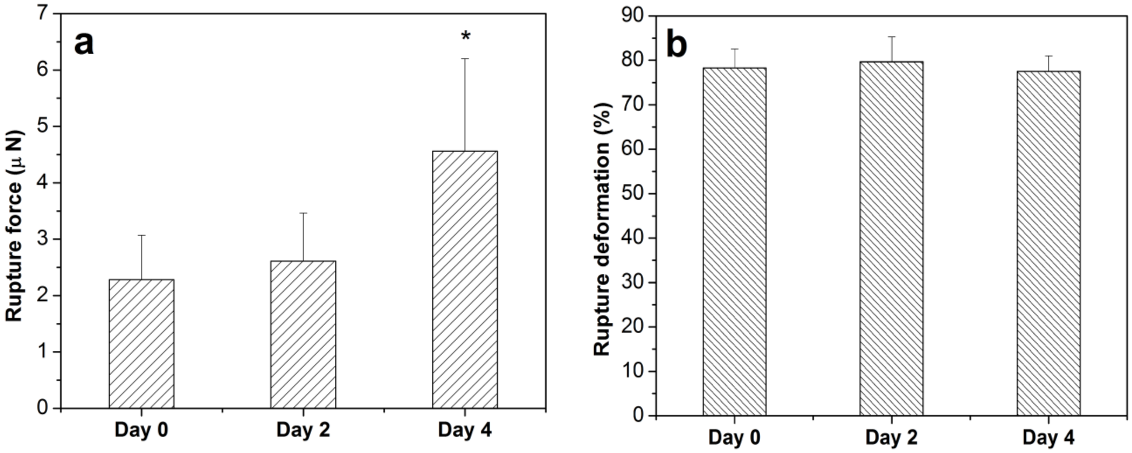

Figure 5.3. Rupture parameters of T lymphocytes in the process of activation. The **(a)** mean rupture force and **(b)** mean rupture deformation of T cells on day 0 prior to activation (resting cells), day 2 post-activation and day 4 post-activation. The force required to rupture cells was larger for activated cells at 4 days post-activation. All cells were ruptured when they reached a % deformation close to 80%. 20 single cells were randomly selected in each sample, experiments were repeated from 3 donors. *$p < 0.05$ as determined using a paired Student t-test.

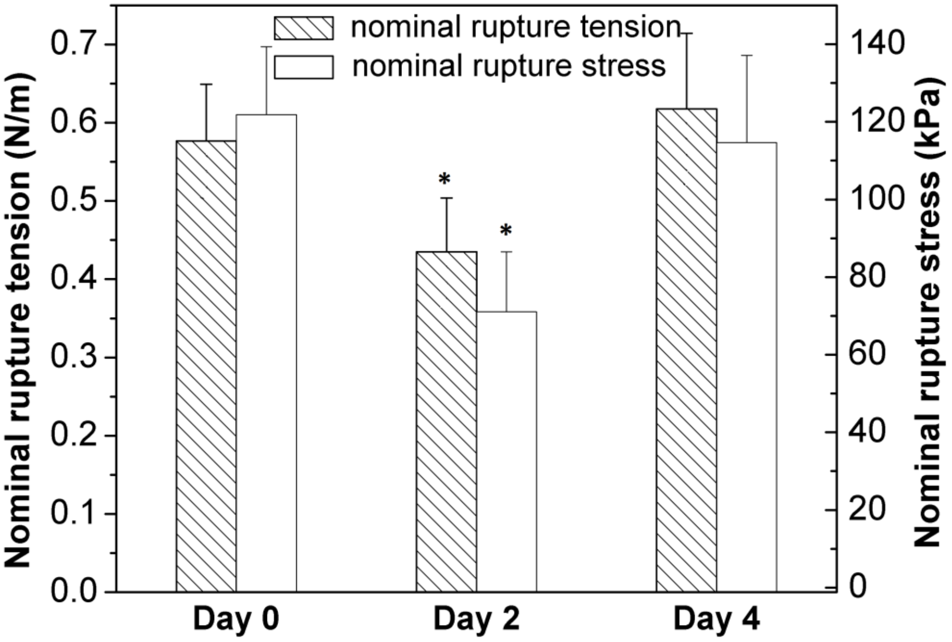

Figure 5.4. Changes of mechanical strength of T lymphocytes in the process of activation. The nominal rupture tension and nominal rupture stress of T cells on day 0 prior to activation (resting cells), day 2 post-activation and day 4 post-activation. Both values significantly decreased for cells at 2 days post-activation. 20 single cells were randomly selected in each sample, experiments were repeated from 3 donors. $^*p < 0.05$ as determined using a paired Student t-test.

5.3.5 Young's Modulus Decreases in Activated CD8+ T Lymphocytes

The Young's modulus was calculated from data obtained corresponding to small deformations of T cells. Typical force versus displacement data with a linear fit based on the Hertz model for cells at day 0, 2 and 4 days post-activation are shown (**Figures 5.5 a-c**). Mean correlation coefficient values of 0.84 ± 0.05, 0.85 ± 0.04 and 0.85 ± 0.06 were obtained for resting cells at day 0 and cells at 2 days post-activation and 4 days post-activation respectively. The values of Young's modulus decreased significantly at both 2 days post-activation ($p < 0.05$) and 4 days post-activation ($p < 0.05$) when compared to resting cells at day 0 (**Figure 5.5d**). Actual calculated mean values for the Young's modulus were 58.0 ± 6.3 kPa, 43.7± 5.0 kPa, and 43.0± 6.3 kPa for T lymphocytes at day 0, day 2 post-activation and day 4 post-activation respectively. There was no significant difference in the mean Young's modulus between T cells activated for 2 days and 4 days ($p > 0.05$).

5.3.6 No Change in the Mechanical Properties of Non-activated CD8+ T Lymphocytes for up to 4 days

The diameter of non-activated T cells did not change significantly upon incubation on day 2 and day 4 when cultured in the medium (**Figure 5.6a**). There was also no significant difference in the nominal rupture tension/stress between the resting samples, as shown in **Figure 5.6b**.

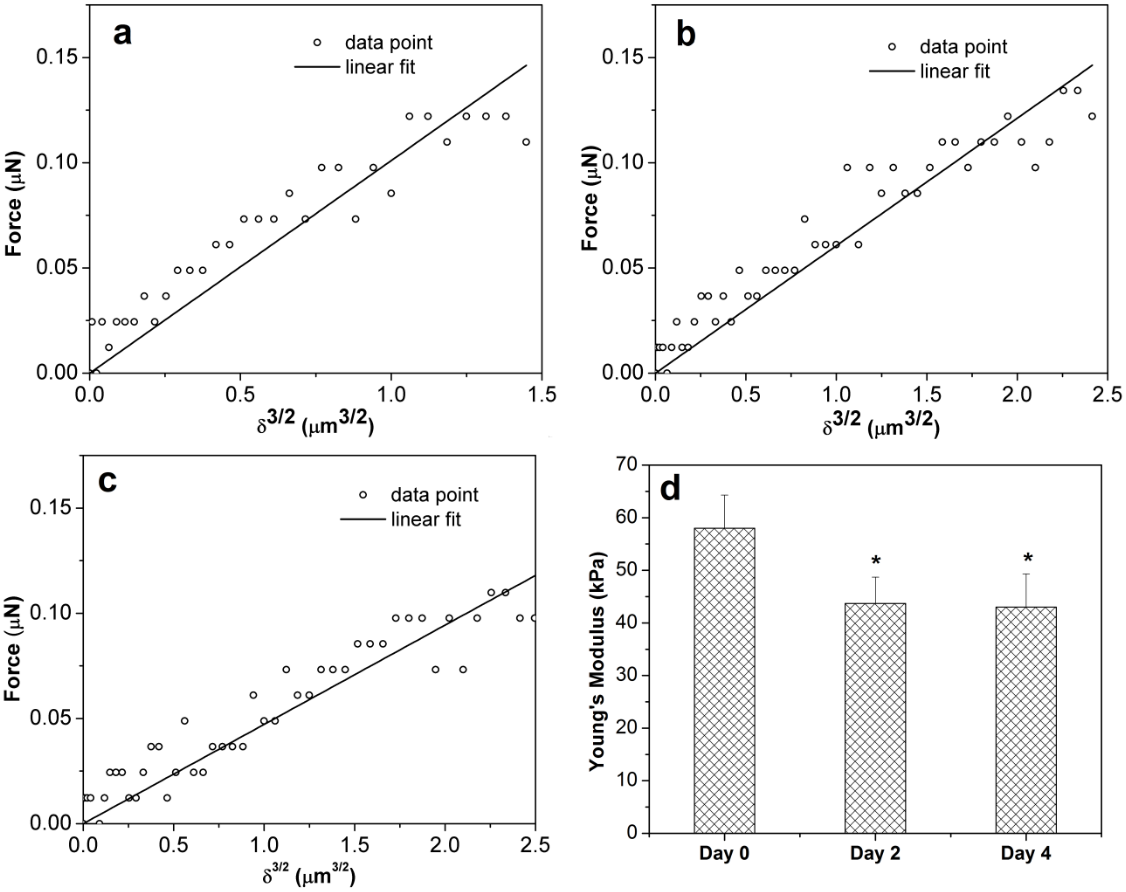

Figure 5.5. Force-displacement data fitted with Hertz model. The typical linear fit (line) of the Hertz model to the obtained force-displacement data (o) for T cells compressed to small deformations on **(a)** day 0 prior to activation (resting cells) **(b)** day 2 post-activation and **(c)** day 4 post-activation. The mean values of the correlation coefficient are 0.84 ± 0.05, 0.85 ± 0.04 and 0.85 ± 0.06 respectively with an overall range of 0.7 to 0.9. **(d)** The Young's modulus was calculated from these data, which decreased significantly as a results of activation. 20 single cells were randomly selected in each sample, experiments were repeated from 3 donors. *$p < 0.05$ as determined using a paired Student t-test.

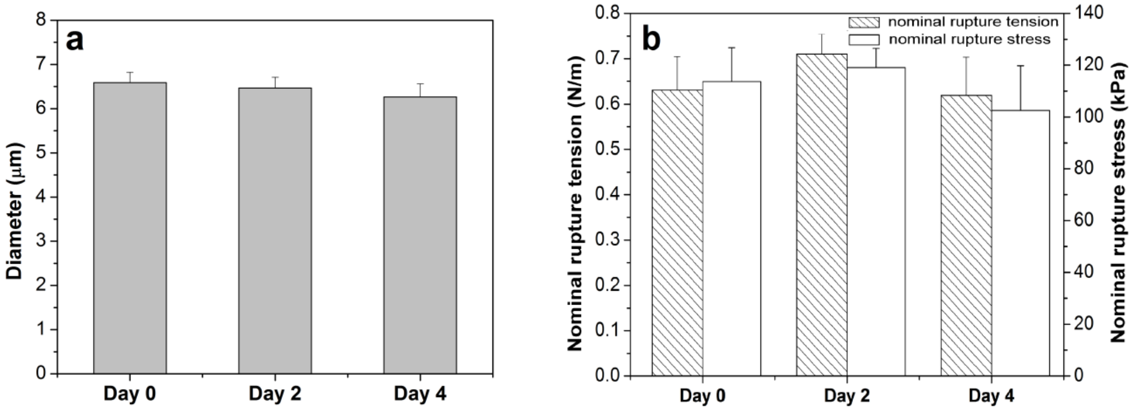

Figure 5.6. Mechanical properties of non-activated T lymphocytes in the process of incubation. No significant changes in the diameter **(a)** and mechanical strength **(b)** of T cells when they were not activated and were maintained in medium for up to 4 days. 20 single cells were randomly selected in each sample, experiments were repeated from 3 donors.

Table 5.1. Summary of the changes in the mechanical properties of human T lymphocytes at 2 days and 4 days post-activation. An increase in cell volume was observed as a result of activation at both 2 and 4 days post-activation. Rupture force increased at day 4 but no changes in ruptre deformation was observed. Rupture stress/tension decreased at 2 days post-activation indicating decreased mechanical strength which increased at dat 4. The Young's modulus at small deformations (up to 10%), decreased at both 2 and 4 days post-activation suggesting the cells became and remained flexible.

All values compared to resting cells	**Cell size**	**Rupture force**	**% Rupture deformation**	**Rupture stress and tension**	**Young's modulus**
2 days post-activation	↑	–	–	↓	↓
4 days post-activation	↑	↑	–	–	↓

5.4 Discussion

This novel study analysed the biomechanical properties of live lymphocytes undergoing activation using a micromanipulation technique, without the need for fixing the cells. An increase in cell volume was observed as a result of activation at both 2 and 4 days post-activation. An initial fall in whole cell mechanical strength was observed at 2 days post-activation as indicated by the decreased rupture stress/tension values. Thereafter, although lymphocytes remained bigger, they regained their mechanical strength at day 4 post-activation, possibly reflecting the tailing off of activation and cellular recovery. However, the Young's modulus at small deformations (up to 10%), decreased at both 2 and 4 days post-activation suggesting the cells became and remained flexible. This is the first time, to my best knowledge, that a micromanipulation technique has been used to directly analyze the biomechanical properties including rupture strength of human T cells at various time points post-activation. A summary of the data obtained is provided in **Table 5.1**.

Rupture forces can be used as an important parameter to compare the mechanical strength of cells. Although all cells ruptured when their compressive displacement reached almost 80% of their original diameter, activated lymphocytes were larger than unactivated cells, as demonstrated by both micromanipulation and flow cytometry techniques. Increases in CD8+ T cell size at similar time points have previously been described microscopically post-OKT3 activation (Wu *et al.*, 2009, Teague *et al.,* 1993) and occurs so that activated lymphocytes can duplicate their contents and divide. The rupture force for activated cells at 4 days post-activation was significantly greater than resting and activated cells at 2 days post-activation. At first glance, this suggested these cells were "stronger", thus requiring the greater force to rupture. However, this data did not take into account that the size of the cells was different for the three groups which could explain their differing rupture force / deformabilities. To make comparisons meaningful, the cells need to have similar diameters and also possess similar deformation at rupture.

To make comparisons between the mechanical properties of resting and activated cells, nominal rupture stress and tension was calculated, which took into account the initial cross-sectional area and diameter of the cells. It should be pointed out that the initial cross-sectional area may be different from the real contact area between the force probe or bottom substrate and cell at rupture, and the latter depends on the deformation at rupture. The deformation at rupture did not change significantly up to 4 days and so the choice of using nominal rupture stress for comparison is still valid. Once corrected for size, it became apparent that resting cells (day 0) and cells at 4 days post-activation were equally strong but more than cells at 2 days post-activation. Hence the nominal stress/tension data indicated that CD8+ T cells became weaker early during activation, while their mechanical strength was regained 4 days later. The higher mechanical strength of the resting lymphocytes is essential functionally to maintain sufficient integrity and thus protect them from damage by the significant hydrodynamic and mechanical stresses exerted on them in the circulation (Brown *et al.,* 2001). Following stimulation by Ag-presenting cells *in vivo*, CD8+ T cells move out of the circulation to the site of infection where they acquire cytolytic effector activity against the pathogen. Therefore, the initial weakened cellular strength observed in this study may functionally correlate with, and enable, the transmigration of circulating lymphocytes between endothelial cells into tissue. After this event, lymphocytes regain their original form and strength/stiffness for mediating effector activity and this functionally correlates with the higher nominal rupture stress/tension observed at 4 day post-activation than day 2. A similar pattern of increased deformability post-activation associated with cellular exit from microvessels, and regaining stiffness once within the surrounding tissue, has also been described for phagocytic granulocytes (unpublished work).

Previous studies have shown that the nucleus of T cells is approximately 5 times stiffer than the cytoplasm and occupies about 80% of the cell (Friedl *et al.,* 2011). This characteristic makes T lymphocytes different from other eukaryocyte cells (mesenchymal cells, endothelial cells, etc.) in which the cell nucleus only occupies ~10% of the cell volume (Tsien *et al*., 1982). When faced with higher compressive forces, the lymphocyte cell nucleus therefore plays an increasingly significant role in resisting the applied force for the whole cell. The reduced nominal rupture stress / tension at 2 days post-activation indicates the cell nucleus, as well as the cell membrane and cytoskeleton of these larger cells, may have become less strong/stiff. However, at the later stage of activation (from day 2 to day 4), these structures regained their mechanical strength while cell volume remained unchanged during this time.

At lower applied force, which compresses the cell to a smaller deformation, the mechanical stiffness of T cells is governed primarily by the membrane which is considered to be largely elastic. The Young's modulus is a measure of the intrinsic stiffness of an elastic material undergoing recoverable compression. The Hertz model was able to determine the Young's modulus of T cells at small deformations (up to 10%), hence providing an indication of the elasticity of the outer region (cell membrane and cytoskeleton) of the cell. Although the noise to signal ratio is relatively big corresponding to small deformations, significant differences between samples were still demonstrated from the values of Young's modulus. The results indicate that depolymerization or reorganization of cytoskeleton polymers probably happened when the cells were activated, resulting in softness of the outer cortex during the 4 days. From the rupture parameters at large deformation and the Young's modulus calculated at small deformation, it is hypothesized that the cytoskeleton remained less stiff post-activation, while the nucleus regained rigidity during the 4 days activation, which remains to be validated in future. In the calculation of Young's modulus, for living cells, the Poisson ratio (υ) is typically between 0.4 and 0.5, which means they are mostly or fully incompressible (Trickey *et al.*, 2006). A value of 0.5 is chosen here since the Poisson ratio of CD8+ T cells has not been studied. Moreover, from the Hertz model, it can be seen that υ has little effect on Young's modulus that increases by only 12% when υ varies from 0.4 to 0.5. For measuring the local Young's modulus of the cell membrane with greater sensitivity, and its spatial distribution, AFM may be used which can measure the forces in the order of pico-Newton to nano-Newton.

5.5 Conclusion

Sorting cells in microfluidic devices based on their difference in mechanical properties is increasingly recognized as a marker-free way to separate biological cells. With the increasing interest in using CD8+ T cells for therapeutic purposes, a separation method in which cells remain unperturbed is important if they are to be transplanted after mechanical characterization and sorting. This study utilizes the micromanipulation technique, a relatively straightforward method to evaluate the mechanical property changes of activated CD8+ T cells. It has been found that there was no significant change in the mechanical property parameters including cell size, nominal rupture stress and rupture tension of non-activated CD8+ T cells in the culture medium for up to 4 days, which is in clear contrast to those activated in vitro using anti-CD3. The activated cells showed a significant increase in size and decrease in rupture stress/tension at day 2 but the mechanical strength recovered at day 4. The data obtained on size and mechanical properties post-activation may be utilized for developing microfluidic devices for their separation. Furthermore, this work obtains complementary data for CD8+ T cells circulating *in vivo* with respect to adapting to the mechanical barriers. The ability to directly measure the biomechanical properties of live lymphocyte subsets not only facilitates the development of a cell separation system based on defined physical properties of cells but also provides a 'biomarker' for assessing the physical state of lymphocytes, that could be used for assessing quality after bioprocessing of cells e. g. cryopreservation.

Chapter 6

Overall Conclusions and Recommendations for Future Work

6.1 Summary of Main Findings

Cellular therapy has offered the basis for developing potentially powerful new therapeutic strategies in the treatment of a broad spectrum of human diseases and injuries (Kim and De Vellis, 2009, Jeevanantham *et al.*, 2012). However, *in vivo* results showed limited benefit due to the failure of sufficient homing of stem cells, even a large number of cells were infused. The molecular adhesive factors regulating cell engraftment have been investigated and pre-treatment methods with SDF-1α or hydrogen dioxide were used to enhance HSC homing (Kavanagh, 2010, Yemm, 2014). In addition to the adhesive molecules, the physical properties of cells may play an important role in the *in vivo* circulation, particularly in the pulmonary first-pass effect where the vast number of cells was stuck in the capillaries of the lung. The size and deformability of cells are mechanical variables that may be manipulated to enhance cell recruitment. Moreover, inertial focusing of particles in microfluidic channels has been actively investigated for separation of animal cells, and diagnosis of diseases based on their physical variations. Microfluidic devices have been demonstrated to be useful for cellular handling as they can offer precise spatial and temporal control in a miniaturize platform (Shields IV et al., 2015). Therefore, the aim of the research presented in this thesis was to isolate relatively smaller and/or more deformable HSCs with the expectation that the recruitment efficiency could be enhanced when cells of interest were infused into injured mice. Prior to microfluidic cell separation, it is essential to characterise the mechanical variations of individual cells in one cell population and between different cell types with reliable methods. The major findings in this study include the following:

- For cell diameter, MSCs > HSCs > neutrophils, and pre-treatment with SDF-1α or H_2O_2 did not affect the cell size of HSCs.
- Neutrophils and HSCs showed rupture behavior when they were compressed to large deformations, while MSCs did not show clear rupture under compression.

- The mechanical strength data obtained suggest that neutrophils were significantly stronger than HSCs when the cells were exposed to forces which were sufficient to induce disruption of the cell structure.
- Values of Young's modulus determined from the force versus data from compression of cells to large deformations demonstrated that neutrophils were significantly stiffer than MSCs and HPC-7's, and MSCs showed similar stiffness to HPC-7's though the former were significantly bigger.
- HSCs became weaker after pre-treating with SDF-1α or H_2O_2 when the cells were compressed by a micromanipulation probe which induced large deformations on the whole cell scale.
- Values of Young's modulus for cell membrane indicated that the surface of cells pre-treated with SDF-1α or H_2O_2 became stiffer than those in the PBS control sample. Moreover, H_2O_2 pre-treatment induced more significant change in stiffness compared to SDF-1α's effects.
- Flow cytometry analyses showed that SDF-1α or H_2O_2 could induce F-actin accumulation compared to PBS control group, H_2O_2 induced a more significant change in F-actin content than SDF-1ɑ which is coordinated with the change of nano-mechanics measured by AFM.
- HSCs pre-treated with SDF-1ɑ or H_2O_2 appeared to lose their characteristic shapes (more rounded morphologies in PBS control group) as F-actin network was disrupted, replaced by a more diffuse pattern.
- In one HSC population, the size and nominal rupture stress of individual cells showed normal distributions, and this suggests that cells were able to be classified based on their mechanical difference.
- The straight microchannel with a higher AR (10) achieved relatively more effective separation than lower AR (5), and a significant difference in σ_R between different sub-populations after the separation was observed at the higher flow rate.
- In a spiral channel, cells were initially dragged towards the outer wall of the channel when the Re was low (< 1.78); with increasing Re, a part of cells shifted to the

inner half of the channel. In this segregate regime ($15 < Re < 36$), cells of interest were isolated from the inner outlet; all cells eventually focused towards the inner wall as Re further increased.

- In spiral channels, at the intermediate flow conditions (5 mL/h, 7.5 mL/h and 10 mL/h), more effective separation was achieved at relatively faster flow rates.
- **Device C** was able to separate cells of interest with higher efficiency at a flow rate of 10 mL/h than 5 mL/h and 7.5 mL/h, and was utilized for subsequent *in vivo* studies.
- HSCs isolated from the inner outlet showed a significant increase of the free flowing cells intravitally compared to those harvested from the outer outlet, but numbers of the adherent cells were similar between the two groups.
- Activation of CD8+ T-cells was accompanied by an increase in T cell volume, and a concurrent decrease in the Young's modulus value as determined by the force versus displacement data up to a nominal deformation of 10% was observed.
- Nominal rupture tension determined by compressing single T cells to large deformation until rupture, decreased from day 0 to day 2, and then recovered on day 4 post-activation.

The mechanical properties of different cell types mirror their *in vivo* functional distinctions. For neutrophils, which naturally exisit in the circulation as spherical entities, and HSCs which can be made to do so, the *'cortical shell - liquid core'* model is an advantageous strategy as their free circulation may be attributed to the self-rotation of individual cells in response to shear stress, similar to liquid drops under a driving flow (Abkarian and Viallat, 2005, Hur *et al.,* 2011, Chau *et al.*, 2013). MSCs, not naturally designed to circulate in the peripheral blood, generally adhere to each other or to their substrate throughout their lifetime, and so the '*homogenous solid state*' cellular structure plays an important role in transmitting and distributing mechanical stress within the cell (Stamenović and Ingber, 2002).

For pretreated HSCs, the cells as a whole became weaker and more deformable after using micromanipulation, while the HSC surface stiffened after pre-treating with SDF-1α and H_2O_2 in AFM test. The softening may be due to the re-organization/disruption of actin filaments from highly-ordered 3-D structure to a more diffuse pattern. And the stiffening of cell surface after pre-treatment can potentially be explained by the expansion and polymerization of F-actin interacting with the plasma membrane. Indeed, the increased immunostaining of F-actin filaments noted (higher component concentration) in the cortical membrane after pre-treatment may allow for the observed increase in the elasticity modulus at small deformations.

The relationships between between cell size / deformability and the inertial lift force in straight channel and the ratio (R_f) of inertial lift force to Dean drag force in curved microchannel were exploited to separate sub-populations of smaller and/or more deformable HPC-7s for *in vivo* studies. The cell focusing behaviours in straight channels could be explained by taking the two competing lift forces into account: the shear-gradient lift force directing to the channel walls and the wall-induced lift force in the direction of the channel centerline. At smaller AR, as increasing flow rate, the shear-gradient lift force may increase more rapidly than the wall-induced lift force, becoming more dominant, and consequently, dragging more cells towards the channel wall. Smaller and softer cells are supposed to migrate more slowly and be entrained near the channel centre. At higher AR, the velocity profile became flattened across the width, with the increase of Re, the increase of wall-induced lift force might be more rapid than that of shear-gradient lift force. Consequently, more cells migrated to the channel centerline, with the bigger cells moved more abruptly than smaller ones.

For curved channels, Dean drag follows the underlying secondary velocity field, directing outwards near the channel centre, and inwards near the up and bottom walls. The curvature can also change the shear-gradient lift force through redistributing the velocity profile which can change the vertical position of particles (De Vriend, 1981, Hille et al., 1985). It is hypothesized that at slow velocities wall-induced inertial became more dominant than the shear gradient inertial in height direction, allowing cells to reach vertical equilibrium positions near the channel centre. By crossing the vertical position, the bigger and/or rigid cells moved faster towards the centre and then experienced a switch in the direction of Dean flow, moving outwards of the channel. Smaller and/or more deformable cells near top or bottom walls moved inwards, thus separation can be achieved. As the increasing Re, the shear gradient may become high enough to counter F_D, more cells tended to move away from the channel centre and were directed towards the inner half, eventually, 100% of cells were dragged inwards.

6.2 Future work

In this study, the mechanical properties of HSCs were characterized at different deformations using both micromanipulation and AFM methods. Evidence has suggested that MSCs can be protective in animal models of injury (Fang *et al.,* 2004), though the molecular mechanisms that govern the retention of these cells to injury sites are unknown, and the physical obstacle is also a problem that needs to be addressed for further investigations. It has been found that the micromanipulation technique based on biometrical compression may not be appropriate to probe the mechanical strength of MSCs which did not show clear rupture under compression, and AFM used was not able to do force scanning on cells that are bigger than the greatest movement of the cantilever (15 µm). Improvement of these techniques or using other techniques is required to further study mechanics of MSCs, as well as their cytoskeletal structures that distinguish them from HSCs in response to a wide range of mechanical loads.

This study has identified ranges of flowing and geometry parameters that allow for deformability/ size-based cell separation and suggested physical principles and forces that are likely responsible for it. Even though the microfluidic devices have been successfully utilized in sorting smaller and more deformable cells, some challenges will exist in that they should be accurately operated, and more robust and reliable microfluidic systems are required. For example, the limited lifespan of microfluidic chips, which are typically shortened due to blocking or clogging, is a barrier to routine research. The commercialization of cell sorting technologies may look for disposable chips to overcome the short lifetimes and enable a sterile, user-friendly operation. Additionally, these microfluidic cell sorting systems require complex sample preparation and channel cleaning that reduce ease-of-use and can compromise sorting accuracies due to user variations. Therefore, building microfluidic devices that require minimal sample preparation is desirable. Finally, the heterogeneity and complexity of biological cells in different proliferation stages could affect the repeatability and reproducibility of cell sorting results. It is believed that these challenges are solvable, and given the great interest and innovation in this area, microfluidic cell assay systems may soon become irreplaceable in cellular biology.

In this study, since cells were sorted from the same population, the separation purity and efficiency which were presented only by the values of size and nominal rupture stress from each outlets may not be able to fully describe the performance of the device. Thus a comparative table of performance metrics that accurately demonstrate the degree of performance will be required. In addition, though some hypotheses on the principle of cell migration have been made, the precise mechanisms by which the cells/particles focus in microchannels still remain to be fully understood. Therefore, further experimental and simulation studies are required to fully predict the behaviours of deformable cells or liquid drops inside the microfluidic devices.

Despite the relative smaller and softer properties of isolated HPC-7 cells, they are still significantly bigger than the capillaries, thus, most infused HPC-7’s were accumulated in the lungs and were finally lost from circulation. In order to further augment the cell recruitment, future work can be focused on increasing separation efficiency of cell in microfluidic systems and combining microfluidic technologies with biological strategies, such as genetic modification and chemical pre-treatment, making more cells migrating to injured sites. In this study, sub-populations of HSCs were isolated merely based on their mechanical differences, followed by intravital study. Since the mechanical properties can be determined by cytoskeletal structure, which is further affected by the physiological condition of cells, therefore, the biological properties of isolated cells should be tested in future work to confirm the contribution of mechanical properties on cell circulation.

References

ABKARIAN, M. & VIALLAT, A. 2005. Dynamics of vesicles in a wall-bounded shear flow. *Biophysical Journal,* 89**,** 1055-1066.

AMINI, H., LEE, W. & DI CARLO, D. 2014. Inertial microfluidic physics. *Lab on a Chip,* 14**,** 2739-2761.

ÄHRLUND-RICHTER, L., DE LUCA, M., MARSHAK, D. R., MUNSIE, M., VEIGA, A. & RAO, M. 2009. Isolation and production of cells suitable for human therapy: challenges ahead. *Cell Stem Cell,* 4**,** 20-26.

ALENGHAT, F. J., FABRY, B., TSAI, K. Y., GOLDMANN, W. H. & INGBER, D. E. 2000. Analysis of cell mechanics in single vinculin-deficient cells using a magnetic tweezer. *Biochemical and Biophysical Research Communications,* 277**,** 93-99.

ALMEIDA-PORADA, G., FLAKE, A. W., GLIMP, H. A. & ZANJANI, E. D. 1999. Cotransplantation of stroma results in enhancement of engraftment and early expression of donor hematopoietic stem cells in utero. *Experimental Hematology,* 27**,** 1569-1575.

AMINI, H., LEE, W. & DI CARLO, D. 2014. Inertial microfluidic physics. *Lab on a Chip,* 14**,** 2739-2761.

ANKLESARIA, P., KASE, K., GLOWACKI, J., HOLLAND, C. A., SAKAKEENY, M. A., WRIGHT, J. A., FITZGERALD, T. J., LEE, C.-Y. & GREENBERGER, J. S. 1987. Engraftment of a clonal bone marrow stromal cell line in vivo stimulates hematopoietic recovery from total body irradiation. *Proceedings of the National Academy of Sciences,* 84**,** 7681-7685.

ANKRUM, J. & KARP, J. M. 2010. Mesenchymal stem cell therapy: two steps forward, one step back. *Trends in molecular medicine,* 16**,** 203-209.

ASMOLOV, E. S. 1999. The inertial lift on a spherical particle in a plane Poiseuille flow at large channel Reynolds number. *Journal of Fluid Mechanics,* 381**,** 63-87.

AURICH, I., MUELLER, L. P., AURICH, H., LUETZKENDORF, J., TISLJAR, K., DOLLINGER, M. M., SCHORMANN, W., WALLDORF, J., HENGSTLER, J. G. & FLEIG, W. E. 2007. Functional integration of hepatocytes derived from human mesenchymal stem cells into mouse livers. *Gut,* 56, 405-415.

BARANIAK P. R. & MCDEVITT T. C. 2010. Stem cell paracrine actions and tissue regeneration. *Regen Med,* 5(1)**,** 121-43.

BANSOD, Y. D. & BURSA, J. 2015. Continuum-based modelling approaches for cell mechanics. *World Academy of Science, Engineering and Technology,* *International Journal of Biological, Biomolecular, Agricultural, Food and Biotechnological Engineering,* 9**,** 921-932.

BERGER, S., TALBOT, L. & YAO, L. 1983. Flow in curved pipes. *Annual review of Fluid Mechanics,* 15**,** 461-512.

BHAGAT, A. A. S., BOW, H., HOU, H. W., TAN, S. J., HAN, J. & LIM, C. T. 2010. Microfluidics for cell separation. *Medical & biological engineering & computing,* 48**,** 999-1014.

BHAGAT, A. A. S., KUNTAEGOWDANAHALLI, S. S. & PAPAUTSKY, I. 2008a. Continuous particle separation in spiral microchannels using dean flows and differential migration. *Lab on a Chip,* 8**,** 1906-1914.

BHAGAT, A. A. S., KUNTAEGOWDANAHALLI, S. S. & PAPAUTSKY, I. 2008b. Enhanced particle filtration in straight microchannels using shear-modulated inertial migration. *Physics of Fluids,* 20**,** 101702.

BOYLE, A. J., SCHULMAN, S. P. & HARE, J. M. 2006. Stem cell therapy for cardiac repair ready for the next step. *Circulation,* 114**,** 339-352.

BROWN, M. J., HALLAM, J. A., COLUCCI-GUYON, E. & SHAW, S. 2001. Rigidity of circulating lymphocytes is primarily conferred by vimentin intermediate filaments. *The Journal of Immunology,* 166**,** 6640-6646.

BUCKLEY, R. H., SCHIFF, S. E., SCHIFF, R. I., MARKERT, M. L., WILLIAMS, L. W., ROBERTS, J. L., MYERS, L. A. & WARD, F. E. 1999. Hematopoietic stem-cell transplantation for the treatment of severe combined immunodeficiency. *New England Journal of Medicine,* 340**,** 508-516.

BUTCHER, E. 1991. Leukocyte-endothelial cell recognition: three (or more) steps to specificity and diversity. *Cell,* 67**,** 1033.

CALDWELL, K. D., CHENG, Z.-Q., HRADECKY, P. & GIDDINGS, J. C. 1984. Separation of human and animal cells by steric field-flow fractionation. *Cell Biophysics,* 6**,** 233-251.

CAI, X. XING, J. CAI, Q. CHEN, S. WU, F. HUANG. 2010. Connection between biomechanics and cytoskeleton structure of lymphocyte and jurkat cells: an AFM study. *Micron,* 41**,** 257-262.

KLEBANOFF, C. A., GATTINONI, L., & RESTIFO, N. P. 2012. Sorting through subsets: which T cell populations mediate highly effective adoptive immunotherapy? *Journal of Immunotherapy,* 35**,** 651-660.

CEPOK, S., ZHOU, D., SRIVASTAVA, R., NESSLER, S., STEI, S., BÜSSOW, K., SOMMER, N. & HEMMER, B. 2005. Identification of Epstein-Barr virus proteins as putative targets of the immune response in multiple sclerosis. *The Journal of clinical investigation,* 115**,** 1352-1360.

CHEN B. P., GALY A. M., & FRASER C. 1997. Delineation of the human hematolymphoid system: potential applications of defined cell populations in cellular therapy. *Immunol Rev*, 157**,** 41-51.

CEPOK, S., ZHOU, D., SRIVASTAVA, R., NESSLER, S., STEI, S., BÜSSOW, K., SOMMER, N. & HEMMER, B. 2005. Identification of Epstein-Barr virus proteins as putative targets of the immune response in multiple sclerosis. *The Journal of clinical investigation,* 115**,** 1352-1360.

CHAUDHURI, O., PAREKH, S. H. & FLETCHER, D. A. 2007. Reversible stress softening of actin networks. *Nature,* 445**,** 295-298.

CHAU, L.-H., LIANG, W., CHEUNG, F. W. K., LIU, W. K., LI, W. J., CHEN, S.-C. & LEE, G.-B. 2013. Self-rotation of cells in an irrotational AC E-field in an opto-electrokinetics chip. *PloS one,* 8**,** e51577.

CHUNG, J. STEFANSKI, O. BORQUEZ-OJEDA, M. OLSZEWSKA. Efficacy and toxicity management of 19-28z car t cell therapy in b cell acute lymphoblastic leukemia. *Science Translational Medicine* 6 (2014) 224RA225-224RA225.

COPELAN, E. A. 2006. Hematopoietic stem-cell transplantation. *New England Journal of Medicine,* 354**,** 1813-1826.

COLLARD, C. D. & GELMAN, S. 2001. Pathophysiology, clinical manifestations, and prevention of ischemia-reperfusion injury. *The Journal of the American Society of Anesthesiologists,* 94**,** 1133-1138.

DARLING, E. M., TOPEL, M., ZAUSCHER, S., VAIL, T. P. & GUILAK, F. 2008. Viscoelastic properties of human mesenchymally-derived stem cells and primary osteoblasts, chondrocytes, and adipocytes. *Journal of biomechanics,* 41**,** 454-464.

DAO, M., LIM, C. T. & SURESH, S. 2003. Mechanics of the human red blood cell deformed by optical tweezers. *Journal of the Mechanics and Physics of Solids,* 51**,** 2259-2280.

DE VRIEND, H. 1981. Velocity redistribution in curved rectangular channels. *Journal of Fluid Mechanics,* 107**,** 423-439.

DI CARLO, D., IRIMIA, D., TOMPKINS, R. G. & TONER, M. 2007. Continuous inertial focusing, ordering, and separation of particles in microchannels. *Proceedings of the National Academy of Sciences,* 104**,** 18892-18897.

DODSON, B. P. & LEVINE, A. D. 2015. Challenges in the translation and commercialization of cell therapies. *BMC Biotechnology,* 15**,** 70-85.

DORWEILER, B., PRUEFER, D., ANDRASI, T. B., MAKSAN, S. M., SCHMIEDT, W., NEUFANG, A. & VAHL, C. F. 2007. Ischemia-reperfusion injury. *European Journal of Trauma and Emergency Surgery,* 33**,** 600-612.

DI CARLO, D. 2009. Inertial microfluidics. *Lab on a Chip,* 9**,** 3038-3046.

DI CARLO, D., EDD, J. F., IRIMIA, D., TOMPKINS, R. G. & TONER, M. 2008. Equilibrium separation and filtration of particles using differential inertial focusing. *Analytical chemistry,* 80**,** 2204-2211.

Du M, KALIA N, FRUMENTO G, CHEN F, ZHANG Z. 2016. Biomechanical properties of human T cells in the process of activation based on diametric compression by micromanipulation. *Med Eng Phys.* 40**,** 20-27.

M.L. DAVILA, I. RIVIERE, X. WANG, S. BARTIDO, J. PARK, K. CURRAN, S.S.

DOERSCHUK, C. M., BEYERS, N., COXSON, H., WIGGS, B. & HOGG, J. 1993. Comparison of neutrophil and capillary diameters and their relation to neutrophil sequestration in the lung. *Journal of Applied Physiology,* 74**,** 3040-3045.

EGGLETON, C. D. & POPEL, A. S. 1998. Large deformation of red blood cell ghosts in a simple shear flow. *Physics of Fluids,* 10**,** 1834-1845.

EINSTEIN, O. & BEN-HUR, T. 2008. The changing face of neural stem cell therapy in neurologic diseases. *Archives of neurology,* 65**,** 452-456.

FANG, B., SHI, M., LIAO, L., YANG, S., LIU, Y. & ZHAO, R. C. 2004. Systemic infusion of FLK1+ mesenchymal stem cells ameliorate carbon tetrachloride-induced liver fibrosis in mice. *Transplantation,* 78**,** 83-88.

FEUCHTINGER, T., MATTHES-MARTIN, S., RICHARD, C., LION, T., FUHRER, M., HAMPRECHT, K., HANDGRETINGER, R., PETERS, C., SCHUSTER, F. R. & BECK, R. 2006. Safe adoptive transfer of virus-specific T-cell immunity for the treatment of systemic adenovirus infection after allogeneic stem cell transplantation. *British journal of haematology,* 134**,** 64-76.

FERGUSON, L. A., MUDDAMALLAPPA, M. & WALTON, J. R. 2015. Numerical simulation of mode-III fracture incorporating interfacial mechanics. *International Journal of Fracture,* 192**,** 47-56.

FLETCHER, D. A. & MULLINS, R. D. 2010. Cell mechanics and the cytoskeleton. *Nature,* 463**,** 485-492.

FLEISCHER, F., ANANTHAKRISHNAN, R., ECKEL, S., SCHMIDT, H., KÄS, J., SVITKINA, T., SCHMIDT, V. & BEIL, M. 2007. Actin network architecture and elasticity in lamellipodia of melanoma cells. *New Journal of Physics,* 420**,** 1-17.

FONG, C. Y., PEH, G. S., GAUTHAMAN, K. & BONGSO, A. 2009. Separation of SSEA-4 and TRA-1–60 labelled undifferentiated human embryonic stem cells from a heterogeneous cell population using magnetic-activated cell sorting (MACS) and fluorescence-activated cell sorting (FACS). *Stem Cell Reviews and Reports,* 5**,** 72-80.

FRATICELLI, A., SERRANO, C. V., BOCHNER, B. S., CAPOGROSSI, M. C. & ZWEIER, J. L. 1996. Hydrogen peroxide and superoxide modulate leukocyte adhesion molecule expression and leukocyte endothelial adhesion. *Biochimica et Biophysica Acta (BBA)-Molecular Cell Research,* 1310**,** 251-259.

FRIEDL, P., WOLF, K. & LAMMERDING, J. 2011. Nuclear mechanics during cell migration. *Current Opinion in Cell Biology,* 23**,** 55-64.

GALLACHER, L., MURDOCH, B., WU, D. M., KARANU, F. N., KEENEY, M. & BHATIA, M. 2000. Isolation and characterization of human CD34− Lin− and CD34+ Lin− hematopoietic stem cells using cell surface markers AC133 and CD7. *Blood,* 95**,** 2813-2820.

GARBERN, J. C. & LEE, R. T. 2013. Cardiac stem cell therapy and the promise of heart regeneration. *Cell stem cell,* 12**,** 689-698.

GARDEL, M., SHIN, J., MACKINTOSH, F., MAHADEVAN, L., MATSUDAIRA, P. & WEITZ, D. 2004. Elastic behavior of cross-linked and bundled actin networks. *Science,* 304**,** 1301-1305.

GE, J., GUO, L., WANG, S., ZHANG, Y., CAI, T., ZHAO, R. C. & WU, Y. 2014. The size of mesenchymal stem cells is a significant cause of vascular obstructions and stroke. *Stem Cell Reviews and Reports,* 10**,** 295-303.

GOODELL, M. A., BROSE, K., PARADIS, G., CONNER, A. S. & MULLIGAN, R. C. 1996. Isolation and functional properties of murine hematopoietic stem cells that are replicating in vivo. *The Journal of experimental medicine,* 183**,** 1797-1806.

GOSSETT, D. R., WEAVER, W. M., MACH, A. J., HUR, S. C., TSE, H. T. K., LEE, W., AMINI, H. & DI CARLO, D. 2010. Label-free cell separation and sorting in microfluidic systems. *Analytical and bioanalytical chemistry,* 397**,** 3249-3267.

GOSSETT, D. R. & CARLO, D. D. 2009. Particle focusing mechanisms in curving confined flows. *Analytical chemistry,* 81**,** 8459-8465.

GUNSILIUS, E., GASTL, G. & PETZER, A. 2001. Hematopoietic stem cells. *Biomedicine & pharmacotherapy,* 55**,** 186-194.

GAO, J., DENNIS, J. E., MUZIC, R. F., LUNDBERG, M. & CAPLAN, A. I. 2001. The dynamic in vivo distribution of bone marrow-derived mesenchymal stem cells after infusion. *Cells Tissues Organs,* 169**,** 12-20.

GOSSETT, D. R., TSE, H. T. K., DUDANI, J. S., GODA, K., WOODS, T. A., GRAVES, S. W. & DI CARLO, D. 2012. Inertial manipulation and transfer of microparticles across laminar fluid streams. *Small,* 8**,** 2757-2764.

GUAN, G., WU, L., BHAGAT, A. A., LI, Z., CHEN, P. C., CHAO, S., ONG, C. J. & HAN, J. 2013. Spiral microchannel with rectangular and trapezoidal cross-sections for size based particle separation. *Scientific reports,* 3**,** 1475.

HIASA, K.-I., ISHIBASHI, M., OHTANI, K., INOUE, S., ZHAO, Q., KITAMOTO, S., SATA, M., ICHIKI, T., TAKESHITA, A. & EGASHIRA, K. 2004. Gene Transfer of Stromal Cell–Derived Factor-1α Enhances Ischemic Vasculogenesis and Angiogenesis via Vascular Endothelial Growth Factor/Endothelial Nitric Oxide Synthase–Related Pathway Next-Generation Chemokine Therapy for Therapeutic Neovascularization. *Circulation,* 109**,** 2454-2461.

HOCHMUTH, R. M. 2000. Micropipette aspiration of living cells. *Journal of biomechanics,* 33**,** 15-22.

HOLM, S. H., BEECH, J. P., BARRETT, M. P. & TEGENFELDT, J. O. 2011. Separation of parasites from human blood using deterministic lateral displacement. *Lab on a Chip,* 11**,** 1326-1332.

HOOD, K., LEE, S. & ROPER, M. 2015. Inertial migration of a rigid sphere in three-dimensional Poiseuille flow. *Journal of Fluid Mechanics,* 765**,** 452-479.

HOULIHAN, D. D., MABUCHI, Y., MORIKAWA, S., NIIBE, K., ARAKI, D., SUZUKI, S., OKANO, H. & MATSUZAKI, Y. 2012. Isolation of mouse mesenchymal stem cells on the basis of expression of Sca-1 and PDGFR-α. *Nature protocols,* 7**,** 2103-2111.

HOULIHAN, D. D. & NEWSOME, P. N. 2008. Critical review of clinical trials of bone marrow stem cells in liver disease. *Gastroenterology,* 135**,** 438-450.

HORWITZ, E. M., PROCKOP, D. J., FITZPATRICK, L. A., KOO, W. W., GORDON, P. L., NEEL, M., SUSSMAN, M., ORCHARD, P., MARX, J. C. & PYERITZ, R. E. 1999. Transplantability and therapeutic effects of bone marrow-derived mesenchymal cells in children with osteogenesis imperfecta. *Nature medicine,* 5**,** 309-313.

HUR, S. C., HENDERSON-MACLENNAN, N. K., MCCABE, E. R. & DI CARLO, D. 2011. Deformability-based cell classification and enrichment using inertial microfluidics. *Lab on a Chip,* 11**,** 912-920.

SWEET, R. G. & HERZENBERG, L. A. 1976. Fluorescence-activated cell sorting. *Sci Am,* 234**,** 108-117.

HILLE, P., VEHRENKAMP, R. & SCHULZ-DUBOIS, E. 1985. The development and structure of primary and secondary flow in a curved square duct. *Journal of Fluid Mechanics,* 151**,** 219-241.

HOU, H. W., WARKIANI, M. E., KHOO, B. L., LI, Z. R., SOO, R. A., TAN, D. S.-W., LIM, W.-T., HAN, J., BHAGAT, A. A. S. & LIM, C. T. 2013. Isolation and retrieval of circulating tumor cells using centrifugal forces. *Scientific reports,* 3**,** 1259.

INGLIS, D. W., LORD, M. & NORDON, R. E. 2011. Scaling deterministic lateral displacement arrays for high throughput and dilution-free enrichment of leukocytes. *Journal of Micromechanics and Microengineering,* 21**,** 054024.

JANMEY, P. A. & MCCULLOCH, C. A. 2007. Cell mechanics: integrating cell responses to mechanical stimuli. *Annu. Rev. Biomed. Eng.,* 9**,** 1-34.

JEEVANANTHAM, V., BUTLER, M., SAAD, A., ABDEL-LATIF, A., ZUBA-SURMA, E. K. & DAWN, B. 2012. Adult bone marrow cell therapy improves survival and induces long-term improvement in cardiac parameters: a systematic review and meta-analysis. *Circulation***,** 111.086074.

JI, H. M., SAMPER, V., CHEN, Y., HENG, C. K., LIM, T. M. & YOBAS, L. 2008. Silicon-based microfilters for whole blood cell separation. *Biomedical microdevices,* 10**,** 251-257.

JOHNSTONE, B., HERING, T. M., CAPLAN, A. I., GOLDBERG, V. M. & YOO, J. U. 1998. In vitrochondrogenesis of bone marrow-derived mesenchymal progenitor cells. *Experimental cell research,* 238**,** 265-272.

KARNIS, A., GOLDSMITH, H. & MASON, S. 1966. The flow of suspensions through tubes: V. Inertial effects. *The Canadian Journal of Chemical Engineering,* 44**,** 181-193.

KARP, J. M. & TEO, G. S. L. 2009. Mesenchymal stem cell homing: the devil is in the details. *Cell stem cell,* 4**,** 206-216.

KAVANAGH, D. P., YEMM, A. I., ALEXANDER, J. S., FRAMPTON, J. & KALIA, N. 2013a. Enhancing the adhesion of hematopoietic precursor cell integrins with hydrogen peroxide increases recruitment within murine gut. *Cell transplantation,* 22**,** 1485-1499.

KAVANAGH, D. P., YEMM, A. I., ZHAO, Y., FRAMPTON, J. & KALIA, N. 2013b. Mechanisms of adhesion and subsequent actions of a haematopoietic stem cell line, HPC-7, in the injured murine intestinal microcirculation in vivo. *PloS one,* 8**,** e59150.

KAVANAGH, D. P. J. & KALIA, N. 2011. Hematopoietic stem cell homing to injured tissues. *Stem Cell Reviews and Reports,* 7**,** 672-682.

KAVANAGH, D. P., SURESH, S., NEWSOME, P. N., FRAMPTON, J. & KALIA, N. 2015. Pretreatment of Mesenchymal Stem Cells Manipulates Their Vasculoprotective Potential While Not Altering Their Homing Within the Injured Gut. *Stem Cells,* 33**,** 2785-2797.

KILIMNIK, A., MAO, W. & ALEXEEV, A. 2011. Inertial migration of deformable capsules in channel flow. *Physics of Fluids (1994-present),* 23**,** 123302.

KIRMIZIS, D. & LOGOTHETIDIS, S. 2010. Atomic force microscopy probing in the measurement of cell mechanics. *Int J Nanomedicine,* 5**,** e45.

KLEBANOFF, C. A., GATTINONI, L. & RESTIFO, N. P. 2012. Sorting through subsets: Which T cell populations mediate highly effective adoptive immunotherapy? *Journal of immunotherapy (Hagerstown, Md.: 1997),* 35**,** 651-660.

KOBAYASHI, M., IMAMURA, M., SAKURADA, K., MAEDA, S., IWASAKI, H., TSUDA, Y., MUSASHI, M., MIYAZAKI, T. & UEDE, T. 1994. Expression of adhesion molecules on human hematopoietic progenitor cells at different maturational stages. *Stem Cells,* 12**,** 316-321.

KOÇ, O. N., GERSON, S. L., COOPER, B. W., DYHOUSE, S. M., HAYNESWORTH, S. E., CAPLAN, A. I. & LAZARUS, H. M. 2000. Rapid hematopoietic recovery after coinfusion of autologous-blood stem cells and culture-expanded marrow mesenchymal stem cells in advanced breast cancer patients receiving high-dose chemotherapy. *Journal of Clinical Oncology,* 18**,** 307-316.

KODITUWAKKU, A. P., JESSUP, C., ZOLA, H. & ROBERTON, D. M. 2003. Isolation of antigen-specific B cells. *Immunology and cell biology,* 81**,** 163-170.

KOLACZKOWSKA, E. & KUBES, P. 2013. Neutrophil recruitment and function in health and inflammation. *Nature Reviews Immunology,* 13**,** 159-175.

KUZNETSOVA, T. G., STARODUBTSEVA, M. N., YEGORENKOV, N. I., CHIZHIK, S. A. & ZHDANOV, R. I. 2007. Atomic force microscopy probing of cell elasticity. *Micron,* 38**,** 824-833.

KING, R. C., BINNS, O. A., RODRIGUEZ, F., KANITHANON, R. C., DANIEL, T. M., SPOTNITZ, W. D., TRIBBLE, C. G. & KRON, I. L. 2000. Reperfusion injury significantly impacts clinical outcome after pulmonary transplantation. *The Annals of thoracic surgery,* 69**,** 1681-1685.

KIM, S. U. & VELLIS, J. 2009. Stem cell-based cell therapy in neurological diseases: A review. *Journal of neuroscience research,* 87**,** 2183-2200.

KUMAR, S. & PONNAZHAGAN, S. 2007. Bone homing of mesenchymal stem cells by ectopic α4 integrin expression. *The FASEB Journal,* 21**,** 3917-3927.

LAZARUS, H. M., KOC, O. N., DEVINE, S. M., CURTIN, P., MAZIARZ, R. T., HOLLAND, H. K., SHPALL, E. J., MCCARTHY, P., ATKINSON, K. & COOPER, B. W. 2005. Cotransplantation of HLA-identical sibling culture-expanded mesenchymal stem cells and hematopoietic stem cells in hematologic malignancy patients. *Biology of Blood and Marrow Transplantation,* 11**,** 389-398.

LI, Y., CHEN, J., CHEN, X., WANG, L., GAUTAM, S., XU, Y., KATAKOWSKI, M., ZHANG, L., LU, M. & JANAKIRAMAN, N. 2002. Human marrow stromal cell therapy for stroke in rat neurotrophins and functional recovery. *neurology,* 59**,** 514-523.

LIM, C., ZHOU, E. & QUEK, S. 2006. Mechanical models for living cells—a review. *Journal of biomechanics,* 39**,** 195-216.

LIU, C., HU, G., JIANG, X. & SUN, J. 2015. Inertial focusing of spherical particles in rectangular microchannels over a wide range of Reynolds numbers. *Lab on a Chip,* 15**,** 1168-1177.

LIU, M. 2010. Understanding the mechanical strength of microcapsules and their adhesion on fabric surfaces. *University of Birmingham.*

LIU, F., WU, D. & CHEN, K. 2014. A Zebrafish Embryo Behaves both as a "Cortical Shell–Liquid Core" Structure and a Homogeneous Solid when Experiencing Mechanical Forces. *Microscopy and Microanalysis,* 20**,** 1841-1847.

LIU, Z., HUANG, F., DU, J., SHU, W., FENG, H., XU, X. & CHEN, Y. 2013. Rapid isolation of cancer cells using microfluidic deterministic lateral displacement structure. *Biomicrofluidics,* 7**,** 011801.

LYDEN, D., HATTORI, K., DIAS, S., COSTA, C., BLAIKIE, P., BUTROS, L., CHADBURN, A., HEISSIG, B., MARKS, W. & WITTE, L. 2001. Impaired recruitment of bone-marrow–derived endothelial and hematopoietic precursor cells blocks tumor angiogenesis and growth. *Nature Medicine,* 7**,** 1194-1201.

LICHTENSTEIN, G. R., HANAUER, S. B. & SANDBORN, W. J. 2009. Management of Crohn's disease in adults. *Am J Gastroenterol,* 104**,** 465-483.

MACKAY, A. M., BECK, S. C., MURPHY, J. M., BARRY, F. P., CHICHESTER, C. O. & PITTENGER, M. F. 1998. Chondrogenic differentiation of cultured human mesenchymal stem cells from marrow. *Tissue Engineering,* 4**,** 415-428.

MCFAUL, S. M., LIN, B. K. & MA, H. 2012. Cell separation based on size and deformability using microfluidic funnel ratchets. *Lab on a chip,* 12**,** 2369-2376.

MARTENS, J. C. & RADMACHER, M. 2008. Softening of the actin cytoskeleton by inhibition of myosin II. *Pflügers Archiv-European Journal of Physiology,* 456**,** 95-100.

MASHMOUSHY, H., ZHANG, Z. & THOMAS, C. 1998. Micromanipulation measurement of the mechanical properties of baker's yeast cells. *Biotechnology Techniques,* 12**,** 925-929.

MERCADÉ-PRIETO, R. & ZHANG, Z. 2012. Mechanical characterization of microspheres–capsules, cells and beads: a review. *Journal of microencapsulation,* 29**,** 277-285.

MIZGERD, J. P. 2002. Molecular mechanisms of neutrophil recruitment elicited by bacteria in the lungs. *Seminars in immunology,* 123-132.

MILTENYI, S., MÜLLER, W., WEICHEL, W. & RADBRUCH, A. 1990. High gradient magnetic cell separation with MACS. *Cytometry,* 11**,** 231-238.

BROWN M. J., HALLAM, J. A., COLUCCI-GUYON, E. & SHAW. S. 2001. Rigidity of circulating lymphocytes is primarily conferred by vimentin intermediate filaments. *The Journal of Immunology,* 166**,** 6640-6646.

MOOSMANN, A., BIGALKE, I., TISCHER, J., SCHIRRMANN, L., KASTEN, J., TIPPMER, S., LEEPING, M., PREVALŠEK, D., JAEGER, G. & LEDDEROSE, G. 2010. Effective and long-term control of EBV PTLD after transfer of peptide-selected T cells. *Blood,* 115**,** 2960-2970.

MORRISON, S. J., UCHIDA, N. & WEISSMAN, I. L. 1995. The biology of hematopoietic stem cells. *Annual review of cell and developmental biology,* 11**,** 35-71.

MARTEL, J. M. & TONER, M. 2012. Inertial focusing dynamics in spiral microchannels. *Physics of Fluids,* 24**,** 032001.

MARTEL, J. M. & TONER, M. 2013. Particle focusing in curved microfluidic channels. *Scientific Reports,* 3**,** 3340-3348.

NAUSEEF, W. M. 2007. Isolation of human neutrophils from venous blood. *Neutrophil Methods and Protocols***,** 15-20.

NGUYEN, B. V., WANG, Q. G., KUIPER, N. J., EL HAJ, A. J., THOMAS, C. R. & ZHANG, Z. 2010. Biomechanical properties of single chondrocytes and chondrons determined by micromanipulation and finite-element modelling. *Journal of The Royal Society Interface,* 7**,** 1723-1733.

NGUYEN, B. V., WANG, Q., KUIPER, N. J., EL HAJ, A. J., THOMAS, C. R. & ZHANG, Z. 2009a. Strain-dependent viscoelastic behaviour and rupture force of single chondrocytes and chondrons under compression. *Biotechnol Lett,* 31**,** 803-9.

NGUYEN, B. V., WANG, Q., KUIPER, N. J., EL HAJ, A. J., THOMAS, C. R. & ZHANG, Z. 2009b. Strain-dependent viscoelastic behaviour and rupture force of single chondrocytes and chondrons under compression. *Biotechnology letters,* 31**,** 803-809.

PARK, I.-H., ZHAO, R., WEST, J. A., YABUUCHI, A., HUO, H., INCE, T. A., LEROU, P. H., LENSCH, M. W. & DALEY, G. Q. 2008. Reprogramming of human somatic cells to pluripotency with defined factors. *nature,* 451**,** 141-146.

PARKS, D., HERZENBERG, L. & HERZENBERG, L. 1989. Flow cytometry and fluorescence-activated cell sorting. Fundamental Immunology, William Paul, Ed. Raven Press, Ltd, New York.

REINHERZ, E. L., KUNG, P. C., GOLDSTEIN, G. & SCHLOSSMAN, S. F. 1979. Separation of functional subsets of human T cells by a monoclonal antibody. *Proceedings of the National Academy of Sciences,* 76**,** 4061-4065.

PEGGS, K. S., VERFUERTH, S., PIZZEY, A., KHAN, N., GUIVER, M., MOSS, P. A. & MACKINNON, S. 2003. Adoptive cellular therapy for early cytomegalovirus infection after allogeneic stem-cell transplantation with virus-specific T-cell lines. *The Lancet,* 362**,** 1375-1377.

RENNERT, R. C., SORKIN, M., GARG, R. K. & GURTNER, G. C. 2012. Stem cell recruitment after injury: lessons for regenerative medicine. *Regenerative medicine,* 7**,** 833-850.

PINTO DO Ó P, RICHTER K, & CARLSSON L. 2002. Hematopoietic progenitor/stem cells immortalized by Lhx2 generate functional hematopoietic cells in vivo. *Blood*, 99, 3939-3946.

PINTO DO Ó P, KOLTERUD Å, & CARLSSON L. 1998. Expression of the LIM-homeobox gene LH2 generates immortalized Steel factor-dependent multipotent hematopoietic precursors. *EMBO Journal*, 17**,** 5744-5756.

POTTER, R. & GROOM, A. 1983. Capillary diameter and geometry in cardiac and skeletal muscle studied by means of corrosion casts. *Microvascular Research,* 25**,** 68-84.

RODRIGUEZ, M. L., MCGARRY, P. J. & SNIADECKI, N. J. 2013. Review on cell mechanics: experimental and modeling approaches. *Applied Mechanics Reviews,* 65**,** 060801.

ROJAS, M., XU, J., WOODS, C. R., MORA, A. L., SPEARS, W., ROMAN, J. & BRIGHAM, K. L. 2005. Bone marrow–derived mesenchymal stem cells in repair of the injured lung. *American journal of respiratory cell and molecular biology,* 33**,** 145-152.

RODRIGUEZ-PORCEL, M. 2010. In vivo imaging and monitoring of transplanted stem cells: clinical applications. *Current Cardiology Reports,* 12**,** 51-58.

RÜSTER, B., GÖTTIG, S., LUDWIG, R. J., BISTRIAN, R., MÜLLER, S., SEIFRIED, E., GILLE, J. & HENSCHLER, R. 2006. Mesenchymal stem cells display coordinated rolling and adhesion behavior on endothelial cells. *Blood,* 108**,** 3938-3944.

SATO, Y., ARAKI, H., KATO, J., NAKAMURA, K., KAWANO, Y., KOBUNE, M., SATO, T., MIYANISHI, K., TAKAYAMA, T. & TAKAHASHI, M. 2005. Human mesenchymal stem cells xenografted directly to rat liver are differentiated into human hepatocytes without fusion. *Blood,* 106**,** 756-763.

SAITO, H., LAI, J., ROGERS, R. & DOERSCHUK, C. M. 2002. Mechanical properties of rat bone marrow and circulating neutrophils and their responses to inflammatory mediators. *Blood,* 99**,** 2207-2213.

SCHREPFER, S., DEUSE, T., REICHENSPURNER, H., FISCHBEIN, M., ROBBINS, R. & PELLETIER, M. Stem cell transplantation: the lung barrier. Transplantation proceedings, 2007. Elsevier, 573-576.

SEGERS, V. F. & LEE, R. T. 2008. Stem-cell therapy for cardiac disease. *Nature,* 451**,** 937-942.

SEGRE, G. & SILBERBERG, A. 1961. Radial Particle Displacements in Poiseuille Flow of Suspensions. *Nature,* 189**,** 209-210.

SHAMBLOTT, M. J., AXELMAN, J., WANG, S., BUGG, E. M., LITTLEFIELD, J. W., DONOVAN, P. J., BLUMENTHAL, P. D., HUGGINS, G. R. & GEARHART, J. D. 1999. Derivation of Pluripotent Stem Cells From Cultured Human Primordial Germ Cells. *Obstetrical & gynecological survey,* 54**,** 177-178.

SIA, S. K. & WHITESIDES, G. M. 2003. Microfluidic devices fabricated in poly (dimethylsiloxane) for biological studies. *Electrophoresis,* 24**,** 3563-3576.

SOHNI, A. & VERFAILLIE, C. M. 2013. Mesenchymal Stem Cells Migration Homing and Tracking. *Stem Cells International*, 1-8

SPANGRUDE, G. J. 1991. Hematopoietic stem-cell differentiation. *Current opinion in immunology,* 3**,** 171-178.

STAN, C. A., ELLERBEE, A. K., GUGLIELMINI, L., STONE, H. A. & WHITESIDES, G. M. 2013. The magnitude of lift forces acting on drops and bubbles in liquids flowing inside microchannels. *Lab on a Chip,* 13**,** 365-376.

STAMENOVIĆ, D. & INGBER, D. E. 2002. Models of cytoskeletal mechanics of adherent cells. *Biomechanics and modeling in mechanobiology,* 1**,** 95-108.

STORM, C., PASTORE, J. J., MACKINTOSH, F. C., LUBENSKY, T. C. & JANMEY, P. A. 2005. Nonlinear elasticity in biological gels. *Nature,* 435**,** 191-194.

SUNG, J., YANG, H.-M., PARK, J., CHOI, G.-S., JOH, J.-W., KWON, C., CHUN, J., LEE, S.-K. & KIM, S.-J. Isolation and characterization of mouse mesenchymal stem cells. Transplantation proceedings, 2008. Elsevier, 2649-2654.

SUMMERS, C., RANKIN, S. M., CONDLIFFE, A. M., SINGH, N., PETERS, A. M. & CHILVERS, E. R. 2010. Neutrophil kinetics in health and disease. *Trends in immunology,* 31**,** 318-324.

SINGH, U. P., SINGH, N. P., SINGH, B., MISHRA, M. K., NAGARKATTI, M., NAGARKATTI, P. S. & SINGH, S. R. 2010. Stem cells as potential therapeutic targets for inflammatory bowel disease. *Front Biosci (Schol Ed),* 2**,** 993-1008.

SUN, J., LIU, C., LI, M., WANG, J., XIANYU, Y., HU, G. & JIANG, X. 2013. Size-based hydrodynamic rare tumor cell separation in curved microfluidic channels. *Biomicrofluidics,* 7**,** 011802.

SUN, J., STOWERS, C. C., BOCZKO, E. M. & LI, D. 2010. Measurement of the volume growth rate of single budding yeast with the MOSFET-based microfluidic Coulter counter. *Lab on a Chip,* 10**,** 2986-2993.

SCHMITZ, B., RADBRUCH, A., KÜMMEL, T., WICKENHAUSER, C., KORB, H., HANSMANN, M., THIELE, J. & FISCHER, R. 1994. Magnetic activated cell sorting (MACS)-a new immunomagnetic method for megakaryocytic cell isolation: comparison of different separation techniques. *European Journal of Haematology,* 52**,** 267-275.

TAKAHASHI K, YAMANAKA S. 2006. Induction of pluripotent stem cells from mouse embryonic and adult fibroblast cultures by defined factors. *Cell.* 126，663-676.

TAKAHASHI, K., TANABE, K., OHNUKI, M., NARITA, M., ICHISAKA, T., TOMODA, K. & YAMANAKA, S. 2007. Induction of pluripotent stem cells from adult human fibroblasts by defined factors. *cell,* 131**,** 861-872.

TEAGUE, T. K., MUNN, L., ZYGOURAKIS, K. & MCINTYRE, B. W. 1993. Analysis of lymphocyte activation and proliferation by video microscopy and digital imaging. *Cytometry,* 14**,** 772-782.

TRELEAVEN, J. & BARRETT, A. J. 2009. Hematopoietic Stem Cell Transplantation: In Clinical Practice, *Churchill Livingstone/Elsevier,* 44，271.

TREPAT, X., DENG, L., AN, S. S., NAVAJAS, D., TSCHUMPERLIN, D. J., GERTHOFFER, W. T., BUTLER, J. P. & FREDBERG, J. J. 2007. Universal physical responses to stretch in the living cell. *Nature,* 447**,** 592-595.

TSE, W. Y., NASH, G. B., HEWINS, P., SAVAGE, C. O. & ADU, D. 2005. ANCA-induced neutrophil F-actin polymerization: implications for microvascular inflammation. *Kidney international,* 67**,** 130-139.

TSIEN, R., POZZAN, T. & RINK, T. 1982. Calcium homeostasis in intact lymphocytes: cytoplasmic free calcium monitored with a new, intracellularly trapped fluorescent indicator. *The Journal of Cell Biology,* 94**,** 325-334.

TURNER, M. L., ANTHONY, R. S., PARKER, A. C. & MCILWAINE, K. 1995. Differential expression of cell adhesion molecules by human hematopoietic progenitor cells from bone marrow and mobilized adult peripheral blood. *Stem Cells,* 13**,** 311-316.

TRICKEY, W. R., BAAIJENS, F. P., LAURSEN, T. A., ALEXOPOULOS, L. G. & GUILAK, F. 2006. Determination of the Poisson's ratio of the cell: recovery properties of chondrocytes after release from complete micropipette aspiration. *Journal of biomechanics,* 39**,** 78-87.

UCCELLI, A., MORETTA, L. & PISTOIA, V. 2008. Mesenchymal stem cells in health and disease. *Nature Reviews Immunology,* 8**,** 726-736.

VARGAS-PINTO, R., GONG, H., VAHABIKASHI, A. & JOHNSON, M. 2013. The effect of the endothelial cell cortex on atomic force microscopy measurements. *Biophysical journal,* 105**,** 300-309.

WARKIANI, M. E., GUAN, G., LUAN, K. B., LEE, W. C., BHAGAT, A. A. S., CHAUDHURI, P. K., TAN, D. S.-W., LIM, W. T., LEE, S. C. & CHEN, P. C. 2014. Slanted spiral microfluidics for the ultra-fast, label-free isolation of circulating tumor cells. *Lab on a Chip,* 14**,** 128-137.

WHETTON, A. D. & GRAHAM, G. J. 1999. Homing and mobilization in the stem cell niche. *Trends in cell biology,* 9**,** 233-238.

WHITE, R. L., NASH, G., KAVANAGH, D. P., SAVAGE, C. O. & KALIA, N. 2013. Modulating the adhesion of haematopoietic stem cells with chemokines to enhance their recruitment to the ischaemically injured murine kidney. *PloS one,* 8**,** e66489.

WIGGS, B. R., ENGLISH, D., QUINLAN, W. M., DOYLE, N. A., HOGG, J. C. & DOERSCHUK, C. M. 1994. Contributions of capillary pathway size and neutrophil deformability to neutrophil transit through rabbit lungs. *Journal of Applied Physiology,* 77**,** 463-470.

WULFF, S., MARTIN, K., VANDERGAW, A., BOENISCH, T., BROTHERICK, I., HOY, T., HUDSON, J., JESPERSGAARD, C., LOPEZ, P. & ORFAO, A. 2006. *Guide to flow cytometry*, Dako Cytomation.

WU, Y., LU, H., CAI, J., HE, X., HU, Y., ZHAO, H. & WANG, X. 2009. Membrane surface nanostructures and adhesion property of T lymphocytes exploited by AFM. *Nanoscale research letters,* 4**,** 942-947.

XU, J., TSENG, Y. & WIRTZ, D. 2000. Strain Hardening of actin filament networks regulation by the dynamic cross-linking protein α-actinin. *Journal of Biological Chemistry,* 275**,** 35886-35892.

YAN, Y., ZHANG, Z., STOKES, J. R., ZHOU, Q.-Z., MA, G.-H. & ADAMS, M. J. 2009. Mechanical characterization of agarose micro-particles with a narrow size distribution. *Powder Technology,* 192**,** 122-130.

YAP, B. & KAMM, R. D. 2005. Mechanical deformation of neutrophils into narrow channels induces pseudopod projection and changes in biomechanical properties. *Journal of Applied Physiology,* 98**,** 1930-1939.

YANG, J., HUANG, Y., WANG, X.-B., BECKER, F. F. & GASCOYNE, P. R. 1999. Cell separation on microfabricated electrodes using dielectrophoretic/gravitational field-flow fractionation. *Analytical Chemistry,* 71**,** 911-918.

YEMM, A. I. 2014. Enhancing haematopoeitic stem cell recruitment to injured murine colon. *University of Birmingham.*

YU, J., VODYANIK, M. A., SMUGA-OTTO, K., ANTOSIEWICZ-BOURGET, J., FRANE, J. L., TIAN, S., NIE, J., JONSDOTTIR, G. A., RUOTTI, V. & STEWART, R. 2007. Induced pluripotent stem cell lines derived from human somatic cells. *Science,* 318**,** 1917-1920.

YUAN, B., JIN, Y., SUN, Y., WANG, D., SUN, J., WANG, Z., ZHANG, W. & JIANG, X. 2012. A strategy for depositing different types of cells in three dimensions to mimic tubular structures in tissues. *Advanced Materials,* 24**,** 890-896.

ZHANG, Z., FERENCZI, M., LUSH, A. & THOMAS, C. 1991. A novel micromanipulation technique for measuring the bursting strength of single mammalian cells. *Applied microbiology and biotechnology,* 36**,** 208-210.

ZHAO, L.-R., DUAN, W.-M., REYES, M., KEENE, C. D., VERFAILLIE, C. M. & LOW, W. C. 2002. Human Bone Marrow Stem Cells Exhibit Neural Phenotypes and

Ameliorate Neurological Deficits after Grafting into the Ischemic Brain of Rats. *Experimental Neurology,* 174**,** 11-20.

ZON, L. I. 1995. Developmental biology of hematopoiesis. *Blood,* 86**,** 2876-2891.

ZSEBO, K. M., WYPYCH, J., MCNIECE, I. K., LU, H. S., SMITH, K. A., KARKARE, S. B., SACHDEV, R. K., YUSCHENKOFF, V. N., BIRKETT, N. C. & WILLIAMS, L. R. 1990. Identification, purification, and biological characterization of hematopoietic stem cell factor from buffalo rat liver-conditioned medium. *Cell,* 63**,** 195-201.